

# DEVELOPMENT, PROCESSING AND FABRICATION OF A NICKEL BASED NICKEL-CHROMIUM-IRON ALLOY

*By*

Dotun Adebayo AKINLADE

A thesis submitted in partial fulfillment of  
the requirements for the degree of

**Doctor of Philosophy**

University of Manitoba

Copyright © 2008 by Dotun A. Akinlade

**THE UNIVERSITY OF MANITOBA**  
**FACULTY OF GRADUATE STUDIES**  
\*\*\*\*\*  
**COPYRIGHT PERMISSION**

**DEVELOPMENT, PROCESSING AND FABRICATION OF A NICKEL BASED NICKEL-  
CHROMIUM-IRON ALLOY**

**BY**

**Dotun Adebayo Akinlade**

**A Thesis/Practicum submitted to the Faculty of Graduate Studies of The University of  
Manitoba in partial fulfillment of the requirement of the degree**

**Doctor of Philosophy**

**Dotun Adebayo Akinlade © 2008**

**Permission has been granted to the University of Manitoba Libraries to lend a copy of this  
thesis/practicum, to Library and Archives Canada (LAC) to lend a copy of this thesis/practicum,  
and to LAC's agent (UMI/ProQuest) to microfilm, sell copies and to publish an abstract of this  
thesis/practicum.**

**This reproduction or copy of this thesis has been made available by authority of the copyright  
owner solely for the purpose of private study and research, and may only be reproduced and copied  
as permitted by copyright laws or with express written authorization from the copyright owner.**

## ACKNOWLEDGEMENTS

I would like to offer my sincerest gratitude to my supervisors, Drs M.C. Chaturvedi, N.L. Richards and W.F. Caley, who have supported me throughout my program with their patience, encouragements and knowledge. One simply could not wish for better or friendlier supervisors.

I acknowledge the financial support from my supervisors and University of Manitoba graduate studies. I also acknowledge Dr D.P. Bishop of Dalhousie University for his support, and for allowing me to use his equipments during my stay at Halifax. My appreciation also goes to Dr. K. Plucknett, Darren and Ian MacKskill of Dalhousie University; Dr J.R. Cahoon for manuscript contribution in combustion synthesis, Dr. Sidhu, Dan, Don, Mike and John Vandorp for their technical assistance and to my fellow graduate students especially Seun and Krutika.

Above all, my greatest appreciation goes to the almighty Jehovah, the source of wisdom, life and strength. Finally, I would like to thank my parents, brothers and sisters for their support and my loving wife Titilola for her understanding throughout my studentship.

## ABSTRACT

An optimal powder metallurgy (P/M) approach to produce a nickel base Superalloy similar in composition to INCONEL™ 600 was carried out utilising a simple uniaxial pressing process. The efficiencies of a lubricant addition, binder, sintering times and temperatures were measured in terms of green and sintered densities as well as microstructural changes that occurred during processing. It was observed that with increasing % polyvinyl alcohol (PVA), an overall decrease in density of compact was obtained and that using 0.75wt % of lubricant (microwax) green densities in excess of 70% can be obtained.

The samples were subsequently sintered in air at 1270°C for times ranging from 0.5h to 5h and also in vacuum (6 millitorr) with temperatures ranging from 1260 through to 1400°C. The air sintering was carried out to optimize sintering time, whereas the vacuum sintering was employed to optimize sintering temperature. On sintering for 5h in air, chromium enrichment occurred at the grain boundaries with subsequent depletion of nickel and iron; this was not noted for 2h sintering or for sintering under vacuum. The optimum sintering conditions were determined to be at 1300°C sintering for 2h in vacuum. The samples processed under the optimum conditions were successfully cold rolled to 40% of the original thickness without cracking.

An investigation was also undertaken to determine the effect of Al concentration (1-12w/o) on the microstructure of the powder metallurgically (P/M) processed Ni-Cr-Fe ternary alloy, with a view to determine the concentration of aluminium that would yield a homogeneously distributed and optimum volume fraction of the intermetallic- $\gamma'$ (Ni<sub>3</sub>Al) phase without the formation of topologically closed packed phases in the ternary alloy.

The phases that were likely to form with the variation in concentration of Al were first simulated by JMatPro™ thermodynamic software package, and then Ni-Cr-Fe alloys with varying concentration of aluminum were produced by P/M processing. The microstructure of the alloys was characterized by X-ray diffractometer (XRD), optical microscope (OM) and scanning electron microscope (SEM) equipped with energy dispersive spectrometer (EDS) and then compared with the thermodynamic predictions. It was observed that the experimental results matched reasonably closely with the thermodynamic predictions in terms of the phases present when Al was added to the ternary alloy, but not the volume fraction of the phases present in the microstructure. It was also observed by SEM image and quantitative EDS analysis that the optimum amount of well distributed Ni<sub>3</sub>Al phase formed when the concentration of aluminium was 6w/o. These results suggest that despite potential problems encountered in high temperature powder processing of Superalloys that often tend to influence the feasibility of using thermodynamic predictions to model such alloy systems, the software and predictions used in this study offer a way to simulate both design and characterisation of the experimental alloy.

To characterize the phases that formed in the 6w/o Al modified ternary Ni-Cr-Fe alloy during heating to the sintering temperature, a differential scanning calorimetric study was carried out to study sequence of phase transformations, their reaction modes and products on heating a green compact from room temperature to the sintering temperature of 1300°C. Two different heating rates were employed for the DSC study, 2.5°C/min and 10°C/min. Transformation reactions were also studied by heating the samples in a DSC to the points of exo/endothermicity and quenching in argon followed

by phase identification by X-ray diffraction, and microstructural analysis by SEM equipped with EDS capability. A series of  $Al_xNi_y$  and  $Al_xFe_y$  type intermetallics were observed to form by phase transformation at temperatures from 540°C to 1120°C.

The sequence of the formation of intermetallics by these phase transformations closely replicated the intermetallics that were predicted by the binary Ni-Al and the Fe-Al equilibrium phase diagrams, with the final microstructure being  $Ni_3Al$  ( $\gamma$ ), AlNi, AlFe in a Ni-Cr-Fe ( $\gamma$ ) matrix. Most of these phase transformations were diffusion controlled, but at 640°C AlNi formed by combustion synthesis. Selected mechanical property of the alloy at 1120°C which corresponds to the completion of transformations was estimated in terms of micro-hardness and compared to the as-sintered Ni-Cr-Fe ternary.

# TABLE OF CONTENTS

Content	Page
ACKNOWLEDGEMENTS	i
ABSTRACT	ii
TABLE OF CONTENTS	v
LIST OF FIGURES	xiii
LIST OF TABLES	xxii
CHAPTER ONE	1
1.0 INTRODUCTION	1
1.1 Powder metallurgy	1
1.2 Powder metallurgy of Superalloys	1
1.3 Thermodynamics compact modeling and compact fabrication	3
1.4 Quantitative analysis of phases formed on sintering	5
1.5 Research objectives	6
CHAPTER TWO	7
2.0 LITERATURE REVIEW	7
2.1 History of powder metallurgy	7
2.1.1 Historical development of nickel	7
2.1.2 Nickel production	8
2.1.3 Nickel alloy applications: Superalloys	10
2.1.4 Nickel alloy (Superalloys) developments	10

2.1.4.1	Physical properties of Superalloys	13
2.1.4.2	Strengthening in Superalloys	14
2.1.4.2.1	Solid solution hardening	14
2.1.4.2.2	Carbide strengthening	15
2.1.4.2.3	Precipitation hardening	16
2.1.5	Historical development P/M processing of Superalloys	21
2.1.6	Advantages of powder metallurgically processed Superalloys	23
2.1.7	Uses of Superalloys	24
2.2	Powder production, characterization and processing	25
2.2.1	Powder production	25
2.2.1.1	Centrifugal atomization	28
2.2.1.2	Vacuum or soluble-gas atomization	30
2.2.1.3	Ultrasonic atomization	30
2.2.1.4	Gas atomization	30
2.2.1.4.1	Process variables in gas atomization	35
2.2.1.4.2	Gas atomization stages	36
2.2.1.4.3	Particle size from adjustable parameters	37
2.2.2.1	Powder purity	41
2.2.2.2	Particle shape	42
2.2.2.3	Powder particle microstructure	44
2.2.3	Powder processing	46
2.2.3.1	Pre-shaping and pre-consolidation processes	46
2.2.3.2	Powder shaping and consolidation	47

2.2.4	Pre-sintering treatment	48
2.2.5	Sintering	48
2.2.5.1	Solid state sintering	49
2.2.5.2	Liquid phase sintering	50
2.2.5.2.1	Mechanisms of liquid phase sintering (thermodynamics and kinetics)	50
2.2.5.2.1.1	Surface energy	50
2.2.5.2.1.2	Solubility	52
2.2.5.2.1.3	Diffusivity	54
2.2.5.2.2	Stages of densification during LPS	55
2.2.5.2.2.1	Re-arrangement	55
2.2.5.2.2.2	Solution-precipitation and grain shape accommodation	56
2.2.5.2.2.3	Final stage sintering	57
2.2.6	Post sintering treatment	57
2.2.6.1	Heat treatment of P/M processed Superalloys	58
2.3	Theoretical considerations	59
2.3.1	Thermodynamics	59
2.4	Thermal analysis	61
2.4.1	Principles of DSC	61
2.4.2	Differential thermal analysis	63
2.5	Diffusion	66
2.6	Corrosion	67
2.6.1	Effect of Cr additions to Superalloys	67
2.6.2	Effect of rare earth additions to Superalloys	68

2.6.3	Effect of Al additions to Superalloys	69
2.6.4	Effect of Cr and Al additions to Superalloys	70
2.6.5	Oxidation mechanisms for pure metals at high temperatures	72
2.6.6	Oxidation mechanisms of alloy metals at high temperatures	74
CHAPTER THREE		78
3.0	EXPERIMENTAL PROCEDURES	78
3.1	Materials	78
3.1.1	Raw materials	78
3.2	Thermodynamic software modeling	78
3.3	Powder processing and characterization	79
3.3.1	Powder size characterization	79
3.3.2	Powder microstructural examination	80
3.3.3	Powder X-ray diffraction	80
3.3.4	Powder flow density calculation	80
3.4	Compact fabrication	81
3.4.1	Optimizing binder and lubricant	81
3.4.2	Pre-sintering	81
3.4.3	Sintering	81
3.4.4	Mercury and water densitometry	82
3.5	Heat treatment	82
3.6	Microstructural examination of sintered specimens	83
3.6.1	Optical and scanning electron microscopy	83

3.7	X-ray diffraction of sintered specimens	83
3.8	Differential scanning calorimetry sample preparation	84
3.9	Phase transformation in DSC	84
3.10	Hardness measurements	85
3.11	Mechanical working	85
3.12	Oxidation test	85
CHAPTER FOUR		87
4.0	RESULTS AND DISCUSSION	87
4.1	Material characterization	88
4.1.1	SEM analysis	88
4.1.2	Chemical analysis	95
4.1.3	Powder particle size analysis and powder flowability	96
4.1.4	XRD analysis of the “as-received” ternary Ni-Cr-Fe powder	98
4.2	Effect of polyvinyl alcohol (PVA) on density distribution of the ternary Ni-Cr-Fe alloy	103
4.3	Effect of lubricant (wax) on density distribution of the ternary Ni-Cr-Fe alloy	104
4.4	Ternary Ni-Cr-Fe alloy powder compaction	105
4.4.1	Uni-axial pressing of the ternary Ni-Cr-Fe alloy	107
4.5	Sintering of ternary Ni-Cr-Fe alloy	109
4.6	X-ray mapping of the air-sintered ternary Ni-Cr-Fe samples	115
4.6.1	Chromium X-ray map of the ternary Ni-Cr-Fe alloy	116
4.6.2	Nickel elemental X-ray map for the ternary Ni-Cr-Fe alloy	117

4.6.3	Iron elemental X-ray map for the ternary Ni-Cr-Fe alloy	118
4.6.4	Oxygen elemental X-ray map for the ternary Ni-Cr-Fe alloy	119
4.7	Air sintered density for the ternary Ni-Cr-Fe alloy	120
4.8	Hardness data of air-sintered ternary Ni-Cr-Fe samples	122
4.9	Vacuum sintering of the ternary Ni-Cr-Fe alloy	123
4.9.1	Effect of temperature on microstructure of vacuum-sintered samples	123
4.9.2	Mode of mass transfer during sintering	131
4.9.3	Estimation of the mechanical properties of the air and vacuum sintered samples	135
4.9.3.1	Hardness profile for the air sintered compacts	135
4.9.4	Relationship between fractional porosity and tensile strength	137
4.9.5	Post sintering operation: cold rolling	139
4.10	Effect of Al on the ternary powder	141
4.10.1	Thermodynamic predictions	141
4.10.2	Ni-Cr-Fe ternary alloy	142
4.10.3	Effect of Al on the density of ternary Ni-Cr-Fe alloy	146
4.11	1w/o Al modified ternary Ni-Cr-Fe alloy	147
4.12	3w/o Al modified ternary Ni-Cr-Fe alloy	152
4.13	6w/o Al modified ternary Ni-Cr-Fe alloy	156
4.13.1	Analysis of the Continuous Cooling Transformation (CCT) Curves of 6w/o Al Modified Ternary alloy	163
4.13.2	Discussion of the phase transformation on cooling 6w/o Al modified ternary	168
4.14	12w/o Al modified ternary Ni-Cr-Fe alloy	171
4.15.1	Differential scanning calorimetry (DSC)/SEM	176

4.15.1.1	SEM/EDS analysis of the DSC sample argon-quenched from 560°C	181
4.15.1.2	SEM/BSE analysis of the DSC sample argon-quenched from 640°C	183
4.15.1.3	SEM/EDS analysis of the DSC sample argon-quenched from 790°C	185
4.15.1.4	SEM/EDS analysis of the DSC sample argon-quenched from 830°C	187
4.15.1.5	SEM/EDS analysis of the DSC sample argon-quenched from 880°C	189
4.15.1.6	SEM/EDS analysis of the DSC sample argon-quenched from 1120°C	191
4.15.2	XRD analysis of phase changes on heating the Ni-Cr-Fe + Al quaternary	196
4.15.3	Mechanisms of reactions observed during heating of 6w/o Al modified ternary Ni-Cr-Fe to the sintering temperature	203
4.16	Heat treatment of the 6w/o Al modified ternary Ni-Cr-Fe alloy	208
4.16.1	Ageing of the 6w/o Al modified compact	208
4.16.2	Dissolution of the gamma prime precipitates	209
CHAPTER FIVE		212
5.0	SUMMARY AND CONCLUSIONS	212
5.1	Optimisation of processing parameters for the ternary Ni-Cr-Fe alloy	212
5.2	Effect of Al on the ternary Ni-Cr-Fe alloy	213
5.3	Thermodynamic modelling of 6w/o Al modified ternary Ni-Cr-Fe alloy	214
5.4	Phase transformation on heating the 6w/o Al modified ternary Ni-Cr-Fe alloy to 1300°C sintering temperature	215

Future work	216
APPENDIX A 217	
Effect of 1w/o and 3w/o Ti on the 6w/o Al modified ternary Ni-Cr-Fe alloy	217
APPENDIX B 219	
B. 1 Catalogue of step calculations for selected compositions	219
REFERENCES	232
ARTICLES FROM THIS THESIS	243

## LIST OF FIGURES

Figure	Page
Figure 2.1 Developmental trends in the alloy and processing of Superalloys [1]	12
Figure 2.2a: Genesis of nickel alloy microstructure 1940 to 1970 [20]	19
Figure 2.2b: Common unwanted phases or structures in nickel alloys from 1940 to 1970 (X10,000) [20]	20
Figure 2.3a: Mechanical methods of powder production [31, 34]	26
Figure 2.3b Chemical methods of powder production [31, 34]	27
Figure 2.4 Schematic of the rotating electrode process (REP)	
(a) Plasma arc rotating electrode process (PREP) [33].	29
(b) Tungsten rotating electrode process showing the rotating arc [33]	29
Figure 2.5 Layout of an atomizer of fine metal powders by close coupled gas atomization [36]	32
Figure 2.6: Two-fluid atomization with a) Free-fall design (gas or water)	
(b) Confined nozzle design (gas only) [33]	33
Figure 2.7 Model for disintegration of a liquid sheet by a high-velocity gas jet [37]	37
Figure 2.8 a) Spherical shaped powder particle typical of the pre-alloyed powder used in this study [43]	43
Figure 2.8 b) Spherical powder particles with satellites [43]	44
Figure 2.9 Dihedral angle and surface energy equilibrium between two intersecting grains with a partially penetrating liquid phase [44]	52
Figure 2.10a Alloy dilute in B showing internal oxidation of B [67]	74
Figure 2.10b Alloy concentrated in B showing external layer of BO [67]	74
Figure 2.11a Alloy concentrated in B showing continuous external BO	76
Figure 3.1 Simplified alloy development process	86
Figure 4.2a: SEM secondary electron image of	

the “ as-received” powder at 250X	89
Figure 4.2b: SEM secondary electron image of the “ as-received” powder at 650X	89
Figure 4.2c: SEM secondary electron image of the “ as-received” powder at 1400X	90
Figure 4.2d: SEM secondary electron image of the “ as-received” powder at 2000X	90
Figure 4.3: SEM mapping image of a typical powder particle to show if there is segregation in the particle. a) Electron Image, b) Ni map, c) Cr map, d) Iron map	92
Figure 4.4 a): SEM-BSE image of the second batch “as-received” ternary	93
Figure 4.4 b): X-ray map for Fe	93
Figure 4.4 c): X-ray map for Ni	94
Figure 4.4 d): X-ray map for Cr	94
Figure 4.5: Powder particle size distribution of the “as-received” ternary Ni-Cr-Fe alloy	97
Figure 4.6: XRD spectrum of the “as-received” ternary Ni-Cr-Fe powder	99
Figure 4.7a: Ni-Cr-Fe ternary phase diagram showing alloy composition at 1300°C [77]	100
Figure 4.7b: Ni-Cr-Fe ternary phase diagram showing alloy composition at solidus projection [77]	101
Figure 4.7c: Ni-Cr-Fe ternary phase diagram showing alloy composition at liquidus projection [77]	102
Figure 4.8: Effect of PVA on the green density of the compact	103
Figure 4.9 Effect of lubricant and compacting pressures on the green density of the compact	104
Figure 4.10: Picture showing cold isostatically pressed powder	106
Figure 4.11: The effect of compacting pressure (at 0.75% lubricant wax) on the theoretical density (present work) with superimposition of various stages of deformation during powder compaction adapted after [2]	108

Figure 4.12: A typical air sintering curve for 2h equilibration at sintering temperature for the ternary Ni-Cr-Fe alloy	110
Figure 4.13: Secondary electron image showing microstructural changes after: a)0.5h, b) 1h, c)2h and d)5h of sintering at 1270°C for the ternary Ni-Cr-Fe	111
Figure 4.14a: Secondary electron image showing changes in the sintered sample after 0.5h of sintering, 1270°C for the ternary Ni-Cr-Fe	112
Figure 4.14b: Secondary electron image showing microstructural changes after 2h of sintering, 1270°C for the ternary Ni-Cr-Fe	112
Figure 4.15: Average porosity concentration as a function of time, air sinter, 1270°C for the ternary Ni-Cr-Fe	113
Figure 4.16: Secondary electron image of microstructural evolution after 5h of sintering for the ternary Ni-Cr-Fe alloy	115
Figure 4.17: X-ray mapping of chromium after 5h of sintering at 1270°C for the ternary Ni-Cr-Fe alloy	116
Fig 4.18: X-ray map of nickel after 5h of sintering at 1270°C for the ternary Ni-Cr-Fe alloy	117
Figure 4.19: X-ray mapping of iron after 5h of sintering at 1270°C for the ternary Ni-Cr-Fe alloy	118
Figure 4.20: X-ray map of oxygen as a function of time for the ternary Ni-Cr-Fe alloy	119
Figure 4.21: Air densification profile of the compact at 1270°C after varying times of sintering	120
Figure 4.22: Schematic representation of pore and oxide formation during air sintering of the ternary Ni-Cr-Fe alloy	121
Figure 4.23: Hardness data of ternary Ni-Cr-Fe samples sintered in air for different times	122
Figure 4.24: Variation in percentage theoretical density of Ni-Cr-Fe alloy as a function of sintering temperature (1h sinter)	123
Figure 4.25a: SEM secondary electron image of ternary Ni-Cr-Fe sample sintered at 1260°C (Vacuum <6 millitorr)	124

Figure 4.25b: SEM secondary electron image of ternary Ni-Cr-Fe sample sintered at 1280°C for 1h (vacuum <6 millitorr)	125
Figure 4.25c: SEM secondary electron image of ternary Ni-Cr-Fe samples sintered at 1300°C for 1h (vacuum <6 millitorr)	126
Figure 4.25e: SEM secondary electron image of ternary Ni-Cr-Fe samples sintered at 1350°C for 1h (vacuum <6 millitorr)	127
Figure 4.25f: SEM secondary electron image of ternary Ni-Cr-Fe samples sintered at 1400°C for 1h (vacuum <6 millitorr)	128
Figure 4.26: Optical micrograph of the sintered ternary Ni-Cr-Fe alloy at a) 1260°C for 1h, b) 1300°C for 1h and c) 1400°C for 1h	129
Figure 4.27: Plot of %TD as a function of sintering time in vacuum (6 millitorr, 1300°C) for ternary Ni-Cr-Fe alloy	130
Figure 4.28: Schematic view of growing bond showing routes of six methods of mass transfer[86] a) surface transfer process (1 and 2); b) bond-line transfer process (3 and 4); c) bulk deformation process (5 and 6)	132
Figure 4.29a: Illustration of the sides from where hardness of the sintered samples was determined.	135
Figure 4.29b: Brinell hardness variation of various samples sintered at 1270°C for 0.5, 1, 2, and 5h	136
Figure 4.30: 3-D deformation diagram for the cold rolled sintered compact	140
Figure 4.31a: The JMatPro thermodynamic calculation for the base ternary Ni-Cr-Fe alloy showing presence of austenite	143
Figure 4.31b: DSC trace of the ternary Ni-Cr-Fe alloy as it was heated to the melting temperature	144
Figure 4.32a: Optical Micrograph of the ternary Ni-Cr-Fe alloy after heating to 1300oC /2h and furnace cooling showing the presence of fine grains and porosity	144
Figure 4.32b: SEM-BSE image of the ternary Ni-Cr-Fe alloy.	145
Figure 4.33: XRD pattern of the ternary powder after sintering	145
Figure 4.34: Effect of Al on the sintered density of the Ni-Cr-Fe ternary alloy	147

Figure 4.35a: JMatPro prediction for the step calculations of the 1w/o Al modified Ni-Cr-Fe ternary alloy	149
Figure 4.35b: JMat Pro prediction of the CCT curve of the 1w/o Al modified Ni-Cr-Fe ternary alloy	150
Figure 4.35c: XRD pattern of the 1w/o Al modified ternary powder after sintering	150
Figure 4.35d: Backscattered electron image showing the area of EDS analysis (Table 4.7) of the 1 w/o Al modified Ni-Cr-Fe alloy	151
Figure 4.36a: JMatPro prediction of the phases expected to form in the 3w/o Al modified Ni-Cr-Fe ternary alloy	152
Figure 4.36b: JMatPro prediction of the CCT curve of the 3w/o Al modified Ni-Cr-Fe ternary alloy	153
Figure 4.36c: XRD pattern of the 3w/o Al modified ternary alloy compact after sintering	154
Figure 4.36d: Backscattered electron image and EDS area analysis of the 3w/o Al modified Ni-Cr-Fe alloy	155
Figure 4.37a: JMatPro predictions for the 6w/o Al modified Ni-Cr-Fe ternary alloy	157
Figure 4.37b: JMatPro prediction of the CCT curve for the 6 w/o Al modified Ni-Cr-Fe ternary alloy at 0.5% transformation	157
Figure 4.37c: JMatPro prediction of the CCT curve for the 6 w/o Al modified Ni-Cr-Fe ternary alloy	158
Figure 4.37d: Backscattered electron image of the 6 w/o Al modified Ni-Cr-Fe alloy	159
Figure 4.37e: SEI-SEM image of the as sintered 6w/o Al modified Ni-Cr-Fe ternary alloy, showing fine (A) and coarse (B) gamma prime precipitates	160
Figure 4.37f: X-ray diffractogram of the 6w/o Al modified ternary Ni-Cr-Fe alloy after sintering for 2h at 1300°C	162
Figure 4.37g: SEM EDS line scan of the interface between Al and ternary Ni-Cr-Fe alloy after sintering, reheating to 1200oC for 4h and quenching. a) SEM-SEI image; b) Al elemental scan, c) Ni elemental scan; d) Fe elemental scan and e) Cr elemental scan	164

Figure 4.37h: JMatPro CCT curves for the 6w/o Al modified ternary Ni-Cr-Fe alloy showing the gamma prime transformation curves based on the 2.5°C/min cooling rate	165
Figure 4.37i: SEM image of the 6w/o Al modified ternary Ni-Cr-Fe alloy after cooling from the sintering temperature at 2.5 °C/min	166
Figure 4.37j: DSC trace of the quaternary (6w/o Al modified ternary Ni-Cr-Fe alloy) as it was cooled from the sintering temperature to room temperature. The onset of $\gamma'$ transformation is noted.	167
Figure 4.38a: JMatPro prediction of phase likely to form in 12 w/o Al modified Ni-Cr-Fe ternary alloy	173
Figure 4.38b: JMatPro prediction of the 0.5% phase detectability limit curve for the 12 w/o Al modified Ni-Cr-Fe ternary alloy	173
Figure 4.38c: Backscattered electron image of the 12 w/o Al modified Ni-Cr-Fe alloy sinter for 2h at 1300°C	174
Figure 4.38d: XRD pattern and analysis of the 12w/o Al modified ternary powder after sintering	175
Figure 4.39: DSC trace of the 6w/o Al modified ternary Ni-Cr-Fe alloy at 10°C/min up to the melting temperature { X1 is onset of exothermic reaction for stage 1 and X2 is the onset of exothermic reaction peak for stage 2 }	178
Figure 4.40 DSC trace of the 6w/o Al modified ternary Ni-Cr-Fe alloy at 2.5°C/min up to the sintering temperature (1300°C) {Y1 is onset of first exothermic reaction peak and Y2 is the onset of the second exothermic reaction peak }	180
Figure 4.41: The differential DSC trace of the 6w/o Al modified ternary Ni-Cr-Fe alloy at 2.5oC/min up to the sintering temperature (1300°C)	180
Figure 4.42: SEM BSE Image showing the points of EDS analyses (a) and EDS line scans for b)Ni, c)Al, d)Cr and e)Fe of the sample heated to 560°C and argon-quenched	182
Figure 4.43: SEM BSE Image showing the points of EDS analyses (a) and EDS line scans for b)Ni, c)Al, d)Cr and e)Fe of the sample heated to 640°C and quenched	184
Figure 4.44. SEM BSE Image showing the points of EDS analyses (a) and EDS line scans for b) Ni, c) Al, d) Cr and e) Fe of the sample heated	

to 790°C and quenched	186
Figure 4.45: SEM BSE Image showing the points of EDS analyses (a) and EDS line scans for b) Ni, c) Al, d) Cr and e) Fe of the sample heated to 830°C and argon-quenched	188
Figure 4.46 SEM BSE Image showing the points of EDS analyses (a) and EDS line scans for b) Ni, c) Al, d) Cr and e) Fe of the sample heated to 880°C and quenched	190
Figure 4.47 SEM BSE Image showing the points of EDS analyses (a) and EDS line scans for b) Ni, c) Al, d) Cr and e) Fe of the sample heated to 1120°C and quenched	192
Figure 4.48 SEM BSE micrograph showing the points of EDS analyses of Table 4.13 that correspond to the Ni <sub>3</sub> Al intermetallic composition	193
Figure 4.49 a): the Al-Ni binary phase diagram [77]	195
Figure 4.49 b): the Al-Fe binary phase diagram [77]	195
Figure 4.50a: X-ray diffractogram of the sample argon-quenched from 560°C	197
Figure 4.50b: X-ray diffractogram of the sample argon-quenched from 640°C	197
Figure 4.50c: X-ray diffractogram of the sample argon-quenched from 790°C	198
Figure 4.50d: X-ray diffractogram of the sample argon-quenched from 830°C	199
Figure 4.50e: X-ray diffractogram of the sample argon-quenched from 880°C	200
Figure 4.50f: X-ray diffractogram of the sample argon-quenched from 1120°C	201
Figure 4.51: Vickers hardness of the alloy versus ageing from 0.5h to 15.5h at 650°C and 800°C	208
Figure 4.52a. Ni-Cr-Fe alloy with 6 w/o Al modified ternary	209
Figure 4.52b: SEM-SEI micrograph of 6w/o Al modified ternary Ni-Cr-Fe alloy after heat treatment at 970°C for 1h followed by air cool	210
Figure 4.52c: SEM-SEI micrograph of 6w/o Al modified ternary Ni-Cr-Fe alloy after heat treatment at 1010°C for 1h followed by air cool	210

Figure 4.52d: SEM-SEI micrograph of 6w/o Al modified ternary Ni-Cr-Fe alloy after heat treatment at 10500C for 1h followed by air cool	211
Figure A.1: The SEM secondary electron image for the 6w/oAl 1w/o Ti modified ternary Ni-Cr-Fe alloy	217
Figure A.2: The SEM secondary electron image for the 6w/oAl 3w/o Ti modified ternary Ni-Cr-Fe alloy	218
Figure A 3: The XRD analysis for the 6w/oAl 3w/o Ti modified ternary Ni-Cr-Fe alloy	218
Figure B. 1: JMatPro step calculations for the 1w/o Al, 6w/o Ti on the ternary Ni-Cr-Fe alloy	219
Figure B. 2: JMatPro step calculations for the 1w/o Al 9w/o Ti modified ternary Ni-Cr-Fe alloy	219
Figure B. 3: JMatPro step calculations for the 1w/o Al 12w/o Ti modified ternary Ni-Cr-Fe alloy	220
Figure B. 4: JMatPro step calculations for the 1w/o Re modified ternary Ni-Cr-Fe alloy	220
Figure B.5: JMatPro step calculations for the 1w/o Ti modified ternary Ni-Cr-Fe alloy	221
Figure B.6: JMatPro step calculations for the 3w/o Al modified ternary Ni-Cr-Fe alloy	221
Figure B.7: JMatPro step calculations for the 3w/oAl 1w/o Ti modified ternary Ni-Cr-Fe alloy	222
Figure B.8: JmatPro step calculations for the 3w/oAl 3w/o Ti modified ternary Ni-Cr-Fe alloy	222
Figure B.9: JmatPro step calculations for the 3w/oAl 6w/o Ti modified ternary Ni-Cr-Fe alloy	223
Figure B.10: JmatPro step calculations for the 3w/oAl 9w/o Ti modified ternary Ni-Cr-Fe alloy	223
Figure B.11: JmatPro step calculations for the 3w/oAl 12w/o Ti modified ternary Ni-Cr-Fe alloy	224
Figure B.12: JmatPro step calculations for the 3w/o Ti modified ternary	

Ni-Cr-Fe alloy	224
Figure B.13: JmatPro step calculations for the 6w/oAl 1w/o Re modified ternary Ni-Cr-Fe alloy	225
Figure B.14: JmatPro step calculations for the 6w/oAl 1w/o Ti modified ternary Ni-Cr-Fe alloy	225
Figure B.15: JmatPro step calculations for the 6w/oAl 3w/o Ti modified ternary Ni-Cr-Fe alloy	226
Figure B.16: JmatPro step calculations for the 6w/oAl 6w/o Ti modified ternary Ni-Cr-Fe alloy	226
Figure B.17: JmatPro step calculations for the 6w/o Al 9w/o Ti modified ternary Ni-Cr-Fe alloy	227
Figure B.18: JmatPro step calculations for the 6w/o Al 12w/o Ti modified ternary Ni-Cr-Fe alloy	227
Figure B.19: JmatPro step calculations for the 6w/o Ti modified ternary Ni-Cr-Fe alloy	228
Figure B.20: JmatPro step calculations for the 9w/o Al modified ternary Ni-Cr-Fe alloy	228
Figure B.21: JmatPro step calculations for the 12w/o Al modified ternary Ni-Cr-Fe alloy	229
Figure B.22: JmatPro step calculations for the 12w/o Al 1w/o Ti modified ternary Ni-Cr-Fe alloy	229
Figure B.23: JmatPro step calculations for the 12w/o Al 3w/o Ti modified ternary Ni-Cr-Fe alloy	230
Figure B.24: JmatPro step calculations for the 12w/o Al 9w/o Ti modified ternary Ni-Cr-Fe alloy	230
Figure B.25: JmatPro step calculations for the 12w/o Al 12w/o Ti modified ternary Ni-Cr-Fe alloy	231
Figure B.26: JmatPro step calculations for the 12w/o Ti modified ternary Ni-Cr-Fe alloy	231

## LIST OF TABLES

Table	Page
Table 2.1 A Summary of the role of elements in nickel and nickel-iron base Superalloys adapted from [23]	18
Table 2.2 Various shapes of powder particles and their typical methods of fabrication adapted from [43]	42
Table 3.1. Summary of Malvern laser particle analyzer specification	79
Table 4.1: Chemical analysis of the as-received powder	96
Table 4.2: Summary of the powder particle size analysis	97
Table 4.3: Table showing the “as-received” ternary Ni-Cr-Fe ternary powder flowability	97
Table 4.4: Hardness profile for the 12700C air sintered ternary Ni-Cr-Fe alloy	136
Table 4.5 HRB hardness profile of the 1h vacuum sintered ternary Ni-Cr-Fe alloy	137
Table 4.6: Table showing the varying Al w/o and the ternary Ni-Cr-Fe alloy	142
Table 4.7: EDS chemical analysis of the SEM-BES image of Figure 4.35d	151
Table 4.8: EDS analysis of the SEM-BES image of Figure 4.36d	155
Table 4.9: EDS chemical analysis of the area shown in Figure 4.37e	160
Table 4.10: EDS analysis of the quaternary compact after quenching from 560°C	183
Table 4.11: EDS analysis of the quaternary compact after heating to 640°C and quenched	185
Table 4.12: EDS analysis of the quaternary compact after heating to 790°C and quenched	187
Table 4.13: EDS analysis of the quaternary compact after heating to 830°C and quenched	187
Table 4.14: EDS analysis of the compact after heating to 880°C and quenched	189
Table 4.15: EDS analysis of the compact after heating to 1120°C and quenched	191

Table 4.16: Selected EDS analysis of the compact after heating to 1120°C and quenched	193
Table 4.17: Summary of the results of EDS analysis of various phases present in the compact at various temperatures during heating to 1120°C	194
Table 4.18: XRD analysis of various points of interest	202

# CHAPTER ONE

## 1.0 INTRODUCTION

### 1.1 Powder metallurgy

Powder metallurgy (P/M) is a process in which powders are processed into compacts and sintered into useable components for various applications. This process (P/M) has evolved to be of prime importance in the manufacturing of a large number of engineering components [1, 2]. In addition, P/M products can exhibit a relatively longer component life expectancy when compared to some cast materials. It has even been suggested that P/M processing of some alloys (e.g., a Superalloy) in the 100% dense condition may improve corrosion resistance of the materials in selected applications [3]. Of all its advantages, improved toughness, machineability, controlled grain size and more uniform heat treatment response are most significant, along with freedom from cast/wrought defects [4]. Additionally, the use of P/M processing can also help to control the amount of alloying elements required or intermetallic phases that form which could be difficult to achieve through traditional casting routes [5].

### 1.2 Powder metallurgy of Superalloys

Superalloys are high temperature, high strength materials having found applications in high temperature industries such as aerospace and power generation. The majority of Superalloys are based on nickel due to its excellent high temperature properties while others are based on cobalt.

Materials used in various applications are fabricated by different techniques. Examples of fabricating techniques used include casting and powder metallurgy. Of these fabricating processes, this thesis focuses on powder metallurgy processing of Superalloys. The raw materials for P/M processing may be in various forms such as elemental, pre-alloyed or master alloy [6], majority of which are found in the aluminum, steel and ceramics industries. In addition, powders are available in elemental, prealloyed or master alloyed form for various families of Superalloys.

Although elemental, pre-alloyed and master alloy powders are available for Superalloys, most Superalloys are fabricated via casting processes such as vacuum induction melting, electron beam melting, plasma melting and vacuum arc melting. These processes are used to tailor Superalloys properties for various applications either by producing equi-axed grains, directionally solidified or single crystal Superalloy products [7]. The reasons for not using P/M for Superalloy may be related to history/experience of using wrought materials, complexity of P/M processing and large formability problems of which compressibility and prior particle boundaries of the Superalloy powders are quite significant [8]. These problems may restrict processing due to inability to achieve a full theoretical density. For example, the compressibility is usually estimated by deformation pressure, density and porosity in the sintered product, while the presence of prior particle boundaries results in poor sintering that leads to the presence of closed porosity in the final sample. This may also lead to segregation in the grains or at the grain boundaries.

Although these problems seem significant, it should be noted that except for special casting processes that may involve directional solidification and single crystal growth, powder metallurgy is still a relatively flexible process and also commercially

attractive. Thus, it will be of interest to produce a Superalloy through P/M processing and at the same time develop a process that reduces the problems associated with P/M for the selected alloy.

Hence, one of the goals of this research involved the P/M processing of a simple nickel-chromium-iron Superalloy with particular emphasis on optimizing parameters such as compacting pressure, lubricant weight, binder types and composition, sintering temperature and time; and by adding elemental Al in order to encourage precipitation hardening.

### **1.3 Thermodynamics, compact modeling and compact fabrication**

In processing Superalloys for various applications, different compositions are employed. The selection of a desired composition for a particular application is expensive, time consuming and usually empirical, especially in the case of Superalloys that typically contain about 10-15 main elements and other trace elements such as boron because engineering materials play a crucial role in any new technological advancement, rapid methods of alloy development are necessary. In many applications, the use of thermodynamic-based modeling tools to explore equilibrium and complex relationships between phases is common [9-12]. These tools provide various benefits which include information about the types of reactions that occur, the types of phases that form, their properties, the materials developed, as well as information about problems that may be encountered in materials at equilibrium and, at times, under non-equilibrium conditions [10, 11]. Furthermore, information can also be obtained such as phase(s) changes in relation to a material's composition, temperature, pressure or time [10].

Several of these thermodynamic-based tools have been studied. For example Chen *et al* [10] listed breakthroughs in thermodynamic calculations using PANDAT software and related the success of the tool (PANDAT software) to its ability to predict some material properties and subsequently verify the predictions experimentally. Unfortunately, some of these thermodynamic predictions still lack the ability to be directly applied to some real situations and processes [11, 12]. These include the inability to predict the effect of parameters that are easily varied experimentally including the time-temperature-transformations (TTT), continuous-cooling-transformations (CCT) and thermophysical properties [11].

The shortcomings in some of the thermodynamic-based tools result in variance between predictions and experiments, which tend to negate the usefulness of such tools. However, if such shortcomings can be eliminated, not only would it give a better understanding of the real situations by simulation, it would also be helpful in predicting the feasibility of some processes such as single crystal growth, directional solidification and powder metallurgical processing. A number of thermodynamic-based tools have focused mainly on commonly-used fabricating processes such as single crystal growth and casting [12]. However, the successful use of such tools in other fabricating processes such as powder metallurgical (P/M) processing, and reliability of prediction has not been fully established and tested.

Therefore, to address this issue, another goal of the research was on using a thermodynamic software package to predict various phases that can form during heating and after cooling the optimized P/M processed material. Specifically, the types and nature of products (phases) were investigated after modification by a suitable element (Al)

addition while optimizing the amount and composition of these phases. Al was chosen for this study because of its beneficial effects on the alloy.

#### **1.4 Quantitative analysis of phases formed on sintering**

After modeling the ternary alloy, there may be a need to add elements in order to improve properties. When elements are added, the actual mixing of desired powders to provide a composition for a specific requirement may or may not lead to the occurrence of a chemical reaction. In some cases the reaction is a spontaneous process giving significant heat, while in others, reactions need to be thermally activated before they occur, and in some cases they may not even occur at all. A differential scanning calorimeter (DSC)/differential thermal analyzer (DTA) can be used for measuring heat flow and other thermo-physical properties of such reactions. Some examples of systems where DSC/DTA has been used to study sintering reaction include Ni-Al [13], Ti-C [14] and alloy systems and those related to the use of pre-alloyed metal powders such as Ni-Cr-Fe.

In this research project, the effect of Al on the P/M processed ternary was studied during heating of a Ni-Cr-Fe and Al compact to the sintering temperature. When heated, Al and the ternary powders would interact with each other forming different types of intermetallics which could be based on the binary systems Ni-Al, Fe-Cr, Al-Fe, Al-Cr, Ni-Cr, Fe-Ni, or ternary and quaternary systems based on Ni, Cr, Fe and Al depending on the thermodynamic and kinetic conditions for their formation being favorable.

In order to understand the sintering mechanism when Ni-Cr-Fe and Al powders are reacted, it is essential to understand the types and sequence of reactions that take

place, especially as Al melts at 660°C, well before the sintering temperature (1300°C) is reached. Hence, another focus of this research was to investigate the type/nature of reactions that occur as well as the phases that form at various temperatures during sintering.

## **1.5 Research objectives**

In summary, the goals and objectives of this research can be simplified and stated as follows.

- ⇒ Develop a nickel base Superalloy using powder metallurgy
- ⇒ Investigate the effects of thermal processing on the microstructural response of Al modified ternary Ni-Cr-Fe alloy and subsequent verification of the thermodynamically modeled properties using JMatPro package.
- ⇒ Investigate the microstructural properties (i.e., phases formed), the types, nature, and temperatures of phases formed during heating to, and cooling from the sintering temperature.

## CHAPTER TWO

### 2.0 LITERATURE REVIEW

#### 2.1 History of powder metallurgy

Powder metallurgy (P/M) processing starts with the production of compacts using powders. Powders are groups of particles larger than the particles present in smoke (0.01 to 1 $\mu$ m) but smaller than sand particles (0.1 to 3mm) [2]. The use of powders can be traced back to the ancient Egyptian times when Egyptians used sponge iron to make tools by heating iron oxide in charcoal and crushing the shell followed by hammering the resultant sponge into final shapes. A similar process was seemed to have been used in India in the fabrication of the Delhi Pillar weighing approximately 6.5 tons [15] made through ancient method of iron-oxide reduction. In addition, there were evidences that P/M practices were used for artefacts fabrication by the Incas before the onset of Christopher Columbus' journey in 1492. However "this art" as it was so called then, was reduced in usage and discontinued, only to be revived in the 18<sup>th</sup> century in Europe with various production methods associated with platinum [15].

##### 2.1.1 Historical development of nickel

Before discussing the use of nickel base alloys and its subsequent powder metallurgy productions and applications, a brief history and analysis of the element nickel would be necessary. The use of nickel has made a significant contribution to the development of present day societies. Evidences exist that nickel metal is contained in various artefacts such as tools, coins, weapons and other materials [7]. The earliest nickel metal was referred to as white copper or Pai-Thong by Chinese. They used Pai-Thong for

manufacturing candlesticks. These metals were brought by the East India Company into Europe [16].

In the early part of the eighteenth century, miners in Germany while smelting copper ores discovered that the white metal produced in the process was too hard to be forged causing the miners to assume that the white metal was cursed. In fact, they referred to the metal as ‘Old Nick’s Copper or Kupfer-Nickel” [7]. It was not until A.F Cronstedt separated the metal and identified it as nickel that the white metal was recognized as not being a cursed metal, but a different type of metal.

### **2.1.2 Nickel production**

The Norwegian mines began nickel mining in the mid-1800s with significant ore discoveries in the south pacific island of New Caledonia. Also, large findings of nickel ore deposits were discovered in Sudbury, Ontario Canada.

To produce nickel from the ore, various methods are used. Examples of techniques used in producing Nickel are:

- a) Pyrometallurgical process. This is a process in which ore concentrates are calcined in a roasting furnace, smelted in a reverberatory furnace and blown with air in a converter [7]. The nickel and copper (because copper is usually found in nickel ores) are refined by removing the remaining unwanted elements such as antimony, arsenic, bismuth, lead, phosphorous, sulfur, tin and zinc, so as to improve the nickel concentration.
- b) Another method of nickel production is through hydrometallurgy. Hydrometallurgical process for producing nickel includes electro-refining and

electro-winning. These are electrolytic methods of nickel production. This process usually involve making the crude nickel the anode and a pure thin nickel the cathode. These electrodes are immersed in suitable electrolyte and direct current is passed through the electrodes. Pure nickel is then deposited on the cathode while impurities go into the solution.

- c) The third method of nickel production is vapometallurgy, this process was discovered by Lord Mond in the late 18<sup>th</sup> century. This is a carbonyl process which uses gas-to-metal transformation to extract nickel from impure nickel oxide [17]. The nickel oxide is reduced by hydrogen and nickel is subsequently made to selectively react with carbon monoxide forming gaseous nickel carbonyl. Following this, the carbonyl gas is then decomposed by heat to yield pure nickel [17].

### **2.1.3 Nickel alloy applications: Superalloys**

Most of the commonly used nickel alloys are grouped under a class of materials known as Superalloys, being materials used at high temperature and high strength applications. Today, Superalloys are classified based on the elements in the group VIIIA and are generally grouped according to their matrix forming elements as:

- Nickel-base Superalloys
- Nickel-iron base Superalloys
- Cobalt base Superalloys.

A Superalloy matrix is usually soluble to a numbers of elements which when added may improve the overall particles of the alloy. When elements are added, strengthening in Superalloys results either by solid solution hardening, precipitation hardening. The strength of Superalloys is expressed in terms of tensile strength, stress rupture and creep properties. Other inherent properties of Superalloys include good ductility and impact resistance, good resistance to high and low cycle mechanical fatigue, and an attractive thermal fatigue resistance.

In this research, nickel and nickel-iron base alloys were used as reference for comparison. This is because of all the Superalloys, nickel and nickel-iron base Superalloys are the most widely used Superalloys. Also, significant properties of the nickel and nickel-iron base Superalloys apply to other type of Superalloys.

### **2.1.4 Nickel alloy (Superalloys) developments**

Since nickel separation/discovery as a metal, there have been various improvements in the design and development of nickel alloys. For example, monel (a

nickel copper base alloy) developed in 1905 was resistant to various environments, Marsh [18] pioneered the discovery of the Nimonic alloys, Elmwood Haynes [19] working on nickel-chromium binary alloys developed more wear-resisting alloys. In addition, Paul D. Merica worked on the use of nickel in cast irons, bronzes and steel and his unique discovery of precipitation strengthening abilities of Al and Ti are the basis for strength in Superalloys that are used in present day applications [7].

Other developments in nickel and its alloys include development by William A. Mudge; the Hastelloy series development during the 1920s, and development of the ferrochrome alloy form the basis of Inconel series of alloys.

Notwithstanding these achievements, serious Superalloy development began in the 1930s which led to the development of the first useful heat resisting alloy around 1940. The main drive for Superalloys was the requirement to have materials that could withstand heat and still maintain strength at high temperatures, necessitated by the development of the gas turbine by Sir Frank Whittle. This research was mostly done in Great Britain and United States before the Second World War. Since then, the demand for Superalloys has been on the increase due to increasing temperature requirement in engineering applications.

Work continued during the Second World War in Great Britain and U.S with improvements in Nimonic, Hastelloy and ferrochrome alloys. Figure 2.1 summarizes the Superalloy development over the years from 1940 to 1970[1, 20].

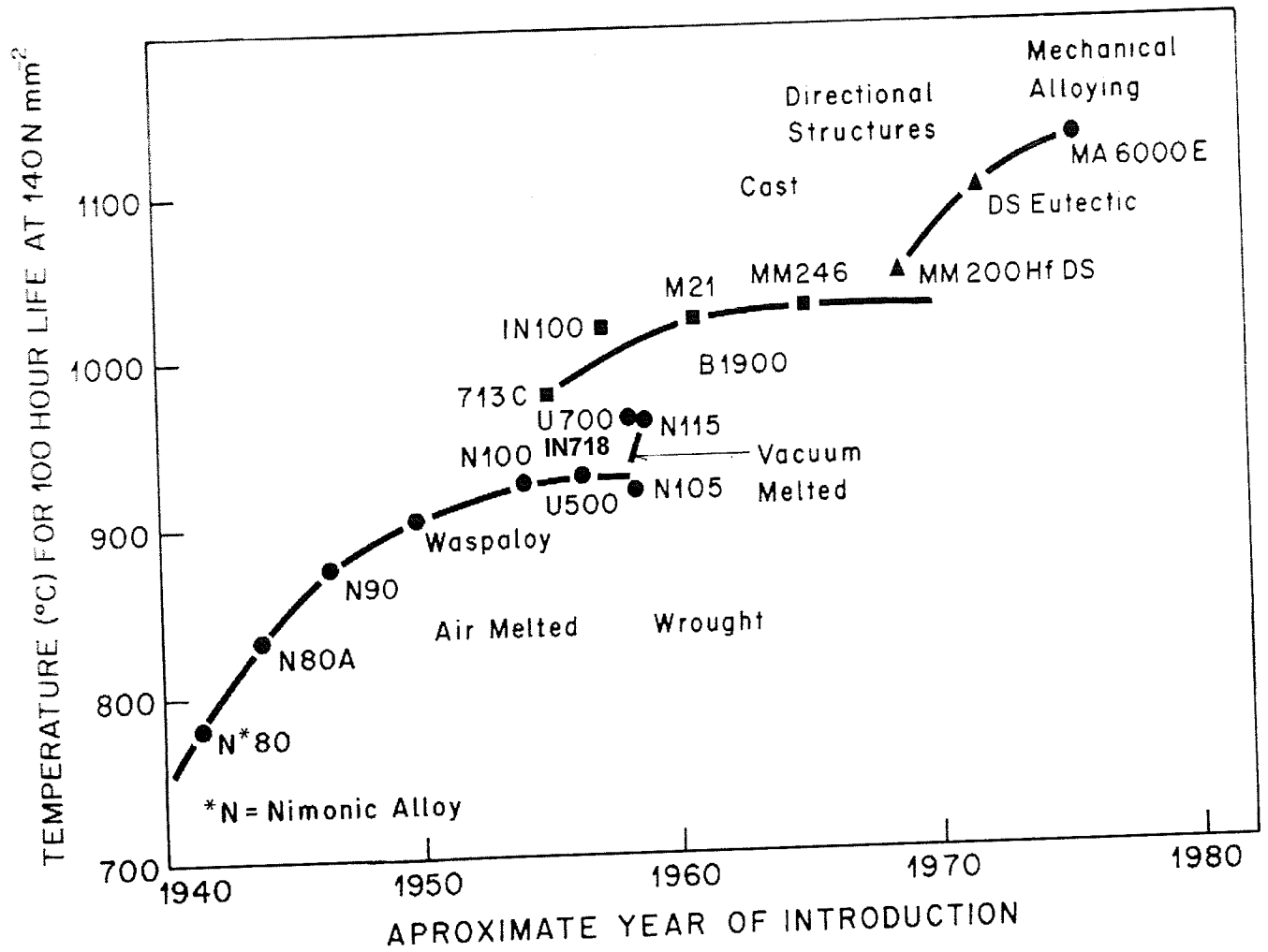


Figure 2.1 Developmental trends in the alloy and processing of Superalloys adapted from [1]

#### 2.1.4.1 Physical properties of Superalloys

Superalloy densities vary with the iron base Superalloys having slightly higher densities than those that are not iron based. The range of densities for the nickel base alloys is wider than that of any other in the Superalloy group. Furthermore, another property of Superalloys is their coefficient of thermal expansion. The thermal expansion coefficient of cobalt and nickel base Superalloys is approximately equal which is lower than that of the iron base Superalloys. Because Superalloys are used where close tolerance is required, it is often important that Superalloys' thermal coefficients be monitored to suit the specific application for which they are being used. Iron base Superalloys are usually more thermally conductive than cobalt based alloys, while nickel based alloys have thermal conductivities between the cobalt and iron based Superalloys.

Another important property of Superalloys is the type of phases present in the microstructure. The phase(s) present in Superalloys are usually not at equilibrium, which results in instabilities occurring when exposed to high temperatures. Phase changes can occur depending on the type of application, temperature and time for which the Superalloy is being used. While phase instability can be desired because heat treatment can be carried out to form desired phases, other deleterious phases such as sigma, mu and laves phases can also form during heat treatment or in service. Such deleterious phases reduce the high temperature properties of the alloys by reducing ductility values.

Superalloys are also known for their excellent oxidation resistance especially in the presence of combustion products of clean fuel usually free of contaminants such as sodium, sulfur and vanadium [20]. In fact, Ni or Ni-Fe base Superalloys with high Cr (>12w/o) and Al (>6w/o) contents have the best oxidation resistance. This subgroup of

nickel base Superalloys resists oxidation by forming a tight continuous surface oxide scale. This scale acts as a diffusion barrier that reduces further oxidation. Also, Superalloys when coated exhibit a fair resistance to hot corrosion. Hot corrosion occurs as a result of combined oxidation and reactions with sulfur and other contaminants ingested from air and contained in the fuel. Generally, Superalloys with high Cr content exhibit good resistance to hot corrosion.

#### **2.1.4.2 Strengthening in Superalloys**

As mentioned earlier, Superalloys are strengthened by solid-solution strengthening and precipitation hardening.

##### **2.1.4.2.1 Solid solution hardening**

When elements that have similar crystal structure and similar sizes (atomic diameter less than 15% difference) are added to nickel and its alloys, solid solution strengthening of the alloy can occur following Hume Rothery conditions for alloying. Examples of solid solution strengthening elements include cobalt, iron, and aluminum. However, at higher temperatures in excess of  $0.6T_m$  (where  $T_m$  is the melting point of nickel or its alloys in Kelvin), the strength in nickel is diffusion dependent. Therefore, for nickel and its alloys to be solid solution strengthened, slow diffusing elements such as molybdenum, tantalum and tungsten are used [21]. These are effective solid solution strengtheners for nickel alloys at higher temperatures [7].

#### 2.1.4.2.2 Carbide strengthening

Another mode of strengthening Superalloys is through carbide precipitation. When carbides are precipitated, especially at the grain boundaries, they pin the grain boundaries preventing grains from sliding. The mechanism of carbide strengthening is applicable to almost all Superalloy types. Also, there are different types of carbides that form in nickel/nickel-iron base Superalloys. These carbides can be divided into two main groups which are those that add positively to the overall properties of the alloy and those that affect the alloy negatively. In its free form, nickel does not readily form carbides, however various alloying elements when added to nickel can readily form carbides in the Superalloys compositions. The types of carbides formed are MC,  $M_6C$ ,  $M_{23}C_6$ , and  $M_7C_3$  (where M is the carbide forming element listed in Table 2.1).

MC carbide is a large, blocky and randomly distributed precipitate. This type of carbide is usually not desired (except when *probably* formed at the grain boundaries). Another type of carbide that is blocky-shaped is  $M_6C$ .  $M_6C$  precipitates at grain boundaries and can be used to control grain size. It can also precipitate as Widmanstätten pattern throughout the alloy. This carbide can impair ductility and rupture life. Another type of carbide common to nickel and nickel-iron base alloys is the  $M_7C_3$ .  $M_7C_3$  can precipitate in discrete particles or can also agglomerate after long time in service. In discrete particle form, it is beneficial. However, when agglomerated, it causes embrittlement of the alloy. Furthermore,  $M_{23}C_6$  has higher tendency to precipitate at the grain boundaries. When  $M_{23}C_6$  precipitates at the grain boundaries, it enhances the alloy's creep rupture properties.

All nickel base alloy carbides can be formed by appropriate heat treatment procedure that is based on the alloy's chemistry. However, there is need to carefully examine an alloy in order to determine the actual heat treatment needed to form the specific carbide desired.

#### **2.1.4.2.3 Precipitation hardening**

Nickel base alloys can also be strengthened by precipitation hardening non-carbide precipitates. An example of this is the gamma prime ( $\gamma'$ ) precipitate. The precipitation of  $\gamma'$ ,  $\text{Ni}_3(\text{Al,Ti})$  provides significant strength to nickel base alloys.  $\gamma'$  has ordered FCC crystal structure with lattice parameter very similar to that of the nickel matrix. When present,  $\gamma'$  introduces lattice distortion which is about 1% or less [21] with the  $\gamma$  matrix allowing low surface energy and long time stability of the  $\gamma'$  phase [7].

The  $\gamma'$  precipitates are formed from oversaturation of  $\gamma'$  forming elements which are Al and Ti in the  $\gamma$  matrix, while the overall alloy's strength increases with ageing time.  $\gamma'$  strengthening is also a function of  $\gamma'$  particle size, because increasing particle size of  $\gamma'$  increases hardness until a peak hardness is reached at which further increase in  $\gamma'$  precipitates size will lead to decrease in hardness. Furthermore, the  $\gamma'$  particle size is diffusion-controlled; hence it is also dependent on temperature and time. Additionally, the volume fraction of  $\gamma'$  in nickel alloys is a key factor in precipitation hardening of Superalloys. This is because the high temperature strength of nickel base alloys increase with increase in the volume fraction of  $\gamma'$ .

$\gamma'$  can also transform to  $(\text{Ni}_3\text{X})$  if the alloy is supersaturated in Ti, Ta, or Nb. For example, Ti-rich metastable  $\gamma'$  can transform to  $(\text{Ni}_3\text{Ti})$  or eta phase which is a hexagonal

close-packed phase. The presence of eta phase can alter mechanical properties. In addition, elements such as Nb and Fe can induce the precipitation of  $\gamma''$ . Excess Nb results in metastable transformation of  $\gamma''$  which is a body centered-tetragonal phase and subsequent formation of  $\text{Ni}_3\text{Nb}$  (orthorhombic) equilibrium phase. Table 2.1 summarizes the effect of various alloying elements on the properties of nickel base Superalloys, while Figure 2.2a shows the trend of carbide formation in Superalloys from 1940 to 1970 [20, 22]. Also, Figure 2.2b shows the trend of unwanted elements in Superalloys from 1940 to 1970 [20, 22].

Table 2.1 A Summary of the role of elements in nickel and nickel-iron base Superalloys adapted from [23]

<b>Effects on nickel base alloy</b>	<b>Elements</b>
Solid-solution strengtheners	Co, Cr, Fe, Mo, W, Ta, Al
<b>Carbide Formers</b>	
MC type	W, Ta, Ti, Mo, Nb
M <sub>7</sub> C <sub>3</sub> type	Cr
M <sub>23</sub> C <sub>6</sub> type	Mo, W, Cr
M <sub>6</sub> C type	Mo, W
Carbonitrides	C, N
Forms $\gamma'$ Ni <sub>3</sub> (Al, Ti)	Al, Ti
Raises solvus temperature of $\gamma'$	Co
Hardening precipitates and/or Intermetallics	Al, Ti, Nb
Forms $\gamma''$ (Ni <sub>3</sub> Nb)	Nb
Oxidation resistance	Al, Cr
Improves hot corrosion resistance	La, Th
Sulfidation resistance	Cr
Increases rupture ductility	B(a), Zr
Cause grain boundary segregation	B, C, Zr

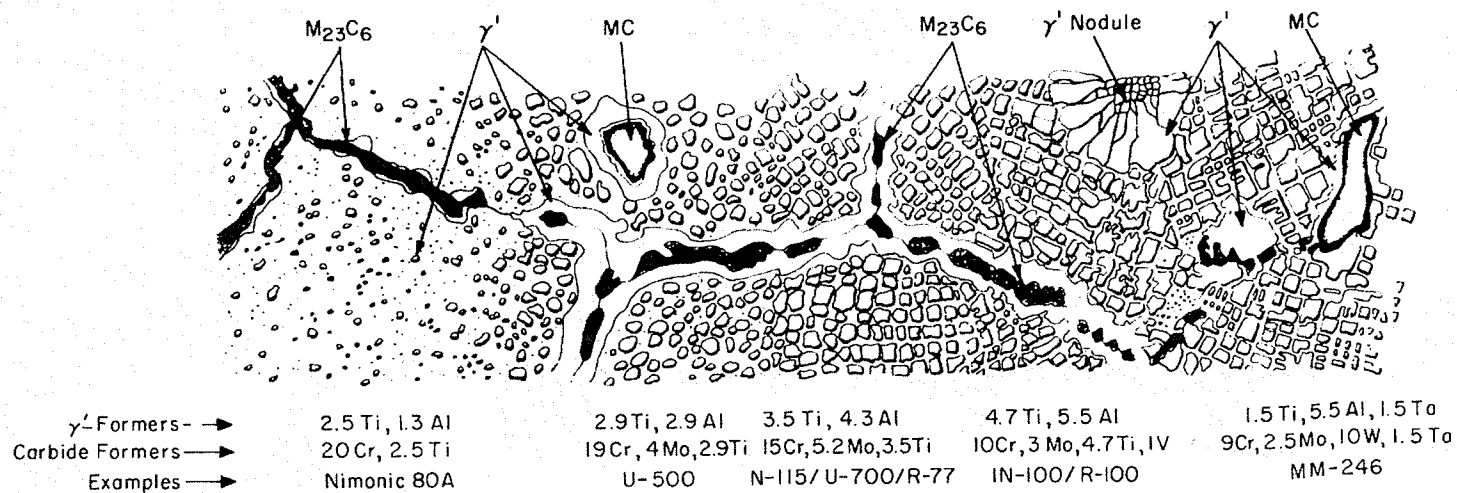
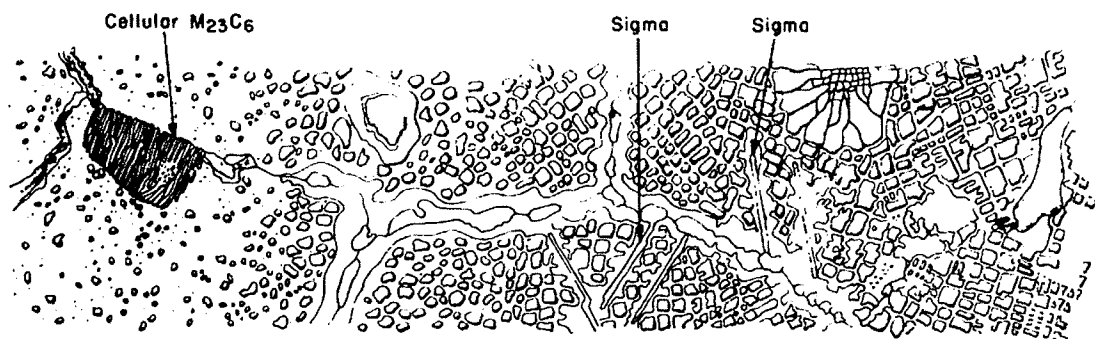


Figure 2.2a: Genesis of nickel alloy microstructure 1940 to 1970 adapted from Sims, *et al.* [20]

Year →	1940	1950	1960	1970
Undesirable phase or structure	Cellular $M_{23}C_6$	None	Sigma phase	None yet
Characteristics	$M_{23}C_6$ grown in cells with $\gamma$ interlayers	—	Hard TCP phase usually occurs as plates similar to $\mu$ or Laves	—
Effect on alloy	Shortened rupture life	—	Shortened rupture life; low-temperature brittleness	—
Cause	Poor control of microstructure	—	Poor control of alloy chemistry	—
Cure	Improve heat treatments	—	Control chemistry through "Phacomp"	—



$\gamma$ -Formers →	2.5Ti, 1.3Al	2.9Ti, 2.9Al	3.5Ti, 4.3Al	4.7Ti, 5.5Al	1.5Ti, 5.5Al, 1.5Ta
Carbide Formers →	20Cr, 2.5Ti	19Cr, 4Mo, 2.9Ti	15Cr, 5.2Mo, 3.5Ti	10Cr, 3Mo, 4.7Ti, 1V	9Cr, 2.5Mo, 10W, 1.5Ta
Examples →	Nimonic 80A	U-500	N-115/U-700/R-77	IN-100/R-100	MM-246

Figure 2.2b: Common unwanted phases or structures in nickel alloys from 1940 to 1970 (X10,000) adapted from [20]

### **2.1.5 Historical development P/M processing of Superalloys**

Powder metallurgy of Superalloys originated from ferrous powder metallurgy. Ferrous powder metallurgy basically involves cold compaction and sintering of iron compacts to a density of more than 90% in a suitable atmosphere. Initially, the drive for P/M processed Superalloys arose from the drive to produce newer ways of cooling turbine blades. Earlier work by General Electric Company laboratories, in Wembley UK [24, 25] revealed that vacuum melted and ball milled Co-Cr-W alloy could be obtained, although the alloy was plagued with inferior creep properties due to residual porosity and the alloy chemistry. Cooling passages were subsequently introduced by compacting Co-Cr-W powders with cadmium, and evaporating the cadmium during sintering. Through this process, an increment in the inlet gas temperature of the turbine engine was increased to about 270°C as compared to those blades that were not cooled. However, this process was very expensive and complex.

Further attempts to produce sintered materials continued in Great Britain in the mid-1950s with no parallel programme in the USA [1]. There was reluctance by the British aero-engine designers to accept a cast alloy in comparison to the high-strength wrought alloys, while the Americans were ready to accept cast alloys in preference to the wrought alloys for elevated temperature use. Then, with the introduction of P/M processing, a possible bridge between cast and wrought alloys properties was envisaged because P/M process can produce uniform grain structure while avoiding brittle eutectic and variable grain size.

The successful development of water atomization at BSA (BSA Metal Powders) Group research centre in Great Britain, led to the production for the first time of sintered

high-temperature alloys [26, 27]. Specifically, alloys with composition of Nimonic-90 and Nimonic-100 were produced by cold pressing and vacuum sintering. The resultant compacts were characterized with improved creep strength due to the alloy chemistry but were plagued with inferior fatigue properties. Vacuum melting for production of the powder alloys was suggested as a way to improve the fatigue properties of these alloys because the powders produced by water atomization were highly oxidized. This led to the development of newer and improved techniques of powder production in the USA.

With the development of purer powders, the drive for P/M Superalloy production changed with more focus on improving the consolidation process. At the same time, research at Pratt and Whitney revealed that cast and wrought Rene 41 and Waspaloy did not have the high-strength requirements for disc production, while newer alloys such as Astroloy exhibited large scatter in mechanical properties. This scattering in mechanical properties of Astroloy was attributed to segregation and lack of homogeneity in the compact leading to the launch of an “all-inert” powder programme by the Pratt and Whitney Company in mid-1960s. Since the 1960s, developments in P/M processing of Superalloys have progressed rapidly. In recent times, P/M processing has led to the formation of mechanically alloyed dispersion-strengthened Superalloys, which are common to nickel base alloys (although this is still not commonly used) [7], and nanotechnology.

Nickel base alloys are usually produced via different methods of which significant amounts are either casting based or castings are used as the starting material during the fabrication process before being processed into wrought form. However, it should be noted that Superalloys (especially nickel and nickel-iron base alloys) are constitutionally

complex alloys and can undergo dendritic segregation during solidification. Segregation in Superalloys usually leads to toughness problems and secondary material loss that is often associated with heterogeneous multiphase alloys [1]. The segregation problem in Superalloys has, however, been reduced with the introduction of powder metallurgy as a fabrication alternative in 1962 [20].

### **2.1.6 Advantages of powder metallurgically processed Superalloys**

Powder metallurgically formed Superalloys have fine grains and can potentially provide a more uniform microstructure and properties in a range of applications at both low and elevated temperatures especially in low cycle thermal fatigue applications, which could be difficult to achieve by conventional melting and casting process. Another advantage of powder metallurgical processed Superalloys is that a complex composition can be readily fabricated. Specifically, prealloyed/master alloyed Superalloy powders were developed essentially for the manufacture of turbine disks whose compositions can be very complex and for which it is not possible to attain the required strength and integrity levels with the relatively coarse structures generally present in castings [28]. Furthermore, Superalloy powders can also be consolidated into large sizes without the formation of high residual stresses intrinsic in large castings. Also, powder metallurgy is quite economical when considering its little or minimal post processing cost common to casting, such as machining. This makes P/M process competitive with respect to the cast and wrought alloy products, while some intricate shaping of non-forgeable alloys can also be produced by powder metallurgy.

### 2.1.7 Uses of Superalloys

Before describing further details of powder metallurgy, a brief discussion of the application of Superalloys is necessary. In general, Superalloys are specially used in various applications. These applications are grouped into the following categories.

- Aircraft gas turbines: The areas of Superalloy applications include the manufacture of disc, combustion chamber, bolts casings, shafts, exhaust systems, cases, blades, vanes and burner cans [23, 29, 30].
- Steam turbine power plants: such as in bolts, blades and stack gas reheaters.
- Reciprocating engines such as in turbochargers exhaust valves, hot plugs and valve seat insert.
- Metal processing mills such as in ovens and exhaust fans

Other applications of Superalloys include: medical applications, space vehicles, heat treating equipment, nuclear power systems, chemical and petrochemical industries. Superalloys can also be used in specialized applications such as in shape memory alloys and as soft magnetic alloys [7]. Of all these Superalloys applications, the focus of this study is on applications where P/M processing is applied in making Superalloys.

## **2.2 Powder production, characterization and processing**

### **2.2.1 Powder production**

Some of the methods used for powder production include: mechanical comminution, chemical precipitation, thermal decomposition, rapid spinning disc, rotating electrode, soluble gas atomization and two-fluid atomization. [31]. Basically, these methods can be classified into two main categories i.e., mechanical and chemical methods, a summary of which is shown in Figures 2.3a, & b.

From the powder production techniques shown in Figure 2.3, the commonly-used methods in industry include atomization, mechanical alloying, electrolysis and chemical reduction of oxides. Among these methods, atomization is usually the preferred method especially for aluminum, brass, iron, steels and Superalloys production [32]. Atomization is used for Superalloy powder production because not only is the process economical and efficient, it can also be used to produce relatively pure powders.

The types of atomization used are classified as follows [33]:

- Centrifugal atomization
- Vacuum or soluble gas atomization,
- Ultrasonic atomization
- Two-fluid atomization.

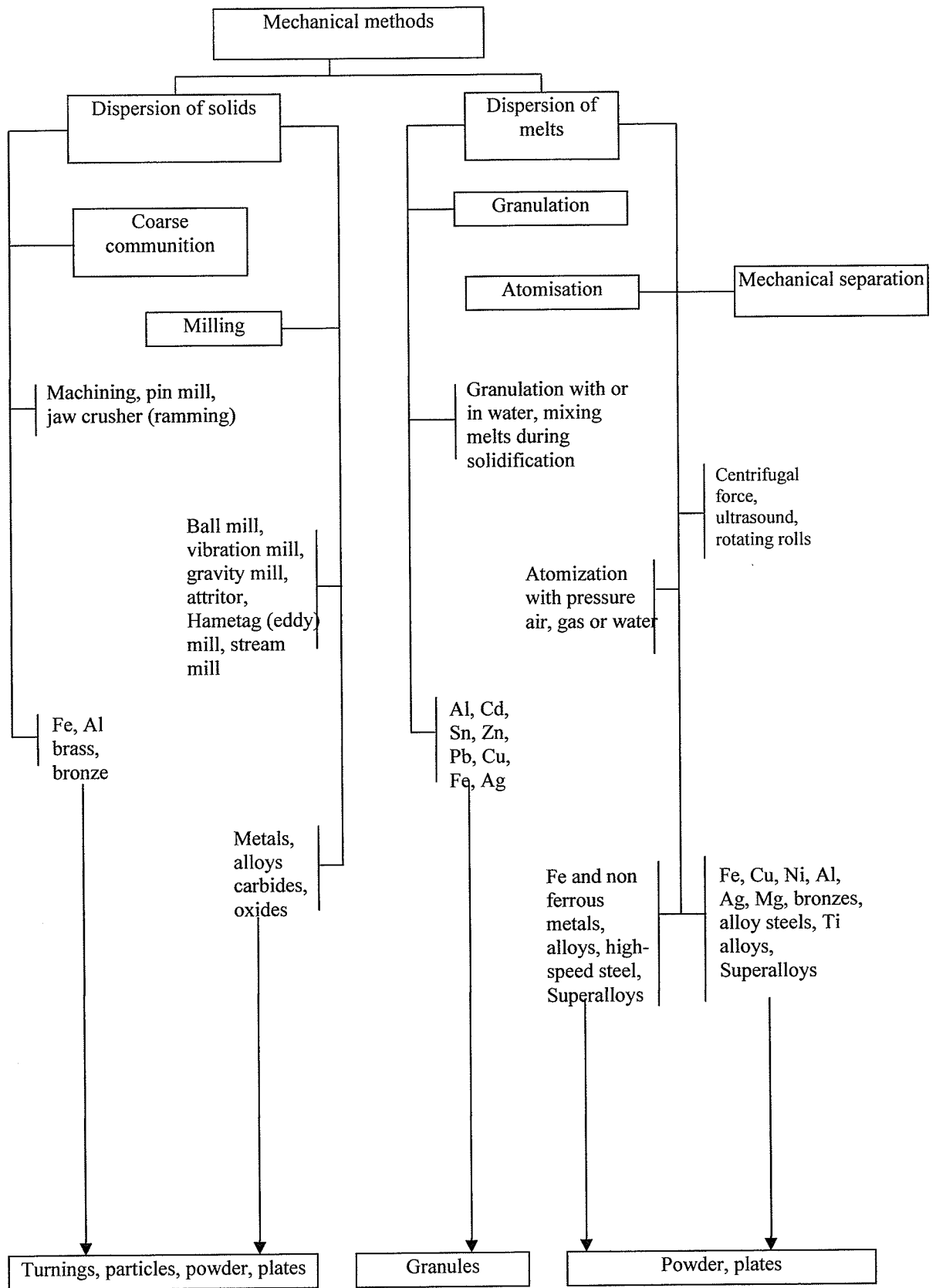


Figure 2.3a: Mechanical methods of powder production [31, 34]

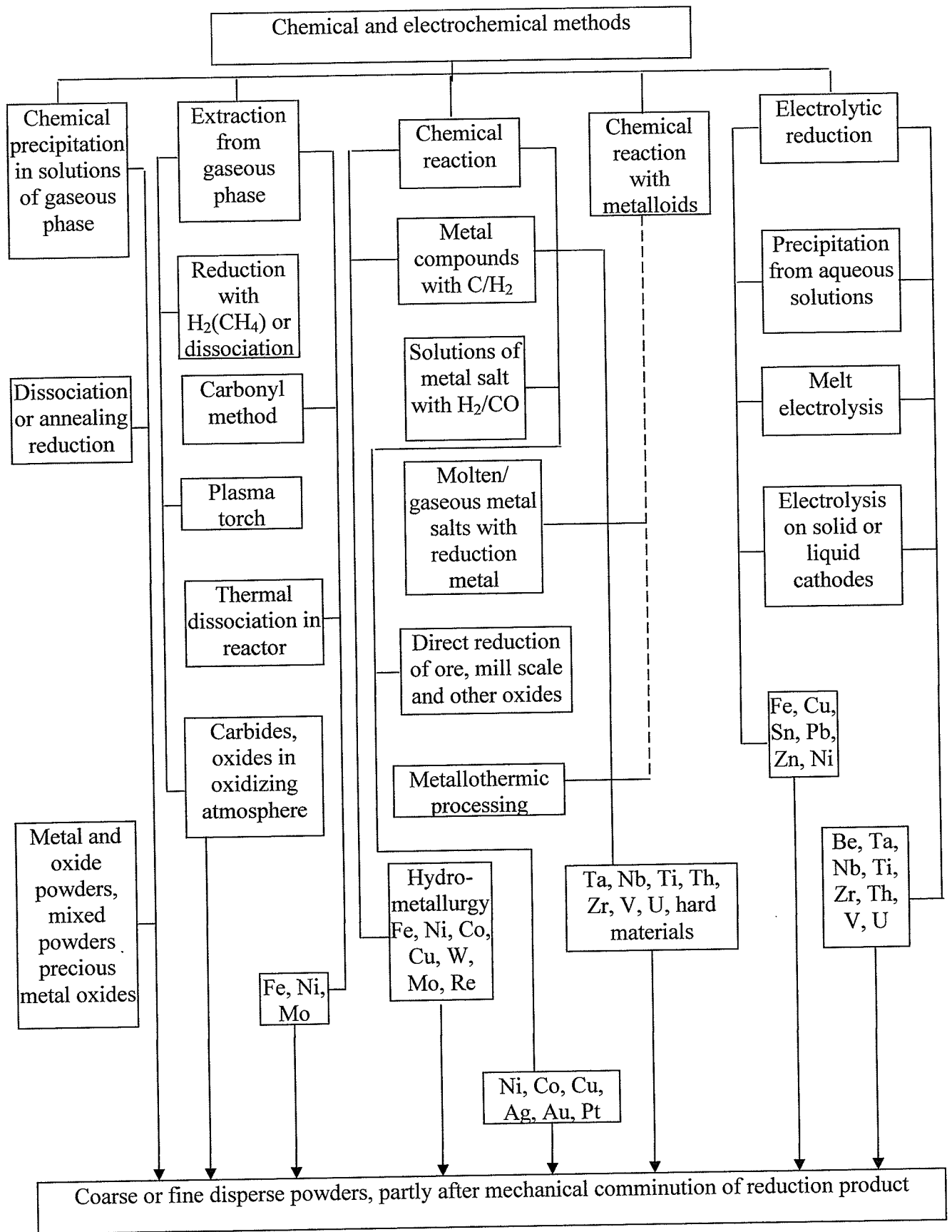


Figure 2.3b Chemical methods of powder production [31, 34]

### **2.2.1.1 Centrifugal atomization**

This is a situation in which a liquid is broken by centrifugal force of a rotating disk, rotating electrode or rotating cup of desired composition. The sizes of powders produced are sensitive to the rate of rotation and angular velocity. The powder particles produced are usually spherical and hollow with satellite particles attached. The main advantage of this process is the low oxygen content of the powders produced. A schematic illustration of the rotating electrode method is shown in Figure 2.4a and 2.4b.

In Figure 2.4a, the plasma arc rotating electrode is shown where the rotating electrode is the actual material that is broken down into particles by stationary helium plasma arc. The other type of rotating electrode is shown in Figure 2.4b. Here, the arc producing electrode is rotated instead of the materials being broken into particles. In both processes, the rotation causes the molten metal droplets to be flung radially outward from where they are subsequently cooled by the inert gas atmosphere and the particles fall down into the bottom of the container.

The main disadvantage of the rotating electrode method is that the cost of the equipment can be quite enormous due to the types of equipment involved. In addition, obtaining a good structural electrode can be difficult. [35].

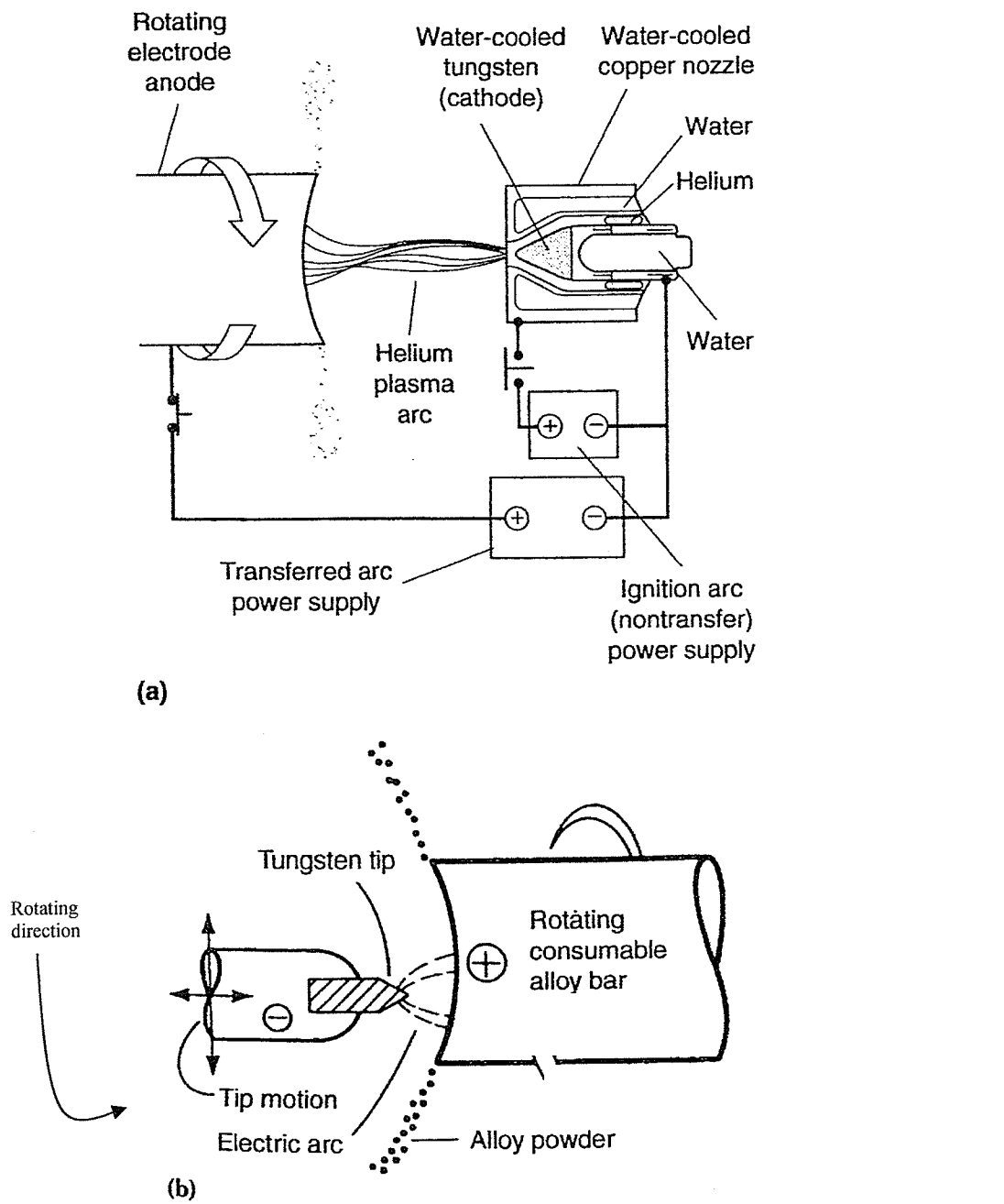


Figure 2.4 Schematic of the rotating electrode process (REP) (a) Plasma arc rotating electrode process (PREP) [33].

(b) Tungsten rotating electrode process showing the rotating arc adapted after [33]

### **2.2.1.2 Vacuum or soluble-gas atomization**

The principle used in this method is based on rapid expansion of dissolved gas into a low pressured chamber. The molten metal of desired composition is saturated with an atomization causing gas in vacuum. This forces the metal droplets outward through an already existing ceramic tube. Shapes can also be re-modified by changing the rate of expansion and rate of cooling. The shapes of the powders produced by this method are usually oval, irregular, or flaky due to the effects of expanding gas and splat cooling of the droplets [35].

### **2.2.1.3 Ultrasonic atomization**

This involves breaking a liquid metal film by application of an ultrasonic vibrating gas. For example, in some P/M industries, a pulsating gas at 40Hz or higher is fired into a molten metal system and the shear force generated causes the liquid break-up [33].

### **2.2.1.4 Gas atomization**

This is a method of powder production in which a vacuum induction melted metal is passed into an atomizing chamber where the melt is atomized under a high pressure of inert gas (argon). It is under the class of two-fluid atomization, a process in which liquid metal of desired composition is broken up into droplets by high-pressure jets of gas, water or oil.

Figure 2.5 shows a schematic of the gas atomization chamber. In this figure, the upper part of the diagram is the melt chamber where metals of desired compositions are added through the melt addition chamber and the melting furnace is underneath. The metal or alloy that is melted in the furnace is then poured into a tundish through the nozzle and die. For gas atomized powders, an inert gas (usually argon) is passed at high pressure through the nozzle into the die through which the molten metal flows which breaks the molten metal into droplets. The molten metal flow rate is related to the diameter of the teeming nozzle, metallostatic head and pressure variation of gas [33].

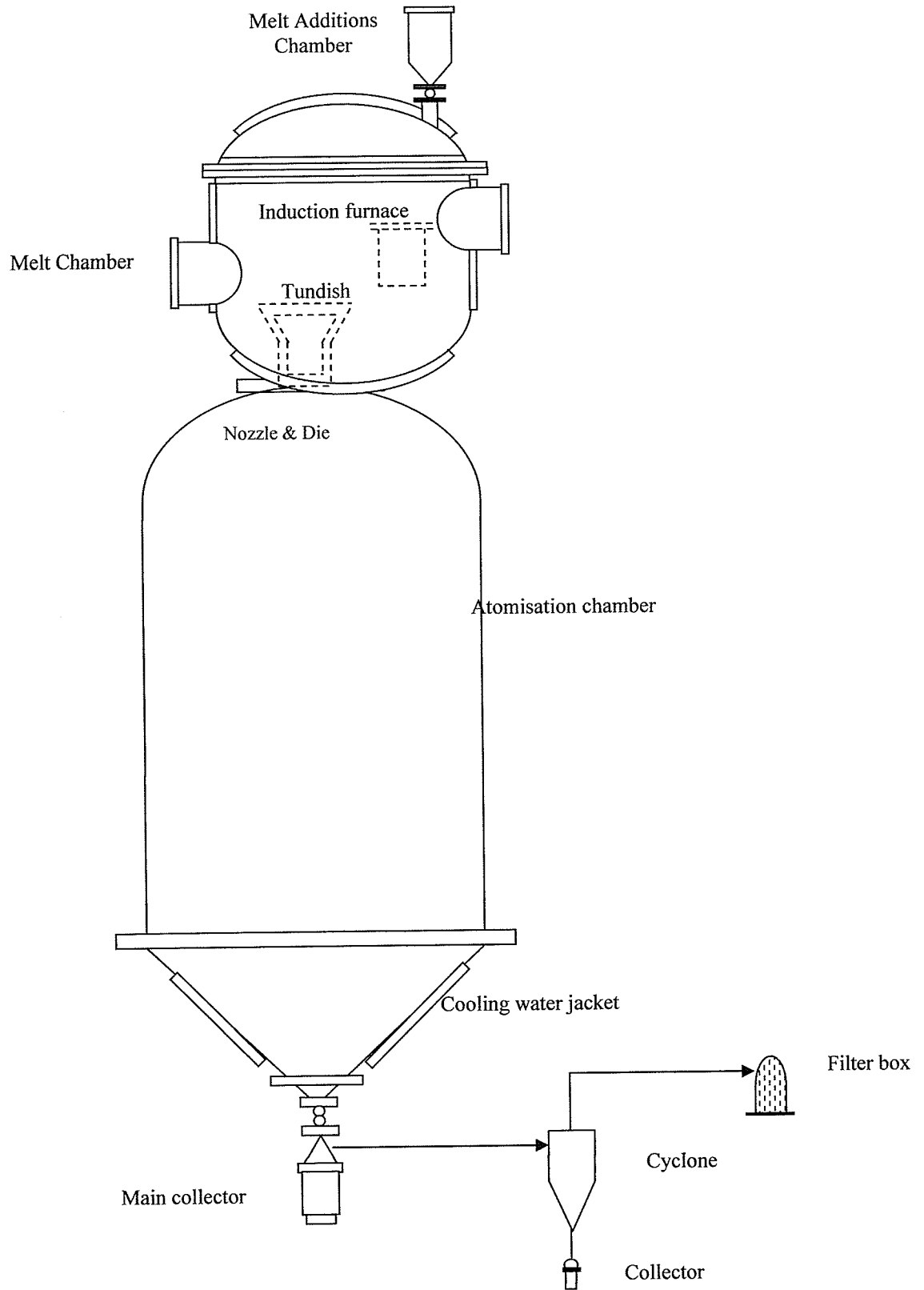


Figure 2.5 Layout of an atomizer of fine metal powders by close coupled gas atomization [36]

There are two types of nozzle-die designs in gas atomization, namely, free fall design and confined design. Their configurations are shown in Figure 2.6.

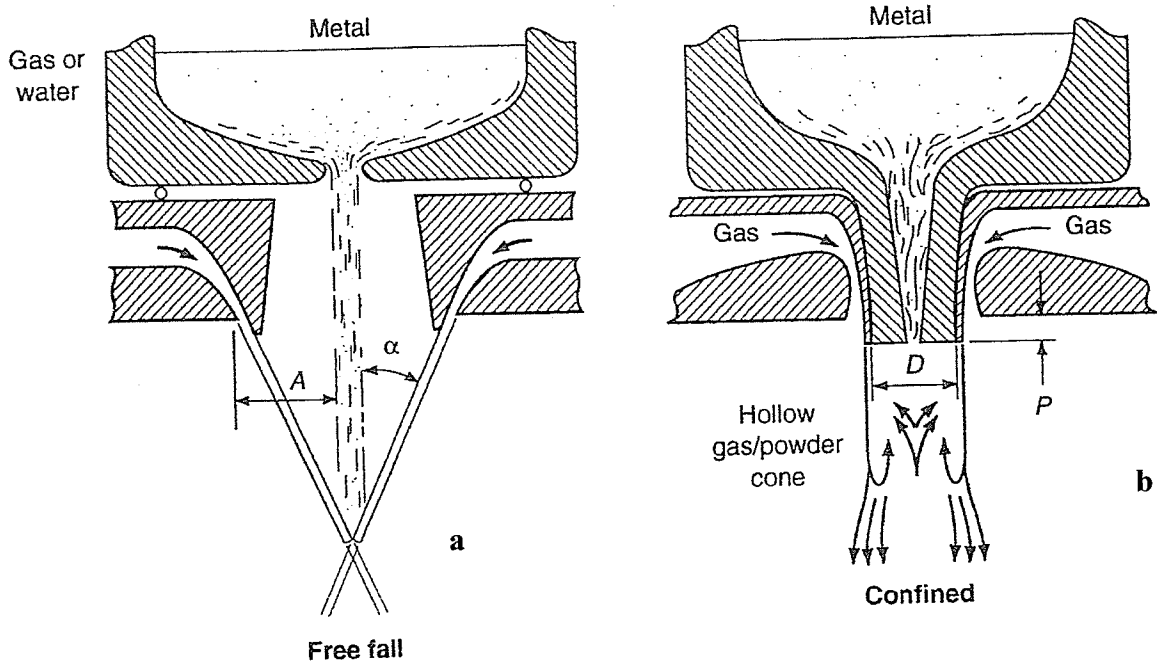


Figure 2.6: Two-fluid atomization with a) free-fall design (gas or water) and (b) confined nozzle design (gas only). Design characteristics:  $\alpha$  angle formed by free-falling molten metal and atomizing medium;  $A$ , distance between molten metal and nozzle;  $D$ , diameter of confined molten metal nozzle;  $P$ , protrusion length of metal nozzle [33]

The free-fall design is shown in Figure 2.6a [33]. The main problem with the free-fall nozzle design is that velocity decreases with increase in distance from the nozzle head. This makes it difficult for some metal alloys, especially iron alloys, to have a mean diameter below 50 to 60 $\mu\text{m}$ . Also high efficiency is difficult to obtain in free-fall designs. However, one of its advantages is that variation in the nozzle arrangements can produce fine powder at some gas-to-metal ratios for high-velocity oxyfuel thermal spray, plasma tungsten arc welding, and hot isostatic pressing applications.

The confined nozzle design (Figure 2.6b) produces powders with diameter of approximately 10 $\mu\text{m}$ . This is achieved by maximizing gas velocity and contact with the molten metal. The disadvantages of the confined nozzle design include its proneness to freezing of molten metal at the end of the tundish nozzle which can block the nozzle. In addition, interaction of the gas and molten metal at the tip of the die can generate a suction which can increase metal flow rate back into the tundish.

From the tundish, the molten metal is forced through the tip of the pressure gas jet and the droplets of molten metal are cooled by convection. Powder particles are collected, and classified into sizes. The majorities of gas atomizers have free fall configurations and give good recoveries for powder sizes above 25 $\mu\text{m}$ .

#### 2.2.1.4.1 Process variables in gas atomization

The pressures applied during gas atomization range from 0.5 to 4MPa and gas velocities are in the range of Mach 1 to 3. The gas velocities for free-fall nozzle designs are in the range of 50 to 150m/s [33]. For the free-fall nozzle designs, the key variables are as follows:

- Melting stage: Chemistry, atmosphere, superheat
- Atomization stage: Metal stream length, nozzle diameter, density of metal, surface tension of metal, viscosity of metal, water/gas pressure/velocity, jet geometry, diameter, length and apex angle ( $\alpha$ ).
- Particle solidification: Melting range, droplet size, heat transfer, quenching medium and flight path.

For the confined nozzle design configuration, the parameters are tundish nozzle tip, gas jet apex angle, gas jet diameter, number of jets, and horizontal spacing between the jets and tundish nozzle centre line. The flow rate through the single orifice nozzle of the conventional gas atomization is between 1 to 90kg/min, while typical gas flow rate ranges from 1 to 50 m<sup>3</sup>/min at gas pressures in the range of 350kPa to 4MPa. The superheating temperature between the metal melting temperature and gas atomization temperature is about 75 to 150<sup>0</sup>C.

For gas nozzle design and size, the average particle size is controlled by atomizing at medium pressure and melt flow rate and nozzle diameter. The amount of gas flow (A) depends on gas pressure, temperature, and nozzle area. In ideal situations the gas flow rate (A) is given as:

$$A = a \left( \frac{2}{k+1} \right)^{k+\frac{1}{2}(k-1)} \frac{p\sqrt{2g}}{\sqrt{RT}} \dots\dots\dots 2.1$$

where a is the cross section of gas nozzle at exit, k equals  $C_p/C_v$ , i.e., the ratio of specific heat at constant pressure to the specific heat at constant volume, p is the gas pressure in the gas reservoir, T is the temperature in the gas reservoir, R is the gas constant, g is the acceleration due to gravity, and k is constant where  $k= 1.4$  for nitrogen [33].

**2.2.1.4.2 Gas atomization stages**

According to Dombrowski [37] the gas atomization of powders is divided into three stages (Figure 2.5 [33] [37]). The first stage is the initiation of sinuous waves or other disturbances that increase the amplitude rapidly in stage one, while the second stage is the stage associated with fragmentation in which ligaments are formed. Stage 3 is typically the breakage of ligaments into droplets. These stages are shown schematically in Figure 2.7.

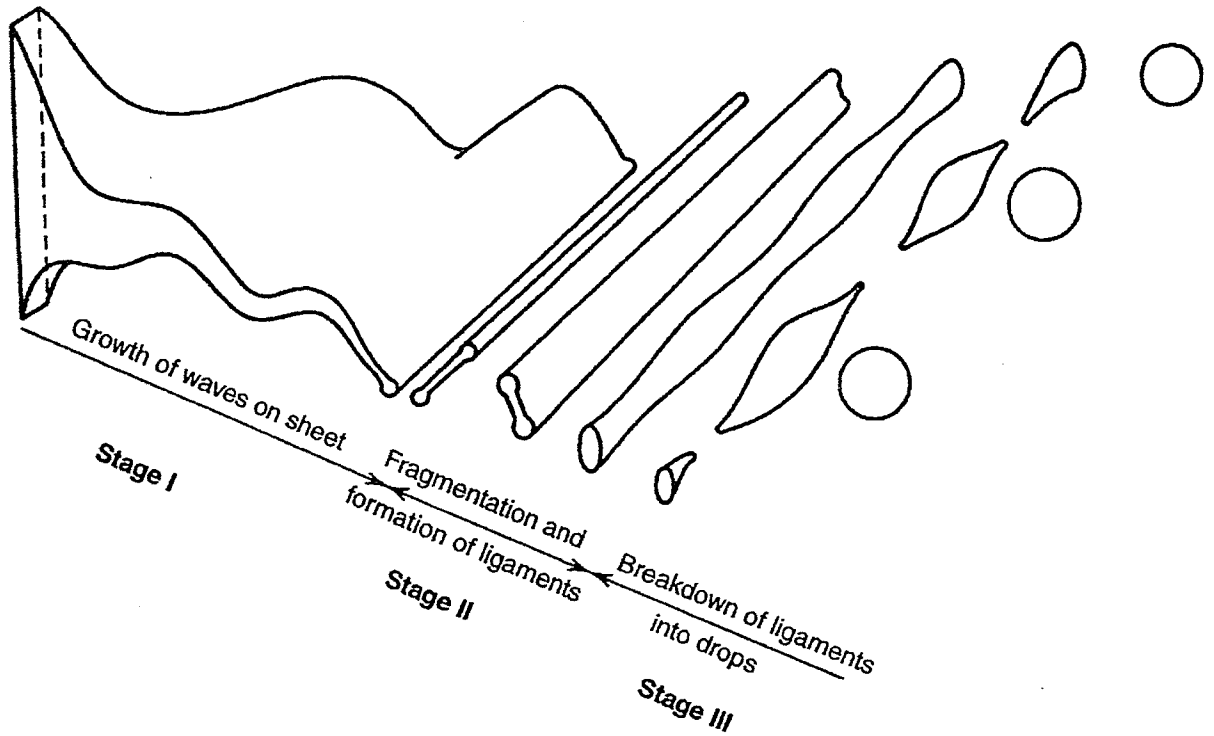


Figure 2.7 Model for disintegration of a liquid sheet by a high-velocity gas jet [37]

#### 2.2.1.4.3 Particle size from adjustable parameters

All atomized powders exhibit a log normal distribution before screening, and can be absolutely defined by two main parameters which are the median mass diameter  $d_m$  and the geometric standard deviation. To produce powder sizes greater than 500 microns, all atomization techniques are suitable while, for powder sizes smaller than 500 microns, all except the water atomization technique may be used for production.

The size of a powder particle is an important parameter during powder production. Therefore it is important to understand how a particle size and size range are derived. According to the literature [38], various methods are used to predict the particle size of gas-atomized powder during the atomization process. In these methods, the particle size diameter,  $d$ , [38] is given as:

$$d = \sqrt{\frac{6 \sigma}{\rho_m a}} \dots\dots\dots 2.2$$

where  $\sigma$  is the surface tension,  $\rho_m$  is the density of the metal and  $a$  is associated with the particular gas/metal interaction. Equation 2.2 can be expanded according to [33] to give:

$$d = \sqrt{\frac{A \sigma}{\rho_m \frac{M_g}{M_m} V_g (1 - B \eta D)}} \dots\dots\dots 2.3$$

where  $\eta$  is the dynamic viscosity of the metal (in N.s/m<sup>2</sup>),  $V_g$  is the velocity of the gas leaving the nozzle,  $D$  is the diameter of the metal stream, and  $M_g$  and  $M_m$  are mass flow rates of the gas and metal respectively. The constants  $A$  and  $B$  are needed to define the atomization system in order to enable the use of the model.

Lubanska [39] also proposed the following empirical equation for the average particle size diameter ( $d_m$ ) of gas-atomized powder:

$$\frac{d_m}{d_{MetStr}} = K \left[ \frac{v_m}{v_g} \frac{1}{W} \left( 1 + \frac{M}{A} \right) \right]^{\frac{1}{2}} \dots\dots\dots 2.4$$

where W is the Weber number:

$$\left( W = \rho V^2 d_{MetStr} / \sigma \right) \dots\dots\dots 2.5$$

$d_m$  is the mass median particle diameter,  $d_{Met Str}$  is the diameter of metal stream, V is the velocity of the atomizing medium,  $v_m$  is the kinematic viscosity of the liquid metal,  $v_g$  is the kinematic variety of the atomizing medium,  $\rho$  is the density of the gas,  $\sigma$  is the surface tension of liquid metal, M is the mass flow rate of liquid metal, A is the mass flow rate of atomizing medium, and K is a constant.

From the Weber number estimate, it can be deduced that particle size decreases with decrease in surface tension of the liquid metal and with increase in velocity of atomizing medium. Other methods of estimation include computation fluid dynamics (CFD) where some success has been reported [33]. Another method includes determining the maximum stability criterion that gives the maximum drop size as a function of surface tension of the liquid metal ( $\sigma$ ), gas density ( $\rho_g$ ) and velocity (V) of the atomizing medium as:

$$d_{crit} \approx \frac{\sigma}{\rho_g V^2} \dots\dots\dots 2.6$$

Equation 2.6 applies to the equation of the ligament break-up stage (stage 3) in Figure 2.7. Subsequent disintegration into particles smaller than  $d_{crit}$  will occur only if dynamic pressure due to gas stream velocity is more than the resulting force of surface tension.

However, it has been very difficult to model gas interaction with metal flow, effect of gas on metal flow involving both intensive momentum and heat transfer due to the fact that atomization is not essentially a steady flow process [40].

### 2.2.2.1 Powder purity

The level of powder cleanliness i.e., the degree of absence of undesirable materials in the powder is defined as the purity. Undesirable materials in atomized powders are classified into three groups:

*-Bulk dissolved impurities*

*-Inclusions, and*

*-Surface dissolved impurities*

In atomized powders the main types of impurities are bulk impurities with oxygen as the primary contaminant, while other impurities are sulfur and carbon. Other forms of defects (i.e., inclusions) which are inherent in powders referred to as “inherent impurities” or “defects” are in the form of ceramic particles [41]. These particles are difficult to remove as they are derived from crucibles, such as alumina used to melt the alloy or from nozzles (zirconia) through which the molten metal flows during powder fabrication. Such a process leads to small pieces of ceramic nozzle being worn or chipped off; as a result, these ceramic particles are incorporated into the powdered alloy [41]. Another type of impurity (dissolved impurity) found in gas atomized powder is gas porosity, usually in the form of dissolved hydrogen in the melt, although oxygen and steam can also be present.

In recent years, the levels of impurities in powders fabricated by inert gas atomization have been reduced to the level such that only a very low amount of oxygen, the main impurity, remains. To reduce the level of turbulence during gas atomization, a bottom pouring re-melting furnace that discharges through a high temperature ceramic pouring nozzle is used. Inclusion pickup is minimized by reducing the level of turbulence

during atomization. The oxygen content in a typical inert gas atomization is between 40 and 200 ppm [33]. Further ways to eliminate inherent particles such as ceramic particles include sieving, since Superalloys are usually finer than the ceramic particles. Alternative methods include physical separation and triboelectric separation (i.e., the use of gas to transport particles and electric field to separate the powders physically after they have been charged in a bipolar manner) [41].

### 2.2.2.2 Particle shape

As stated earlier, powders are produced by different processes. However, it should be noted that these different production processes did produce different shapes of powders [42]. Hence, the fabrication route is usually specific to various powder shapes. Examples of typical powder shapes and their corresponding fabrication routes are shown in Table 2.2.

Table 2.2 Various shapes of powder particles and their typical methods of fabrication adapted from [43]

<i>Acicular</i> : Chemical decomposition	<i>Irregular rod-like</i> : Chemical decomposition, mechanical comminution
<i>Dendritic</i> : electrolytic	<i>Flake</i> : Mechanical comminution
<i>Spherical</i> : atomization, carbonyl precipitation from a gas	<i>Nodular</i> : atomization, chemical decomposition
<i>Irregular</i> : atomization, chemical decomposition	<i>Porous</i> : reduction of oxides

Ideally, inert gas fabricated powders are smooth and spherical, as shown in Figure 2.8a. In some situations, satellites can be seen (Figure 2.8b). Satellites on powder particles are caused by circulation of gas within the atomizing chamber that lifts finer particles back into the spray plume. This causes the finer particles to collide with the partially molten atomized powders coming from the nozzle. The presence of satellites can be minimized by increasing the cooling rate, increasing the cold air flow rate into the cooling chamber or by using water quenching.

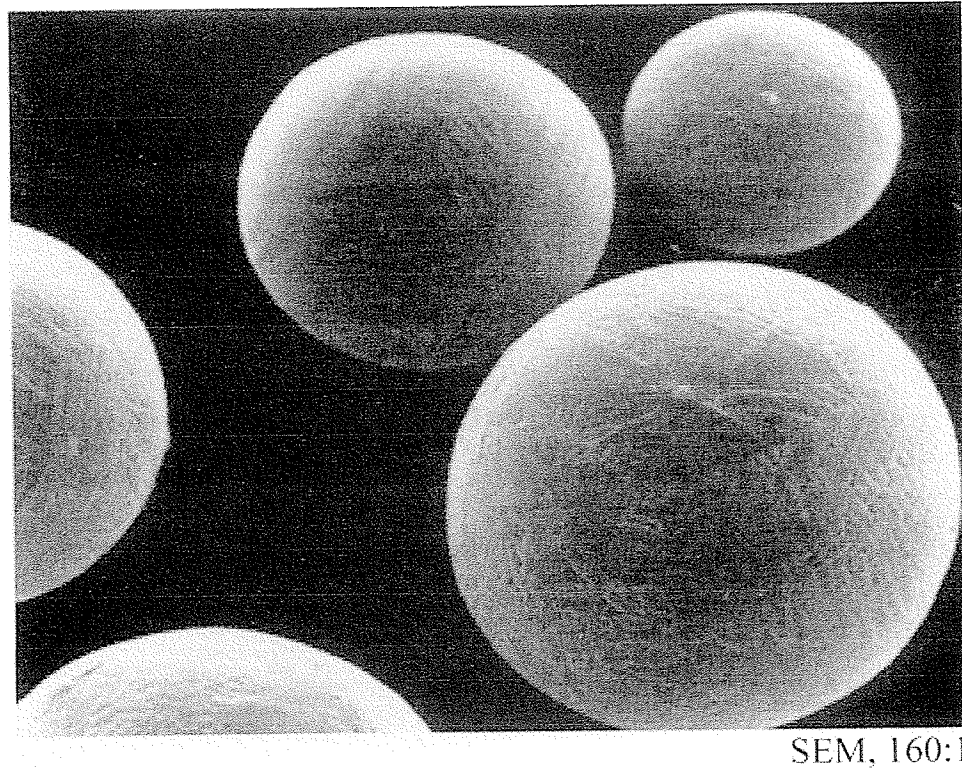


Figure 2.8 a) Spherical shaped powder particle typical of the prealloyed powder used in this study [43]

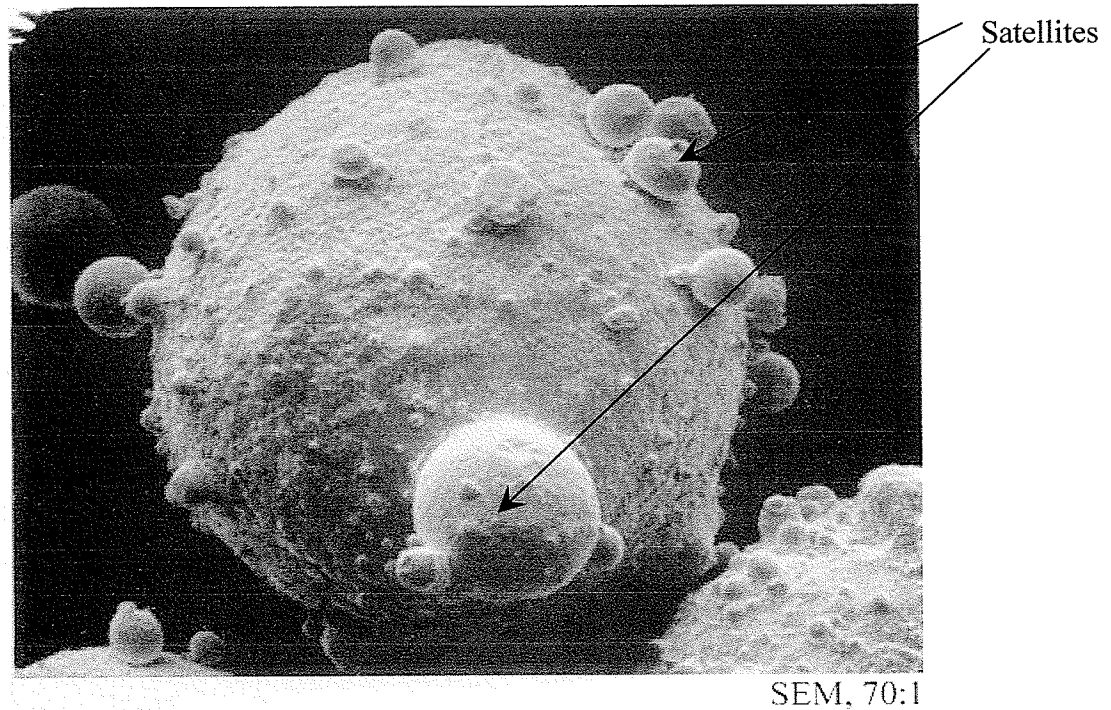


Figure 2.8 b) Spherical powder particles with satellites [43]

### 2.2.2.3 Powder particle microstructure

The composition of atomized powders can be readily varied because the process is very flexible. Atomization can be used for any composition as long as the material can be liquefied. However, the limit of how many alloying elements that can be accommodated is set by miscibility, cooling rates and volatility considerations [1, 2].

The microstructure of a powder particle is largely influenced by cooling rate. When cooling powders from a melt, two main different driving forces help powders to solidify. These are thermal supercooling and constitutional supercooling [1, 2]. Thermal supercooling is the type of cooling in which the solid-liquid interface moves into the liquid resulting into heat of fusion being released at the interface. The released heat of

fusion raises the temperature at the interface (i.e., temperature inversion). The relative increase in the temperature of the solid-liquid interface due to heat of fusion as compared to the liquid temperature creates an unstable liquid that results into the formation of dendritic patterns [1].

The other driving force is the constitutional supercooling which is a function of temperature gradient in liquid ahead of the liquid surface interface. This results when solid freezes, resulting in a different composition from the liquid, caused by solute rejection as the solid forms. The rejected solute creates a concentration gradient into the liquid. Therefore, the solute-rich region of the liquid solidifies first. If the depth of supercooling is large, a dendritic pattern results, while if the supercooling layer is thin, a cellular structure results in which the cell walls are rich in solute [1].

The controlling equation for surface segregation is given as:

$$\frac{C_i}{1 - C_i} = \left( \frac{C_b}{1 - C_b} \right) \exp\left( \frac{-E}{KT} \right) \dots\dots\dots 2.7$$

where  $C_i$  is the interface concentration,  $C_b$  bulk concentration,  $E$  is the free energy of adsorption at the interface which can vary from 0.1 to 1.0 eV[1, 2, 44]. Surface segregation will also result in a change in the distribution of solute in the interior of the powder particles.

Powders can also be rapidly solidified while still utilizing the mechanisms of solidification. Rapidly solidified powders have a range of microstructures. In large

particles ( $>50\mu\text{m}$ ) a branched dendritic solidification structure has been observed and each powder is typically composed of two to three grains. In smaller particles, a dendritic structure is usually absent while microcrystalline morphology consisting of uniformly sized fine grains is observed.

### **2.2.3 Powder processing**

#### **2.2.3.1 Pre-shaping and pre-consolidation processes**

After production, powders will have to be processed. There are various operations used to tailor powders to the desired properties prior to compaction. Examples of such processes include powder classification, blending, mixing, agglomeration, de-agglomeration, annealing, cleaning, and lubrication. The commonly used pre-compaction steps are blending and mixing. The goals of such processes (blending and mixing) are to homogenize the distribution of powder particles and to achieve the desired composition. This is achieved by either adding elemental powders together or using prealloyed/master alloy powders followed by blending to homogenize the composition. Lubricants are also added to powders during mixing which will reduce friction between the die wall and the powders and also reduce interparticle friction. Lubricants are usually organic and can be burnt off either during a pre-sintering or during the actual sintering process.

### **2.2.3.2 Powder shaping and consolidation**

Low porosity is highly desirable in most P/M processed Superalloys to achieve optimum density during sintering. According to [2], densification during powder metallurgy can be achieved either by sintering a low density preform, pressing prior to sintering, or sintering and pressing simultaneously to achieve full density. There are other processes/materials that can be incorporated during preforming of powders. An example of such a process is the addition of another element e.g., cadmium to a cobalt base Superalloy which vaporizes on sintering. This leaves cavities in the cobalt base alloy which is useful in the cooling of such Superalloy in service. Other additives are binders. During powder shaping, binders are essential components as they help hold the powder particles together. Polyvinyl alcohol is an example of a typical binder used for Superalloys and was investigated in this research.

Superalloys can also be consolidated by a variety of other techniques including uniaxial pressing, isostatic pressing and hot isostatic pressing (HIP). Uniaxial pressing involves pressing the compacts in a single direction (either up and down, or left and right directions) prior to sintering. Isostatic pressing involves the application of equal pressures in all directions, while hot isostatic pressing is isostatic pressing at elevated temperatures.

Essentially, HIP involves application of pressure and temperature in an inert (usually argon) medium. Near net shapes are obtained through shaping of the container which is filled with the powders, evacuated and sealed prior to the HIP treatment. HIP imposes no restriction to the container shape, which makes size reduction possible, leading to a more economical process.

Although HIP is quite an attractive process, the instrument is complex and not readily available. Therefore, this research focused on using uniaxial and to a lesser extent isostatic pressing for compacting powder particles.

#### **2.2.4 Pre-sintering treatment**

In most P/M processing, this stage is usually associated with a consolidation process. It usually involves the process that prepares the compact for the actual sintering process. Such processes range from simple de-lubrication to pre-heat treatment. This is done to either change or modify the compact properties prior to sintering.

#### **2.2.5 Sintering**

Material transport driven by surface energy or capillary force is known as sintering [45]. The bonding of particles occurs when particles are heated to relatively high temperatures but below the melting point or liquidus temperatures and movement of atoms between the powder particles occurs. This is because particles with high surface areas will attempt to minimize their surface energy by reducing their high surface area to volume ratio. The principal driving forces are capillary forces due to the surface and interfacial tensions, specific interfacial free energies of the surface and free energy surfaces between the grains [46]. During sintering, surfaces are reduced by channel closing, by smoothening of the pore/solid interface, or by a combination of both. Consequently, sintering generally involves loss of surface area and an increase in strength of the powder compact [47].

Sintering consists of six main, but not distinct, stages. These are:

- ✓ Initial particle bonding
- ✓ Neck growth
- ✓ Pore rounding
- ✓ Pore channel closure
- ✓ Densification and pore shrinkage
- ✓ Grain coarsening.

For simplicity, sintering can be classified under three main stages which are the initial sintering stage, intermediate sintering stage and the final sintering stage. Classification into the three stages is based on the reaction(s) occurring at each stage. Also there are two main types of sintering, these are:

- ⇒ Solid state sintering
- ⇒ Liquid state sintering

#### **2.2.5.1 Solid state sintering**

Solid state sintering is the process in which compacts are heated to a temperature that allows sufficient diffusion of atoms to eliminate porosity and prior particle boundaries. During solid state sintering compacts are not heated above the solidus.

### **2.2.5.2 Liquid phase sintering**

Liquid phase sintering is the process in which powders are sintered at temperatures such that a liquid phase is present during the sintering process. This enhances the reduction of structural defects thereby increasing density. There are two types of liquid phase sintering.

The first type is the sintering process in which the liquid phase once formed is persistent throughout the entirety of the sintering process. Such persisting liquid phase is formed either by inducing the liquid phase to form (i.e., persistent/classic liquid phase sintering (LPS), a typical example being Al plus the prealloyed Ni-Cr-Fe ternary particles used in this project) or by using an activator (activated liquid phase sintering ALPS) to form a liquid [44]. Here a low inter-solubility can exist even with the liquid formation (e.g., W-Cu and Mo-Cu systems).

The other form of liquid phase sintering is transient liquid-phase sintering (TLPS). Transient liquid-phase sintering (TLPS) is the process in which the liquid phase exists for sometime before it finally disappears via reaction to form a new higher melting point solid phase during the sintering process [44].

#### **2.2.5.2.1 Mechanisms of liquid phase sintering (thermodynamics and kinetics)**

##### **2.2.5.2.1.1 Surface energy**

During liquid phase sintering, three main phases are present. These are the liquid, solid and vapor phases [44]. For effective LPS, surface energy must be reduced as liquid spreads into the solid particles. However for this to occur, the solid-liquid interfacial

energy must be smaller than the solid-vapor energy so as to prevent the solid from vaporizing during sintering, and to also enable effective interaction. Another important factor during LPS is that the liquid must effectively wet the surface of the solid particles which increases bonding that will enhance densification of the compact. Wetting is enhanced by solubility of solid in the liquid, formation of intermediate compounds, and effective diffusion [44]. Impurities can also reduce the interfacial energy; hence powder particles should be free of impurities before LPS is carried out. For some of the metals produced by LPS, their reactivity leads to formation of oxide layers which are broken during LPS by reductive atmosphere or by sufficient capillary action that mechanically break the oxide layers. Surface energies are also affected microstructurally by the surface area of solid-solid contacts as a fraction of total interfacial area, the number of contacts per grain in two-dimensional cross section, grain size and dihedral angle [48].

The relationship between grain boundaries and ratio of solid-liquid interfaces changes with sintering time. This also affects the overall microstructure i.e.,  $\gamma_{ss} = 2\gamma_{sl} \cos \phi / 2$  where  $\phi$  is the dihedral angle,  $\gamma_{ss}$  = solid-solid interfacial energy, and  $\gamma_{sl}$  = solid-liquid interfacial energy.

The relationship is characterized by the dihedral angle and is shown in Figure 2.9.

A small dihedral angle enables effective LPS.

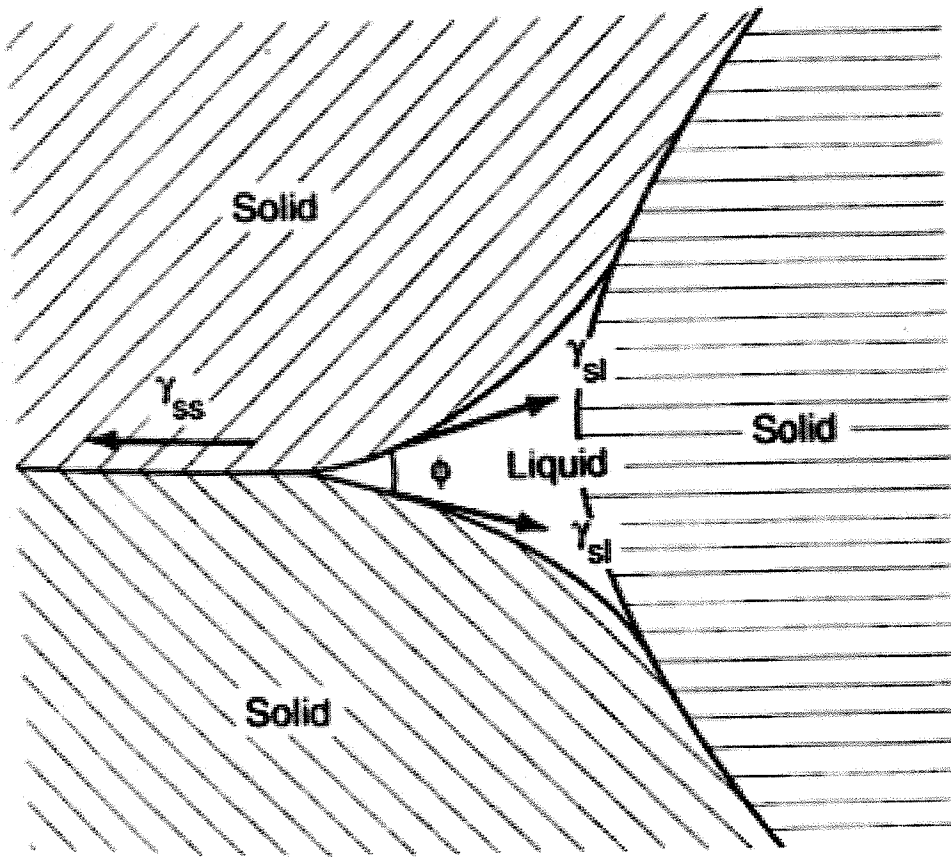


Figure 2.9 Dihedral angle and surface energy equilibrium between two intersecting grains with a partially penetrating liquid phase [44]

#### 2.2.5.2.1.2 Solubility

Solid solubility in the liquid permits solution reprecipitation and enables effective and efficient packing of grains which leads to an increase in sintered densities [49]. However, the solubility of liquid in the solid is usually undesirable as this leads to swelling of the compact as liquid diffuses into the solid grains leaving behind large pores that are difficult to eliminate during further sintering. A measure of solubility in LPS is the use of solubility parameter. The solubility parameter adapted from [44] is defined as follows:

$$sol.par = \frac{s.sol.liquid}{l.sol.solid} \dots\dots\dots 2.8$$

where sol. par is the solubility parameter, s.sol.liquid is the solid solubility in liquid and l.sol.solid is the liquid solubility in solid. If the solubility is less than one, then the system is likely going to swell, while if the solubility is greater than one the system will shrink.

A phase diagram is useful in identifying solubility parameters and in estimating the segregation tendency of alloy and impurities (i.e., the greater the separation of solidus and liquidus, the greater the solute segregation to the interface; while a downward sloping of the solidus and liquidus shows a tendency for solute segregation and lower surface energies and other LPS characteristics) [44]. Hence, eutectics are favored during LPS because they reduce the sintering temperature with liquid formation. Intermediate compounds such as intermetallics are usually not desired during LPS as high temperature intermetallic phases reduce diffusion rates, while brittle intermetallics negatively affect mechanical properties of the compacts. For systems that have very little or no solid solubility, the resultant structure is a rigid skeletal structure with densification governed by solid state diffusion. Hence, in order to obtain a high density, fine starting powders are necessary; activators that enhance solid-state sintering in the presence of a liquid phase can also be used.

### 2.2.5.2.1.3 Diffusivity

High diffusivities of base metal atoms in liquid lead to rapid densification and homogenization. This can be achieved by adding low temperature additives which lower the activation energies and subsequently increase the diffusivities at relatively lower temperatures. For systems that undergo significant solid state densification during heating, diffusivity increases exponentially with temperature until the additive melts. As a liquid phase forms during heating, there is a large increase in solubility and diffusivity due to the much weaker bond associated with a liquid phase [44]. As temperature increases, diffusivity increases exponentially; hence, high temperature enhances effective densification. Preferential evaporation of liquid can change the overall composition of a sintered component and can also damage a furnace during sintering. For practical purposes, a vapor pressure of  $10^{-3}$  Pa is desired as a vapor pressure of 1Pa can lead to significant weight loss [44]. Generally, for LPS to be effective, materials must have different melting temperatures and unequal diffusivities.

### **2.2.5.2.2 Stages of densification during LPS**

Liquid phase sintering is usually preceded by a significant amount of solid state sintering. In some cases the solid state sintering may account for a large amount of densification in the system. Therefore the relative contribution of solid state sintering is an important part of the LPS process. Densification arising from solid state sintering increases with an increase in solubility of the base material in the compact mix. Densification also increases with a decrease in particle size, decrease in heating rate, and homogeneity of additives. Furthermore, for a liquid phase to enhance densification, the liquid must dissolve the solid state sintering bond initially formed during the solid state sintering [44].

In summary, the stages involved in LPS are as follows:

*Re-arrangement*

*Solution-reprecipitation and*

*Final stage sintering*

#### **2.2.5.2.2.1 Re-arrangement**

This occurs as the liquid forms in the system which enables the liquid to pull the wetting liquid into particle neck and pores via capillary action [50]. A rapid attractive bonding force is also applied to particles due to capillary action leading to shrinkage in the compact. Secondary re-arrangement also occurs after the capillary action which repacks the particles in the compact. Pores are subsequently eliminated by viscous flow during rearrangement.

#### **2.2.5.2.2.2 Solution-reprecipitation and grain shape accommodation**

Due to the presence of insufficient liquid to fill the pores after rearrangement during LPS, further densification is achieved by mass transport or solution-reprecipitation which changes the grain shape and size distribution of the compact. Changes in shape and size are geared towards increase in packing density. Atoms at convex surfaces have higher solubility in liquid than atoms at concave surfaces. Therefore, atoms at the convex surfaces will diffuse through the liquid at the boundary and reprecipitate at the concave surfaces. Furthermore as the grain shapes are changed, the liquid flows into the remaining pore areas filling the pores. Densification is therefore obtained as the centers of particles get closer to each other. Also, the reduction in energy associated with pore elimination is offset by increase in solid-liquid surface area, while the final equilibrium shapes of the grains are determined by packing characteristics, surface energies and liquid volume fraction [51].

The shrinkage rate of solute reprecipitation is lower relative to the rearrangement stage of LPS. Kinetics of solute reprecipitation is governed by either interfacial dissolution or reprecipitation or mass transfer rate through liquid. Grain growth occurs simultaneously with shape accommodation as grains grow by dissolution and reprecipitation through either grain coalescence or solid state grain growth of skeleton. The driving force for grain growth during LPS is the reduction in both the amount and curvature of the solid-liquid interfaces along with a decrease in interfacial energy.

The coarsening rate can be described by [52]:

$$G^n - G_o^n = K(\phi, T)(t - t_o) \dots\dots\dots 2.9$$

where  $G_o$  is the initial grain size,  $G$  is the average grain size after time  $t$ ,  $K(\phi, T)$  is the growth rate constant that is dependent on the solid volume fraction  $\phi$  and temperature  $T$  and,  $n$  is the growth exponent which depends on transport mechanism.

### **2.2.5.2.2.3 Final stage sintering**

The slow densification of a solid skeleton structure occurs at the final stage of LPS. Microstructure coarsening continues while enlargement of pores occurs in the presence of entrapped gas [53]. If the entrapped gas has no solubility in the material, the gas pressure inside the pores prevents further densification. However, for gas with slight solubility in the material larger pores grow at the expense of smaller ones via Oswald ripening leading to compact swelling. Conversely, entrapped gas can be avoided through vacuum sintering.

### **2.2.6 Post sintering treatment**

Basically, reducing the amount of pores in a sintered compact is often necessary in P/M processing. Such processes are also referred to as net shaping or full density processing. This processing is usually done so as to remove the residual pores that do not have gas filling them. An advantage of full density processing includes the ability to improve properties after sintering compacts. Also, dimensional control can be introduced. All these processes will enhance the overall performance of the compact.

An example of such a process is the heat treatment process, while another example is mechanical deformation applied after processing, prior to final application in service. Sintered compacts may be mechanically deformed by rolling swaging, or drawing. This is done to increase densification and enhance the fatigue property of the material in service.

#### **2.2.6.1 Heat treatment of P/M processed Superalloys**

There are various processes that may be carried out on P/M processed Superalloys after sintering. Some of these processes are used to unify grain structures while others are used to reengineer the alloy properties for desired application(s). Prior to a P/M compact being placed in service, the compact can be subjected to solution and ageing treatment. This is done to either form a desired phase which could not precipitate during sintering or to produce a specific phase for a specific application.

## **2.3 Theoretical considerations**

### **2.3.1 Thermodynamics**

Since the application of Superalloys in the first jet engine (Whittle W1) flown by Sir Frank Whittle in the late 1930s over Gloucester E28/39 on May 14, 1941, [54] there have been significant developments in processing of such alloys. In today's applications, there is a constant need to develop newer Superalloys with improved properties. However, the design of Superalloys for today's application especially in turbine applications is quite expensive and can be very complex. According to Small [54], Superalloy development can take up to 10 years or more before they could be used in service. Prominent among the problems of Superalloy development includes the determination of the chemistry mix needed to make the required part.

The traditional method of alloy development relies on the combination of experience, empirical wisdom, and a limited calculations based on electron valency theory (PHACOMP) [20] [54]. Although, this may have produced results, there is greater demand for more complex alloys in today's applications. Therefore, it is necessary to have a method of reducing time to market relative to alloy development and elimination of empirical wisdom in Superalloy development.

A viable alloy development technique is the calculation of phase-diagram (CALPHAD) technique [55]. This technique has grown in applications for alloy development over the years. With advancement in computer technology, it is now possible to calculate equilibrium phase diagrams for Superalloys in minutes.

The CALPHAD technique is based on sound mathematical models using thermodynamic proofs for description of the properties of various phases present in the

alloy under consideration. The mathematical coefficients used by the models are held in an extensive database. This data base is assessed by various software packages and an example of one such package is Thermocalc [56]. As a comprehensive package, Thermocalc performs a series of calculations via Gibbs energy minimization providing detailed information on the alloy phase equilibria.

Furthermore, various works have been done on the modeling of Superalloys [57] which were however concentrated on ternary sub-systems [57-60]. Recent developments include applying CALPHAD techniques to Superalloy development.

Another trend in modeling of Superalloys is in comparing thermodynamic predictions to the experimental results [61]. This is one of the goals of this research project. Specifically, a Java Base Materials processing software (JMatPro) was used to estimate the phase diagram of the alloy that was being developed. JMatPro modeling uses CALPHAD described previously to describe the thermodynamic properties of the components i.e., a mathematical description of the thermodynamic properties of the system of interest using stoichiometry for simple alloy and pure compounds, as well as more complex models to calculate the thermodynamic properties of complex alloys [57].

## 2.4 Thermal analysis

During powder metallurgy processing, reactions can occur with a change in enthalpy. A way of determining such reaction would be to thermally analyze such reaction(s). Instruments for measuring such reaction(s) include differential scanning calorimetry (DSC), differential thermal analyzer (DTA), and thermogravimetric analysis (TG). The former instruments depend on temperature difference between reactive and non reactive reference to determine as a function of time, useful information about the reaction types being studied [62], while the TG measures a change in weight as temperature changes. Furthermore, DSC has a similar output as the DTA and TG except that it has an output that can directly measure the sample energy during transformation.

Because of its relevance to this research project, more emphasis will be placed on the DSC and DTA instruments. To this end, a brief review of its operating principles would be beneficial.

### 2.4.1 Principles of DSC

From the first law of thermodynamics

$$dU = dQ - dW \dots\dots\dots 2.11$$

where U is the internal energy, Q is the heat quantity and W is the work done.

If it can be assumed that the only type of work is the PV work, then the work done

$$dW = PdV + VdP \dots\dots\dots 2.12$$

where P is the pressure and V is the volume. If it is assumed that the system under study is in the DSC/DTA, then P would represent the pressure in the instrument during the

reaction and  $V$  is the volume of the crucible in which the reaction is taking place. Also,  $V$  would apply to the volume of the reference which is empty in this study.

Therefore, for a sample heated in a container under constant volume at constant pressure then its work done  $dW=0$  since  $PdV=0$  and  $VdP=0$ . This implies that

$$dU = dQ \text{ from equation 2.11[63].}$$

But it is known that

$$H = U + PV \dots\dots\dots 2.13$$

where  $H$  is the enthalpy.

Therefore for a change in enthalpy

$$dH = dU + PdV + VdP \dots\dots\dots 2.14$$

and at constant  $P$

$$dH = dU + PdV \dots\dots\dots 2.15$$

If the value of  $dU$  in equation 2.11 (i.e.  $dQ=dU$  at constant volume and pressure), is inserted and  $dV =0$ .

Then

$$dH = dQ \dots\dots\dots 2.16$$

Therefore the amount of heat supplied per unit mass, which in a DSC/DTA instrument is measured by current flow into the heater in the DSC/DTA sample relative to the reference, is equal to the enthalpy, provided no work is done by or to the system (sample). Also, the change in enthalpy is the difference between the products and the reactants. i.e.,

$$\Delta H = \sum H_{\text{Product}} - \sum H_{\text{Reactant}} \dots\dots\dots 2.17$$

where  $\Delta H_{product}$  is the enthalpy of formation of product(s) and  $\Delta H_{reactants}$  is the enthalpy of formation of reactants respectively.

### 2.4.2 Differential thermal analysis

As stated earlier, an instrument used for calculating enthalpy involved in reactions is the differential thermal analyzer or differential scanning calorimetry DTA/DSC. In a DTA/DSC, when reaction occurs the heat change in the reaction is indicated by a deflection or peak. It is therefore important to know how a DSC/DTA actually calculates the enthalpy involved in a typical reaction. Therefore, for a reaction proceeding at a rate which varies with temperature (i.e., reaction that possesses activation energy), the peak position varies with the heating rate, provided other conditions are fixed [62].

As noted earlier, thermal analyzer measures the temperature difference between the sample and a reference. However, in the reference no reaction occurs ( $dq/dt=0$ ), therefore the temperature distribution in the reference can be stated as:

$$\frac{\partial T}{\partial t} = \frac{k}{\rho c} \nabla^2 T \dots\dots\dots 2.18$$

Usually, in a DTA/DSC analyzers the heat flow follows a general equation [64]:

where T is the temperature at which reaction occurs, t is the time, k is the thermal conductivity,  $\rho$  is the density, c is the specific heat

$$\frac{\partial T}{\partial t} - \frac{k}{\rho c} \nabla^2 T = \frac{1}{\rho c} \frac{dq}{dt} \dots\dots\dots 2.19$$

$dq/dt$  is the rate of heat generation due to chemical reaction per unit volume of sample [64].

Furthermore, the crucible used in the DSC/DTA is usually cylindrical and the temperature of the cylinder is given as [62]:

$$T = T_o + \phi t \dots\dots\dots 2.20$$

where  $\phi$  is the constant rate of temperature rise and  $T_o$  the initial temperature before the occurrence of the reaction in the sample holder. Therefore the temperature at centre of the crucible  $T_r$  can be obtained by integrating equation 2.18 to the stage at which reaction occurs.

This gives the temperature of the reference as:

$$T_r = T_o + \phi t - \frac{\phi \rho c a^2}{4k} \dots\dots\dots 2.22$$

While the solution expressing the temperature at the centre of the sample will, as derived by Kissinger, [64] is given by:

$$T_s = T_L + \phi t - f\left(\frac{\partial q}{\partial t}\right) \dots\dots\dots 2.23$$

where  $f\left(\frac{\partial q}{\partial t}\right)$  is the function of reaction rate including the secondary effects of

the reaction e.g., volume, density or thermal properties.

Therefore differential temperature as measured by the DSC/DTA which is the difference between the temperature of the sample and the reference is given by  $\theta$  [64] obtained by subtracting equation 2.22 from 2.23 which gives

$$\theta = T_{\text{sample}} - T_{\text{reference}}$$

$$\text{i.e., } \theta = f\left(\frac{\partial q}{\partial t}\right)_{\text{sample}} - \left(\frac{\phi \rho c a^2}{4k}\right)_{\text{reference}} \dots\dots\dots 2.24$$

which when differentiated with respect to time gives

$$\frac{d\theta}{dt} = f'\left(\frac{dq}{dt}\right) \frac{d^2q}{dt^2} \dots\dots\dots 2.25$$

and  $\theta$  is maximum at  $\frac{d\theta}{dt} = \text{zero}$ .

It can also be seen that when  $\frac{d^2q}{dt^2}$  (i.e., the derivative of the rate of heat absorption is zero),  $\frac{d\theta}{dt}$  is also zero.

The main assumption is that the heating rate is constant and a good example of a reaction that can be measured with the DTA/DSC is the combustion synthesis reaction.

## 2.5 Diffusion

For most metals, elimination of structural defects such as porosity and other defects and formation of reaction products is achieved by diffusion of atoms. Generally, diffusion occurs to produce a decrease in Gibbs free energy. Atoms diffuse from a higher chemical potential gradient to a lower chemical potential gradient or from a region of high chemical potential to a region of low chemical potential. Furthermore, diffusion ceases when the chemical potential of atoms is the same in every part of the material system.

For example, if two pieces of metal are held together and heated to a temperature at which atoms of each piece of metal diffuses into the other, the diffusion occurring in this material may be described by Fick's first law of diffusion:

$$J = -D \frac{dc}{dx} \dots\dots\dots 2.26$$

where J is the material flux i.e., the number of atoms diffusing down concentration gradient of each metal per second unit area in each material and is expressed as  $\text{kgm}^{-2}\text{s}^{-1}$ , c is the concentration of atoms in the each material in  $\text{kgm}^{-3}$  and D is the diffusion coefficient between two diffusing materials.

Also, the diffusion of atoms is achieved by two mechanisms, namely, substitutional diffusion or interstitial diffusion. The substitutional mechanism is prevalent in atoms that are similar in crystal structure and atomic size. In substitutional diffusion, movements of atoms are limited by their neighbors and atoms cannot move to another site being occupied by a similar atom. However, an atom can be present at the surrounding neighboring vacant site when sufficient vibrational energy is supplied, while

the rate at which an atom will move depends on frequency with which such atom is vibrating [65].

## **2.6 Corrosion**

Another parameter considered is corrosion. Simply defined, corrosion is degradation of materials as a result of interactions with the environment. The type of environments causing corrosion can either be oxidizing or reducing. However, the focus in this research was to be the degradation of materials as a result of interaction with oxygen (i.e., oxidation). By definition, oxidation is the gradual disintegration of materials usually in the presence of oxygen. The process is insidious and affects a great deal of materials in everyday applications. For example, in aerospace applications, the hottest part of the engine is usually subjected to corrosion more than any other part of the engine. Earlier materials for aerospace applications, especially gas turbine materials were based on Ni-Cr or cast cobalt based alloys [66].

### **2.6.1 Effect of Cr additions to Superalloys**

Specifically for nickel and nickel-iron based Superalloys, chromium is added to improve oxidation resistance and to also increase strengthening by solid solution [67]. The classes of Superalloys that depend on Cr addition for oxidation resistance are as follows: [67]:

- Group I: The Cr content in this group is less than 10%, resulting in a morphology in which NiO scales and internal Cr<sub>2</sub>O<sub>3</sub> precipitates (explanation is given in section 2.9.2 after [65, 66, and 67]).

- Group II: This group of Superalloys has Cr content of less than 30%. In this group, external scales of  $\text{Cr}_2\text{O}_3$  form over the alloy grain boundaries in addition to the formation of external NiO scales. Further, more  $\text{Cr}_2\text{O}_3$  forms internally.
- Group III are the group with Cr concentration over 30%. The type of oxidation mechanism is shown in Figure 2.10b in which an external  $\text{Cr}_2\text{O}_3$  scale forms.

### 2.6.2 Effect of rare earth additions to Superalloys

Small amount of rare-earth elements can also be added to Superalloys. In this thesis, rare-earth effects were not specifically investigated. However, the possibility of being subsequently added to improve the quality of the compact is of interest. Hence, brief discussion on rare earth is considered to be desirable. Rare-earth additions have been found to alter the oxidation resistance of  $\text{Cr}_2\text{O}_3$  forming alloys. The resulting effects of adding rare-earth include:

- Formation of continuous  $\text{Cr}_2\text{O}_3$  scales at lower alloy Cr concentration.
- Reduction in the rate of  $\text{Cr}_2\text{O}_3$  growth
- Improved scale adhesion
- Change in the primary growth mechanism of oxide from outward cation migration to inward anion migration
- Reduction of the grain size in the  $\text{Cr}_2\text{O}_3$  scale.

While it is established that when the Cr content is sufficient, it offers protection by forming a layer of Cr<sub>2</sub>O<sub>3</sub>, this protective layer is unstable at temperatures above 1000°C (equation 2.27) [67].



Therefore, alloys that depend on the formation of Cr<sub>2</sub>O<sub>3</sub> are very susceptible to accelerated degradation at temperatures above 1000°C.

The evaporation of CrO<sub>3</sub> results in thinning of the scale so that diffusive transport through the scale becomes rapid. This problem is one of the major limitations on the very high temperature use of Cr<sub>2</sub>O<sub>3</sub> forming alloys and coatings. This effect becomes significant at temperatures around 1000°C and even lower in the presence of high velocity gases.

To this end, it was concluded that Cr protection in a Superalloy is restricted to temperatures below 850°C [68]. Hence, to improve the corrosion resistance of Superalloys at temperatures above 850°C, another element was determined to be more suitable. This element is aluminum (Al).

### 2.6.3 Effect of Al additions to Superalloys

Al plays a crucial role in the gamma prime (γ') precipitation of gamma prime precipitate strengthened Superalloys and also in the oxidation resistance of Superalloys. Al forms an ordered γ' phase with the formula Ni<sub>3</sub>(Al, Ti), its presence in Superalloys can lead to an increase in the solvus temperatures of Superalloys. Also, the element is the basis of providing oxidation resistance to the Ni-Al systems [67]. Thermodynamically, Al

should form a protective oxide on alloys containing any amount of Al. In reality however, due to the opposing diffusional fluxes of oxygen inward and Al outward, this is often not the case.  $\text{Al}_2\text{O}_3$  can only precipitate to protect when its percentage is sufficiently high to produce a critical mole fraction of oxide particles required for particle line-up, while the growth of such a scale ( $\text{Al}_2\text{O}_3$ ) is only sustained when the flux of Al in the alloy exceeds that consumed by scale thickening i.e.,  $J_{\text{alloy}}^{\text{Al}} > J_{\text{oxide}}^{\text{Al}}$

Ni-Al systems that are protected by Al oxide scale (without Cr) are subdivided into three main categories. These categories are given following [67] as:

1. Alloys that have 0 to less than 6w/o Al;  $\text{Al}_2\text{O}_3$  usually results internally with an external unprotective NiO scale
2. The second category is those that have between 6 and 17 w/o Al. In these alloys external  $\text{Al}_2\text{O}_3$  forms initially but is not sustained due to inadequate supply of Al resulting in the overtaking of  $\text{Al}_2\text{O}_3$  scale by the faster growing but unprotective NiO.
3. The third group are those that have Al content that is more than 17w/o. This group of alloys readily forms a protective  $\text{Al}_2\text{O}_3$  scale due to sufficient supply of Al.

#### **2.6.4 Effect of Cr and Al additions to Superalloys**

Nickel, nickel-iron and cobalt base Superalloys having Cr and Al simultaneously added benefit from a remarkable synergistic effect of Al and Cr alloying elements which

is of great technological importance [67]. The addition of about 10w/o Cr or more can enhance  $\text{Al}_2\text{O}_3$  scale on alloys having Al levels that are as low as 5w/o. Consequently, with the addition of Cr to Al containing alloys three primary main regions are seen to occur [67]. These are:

- I      NiO external scale +  $\text{Al}_2\text{O}_3/\text{Cr}_2\text{O}_3$  subscales
- II      $\text{Cr}_2\text{O}_3$  external scale +  $\text{Al}_2\text{O}_3$  subscales
- III    External scales of only  $\text{Al}_2\text{O}_3$

The role of Cr in producing  $\text{Al}_2\text{O}_3$  scales at a lower Al content than often required in binary Ni-Al alloys can be described by the phenomenon known as “gettering” [69]. Gettering is a process in which an oxidation resisting mechanism of one element renders the oxidation promoting effect of another element inactive or harmless. High Cr content in Superalloys results in a continuous  $\text{Cr}_2\text{O}_3$  subscale that defines a lower scale-alloy oxygen activity; reduces oxygen diffusion into the alloy, and curtails internal  $\text{Al}_2\text{O}_3$  formation. In addition to this, high Cr content blocks the growth of NiO while  $\text{Al}_2\text{O}_3$  subscale eventually becomes continuous and rate controlling. Furthermore, the time for formation of such scale could be achieved at  $1000^\circ\text{C}$  in less than one hour [67].

Addition of rare earths to alloys containing Al and Cr can also improve the quality of the oxide scale. It is known that rare earth or oxygen active elements can produce dramatic modifications to oxidation behavior which are equally important to those arising from Al or Cr additions [67]. Small amounts of rare earth can prevent the  $\text{Al}_2\text{O}_3$  scales from otherwise spalling at the oxide-metal interface. An example of a refractory element

added is yttrium, although hafnium can also be added to supplement yttrium in some cases.

### 2.6.5 Oxidation mechanisms for pure metals at high temperatures

For pure metals, the oxidation rate is usually diffusion-controlled. Therefore to estimate the rate of growth of oxide on pure metals, it is important to incorporate some basic oxidation reactions. From the literature, the growth rate of an oxide layer of thickness  $x$  follows the equation [69]:

$$\frac{dx}{dt} = \frac{k'}{x} \dots\dots\dots 2.25$$

where  $k'$  is the parabolic rate constant with units  $\text{cm}^2/\text{sec}$  and  $t$  is the time in seconds.

Integrating [69] equation 2.25 gives:

$$x_t^2 - x_{t_0}^2 = 2k'(t - t_0) \dots\dots\dots 2.26$$

where  $t_0$  is the time when diffusion begins. Also, the extent of diffusion may also be

expressed in terms of mass change per unit area  $\left(\frac{\Delta m}{A}\right)$ .

$$\left(\frac{\Delta m}{A}\right)_t^2 - \left(\frac{\Delta m}{A}\right)_{t_0}^2 = 2k''(t - t_0) \dots\dots\dots 2.27$$

where

$$k'' = \left(\frac{8}{V}\right)^2 k' \dots\dots\dots 2.28$$

and  $V$  is the equivalent volume of the oxide.  $k''$  has the unit of  $\text{g}^2/\text{cm}^4$  [70].

According to Wagner [69], the theoretical treatment for  $k'$  is based on the following assumptions.

1. That the oxide is compact, perfectly adherent scale,
2. The migration of ions or  $e^-$  across the scale is the rate-controlling process
3. Thermodynamic equilibrium is established at both the metal-oxide and oxide gas interface
4. Thermodynamic equilibrium is established locally throughout the scale, while the scale is thick as compared with the distance over which scale changes.

Also, it was assumed that oxygen solubility in the metal may be neglected.

Therefore, the rate of oxidation for a diffusion-controlled growth rate can be represented

$$\text{as } x_t^2 - x_{t_o}^2 = 2k'(t - t_o) \text{ or } \left(\frac{\Delta m}{A}\right)_t^2 - \left(\frac{\Delta m}{A}\right)_{t_o}^2 = 2k''(t - t_o).$$

## 2.6.6 Oxidation mechanisms of alloy metals at high temperatures

The oxidation of alloys is more complex than that of pure metals. Following Wagner's work, [69] the oxidation properties of alloys can be grouped as:

- a. Noble parent metal with alloying elements that are less noble (more base in nature) in nature
- b. Base parent with base alloying element

These are illustrated in Figure 2.10 and Figure 2.11 following [67].

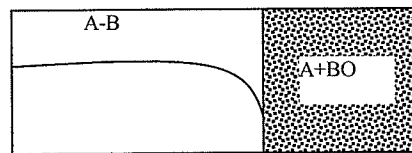


Figure 2.10a Alloy dilute in B showing internal oxidation of B [67]

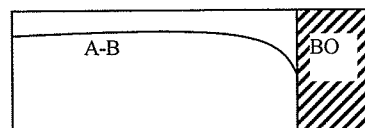


Figure 2.10b Alloy concentrated in B showing external layer of BO [67]

For 2.10a to occur, A must be noble and B must be less noble, in addition to this, oxygen must be soluble in A. In the simplest case for which BO is very stable and  $D_B \ll D_O$  in the alloy, the depth of internal oxidation may be written as [67]:

$$x(f) = \left( \frac{2N_O^{(s)} D_O t}{N_B^{(O)}} \right)^{\frac{1}{2}} \dots\dots\dots 2.29$$

where  $N_O^{(s)}$  is the oxygen solubility and  $N_B^{(O)}$  is the bulk alloy concentration of B expressed as atomic fraction. The equation 2.29 indicates that  $x(f)$  decreases as  $N_B^{(O)}$  increases and when sufficient B is present, outward flux of B results in BO being formed as a continuous surface layer (Figure 2.10b) while transition from internal to external oxidation occurs when

$$N_B^{(O)} > N_B^{(Critical)} \dots\dots\dots 2.30$$

Where,  $N_B^{(Critical)} = \left( \frac{\pi g^*}{3} N_O \frac{D_O V_M}{D_B V_{OX}} \right) \dots\dots\dots 2.31$

Where,  $V_m$  and  $V_{ox}$  are molar volumes of alloy and oxides respectively,  $g^*$  is the critical volume fraction of oxide required for the transition which is often around 0.3.

Figure 2.11 is the schematic cross section of an alloy A-B where both components form stable oxides but BO is more stable than AO

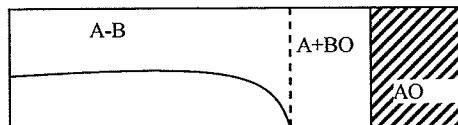


Figure 2.11a Alloy dilute in B showing internal oxidation of B under external layer AO

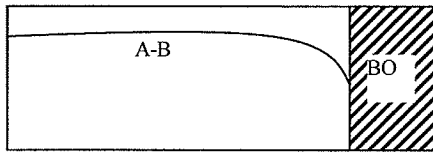


Figure 2.11a Alloy concentrated in B showing continuous external BO

Figure 2.11 represents a more general case where the oxides of both A and B are stable in the gas but BO is more stable than AO (in Superalloys A generally represents Ni or Co and B represents Cr, Al, Ti ). For low concentration of B, an external layer of AO will form and an internal oxide of BO will precipitate in the alloy, Figure 2.11a. If the concentration of B is increased to exceed the critical concentration needed for transition into external oxidation, the morphology that was shown in Figure 2.11b would result.

Formation of a continuous layer of BO precludes any further formation of the less stable AO, although some AO will generally form before the BO layer becomes continuous. Such a phenomenon is referred to as “transient oxidation” [67]. The objective of alloying for oxidation resistance is depicted in Figure 2.11b. This figure represents alloying element B that forms an oxide that is both very stable and slow growing. This type of layer can be formed when sufficient quantity of B is added and is referred to as “selective oxidation”[71].

The oxidation rate for an alloy as seen in Figure 2.11b can be essentially parabolic with a rate constant characteristic of BO. However, selective oxidation depletes B from the alloy under the scale. This will eventually result in an enrichment of oxides of A in the scale with rate increasing toward that of characteristic AO. The length of time required for transition to a more rapid rate depends on a number of factors such as

temperature, specimen size, diffusivities in the alloy and scale and initial concentration of B in the alloy.

Furthermore, the transition is hastened by any process that lessens the protectiveness of the BO layer which can occur by evaporation of a volatile oxide e.g.,  $\text{Cr}_2\text{O}_3$  that thins the protective layer or by mechanical damage to the scale by action of erosive particles or cracking and spalling due to applied or generated stresses. This is common in Superalloys because of the cyclic thermal loading they undergo [67].

## **CHAPTER THREE**

### **3.0 EXPERIMENTAL PROCEDURES**

#### **3.1 Materials**

##### **3.1.1 Raw materials**

The powders used in this study were produced by Alfa Aesar Inc USA, using inert gas atomization. The ternary alloy was obtained in prealloyed form with the reported composition of Ni: 72, Cr: 14-16 and Fe: 7-10 w/o; while the Al powder was 99.98% pure and was also obtained from Alfa Aesar. This powder was 99.98% pure and also obtained from Alfa Aesar.

#### **3.2 Thermodynamic software modeling**

JMatPro was used to predict the effects of green compact composition and sintering parameters on the formation of different phases on heating and cooling. As stated in Chapter 2 of this thesis, the software uses a step-calculation method, based on CALPHAD (CALculation of Phase Diagrams) that requires a mathematical description of the thermodynamics of the system of interest. The described thermodynamic properties of the phases in the system are then input into application software to calculate phase equilibria by a Gibbs energy minimization process [57].

### 3.3 Powder processing and characterization

#### 3.3.1 Powder size characterization

The size distribution was determined using a Malvern<sup>TM</sup> (Master Particle Sizer M3.1) laser particle-size analyzer. To obtain the data a 0.2g Ni-Cr-Fe powder was mixed with methanol (10ml) for blending, and subsequently mixed with about 200ml of distilled water at room temperature. A constant flow rate of about 4ml/s was maintained, while simultaneously stirring the mixture. The results were then recorded from the average readings taken over a period of 1.7s. Table 3.1 summarizes the equipment specification. From the table, the focal length which represents the distance of powder image to the laser is given as 63mm and the beam length (i.e., the total length of the laser) in the instrument is given as 300mm, the obscuration level is given as 0.0502 while the volume concentration is 0.0001%.

Table 3.1. Summary of Malvern laser particle analyzer specification

Equipment	Malvern Instruments MASTER particle sizer M3.1
Focal Length	63mm
Beam Length	300.00mm
Obscuration	0.0502
Volume Concentration	0.0001%

### **3.3.2 Powder microstructural examination**

In characterizing the powder for compositional analysis, two main methods were employed, namely wet chemical analysis and SEM-EDS. Results were subsequently compared to the manufacturer's specification. The shape analysis of the powder was carried out using a Hitachi scanning electron microscope. Prior to examination, the powder was mixed with carbon paste, spread on a SEM specimen holder and allowed to cure for more than 24h. An accelerating voltage of 5 kV and current of 10  $\mu$ A were used during the shape examination thereby avoiding the need to coat the sample.

### **3.3.3 Powder X-ray diffraction**

X-ray diffraction analysis of the as-received powder was carried out using Cu,  $K\alpha$  radiation, using a wavelength  $\lambda = 1.54056\text{nm}$  and 40mA current and a voltage of 44kV. The instrument was manufactured by Rikagu.

### **3.3.4 Powder flow density calculation**

The flow density is the density that describes the powder's flowability and its ability to fill the die without the application of external pressure. Flow density is important for powders as it helps to determine the ability of the powders to agglomerate. Agglomerated powders are not desired during powder processing as this can lead to non-uniform compositional distribution. In this research, flow density was calculated by using a cylindrical container whose parameters were known and measuring the weight of the powder that fills the cylinder.

## **3.4 Compact fabrication**

### **3.4.1 Optimizing binder and lubricant**

In order to optimize powder compressibility, additives such as binder and/or lubricants can be employed. In this study, an organic binder, polyvinyl alcohol, and a lubricant, microwax, were investigated. Powders were subsequently blended with the optimized additive for a period of 0.5h in a Turbula™ blender. Finally, the powders were compacted into transverse rupture (TRS) bars in accordance with Metal Powder Industries Federation (MPIF) standards at compacting pressures from 100 to 550MPa using an Instron™ test frame (1000kN capacity). In this way an optimum binder, lubricant and compacting pressure were determined.

### **3.4.2 Pre-sintering**

Prior to sintering, green compacts were de-lubricated in a horizontal tube furnace equipped with a stainless steel chamber at 400°C for 0.5h under flowing nitrogen.

### **3.4.3 Sintering**

The samples were first subjected to solid state sintering in air at 1270°C, to minimize closed porosity. This temperature also corresponds to >90%  $T_m$  (the melting temperature) of the alloy according to the equilibrium phase diagram and thus significant diffusion is expected to occur. For simplicity, air was first chosen as the sintering atmosphere and time was varied from 0.5h to 5h so as to obtain the best time for sintering and to examine the oxidation effect. To optimize the sintering temperatures, samples

were heated under vacuum ( $< 6$  millitorr) for a constant time (1h) while temperatures were varied from 1260 to 1400<sup>0</sup>C. Experiments to optimize sintering time under vacuum were also conducted. The effects of Al addition to the ternary Ni-Cr-Fe were also investigated by adding different amounts ranging from 1, 3, 6 and 12w/o of aluminum to the ternary alloy. Finally, the effect of 1 and 3w/o Ti on the optimized ternary Ni-Cr-Fe + aluminum quaternary was investigated.

#### **3.4.4 Mercury and water densitometry**

The sintered alloy was characterized in terms of theoretical density. The density of the compact was measured by applying the Archimedes principle (mercury medium) for both the green and sintered compacts. These density calculations were also verified by measuring in water medium.

#### **3.5 Heat treatment**

A heat treatment was carried out on the selected samples as follows. First the samples were solution treated at about 1200<sup>0</sup>C for 4h and quenched in water. This was followed by various heat treatments. For ageing heat treatment, two temperatures were tested namely 650<sup>0</sup>C and 800<sup>0</sup>C. Samples were then held at these temperatures for times 0.5h, 1.0h, 3.5h 7.5h and 15.5h and air cooled. For the precipitate dissolution heat treatment, selected samples were heated to 910<sup>0</sup>C, 1010<sup>0</sup>C and 1050<sup>0</sup>C and held for 1h each at these temperatures.

### **3.6 Microstructural examination of sintered specimens**

For metallographic assessment of the sintered specimens, a cross-section of each sintered sample was cut using a diamond blade and mechanically polished to 1 $\mu$ m diamond paste. The “as-sintered” polished specimens were subsequently electrolytically etched in a solution of 12ml of 70% H<sub>3</sub>PO<sub>4</sub>+ 40ml of 70% HNO<sub>3</sub>+48ml of 98% H<sub>2</sub>SO<sub>4</sub> at 5V for 10s and specimens of the heat treated materials (section 3.5) were etched in a solution of 3ml of 49% HF+ 20ml of 70% HNO<sub>3</sub> at 50°C.

#### **3.6.1 Optical and scanning electron microscopy**

The sintered alloy was prepared using standard metallographic techniques. The polished and etched specimens were examined by a Zeiss Axiophot optical microscope equipped with Clemex<sup>™</sup> image analysis and also using a JEOL 5900-LV scanning electron microscope (SEM) equipped with ultra thin window Oxford link EDS spectrometer. For SEM/EDS the voltage used was between 10kV and 20kV.

### **3.7 X-ray diffraction of sintered specimens**

The phase(s) formed in the alloys after cooling from the sintering temperature were also identified using a Rikagu XRD with Cu K $\alpha$  radiation, wavelength  $\lambda = 1.54056\text{nm}$ , operating at an applied voltage of 44kV and a current of 40mA. An analyzing software (WINJADE<sup>™</sup>) was used for identification of the phases. Sample preparation for the XRD analysis involved cutting a flat surface, cutting and polishing.

### **3.8 Differential scanning calorimetry sample preparation**

The DSC analysis instrument (NETZSCH DSC 404C) was first calibrated following the ASTM E967-03 standard [72] using indium, aluminum, silver, gold and nickel at 2.5<sup>0</sup>C/min, 5.0<sup>0</sup>C/min, 10.0<sup>0</sup>C/min, 15.0<sup>0</sup>C/min, 20.0<sup>0</sup>C/min and 25.0<sup>0</sup>C/min heating rates. The differential scanning calorimetry (DSC) analysis for both the investigated powders and sintered compacts were done using 5mg slices (about 3mm diameter) that were cut from either the green compacts or the sintered compacts as appropriate.

### **3.9 Phase transformation in DSC**

The process used for sample preparation for phase transformations involved mixing 6w/o Al powder with Ni-Cr-Fe powder in a Turbula<sup>TM</sup> mixer, compacted at 500MPa, and delubricated in a tubular furnace at 400<sup>0</sup>C for 0.5h under a flow of 50ml/min argon. This yielded a compact with an as-prepared composition of Cr:11.3; Fe:8.5; Al:6; balance Ni(w/o). Transformation reactions were studied by heating the samples in a DSC to the points of exo/endoothermicity and quenching in argon followed by phase identification by X-ray diffraction, and microstructural analysis by SEM equipped with EDS capability.

In a subsequent study, green compacts were heated to 560<sup>0</sup>C and 640<sup>0</sup>C for times varying from 0, 10 and 30mins to assess the effect of hold time prior to argon-quench.

### **3.10 Hardness measurements**

The hardness values were obtained using Vickers and Rockwell (scale A and B) testers. For Vickers hardness, the test load used was 10 kgf for 5 seconds and nine readings were taken. The Rockwell hardness tester was automated and the test load used was 50kgf. For the Rockwell hardness tester, six readings were taken. In both types of hardness testers the average values of hardness readings were taken eliminating the top and the bottom values typical of the procedures for porous specimens.

### **3.11 Mechanical working**

The optimized and selected sintered compacts were mechanically deformed (cold rolled) through multipass rolling mill. For the as-sintered ternary compacts, the reduction was carried out using a progressive increase of 5-10% per pass; about five passes were carried out. Also, for the Al-modified compacts, mechanical deformation was carried out at a progressive increase of about 2-5% (to minimize cracking) while between four to eight passes were carried out before cracks were noticed. For some selected samples, a solutionized heat treatment at 1200°C for 4hs was carried out prior to deformation.

### **3.12 Oxidation test**

The oxidation tests of selected sintered samples were carried out in a muffle furnace. Prior to oxidation testing, samples were solutionized at 1200°C for 4h and quenched in water in order homogenize the microstructure. The oxidation tests were carried out at 1000°C for times ranging from 0.5h to 36h. The weights of the test samples

were measured before and after oxidation tests while microstructural examination of the oxidized samples was carried out in the SEM.

The chart below shows the simplified process for the alloy development.

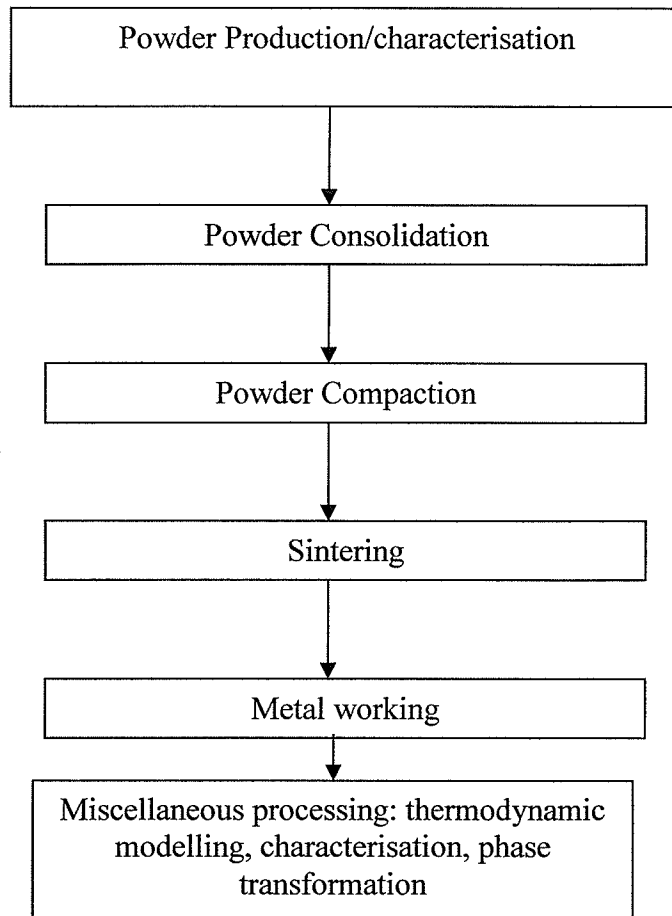


Figure 3.1 Simplified alloy development process

## CHAPTER FOUR

### 4.0 RESULTS AND DISCUSSION

In this thesis, the results presented and discussed are as follows: First, the P/M processing of the alloy was optimized including the effects of binder, lubricant, compacting pressures, sintering temperature and sintering time. This was followed by examining the effects of Al content and its subsequent modeling using JMatPro thermodynamic processing tool. Following these, phases that formed on heating and on cooling on the optimized Al composition were investigated by the DSC, followed by heat treatment, oxidation investigation and effect of 1 and 3w/o Ti on the optimized quaternary (appendix). The summary of these processes is shown in Figure 4.1.

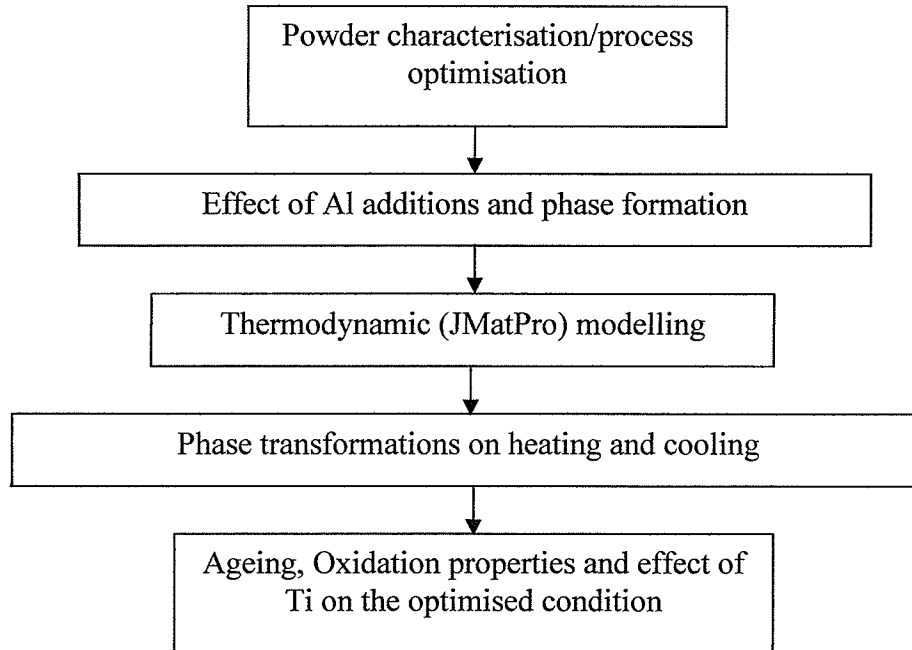


Figure 4.1: Illustrations of the results and discussion as presented in this thesis

## **4.1 Material characterization**

All powder material used in this study was first characterized for shape, composition, size and flowability.

### **4.1.1 SEM analysis**

SEM images of the as-received powder are shown in Figures 4.2a-e. From the figures, it can be seen that the shape of the powder was spherical with the absence of satellites, or secondary attachments that often affix themselves to powder particulates, which in turn prevent attainment of good mechanical properties. In each powder particle, micrograins and grooves were also observed, as seen in Figures 4.2c, 4.2d and 4.2e. The micrograin structure obtained may be due to the cooling rate of the molten alloy during atomization. Because of the numerous boundaries between micrograins, sintering by diffusion is enhanced due to the higher migration tendency of atoms at the boundaries.

Figure 4.3 and Figure 4.4 also show the EDS X-ray maps of different batches of ternary powders received. It can be seen that while one batch of powder (Figure 4.3) shows a fairly homogeneous distribution of the alloying elements, another batch (Figure 4.4) shows a non-homogeneous distribution of alloying elements. Specifically, Figure 4.4 shows a typical SEM backscattered electron (BSE) image and X-ray elemental maps of various elements present in the as-received ternary powder of a batch different from that of Figure 4.3. Similar to the powder in Figure 4.3, most of the powder particles were observed to be spherical. However, at times some spongy particles were also observed. X-ray mapping revealed the latter to be iron particles.

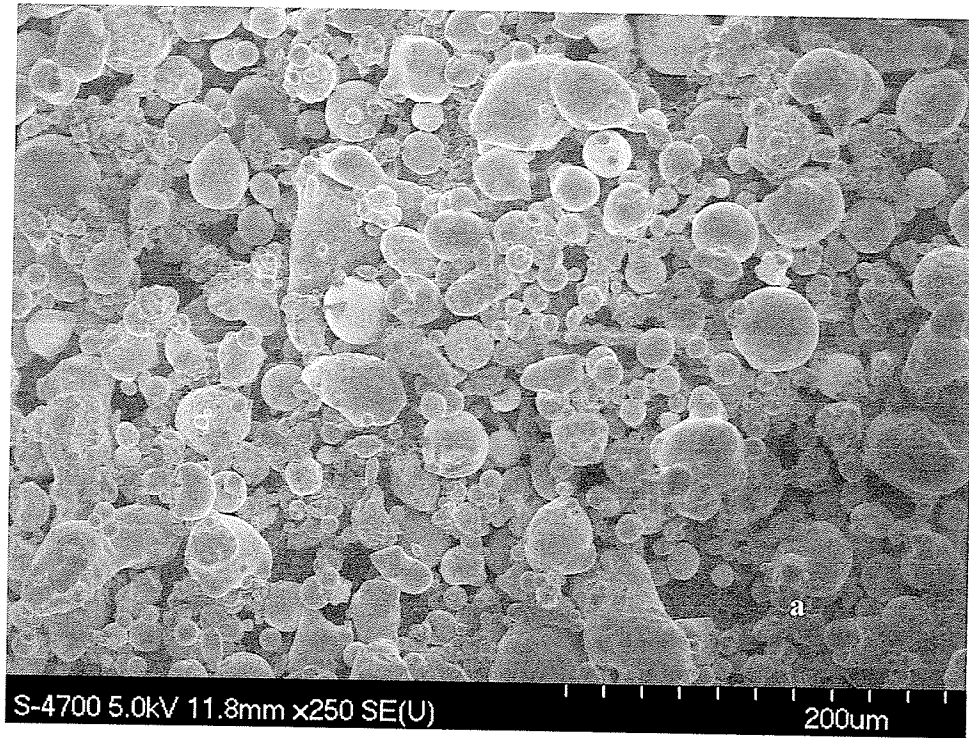


Figure 4.2a: SEM secondary electron image of the “as-received” powder at 250X

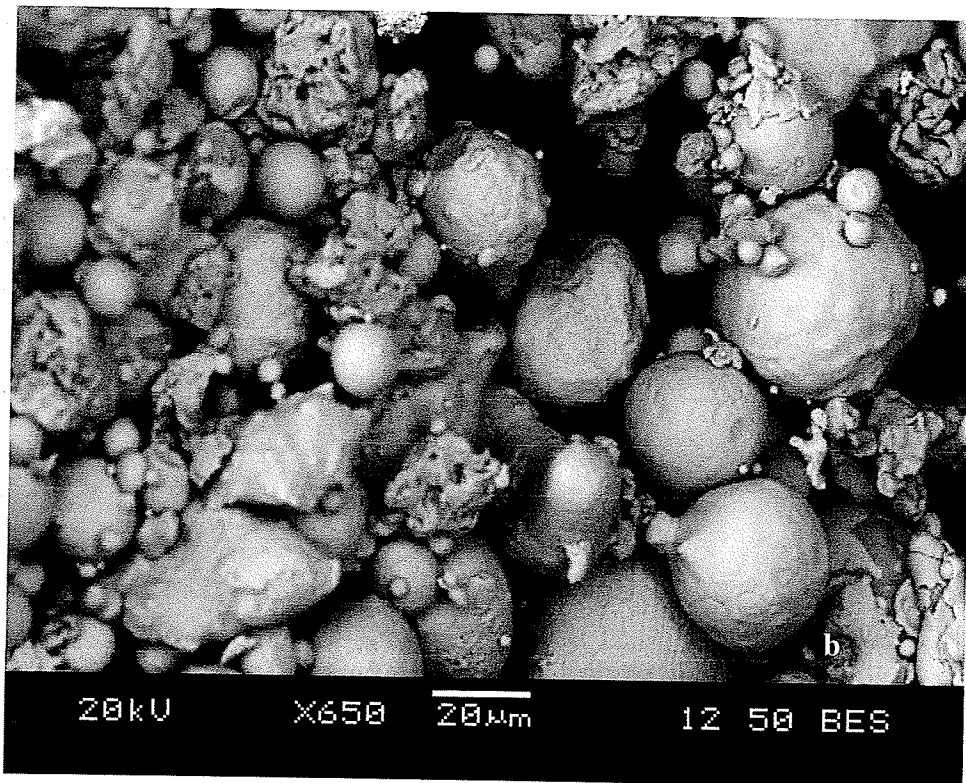


Figure 4.2b: SEM secondary electron image of the “as-received” powder at 650X

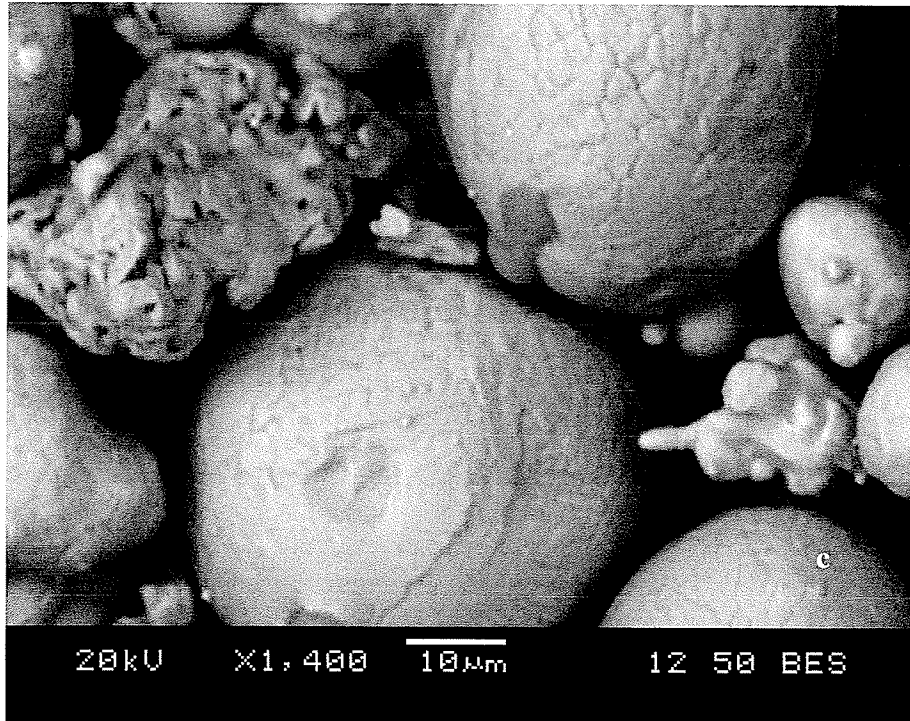


Figure 4.2c: SEM secondary electron image of the “as-received” powder at 1400X

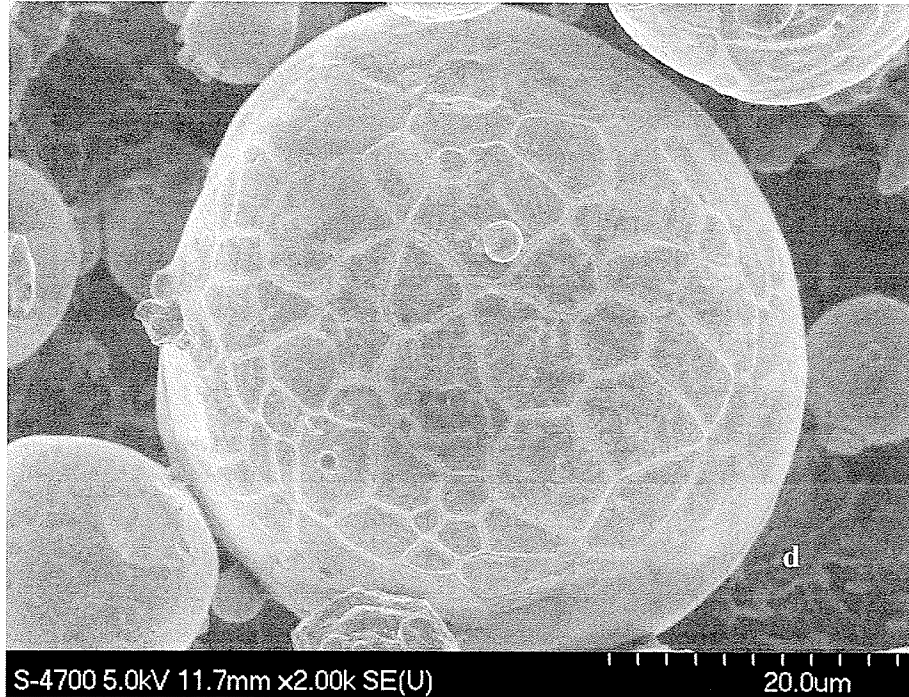


Figure 4.2d: SEM secondary electron image of the “as-received” powder at 2000X

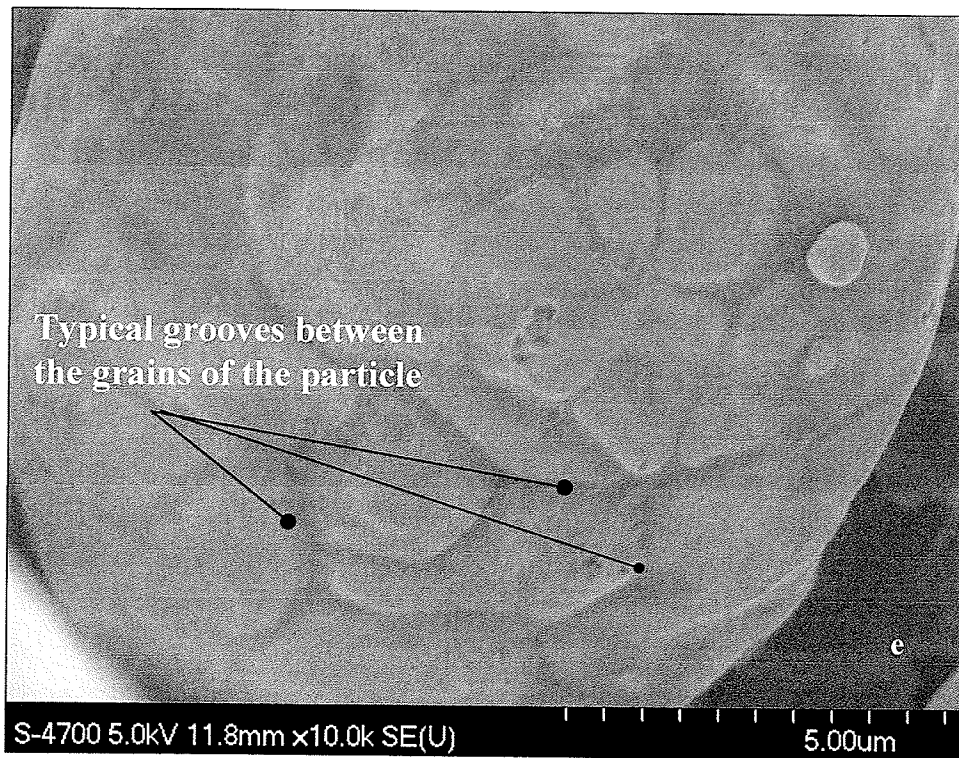


Figure 4.2e: SEM secondary electron image of the “as-received” powder at 10,000X showing groove at the grains intersection of the powder particle.

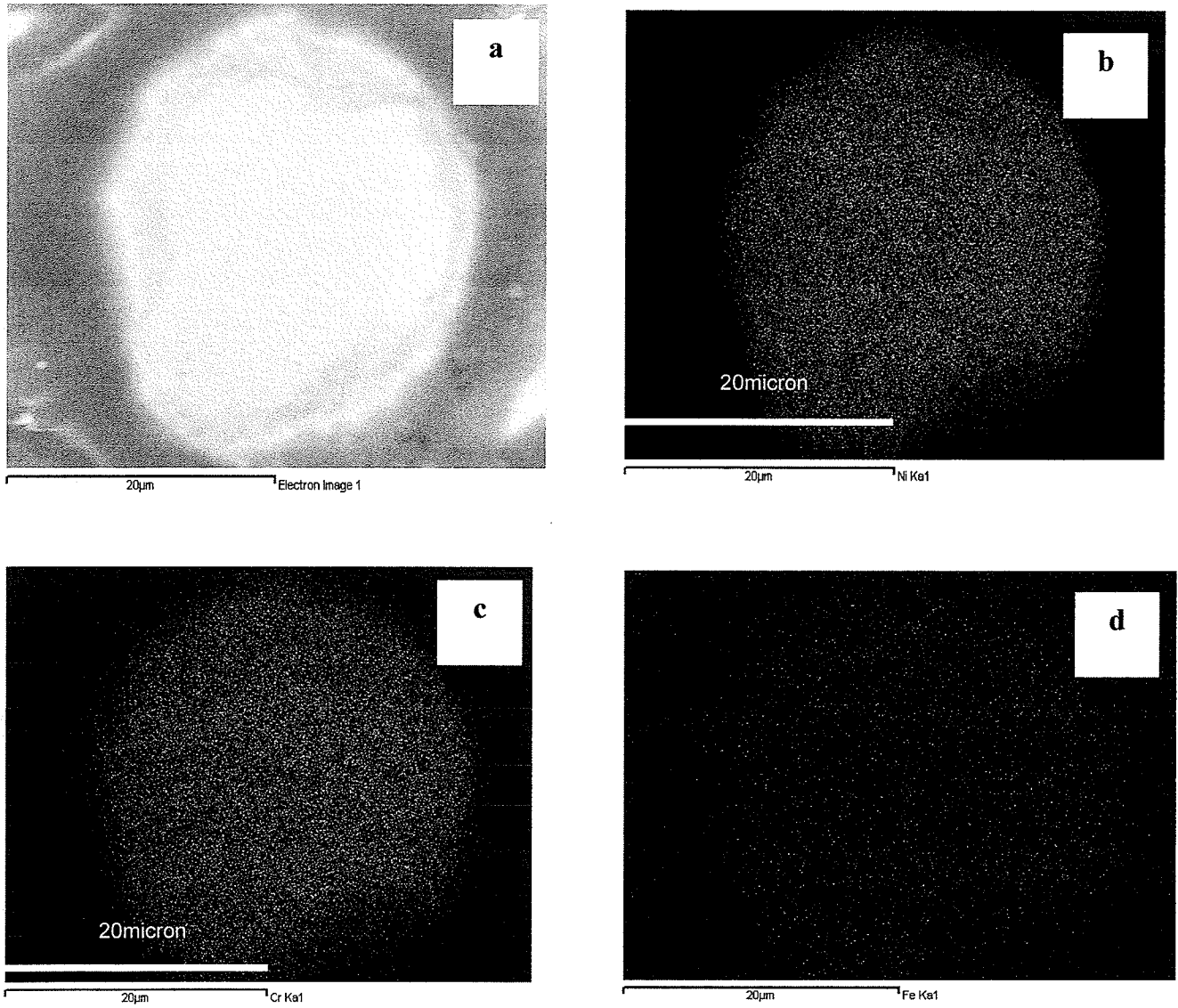


Figure 4.3: SEM mapping image of a typical powder particle to show if there is segregation in the particle. a) Electron Image, b) Ni map, c) Cr map, d) Iron map

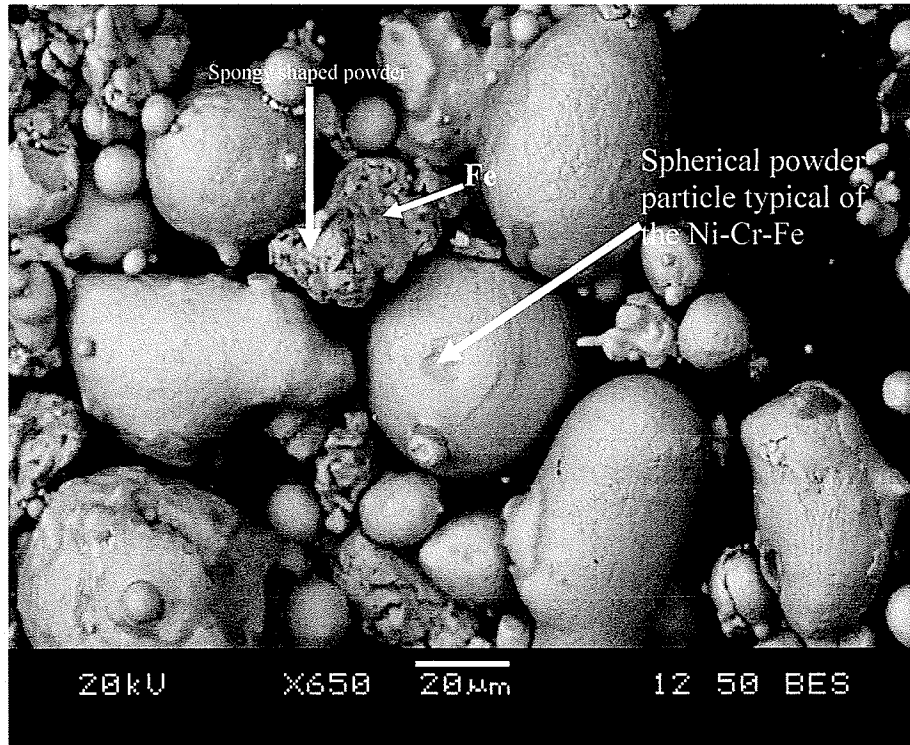
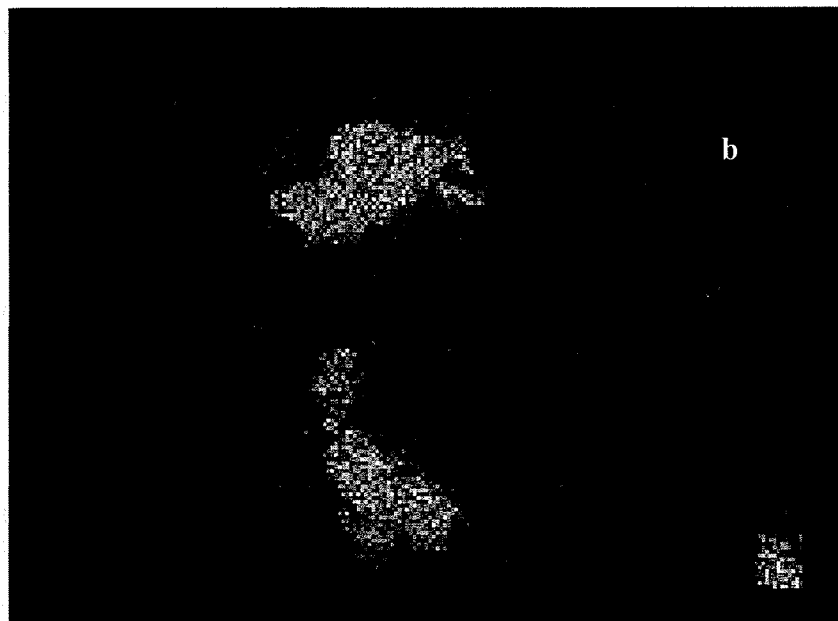
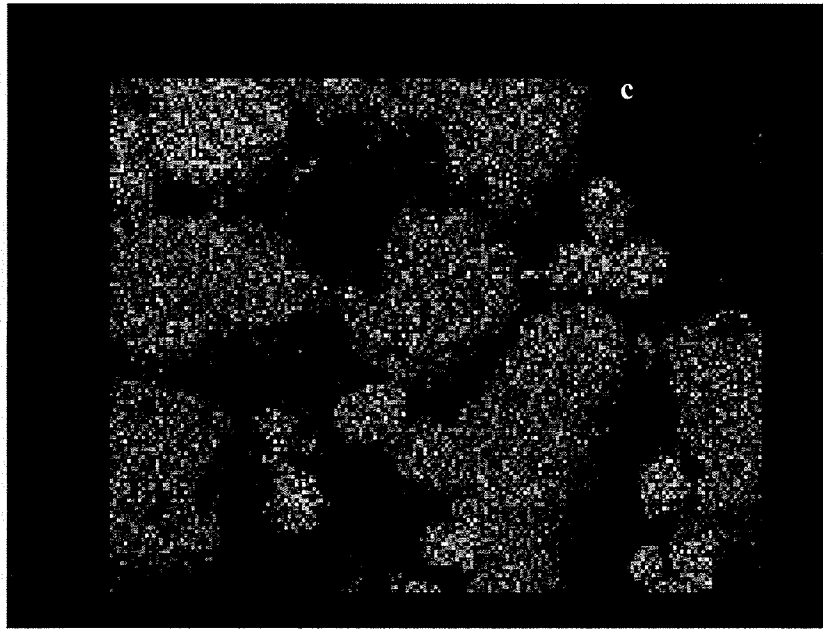


Figure 4.4 a): SEM-BSE image of the second batch “as-received” ternary



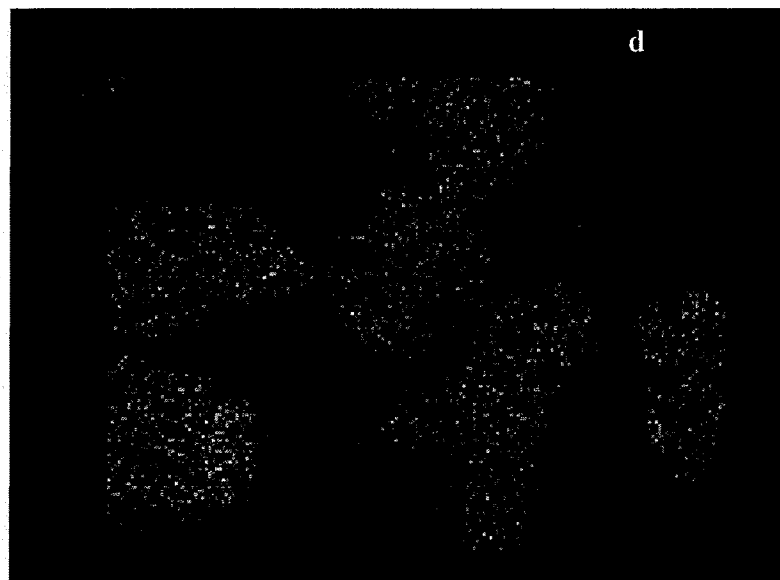
Iron Ka1

Figure 4.4 b): X-ray map for Fe



Nickel Ka1

Figure 4.4 c: X-ray map for Ni



Chromium Ka1

Figure 4.4 d: X-ray map for Cr

#### 4.1.2 Chemical analysis

Two types of analyses were carried out to confirm the alloy composition of the two batches of powders received. These were wet chemical and EDS analyses. The values obtained by the wet chemical analysis are shown in Table 4.1. For SEM/EDS analysis, nine points were randomly selected and analyzed (SEM/EDS) and the results compared with the manufacturer's specification. The summary is shown in Table 4.1 and the average composition obtained by the SEM/EDS analysis was found to be: Ni: 79: Cr: 12: and Fe: 9 wt. %. Table 4.1 shows that the content of some elements present varies from either ASTM or the manufacturer's specification. This could be related to the processing conditions under which the powders were produced (e.g., inert gas atomization). However, it is not unusual for such powders, and underlines the necessity for analyzing a P/M material prior to use.

The analysis, shown in Table 4.1, reveals different elemental compositions. For example, chromium was observed to be approximately 12w/o. Chromium is essential for corrosion prevention, and also tends to segregate in the melt during the atomization process. This is usually caused by the uneven migration of Cr in relation to other elements present. It is reported that in Inconel 600, chromium has lower activation energy because of the presence of iron [73], which increases its migration rate. This could result in a lower w/o in the quantity of chromium. Overall, EDS analysis showed an even distribution of chromium in the powder batch used for optimizing processing parameters for the ternary Ni-Cr-Fe alloy, this suggests an absence of Cr enrichment in the grains prior to processing.

Table 4.1: Chemical analysis of the as-received powder

Element	Cr w/o		Fe w/o		Ni w/o		Error ±	
EDS analysis 1	10.0		11.3		78.7		0.0	
EDS analysis 2	10.0		8.5		80.9		0.6	
EDS analysis 3	9.1		8.5		82.4		0.0	
EDS analysis 4	11.3		10.0		78.7		0.0	
EDS analysis 5	12.1		8.4		79.4		0.0	
EDS analysis 6	10.1		11.6		77.9		0.4	
EDS analysis 7	12.1		10.5		77.4		0.1	
EDS analysis 8	11.9		7.1		81.0		0.1	
EDS analysis 9	11.6		7.2		81.2		0.1	
Wet chemical analysis	12.4		7.2		77.5		2.9	
	Cr w/o	Fe w/o	Ni w/o	Al w/o	Mn w/o	C w/o	Cu w/o	Error
ASTM specification for IN600 (Cast or wrought)	14-17	6-10	72	1.0-1.7	1	0.2max	0.5	Unknown
Manufacturers specification	14-18	6-10	72	-	-	-	-	Unknown

#### 4.1.3 Powder particle size analysis and powder flowability

In this study, the Malvern laser particle analyzer was used for size analysis and the results obtained are shown in Figure 4.5 and Table 4.2. From the data shown in Figure 4.5 and Table 4.2, the median size was determined to be 25.8 $\mu$ m. 90% of the powder particles were less than 54 $\mu$ m in size, while the size of 10% of the powder was below 9.4 $\mu$ m. This is a reasonable particle size distribution to ensure that voids between larger grains are filled, thereby offering maximum possible green density prior to sintering.

The flowability of the powder, defined as the ability of the powder to fill a given shaped container without application of pressure, is given in Table 4.3. The significance of this parameter is to assess how easy the powder will fill a die during processing.

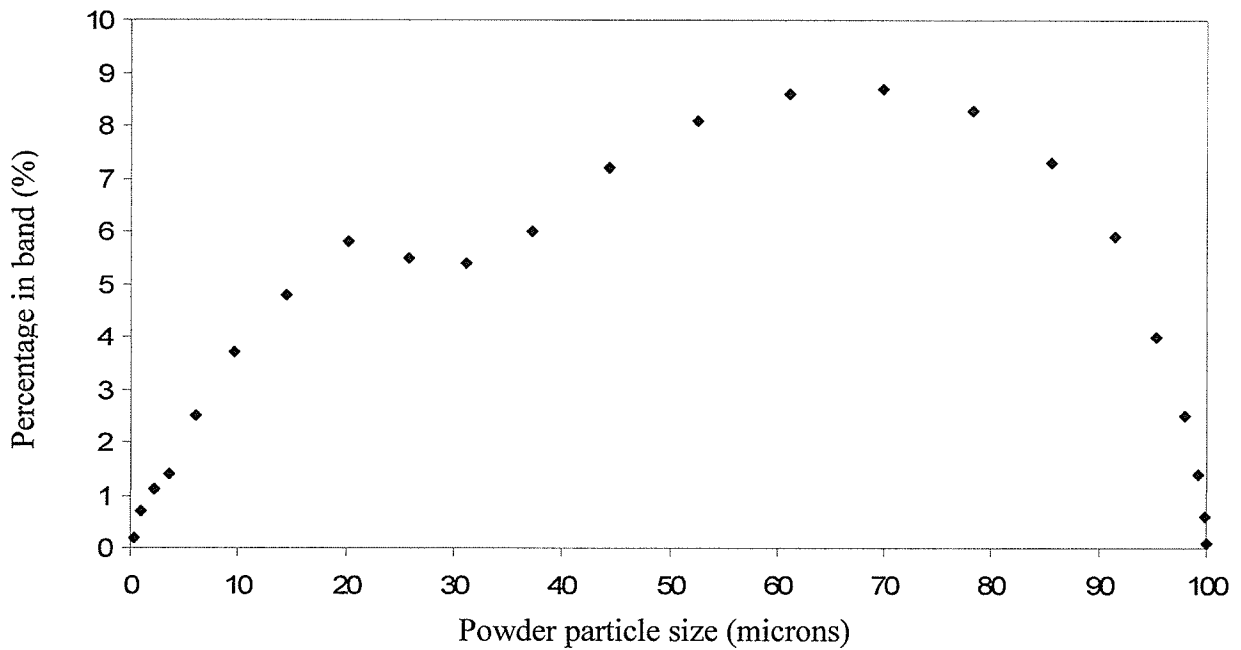


Figure 4.5: Powder particle size distribution of the “as-received” ternary Ni-Cr-Fe alloy

Table 4.2: Summary of the powder particle size analysis

Log. Diff.	6.37
D(v, 0.5)	25.8 $\mu$ m
D(v, 0.9)	54.4 $\mu$ m
D(v, 0.1)	9.7 $\mu$ m
D(4,3)	29.5 $\mu$ m
D(3,2)	19.3 $\mu$ m
Span	1.7seconds
Specimen surface area	0.11sq.m./cc.

Table 4.3: Table showing the “as-received” ternary Ni-Cr-Fe ternary powder flowability

Height of Cylinder	Diameter of Cylinder (cm)	Radius of cylinder	Volume of Cylinder (cm <sup>3</sup> )	Mass of powder that filled the cylinder (g)	Flow density (g/cm <sup>3</sup> )
2.54	3.13	1.57	19.54	85.68	4.38
2.54	3.13	1.57	19.54	86.52	4.43
2.54	3.13	1.57	19.54	85.70	4.38
2.54	3.13	1.57	19.54	85.11	4.35
2.54	3.13	1.57	19.54	85.45	4.37
Average flow density =4.38g/cm <sup>3</sup>					

$$S_w = \frac{2.56}{\log\left(\frac{D_{90}}{D_{10}}\right)} \dots\dots\dots 4.1$$

where,  $S_w$  is defined as width of the distribution curve which is also the slope of the linear part of the sigmoidal curve [74], and  $D_{90}$  and  $D_{10}$  are the average particle size below 90 and 10%, respectively. According to Iococca and German [74], if the value of  $S_w$  is high (i.e., greater than 1.00) this is an indication that the material has good flowability and will subsequently fill the die properly. The  $S_w$  calculated in the present work was found to be 3.41 while the “flow density” (i.e., filling of the die by the powder without tapping or pressure application) was found to be  $4.38\text{g/cm}^3$ . This value is 50% of the theoretical green density of the powder suggesting that the material should have a reasonably good compressibility [74].

#### 4.1.4 XRD analysis of the “as-received” ternary Ni-Cr-Fe powder

Results of X-ray diffraction and indexed peaks of the as-received powder are shown in Figure 4.6. The XRD spectrum of as-received powder was compared to the JCPDS standard and was found to compare well with the standard Ni and Ni/Cr/Fe (JCPDS) alloys because they both have similar FCC crystal structures. Also, XRD pattern analysis of some powder batches (e.g., batch 2) indicated presence of traces of pure Fe. The XRD analysis suggests that the phase present has an FCC structure as the planes of diffraction were either all odd  $\{(111), (311)\}$  or all even  $\{(200), (220), \text{ and } (222)\}$  while the first diffracting plane was the (111) [75]. EDS analysis indicated that the elements present were Ni, Cr, Fe. By comparing the EDS and XRD analyses relating them to the

equilibrium phase diagram, the main phase present in the particle is concluded to be NiCrFe  $\gamma$ -fcc.

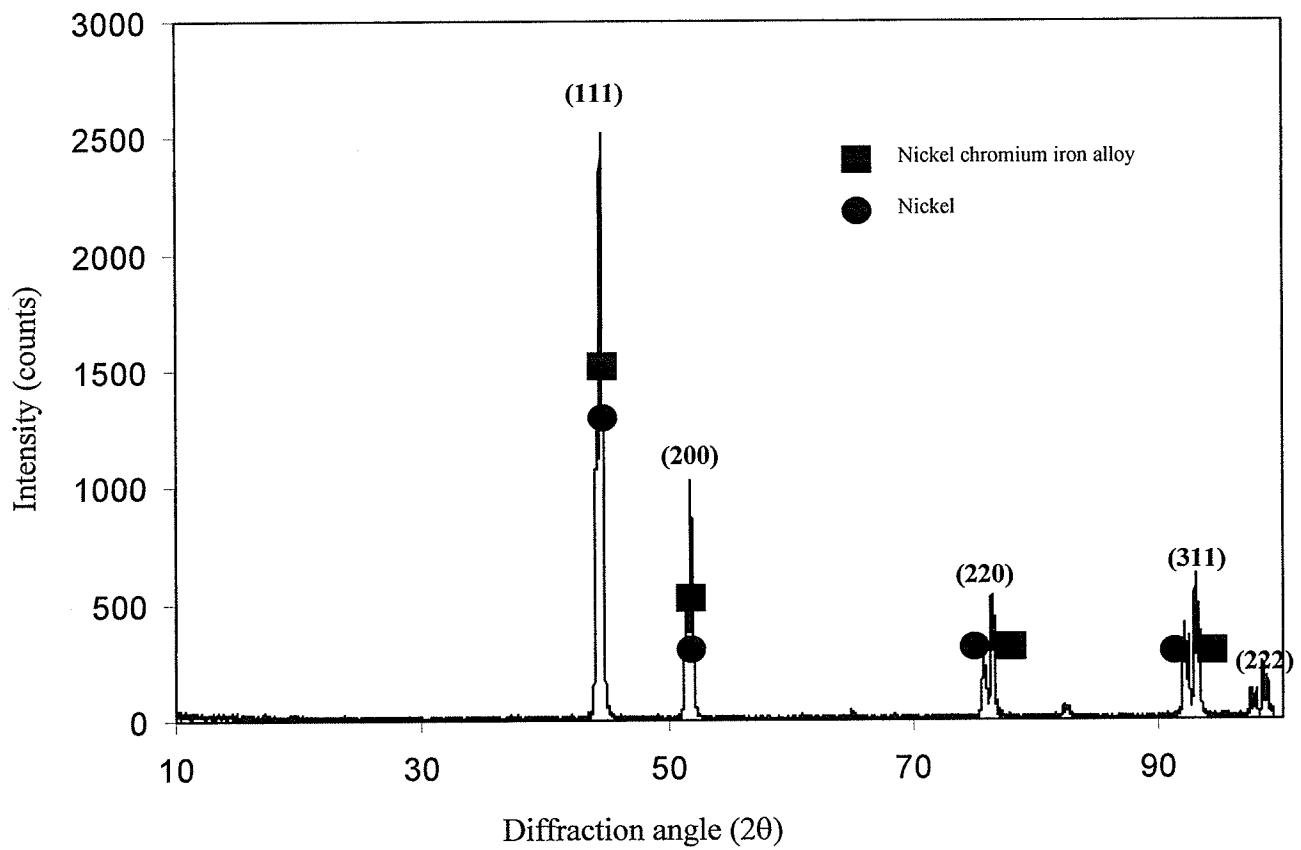
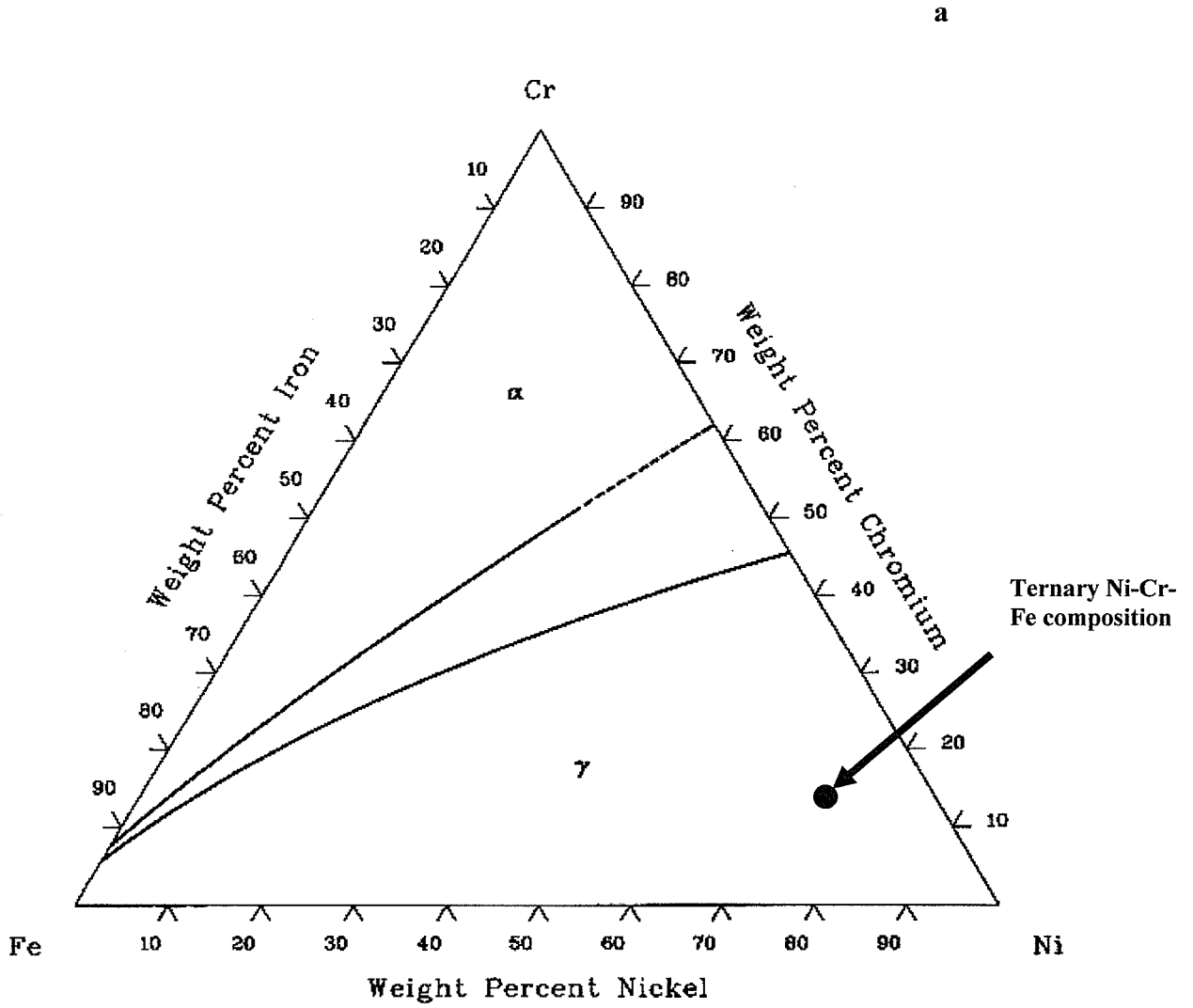


Figure 4.6: XRD spectrum of the “as-received” ternary Ni-Cr-Fe powder

Finally, from the Ni-Cr-Fe equilibrium phase diagram [76], the  $\gamma$  phase is expected to be present from room temperature to 1420°C as a solid phase and as liquid up to about 1450°C (Figure 4.7).



**Note:  $\alpha = (\alpha_{Fe,Cr}); \gamma = (\gamma_{Fe,Ni})$**

Figure 4.7a: Ni-Cr-Fe ternary phase diagram showing alloy composition at 1300°C [77]

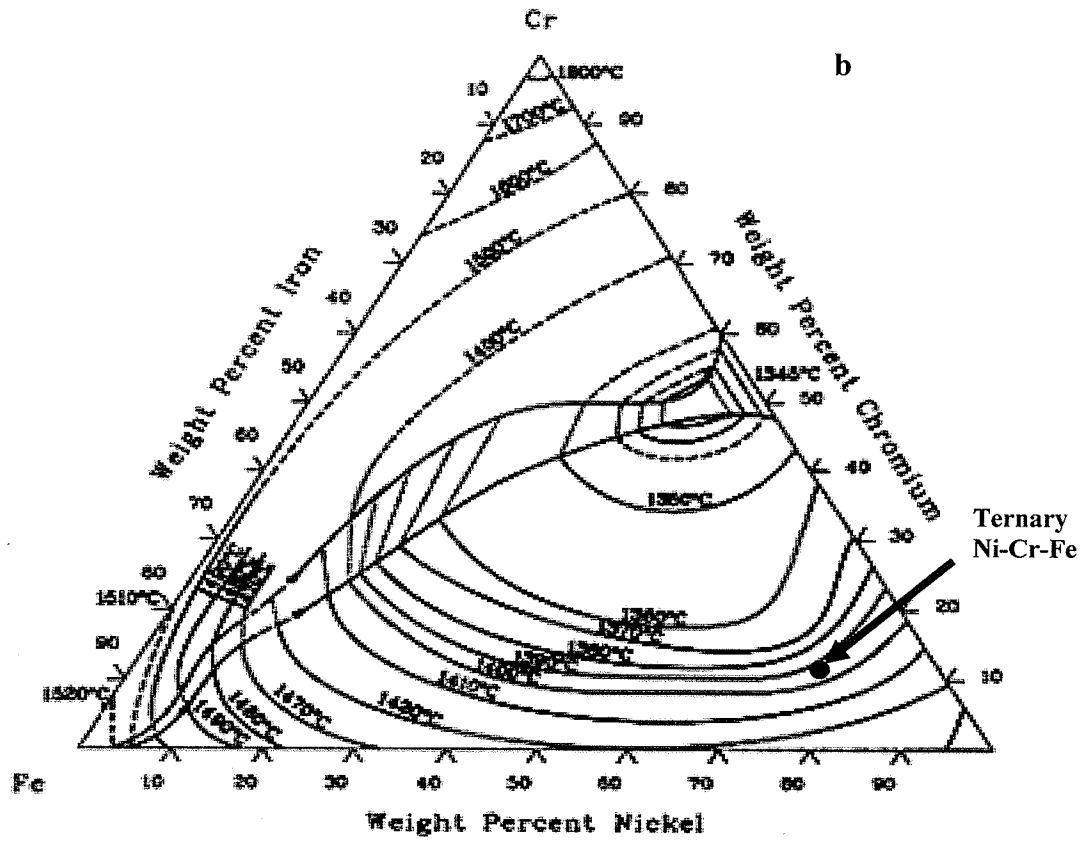


Figure 4.7b: Ni-Cr-Fe ternary phase diagram showing alloy composition at solidus projection [77]

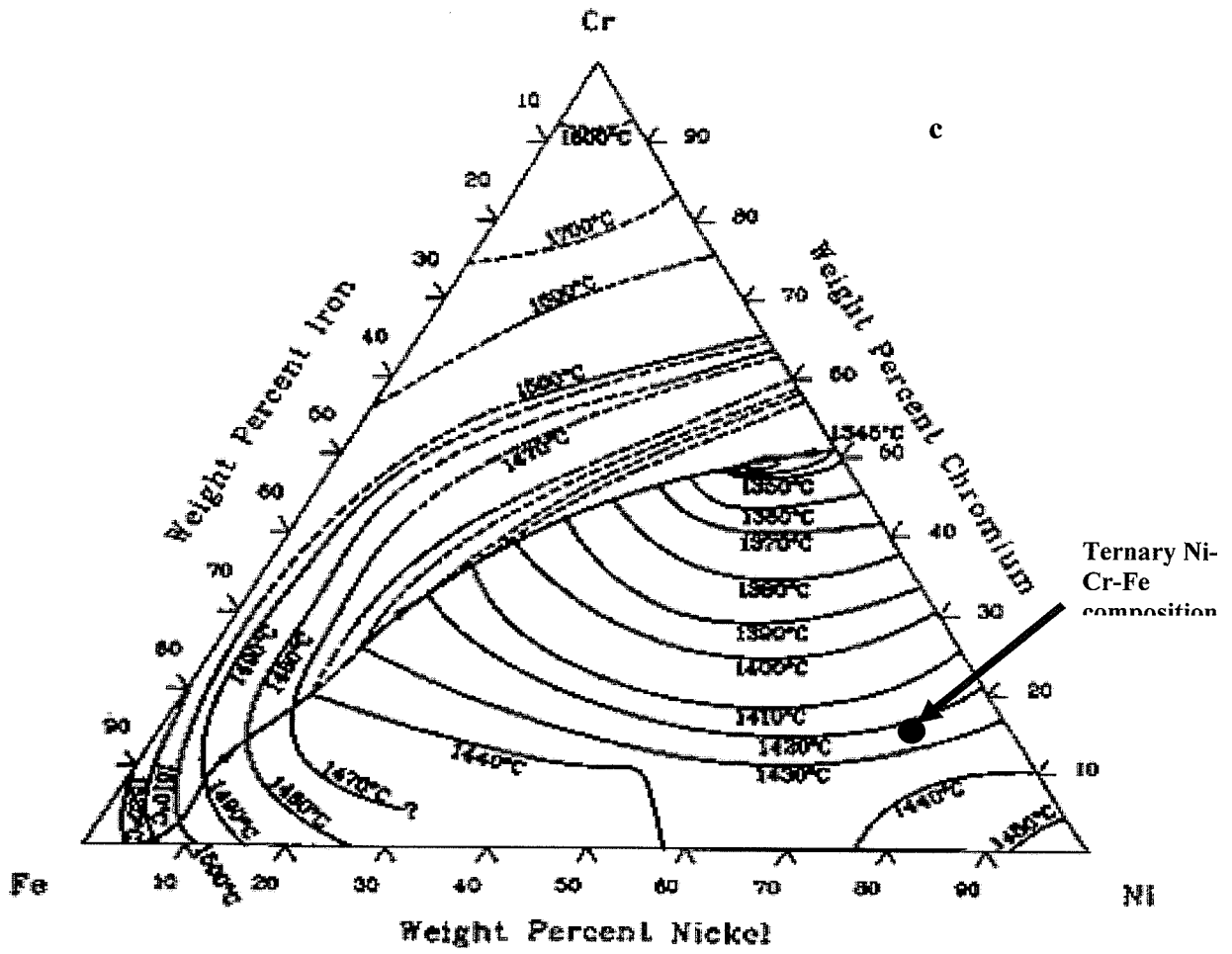


Figure 4.7c: Ni-Cr-Fe ternary phase diagram showing alloy composition at liquidus projection [77]

## 4.2 Effect of polyvinyl alcohol (PVA) on density distribution of the ternary Ni-Cr-Fe alloy

Binders usually have a positive effect on the green density of powder metallurgical products; for example, PVA has been used successfully to produce Udimet 700 by powder metallurgy processes [78]. However, in the present work, addition of PVA resulted in an overall decrease in the green density, as can be seen in Figure 4.8, even after the increase in compacting pressure from 400 to 500 MPa. Hence, PVA was not used as an additive in this work.

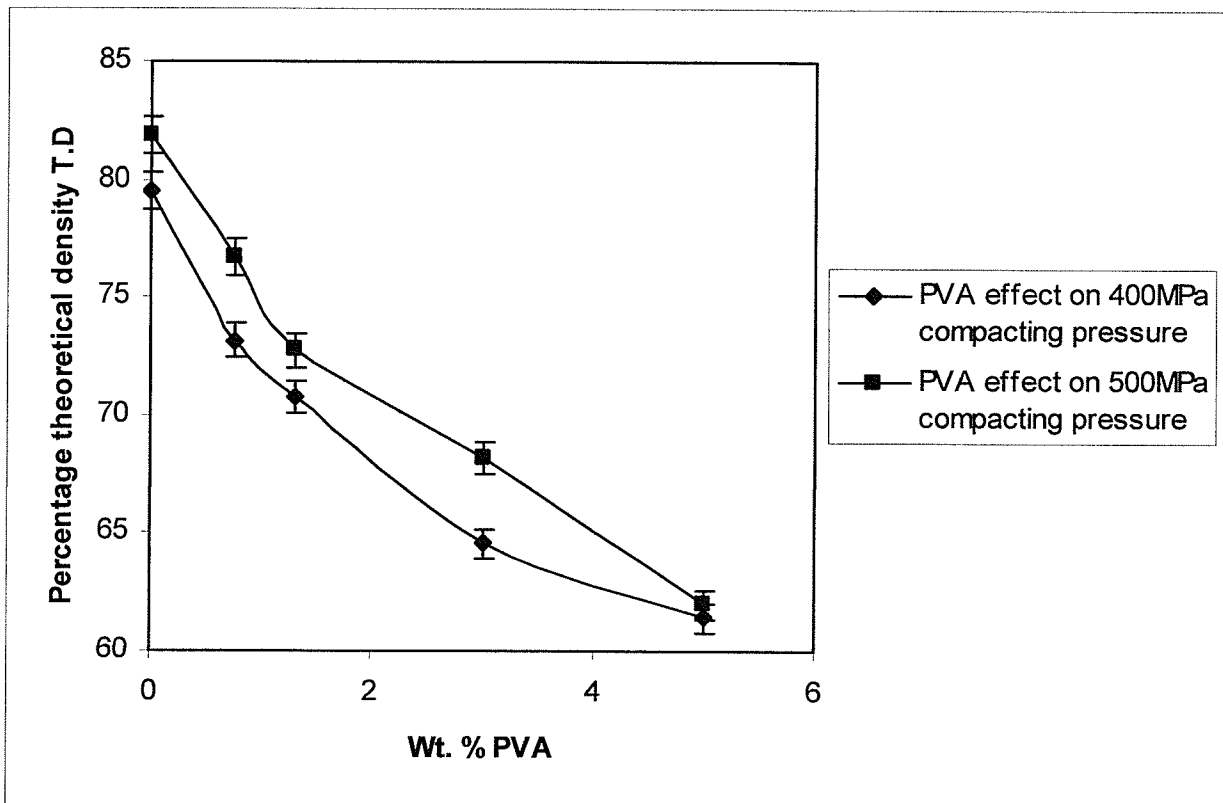


Figure 4.8: Effect of PVA on the green density of the compact

### 4.3 Effect of lubricant (wax) on density distribution of the ternary Ni-Cr-Fe alloy

The effect of lubricant (wax) on the green compact is shown in Figure 4.9. Here, it can be seen that with increase in compacting pressure the effect of lubricant on green density is diminished.

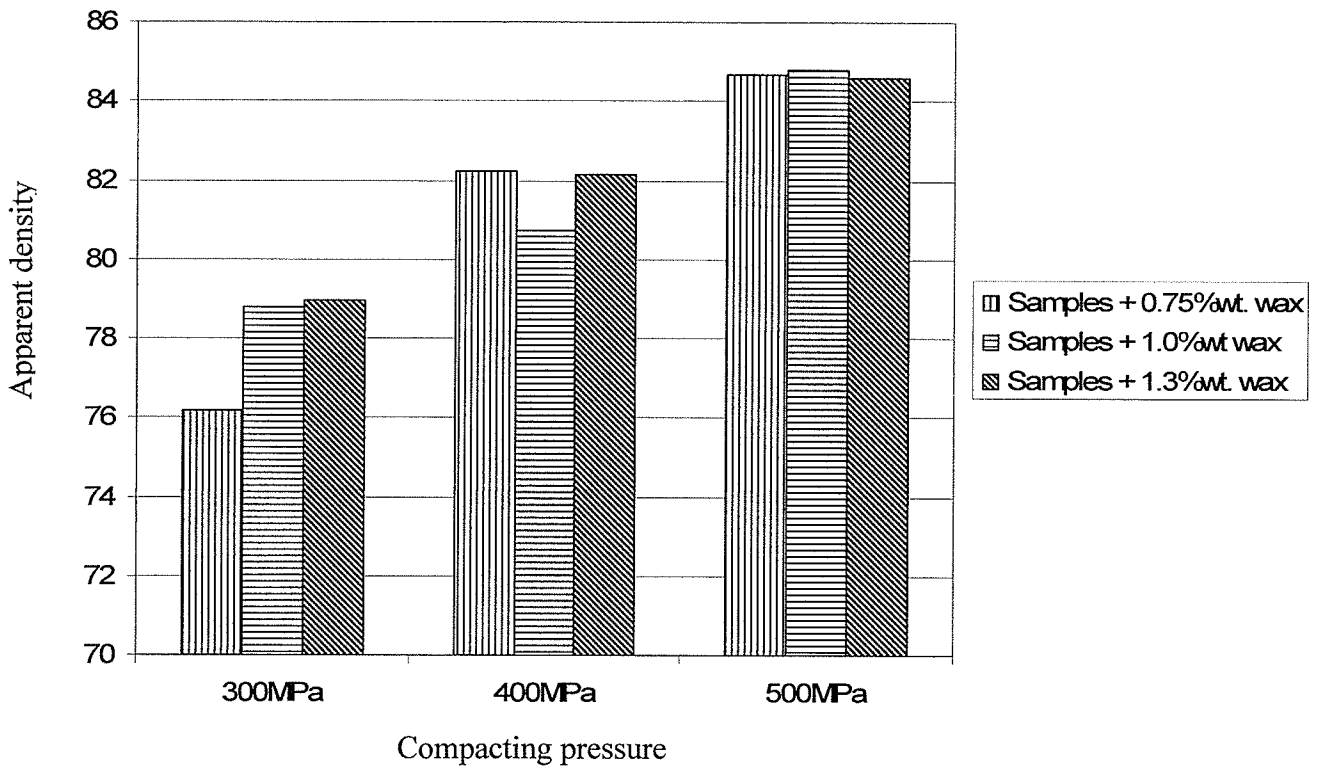


Figure 4.9 Effect of lubricant and compacting pressures on the green density of the compact

A lubricant can be added to powder particles, either by application to the wall of the compacting instrument or by being mixed with the powder prior to compaction [1, 2, 79]. Various authors have studied the effect of pressure and lubricant on green density. For example, according to Armstrong [80], and Bochini [81], at low pressures lubricant promotes compact homogenization by promoting interparticle contact through friction reduction. However, at higher compacting pressures, lubricant may limit the density that is obtainable by occupying space between particles.

In the present study the effect of lubricant (microwax) was examined and is presented in Figure 4.9. At relatively low compacting pressure (300 MPa) an increase in density with increase in the quantity of lubricant was noted as was that observed by Armstrong [80], Bochini [81] and Jiang [79]. However, it is seen that as the compacting pressure increased to 500 MPa the effect of increasing the amount of lubricant used seems to be diminished. This is in agreement with the concept that at high compacting pressures lubricant fills the voids between powder particles and therefore does not necessarily enhance contact.

#### **4.4 Ternary Ni-Cr-Fe alloy powder compaction**

During the course of this work, an experiment was carried out to investigate cold isostatic pressing as a process to compact the ternary powder. The result of the cold isostatic pressing is shown in Figure 4.10. Here, it can be seen, while some bonds formed in some regions, other parts of the powder were not properly compacted, resulting in a poor product. A noticeable difference between cold isostatic pressing and uniaxial compaction was that the shape of the pressed powders obtained after compacting at

100MPa were similar. However, since the equipment available for cold isostatic pressing could not be used beyond 150MPa, the results could not be compared to uniaxial pressing that had the capability of reaching 600MPa. Hence, uniaxial pressing was used during the course of this work.



Figure 4.10: Picture showing cold isostatically pressed powder

#### **4.4.1 Uni-axial pressing of the ternary Ni-Cr-Fe alloy**

In this study, powder compressibility was investigated between 100 MPa and 550 MPa. The results are given in Figure 4.11, which were labeled after [2]. It is seen that at compacting pressures increased above 400 MPa, the compacts had an apparent green density in excess of 80% of the theoretical density (TD). In addition to this, it was observed that the deformation was not significant. Apparent green density values of ~ 84% (Figure 4.11), suggests that a good contact between the powder particles was obtained, which is a function of both the starting particle size distribution, shown in Figure 4.5, and the compacting pressure used. An optimized compacting pressure of 500 MPa was therefore selected for all future work.

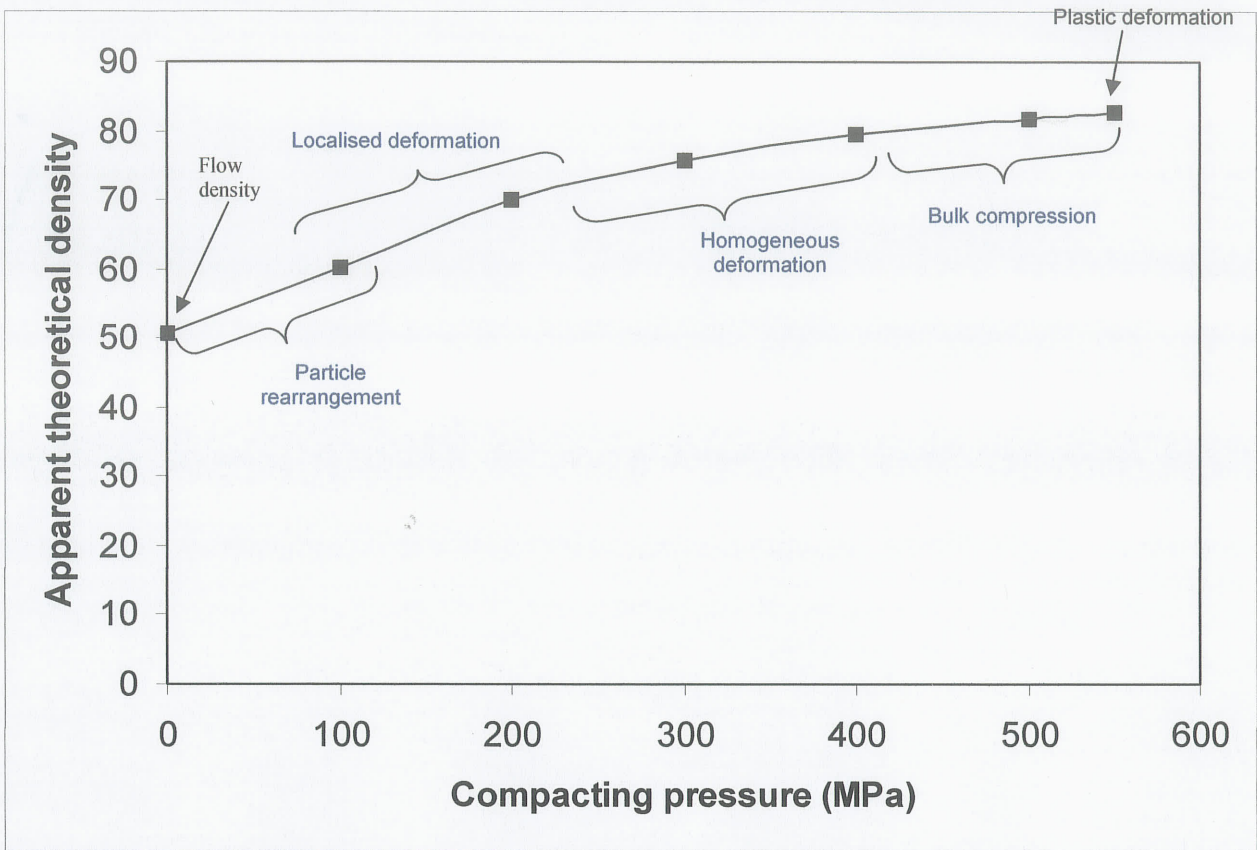


Figure 4.11: The effect of compacting pressure (at 0.75% lubricant wax) on the theoretical density (present work) with superimposition of various stages of deformation during powder compaction adapted after [2]

#### 4.5 Sintering of ternary Ni-Cr-Fe alloy

Material transport driven by surface energy or capillary force is known as sintering [82]. The bonding of particles occurs when particles are heated to relatively high temperatures but below the melting point or solidus temperatures. During sintering surfaces are reduced by channel closing, by smoothening of the pore/solid interface, or combination of both. Consequently, sintering generally involves loss of surface area and increase in strength of the powder compact [47].

Huppman [45] classified sintering process into three main parts namely, activated, liquidus and solidus (subsolidus). The focus of this study was mainly to sinter in the solid state by operating below the melting temperature of the alloy but close to the mushy zone (between the solidus and liquidus), and holding for a relatively short time to prevent possible liquation and subsequent grain growth. The sintered samples were then observed under SEM.

Furthermore, in this study, the sintering of a powder compact was first carried out in air at temperatures of  $1270 \pm 10^0\text{C}$ , and subsequently, in vacuum. This corresponds to temperatures below the melting point of the alloy, but high enough ( $>90\% T_m$  where  $T_m$  is the melting temperature of the alloy) for bonding of the powder particles to occur. Also, the sintering times were varied from 0.5h to 5h in both air and vacuum. This was done to observe changes in microstructure with time. A typical air sintering curve for 2h is shown in Figure 4.12. The dimensions for the green compact were 31.8mm X 12.7mm X 6.71mm.

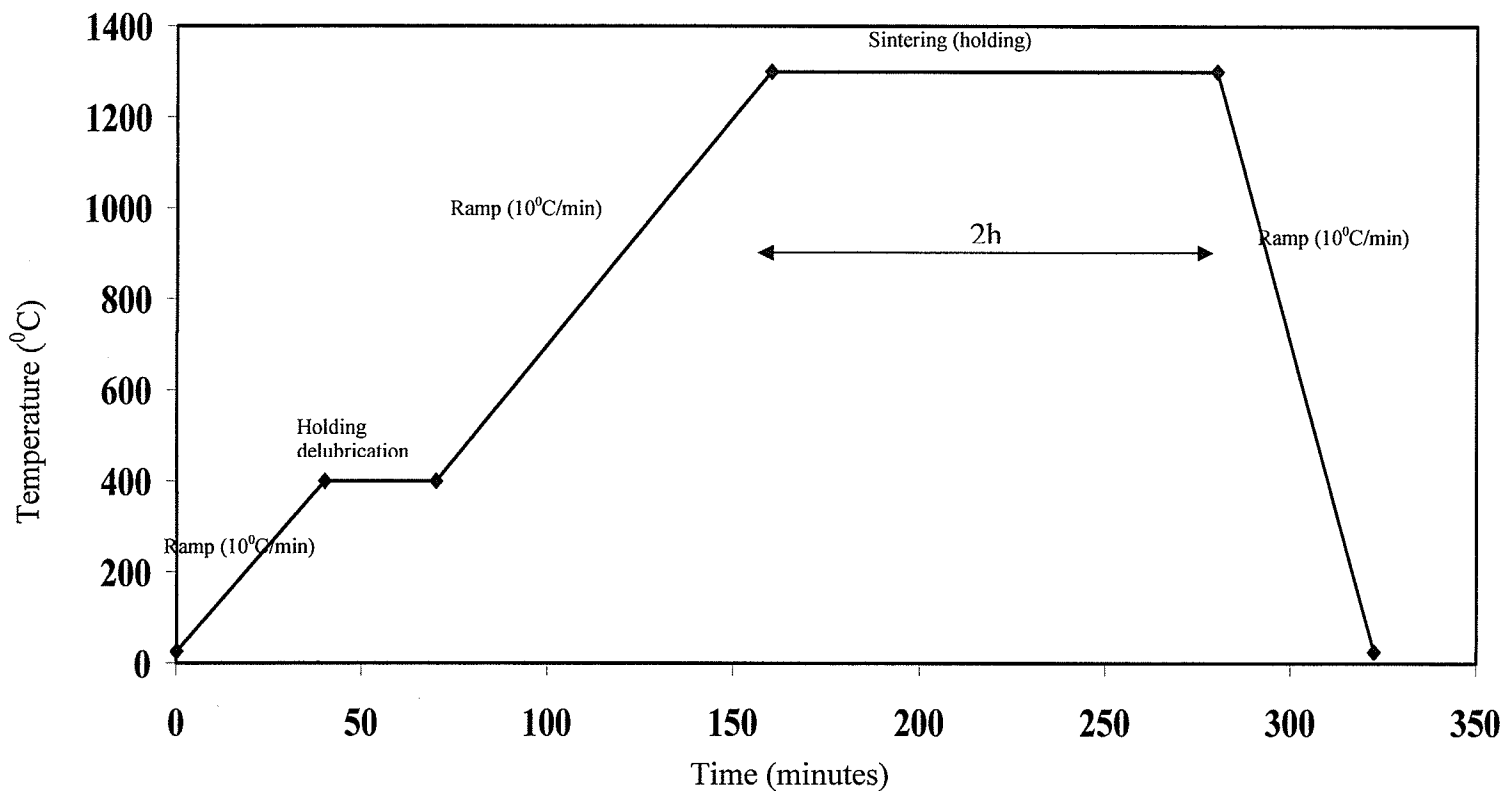


Figure 4.12: A typical air sintering curve for 2h equilibration at sintering temperature for the ternary Ni-Cr-Fe alloy

Figures 4.13 and 4.14 show the microstructural changes as a function of time at 1270°C for the minimum (0.5 h) and maximum (5h) times investigated for the air sintered samples.

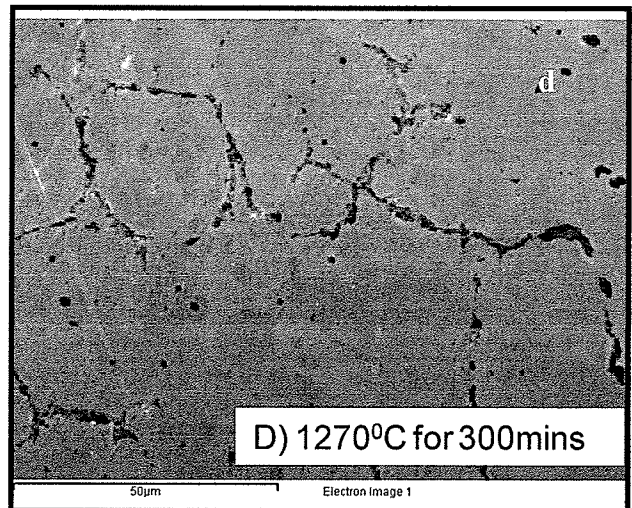
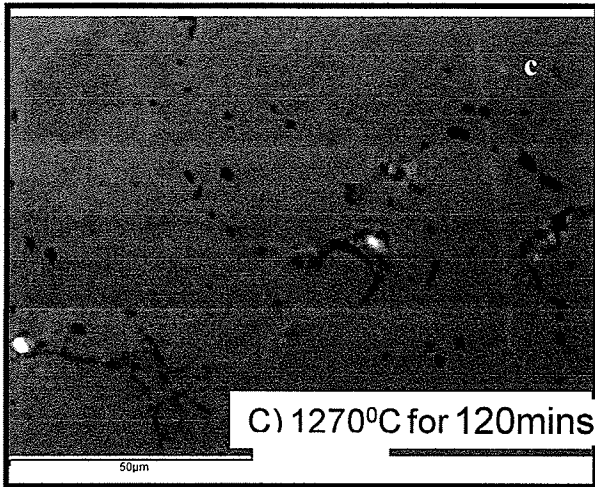
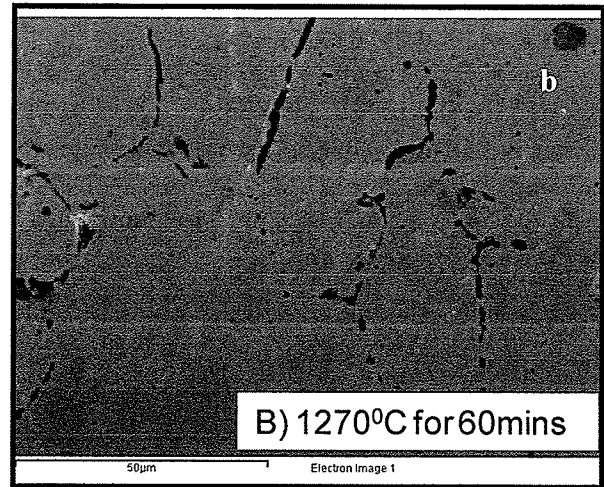
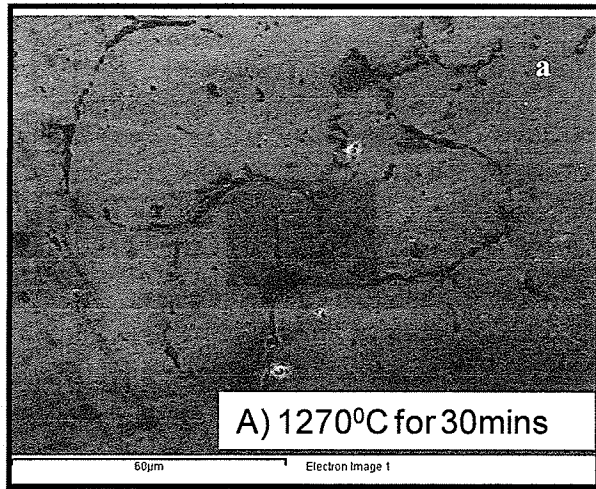
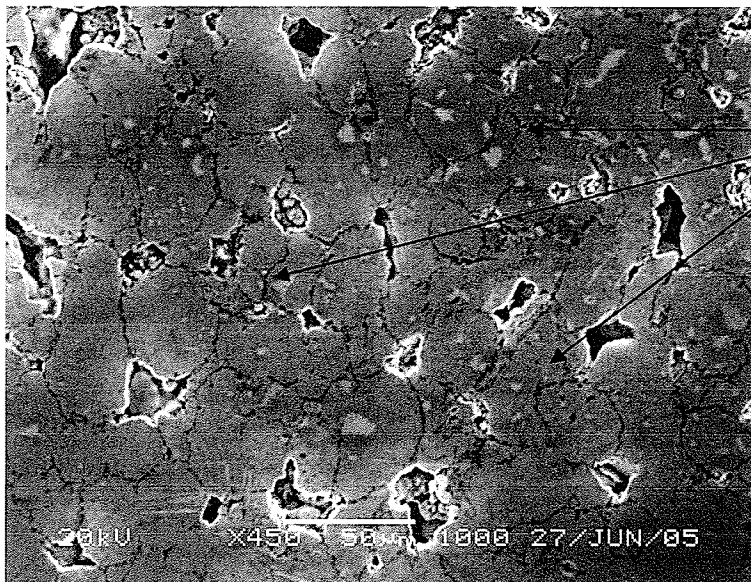
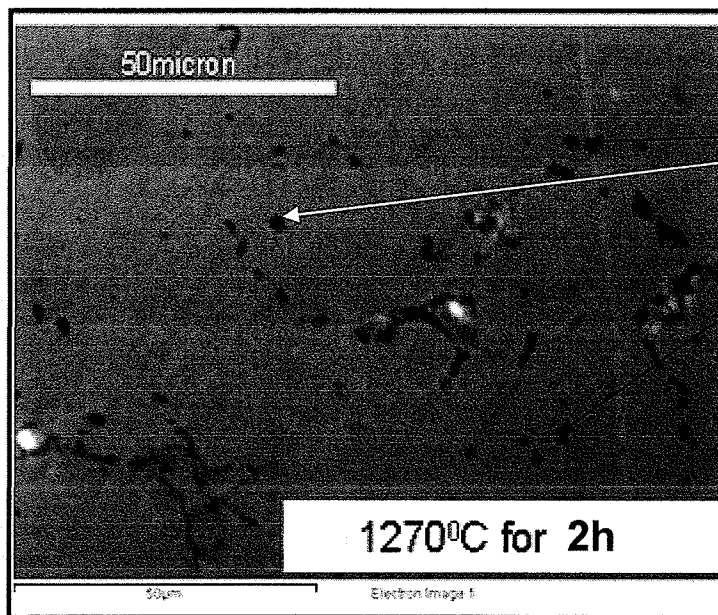


Figure 4.13: Secondary electron image showing microstructural changes after: a)0.5h, b) 1h, c)2h and d)5h of sintering at 1270°C for the ternary Ni-Cr-Fe



Good particle contacts made after 0.5h of sintering, suggesting that prior particle boundaries were well bonded after 0.5h

Figure 4.14a: Secondary electron image showing changes in the sintered sample after 0.5h of sintering, 1270°C for the ternary Ni-Cr-Fe



Pores become more isolated after 2h showing the possibility of reaching the final stage of sintering

Figure 4.14b: Secondary electron image showing microstructural changes after 2h of sintering, 1270°C for the ternary Ni-Cr-Fe

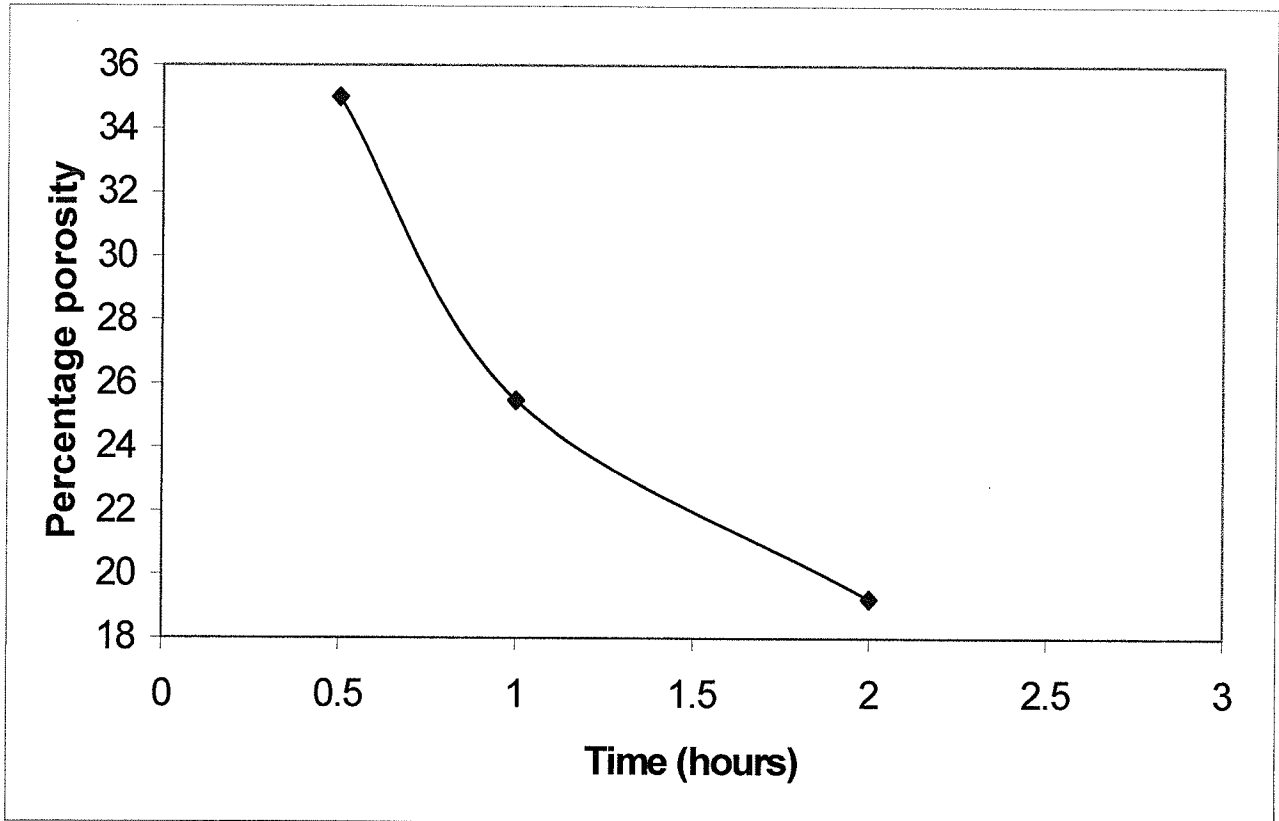


Figure 4.15: Average porosity concentration as a function of time, air sinter, 1270°C for the ternary Ni-Cr-Fe

As seen in Figure 4.13a and 4.14a after 0.5h of sintering inter-particle particle contacts were increased. In addition, a reasonable bonding of prior particle boundaries is evident. In most sintering processes, the intermediate sintering stage is characterized by initial interparticle pores becoming smaller and/or reduced in number. It may be noticed from Figure 4.15 that reduction in porosity occurred between 0.5h and 1h, while after 2h sintering, the SEM image (Figures 4.13 b and 4.14b) showed interparticle pores that metamorphosed from a long cylindrical shape to being round and more isolated. This was

also accompanied by coarsening of the grains and subsequent reduction in the number of pores. Hence, it may be postulated that the sintering process has reached its final stage after 2h.

The extent of sintering can be estimated by a variety of methods including shrinkage, neck to particle size ratio and density. Indications from this study were that no shrinkage had occurred in the air sintered ternary Ni-Cr-Fe alloy, as compact dimensions were similar before and after sintering. Interestingly, as sintering time increased to 5h, there was a reappearance of a “boundary-like” feature as seen in Figure 4.13d and Figure 4.16. Also, the distribution of the grain size after air sintering was found to be comparable to the prior grain size distribution.

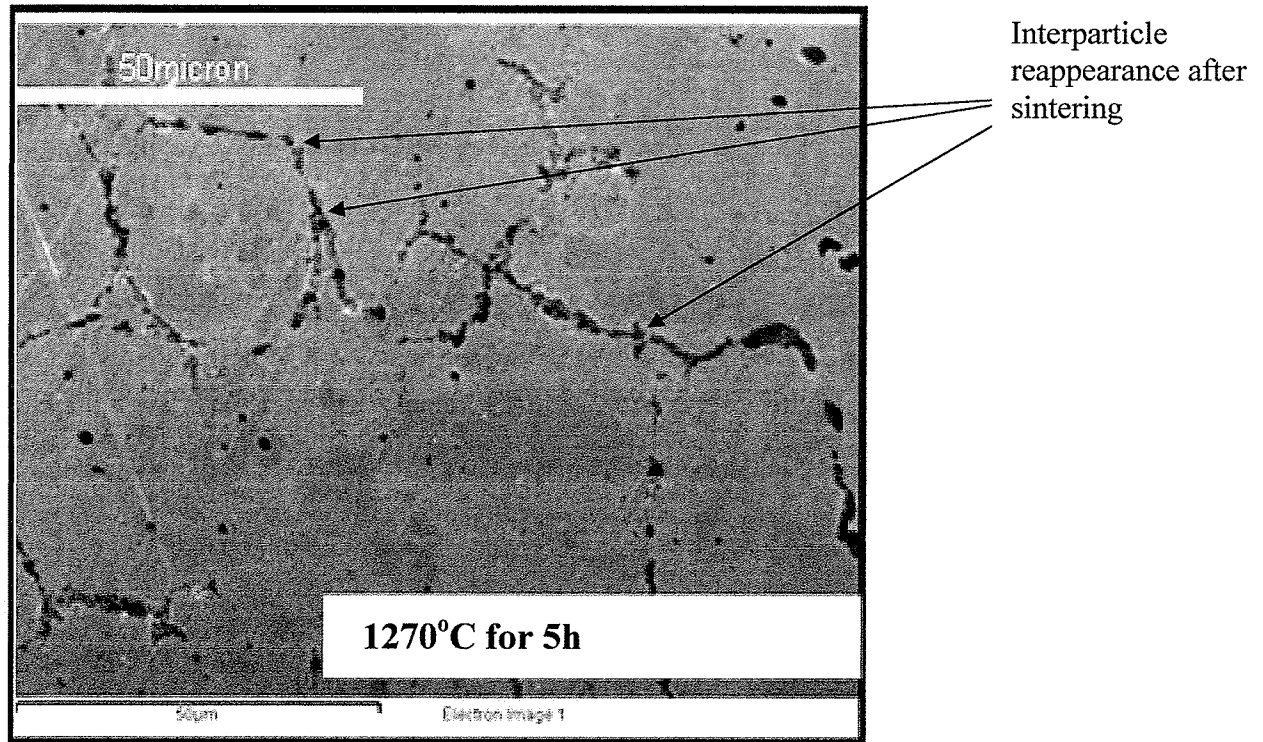


Figure 4.16: Secondary electron image of microstructural evolution after 5h of sintering for the ternary Ni-Cr-Fe alloy

#### 4.6 EDS-X-ray mapping of the air-sintered ternary Ni-Cr-Fe samples

In order to examine the different reactions occurring during air sintering, EDS analysis was carried out to provide a qualitative assessment of the constituent elements in the sintered alloy. In this way depletion or enrichment of any of the alloying elements that might have occurred during the air sintering process can be evaluated. Whereas specimens that were sintered for 0.5, 1, 2 and 5h were examined, only the 5h micrographs are presented (0.5 and 5h for oxygen).

#### 4.6.1 Chromium X-ray map of the ternary Ni-Cr-Fe alloy

Figure 4.17 shows an X-ray map of Cr after sintering at 1270°C for 5h. it was observed that after 0.5h Cr was homogeneously distributed. However, as sintering time was increased to 5h at 1270°C, there was an enrichment of chromium at the interparticle boundaries, similar to what was observed in IN600[83].

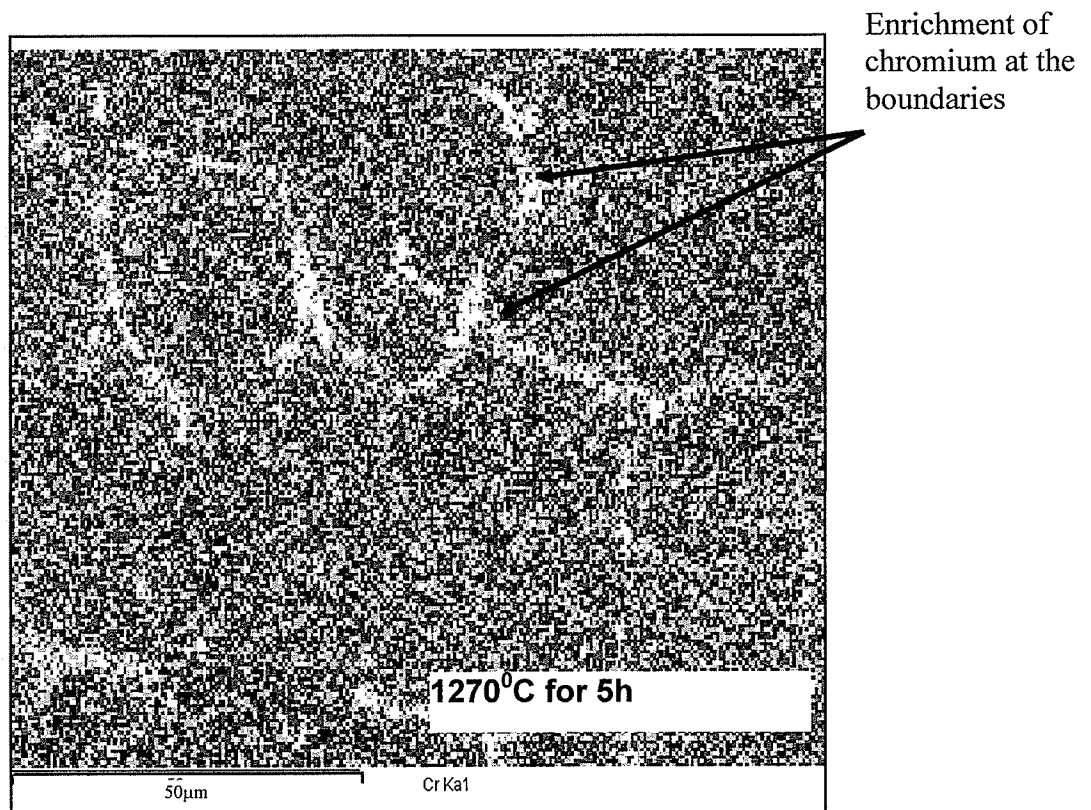


Figure 4.17: X-ray mapping of chromium after 5h of sintering at 1270°C for the ternary Ni-Cr-Fe alloy

#### 4.6.2 Nickel elemental X-ray map for the ternary Ni-Cr-Fe alloy

Specimens were sintered (in air) for times 0.5, 1, 2 and 5h, however only the 5h micrograph is presented. Figure 4.18 shows X-ray elemental maps of a sample sintered at 1270°C for 5h. EDS data were collected for a varying period up to 1h. Whereas a homogenous distribution of Ni was observed after 0.5h sintering, it is seen in the Figure that after 5h sintering, depletion of nickel was noted at interparticle boundaries.

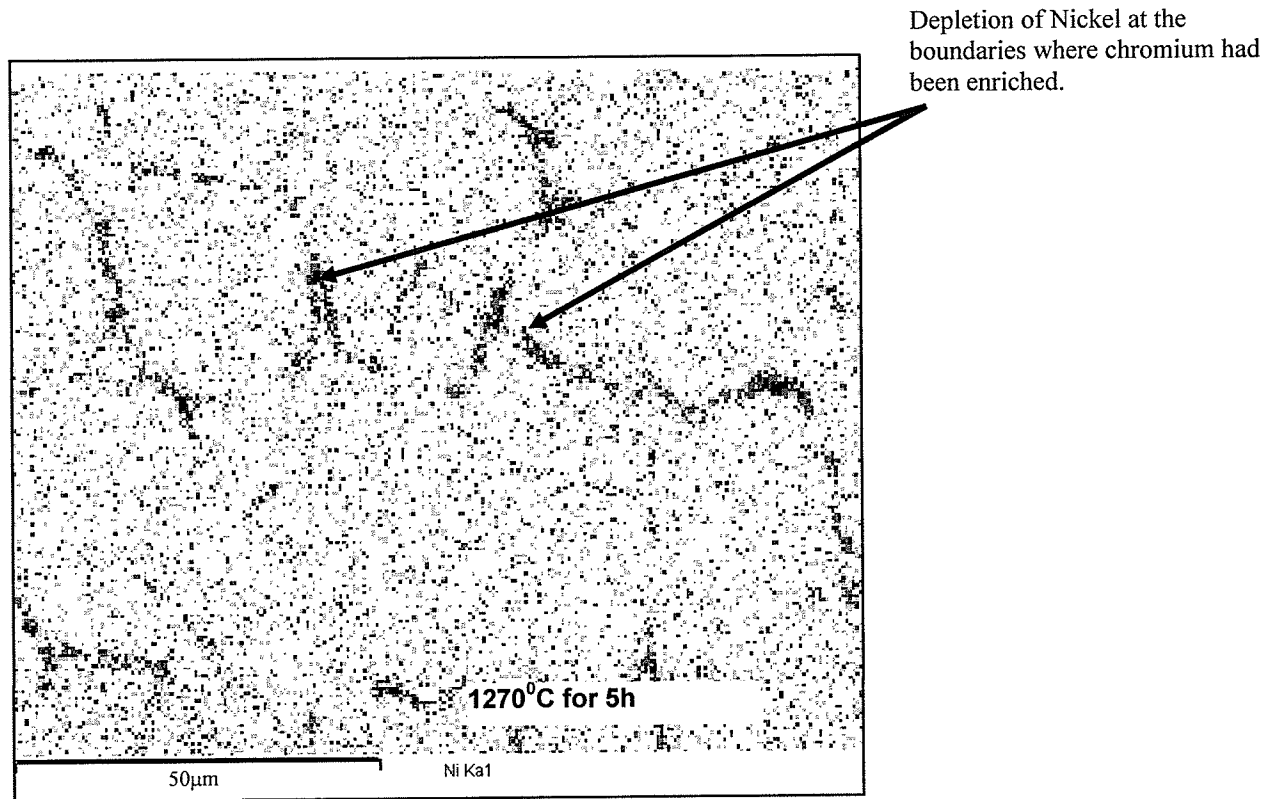


Fig 4.18: X-ray map of nickel after 5h of sintering at 1270°C for the ternary Ni-Cr-Fe alloy

### 4.6.3 Iron elemental X-ray map for the ternary Ni-Cr-Fe alloy

The iron elemental map is shown in Figure 4.19. From the figure it can be seen that iron depletion was also pronounced after 5h of sintering at 1270°C.

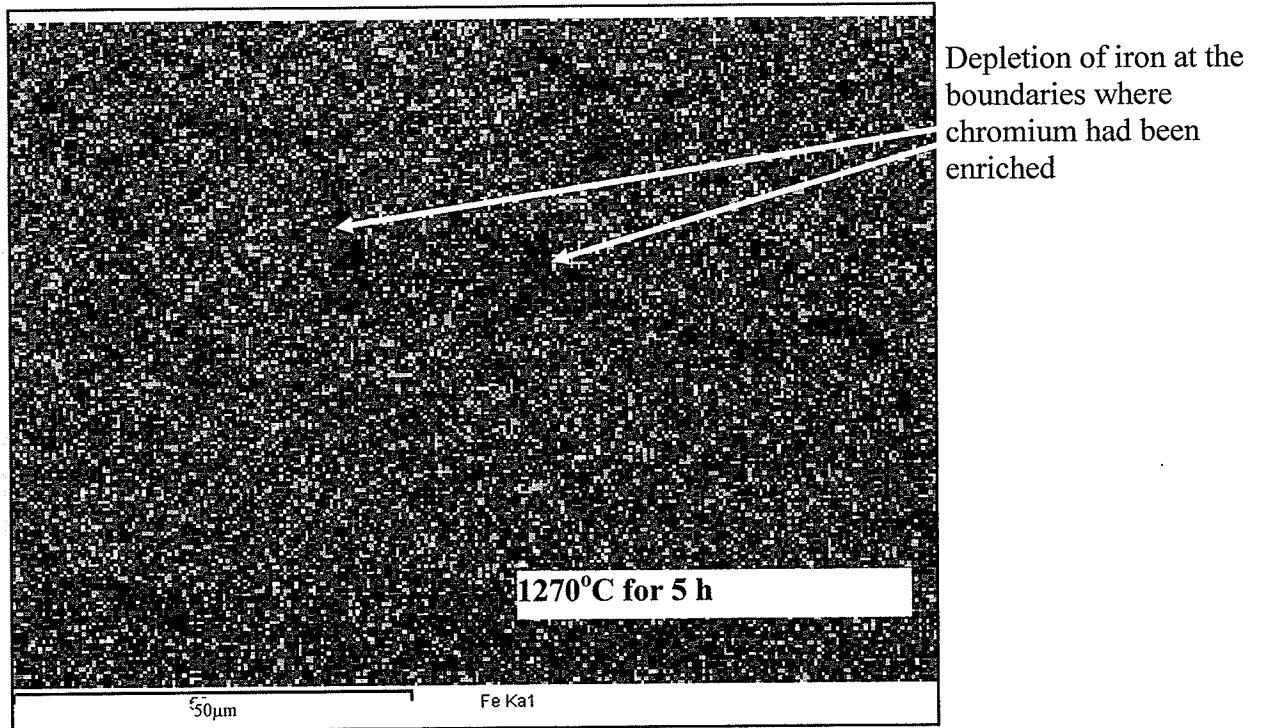


Figure 4.19: X-ray mapping of iron after 5h of sintering at 1270°C for the ternary Ni-Cr-Fe alloy

#### 4.6.4 Oxygen elemental X-ray map for the ternary Ni-Cr-Fe alloy

The corresponding X-ray maps of oxygen are given in Figures 4.20a-b. It appears that once formed, the oxide layer remained relatively stable even after 5h of sintering. Thermodynamically, this is expected to be predominantly chromia i.e. chromium oxide [84], and although the onset of formation of chromium oxide and chromium enrichment may have occurred after 2h sintering, it was not particularly evident until after 5h of sintering (Figure 4.17). This latter aspect is suggested to be responsible for the reappearance of the grain boundary features noted in Figure 4.16.

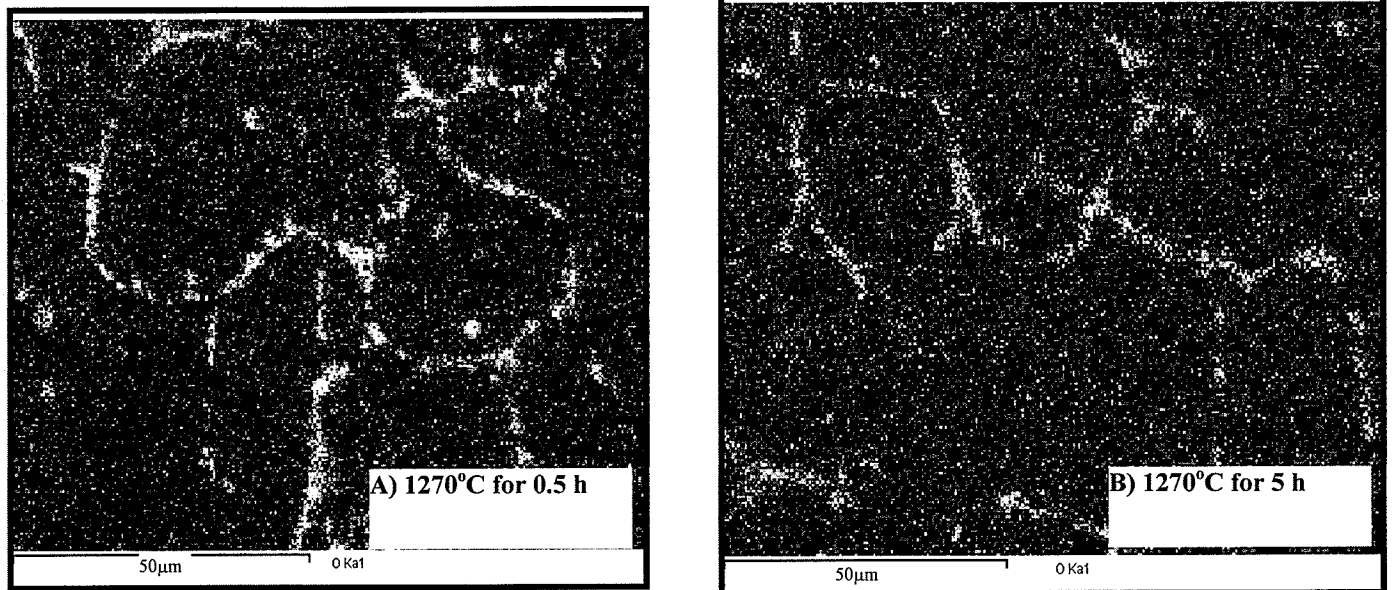


Figure 4.20: X-ray map of oxygen as a function of time for the ternary Ni-Cr-Fe alloy

#### 4.7 Air sintered density of the ternary Ni-Cr-Fe alloy

The sintered density curve of the air-sintered samples is shown Figure 4.21. The graph shows that there was limited change in densification with time and that in fact after 5h a small decrease in density was observed. This decrease in density could be related to oxidation after 5h sintering that would affect the mass to volume ratio. As a result, sintering times in excess of 5h were not investigated.

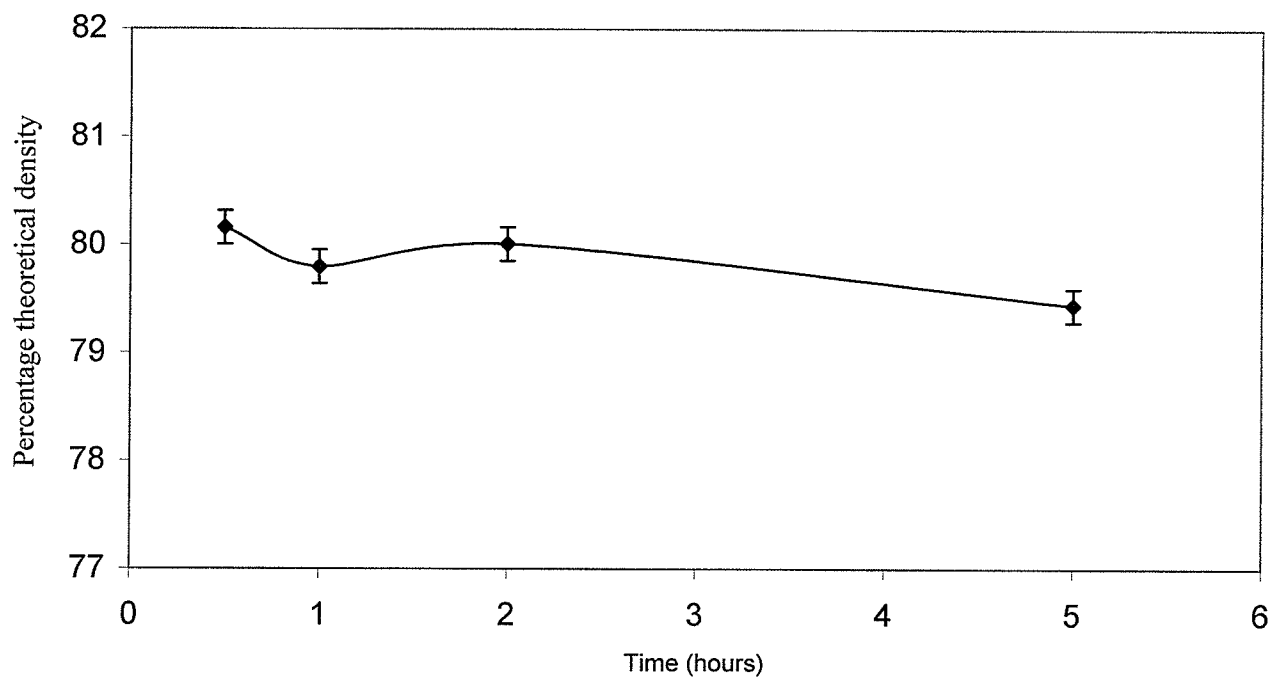


Figure 4.21: Air densification profile of the compact at 1270<sup>0</sup>C after varying times of sintering

The microstructural changes and porosity values of the air-sintered samples are summarized in Figure 4.22. This is a schematic representation of the main changes that occurred during air sintering based upon EDS and microscope images.

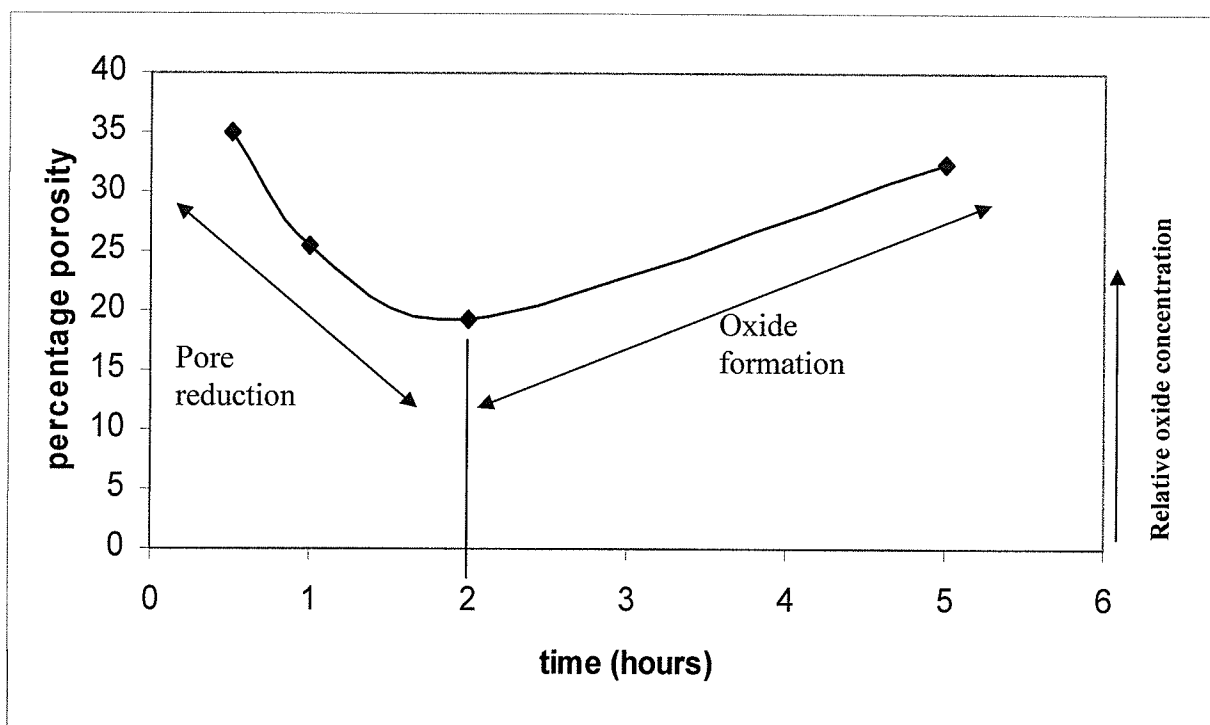


Figure 4.22: Schematic representation of pore and oxide formation during air sintering of the ternary Ni-Cr-Fe alloy

#### 4.8 Hardness data of air-sintered ternary Ni-Cr-Fe samples

Figure 4.23 shows the hardness of the air-sintered samples after sintering at 1270°C for varying times. The values shown in the figure are an average of a minimum of eight points across the sample cross-section. These data may be used to estimate the mechanical behavior of the compact as previously used in [85]. The hardness of the alloy used in this study was approximately 48HRB (~75 Vickers hardness).

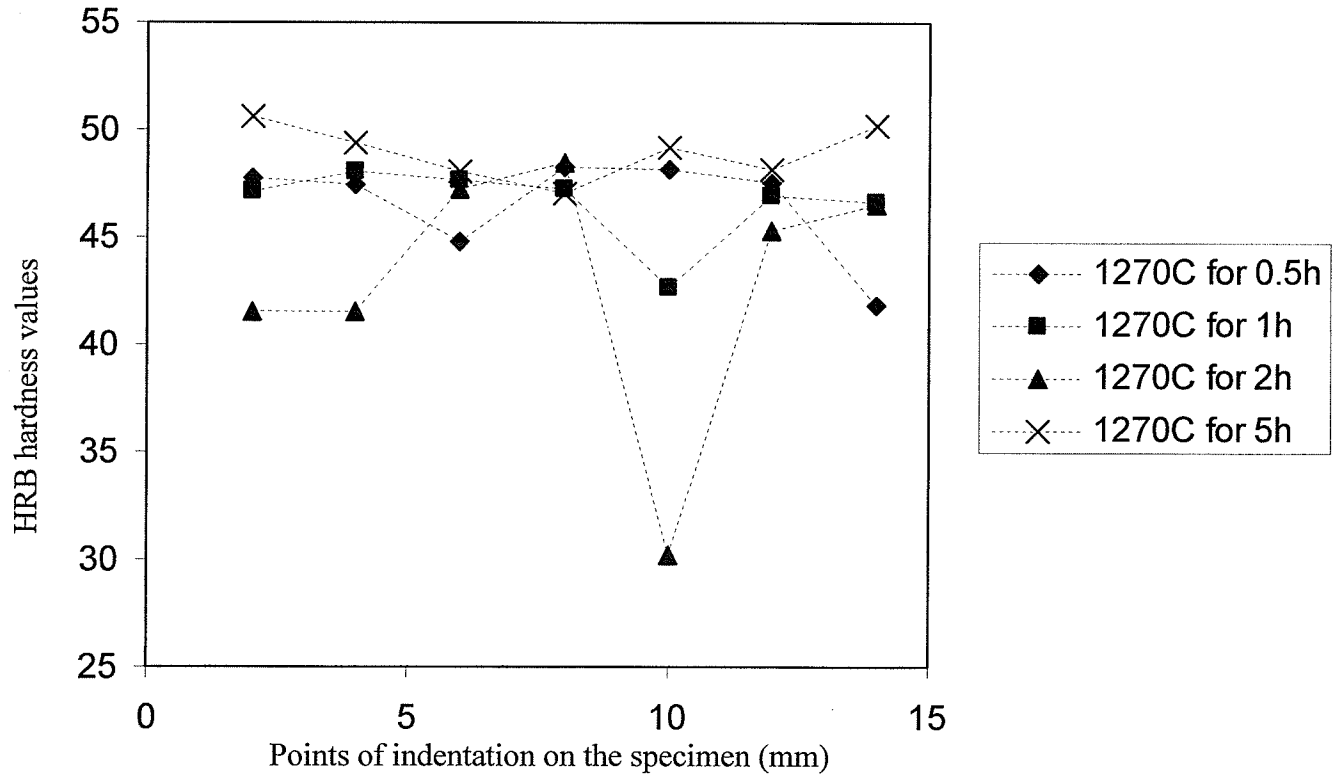


Figure 4.23: Hardness data of ternary Ni-Cr-Fe samples sintered in air for different times

## 4.9 Vacuum sintering of the ternary Ni-Cr-Fe alloy

### 4.9.1 Effect of temperature on microstructure of vacuum-sintered samples

Figure 4.24 shows the densification curve for specimens sintered under vacuum. To determine the relationship between sintered density and sintering temperature, time was kept constant at 1h while the temperature was varied from 1260 to 1400 °C.

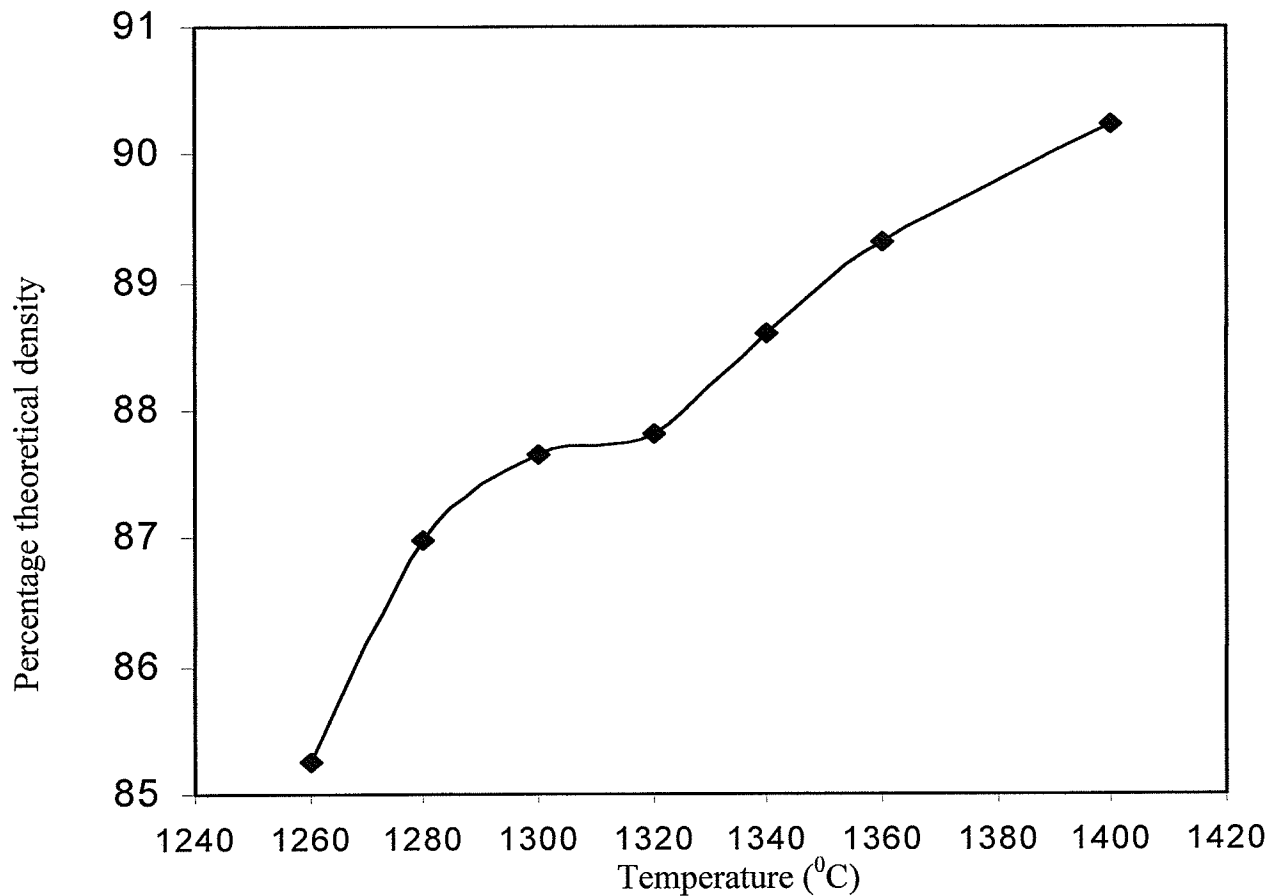


Figure 4.24: Variation in percentage theoretical density of Ni-Cr-Fe alloy as a function of sintering temperature (1h sinter)

From Figure 4.24 it can be seen that the theoretical density (TD) of the sintered samples increased from 85.25% (1260<sup>0</sup>C) to 90.24% (1400<sup>0</sup>C). This densification can be related to a decrease in porosity; representative micrographs are given in Figures 4.25a, 4.25b and 4.25c. Referring to Figure 4.25a, at 1260<sup>0</sup>C, the interparticle pores created during the powder compaction were still present, typical of an early stage of sintering during which pores start to grow and may tend to join in order to reduce internal energy. At the same time, the grain size was measured according to the ASTM standards to be 45 $\mu$ m, which compares well with the initial particle size (90% less than 54 $\mu$ m).

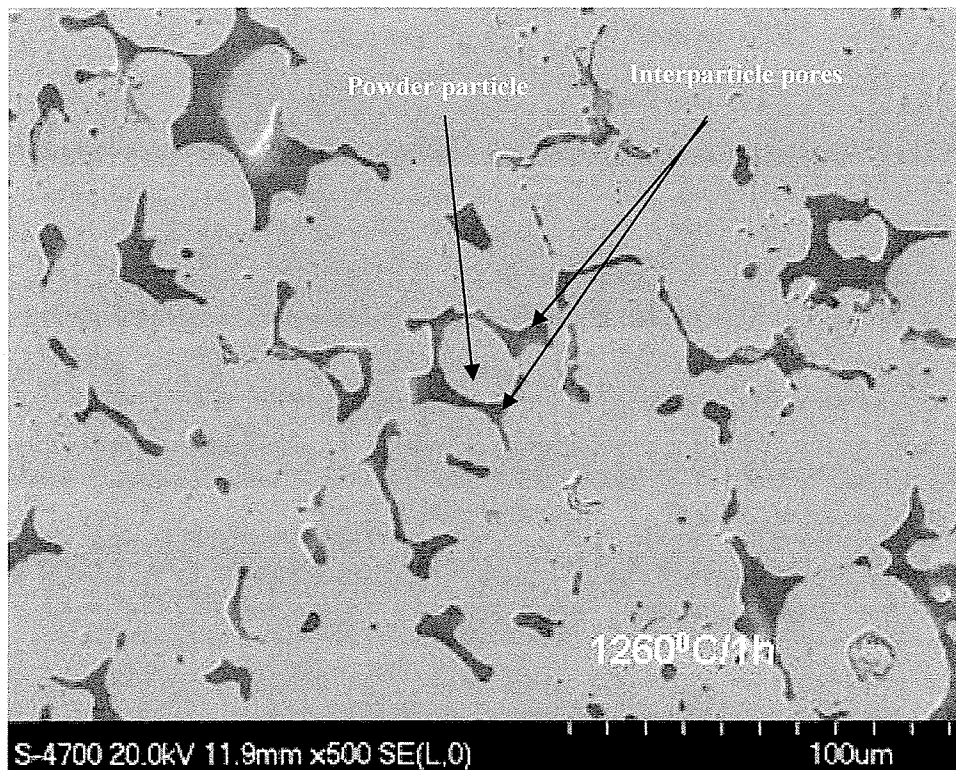


Figure 4.25a: SEM secondary electron image of ternary Ni-Cr-Fe sample sintered at 1260<sup>0</sup>C (Vacuum <6 millitorr)

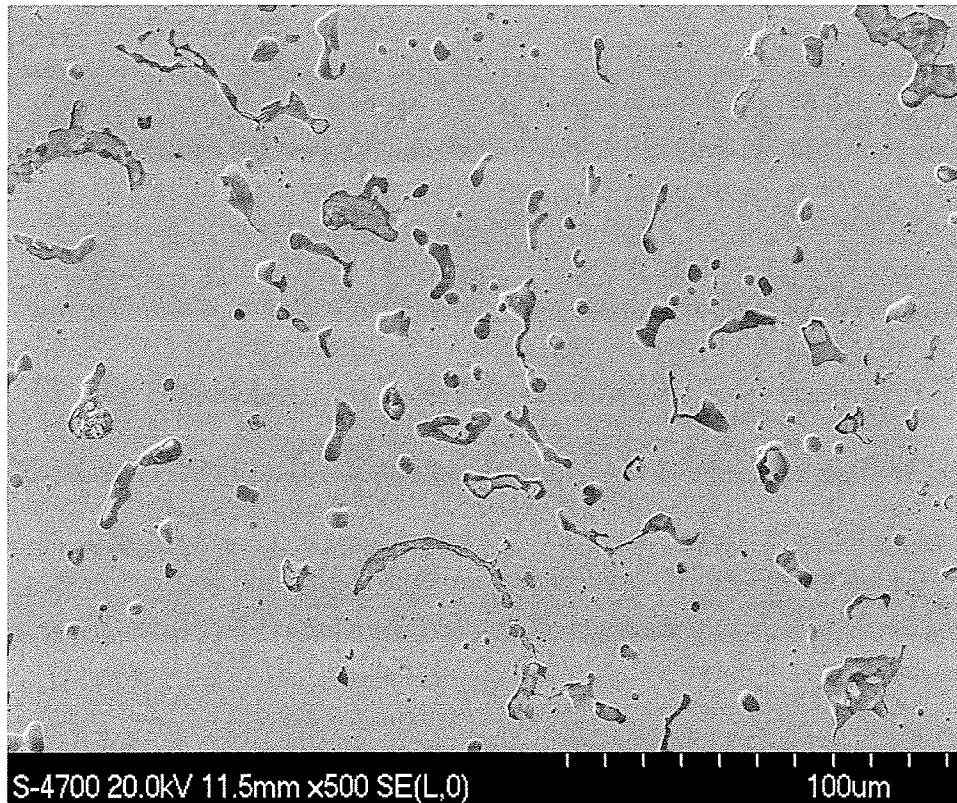


Figure 4.25b: SEM secondary electron image of ternary Ni-Cr-Fe sample sintered at 1280<sup>0</sup>C for 1h (vacuum <6 millitorr)

Figure 4.25b shows the micrograph of the 1280<sup>0</sup>C/1h sample, while Figure 4.25c shows a micrograph of a 1300<sup>0</sup>C/1h sintered specimen. From Figure 4.25c it can be seen that many pores were rounded and isolated. This indicates 1280<sup>0</sup>C to be proximity to an almost optimum sintering temperature although significant grain growth has not begun.

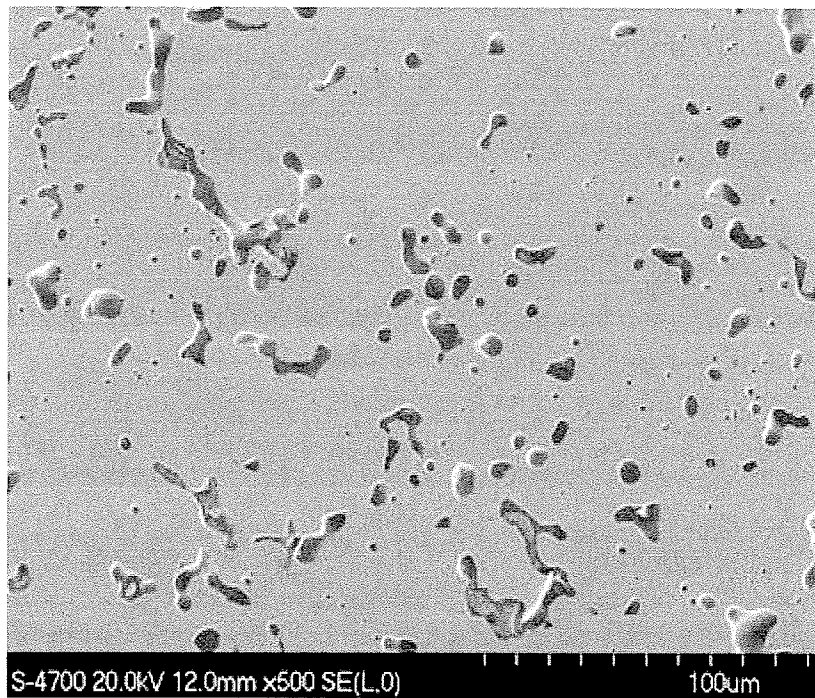


Figure 4.25c: SEM secondary electron image of ternary Ni-Cr-Fe samples sintered at 1300<sup>0</sup>C for 1h (vacuum <6 millitorr)

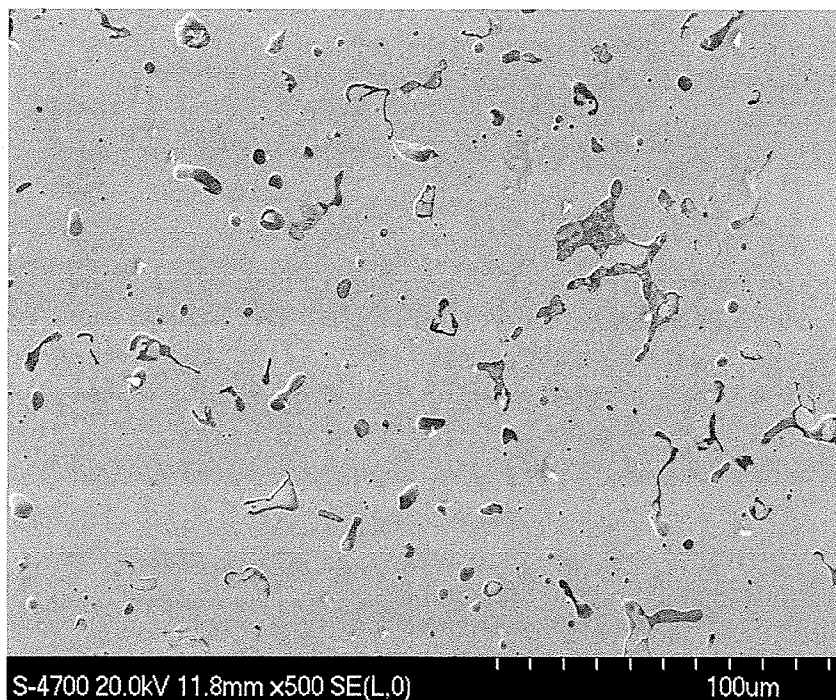


Figure 4.25d: SEM secondary electron image of ternary Ni-Cr-Fe samples sintered at 1320<sup>0</sup>C for 1h (vacuum <6 millitorr)

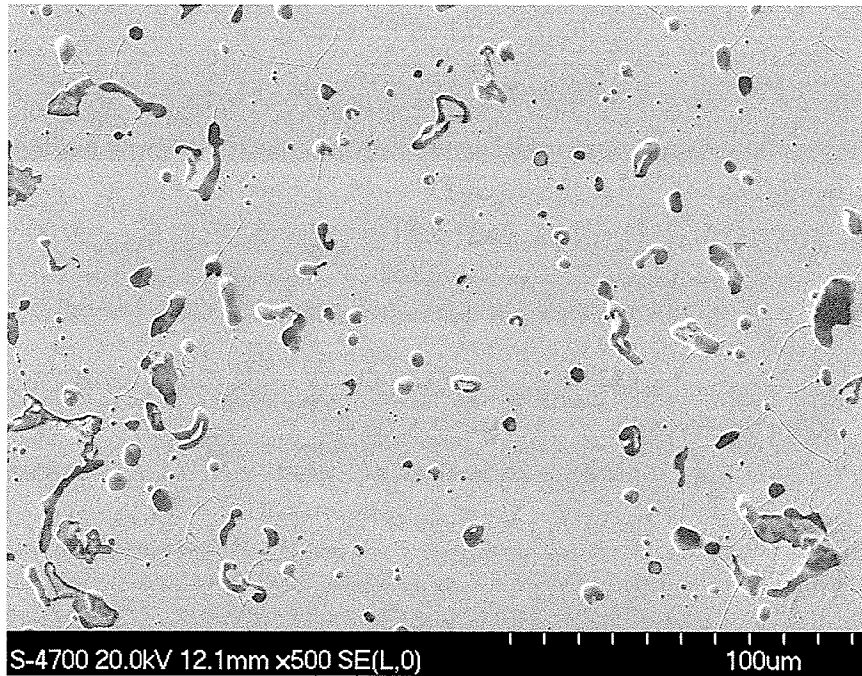


Figure 4.25e: SEM secondary electron image of ternary Ni-Cr-Fe samples sintered at 1350<sup>0</sup>C for 1h (vacuum <6 millitorr)

As expected, further increase in temperature led to a decrease in porosity near grain boundaries and finally at 1400<sup>0</sup>C, significant grain growth occurred leading to closing in the pores, as can be seen in Figure 4.25f. Finally, grain size of samples after sintering at various temperatures is shown in Figures 4.26a-c. It is seen that some level of grain growth occurred after heating above 1300<sup>0</sup>C (final grain size was approximately >60 $\mu$ m after sintering at 1400<sup>0</sup>C, Figure 4.26c) and therefore 1300<sup>0</sup>C was determined to be the sintering temperature most suitable to maximize density while minimizing grain growth.

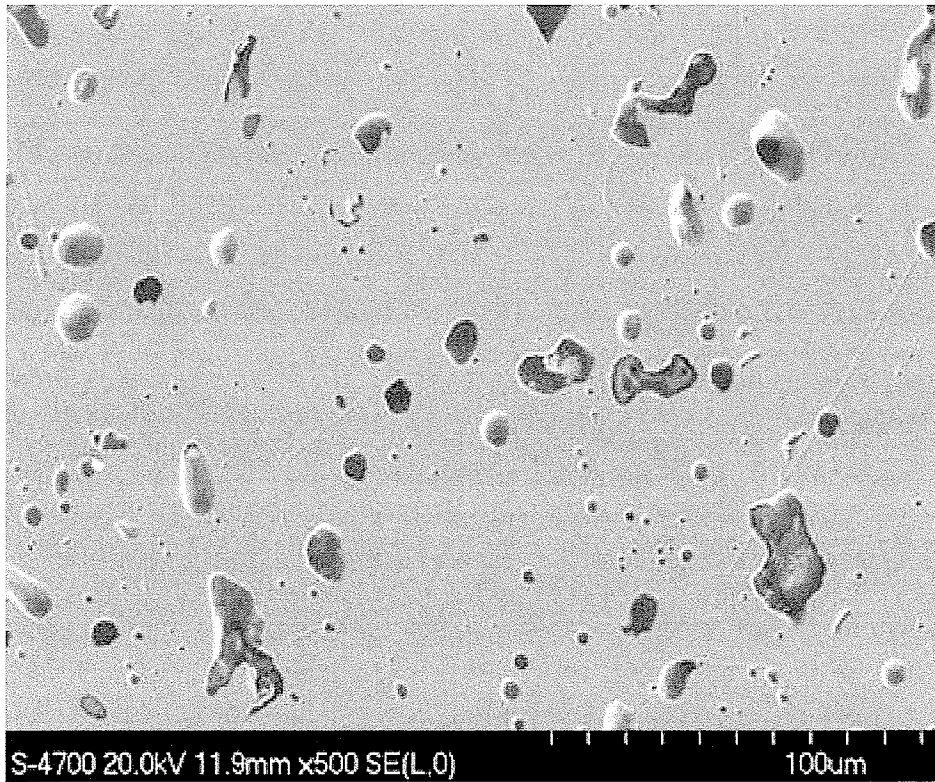


Figure 4.25f: SEM secondary electron image of ternary Ni-Cr-Fe samples sintered at 1400<sup>0</sup>C for 1h (vacuum <6 millitorr)

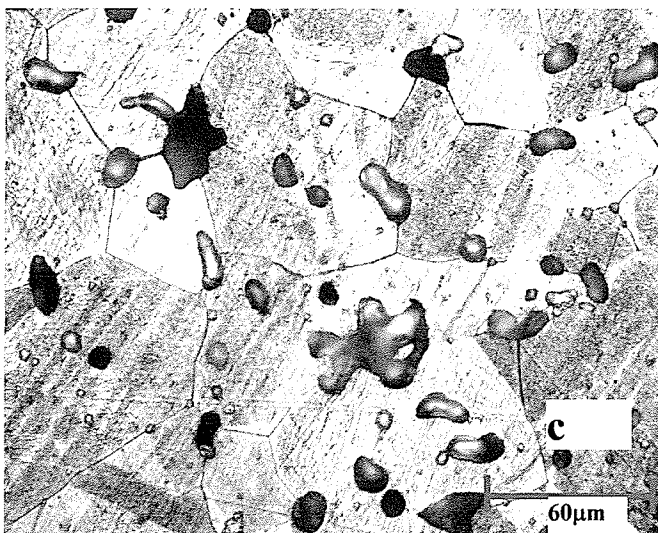
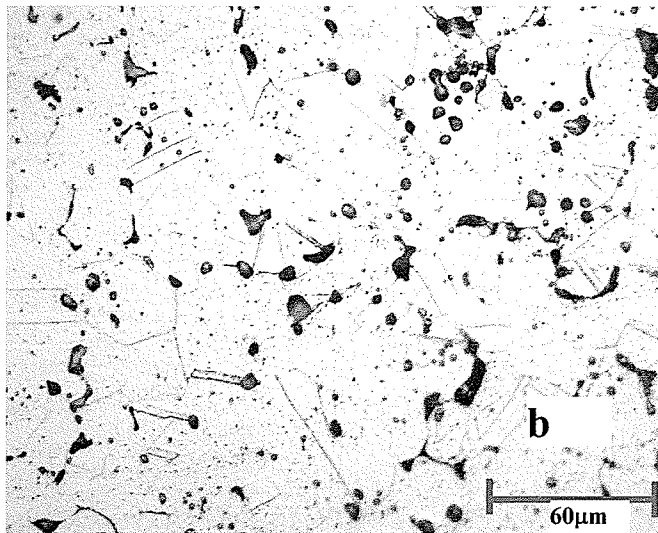
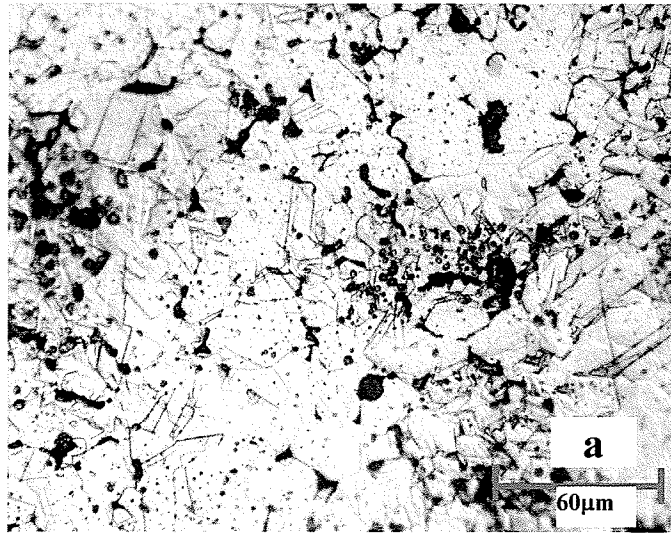


Figure 4.26: Optical micrograph of the sintered ternary Ni-Cr-Fe alloy at a) 1260°C for 1h, b) 1300°C for 1h and c) 1400°C for 1h

In order to determine the best sintering time to achieve maximum sintered density, the percentage theoretical density values of specimen vacuum sintered at 1300<sup>0</sup>C for times varying from 0.5 to 5h are shown in Figure 4.27. It can be seen that as sintering time increased from 0.5 to 2h a gain of about 2% in theoretical density was achieved. However, little improvement in densification occurred after times greater than 2h, suggesting that a 2h sinter was sufficient for this purpose. This also agrees with the air-sintering data which indicated that 2h may be sufficient for sintering without enrichment or depletion of any of the alloying elements.

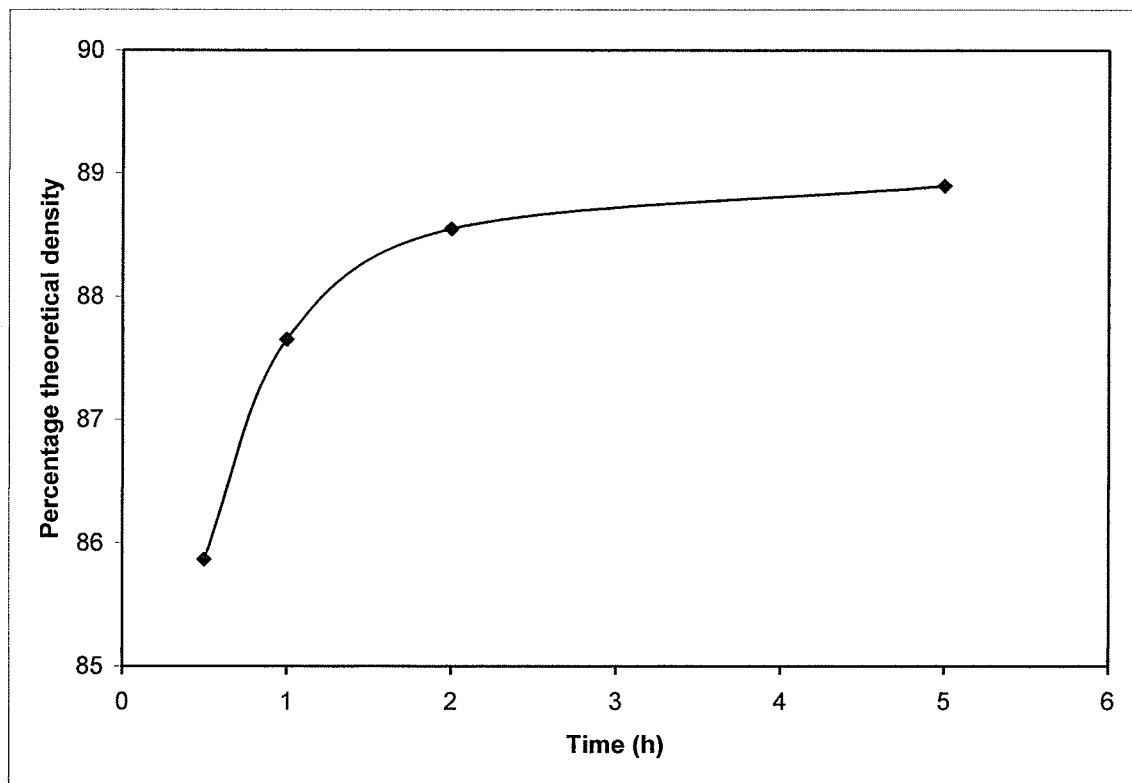


Figure 4.27: Plot of %TD as a function of sintering time in vacuum (6 millitorr, 1300<sup>0</sup>C) for ternary Ni-Cr-Fe alloy

From the air and vacuum sintering processes carried out it is suggested that the optimum sintering conditions were obtained at 1300<sup>0</sup>C, 2h sintering in vacuum.

#### **4.9.2 Mode of mass transfer during sintering**

In order to determine what happens during the sintering process, it is necessary to consider parameters such as sintered density, shrinkage, pore size, and size to neck ratio [2] that changes during sintering. Sintering that leads to densification that is aided by external stress application is known as stress-assisted sintering [82]. However in pressureless sintering (the mode used in this study), sintering is enabled mainly by diffusion, especially for small particle sized crystalline materials, as was the case in the ternary Ni-Cr-Fe powder. Derby and Wallach [86] identified the following methods for mass transfer.

1. Surface diffusion from the sources to a neck
2. Volume diffusion from surface sources to a neck
3. Diffusion along the bond interface from interfacial sources to a neck
4. Volume diffusion from interfacial sources to a neck
5. Creep
6. Plastic deformation

These mass transport modes are illustrated in Figure 4.28:

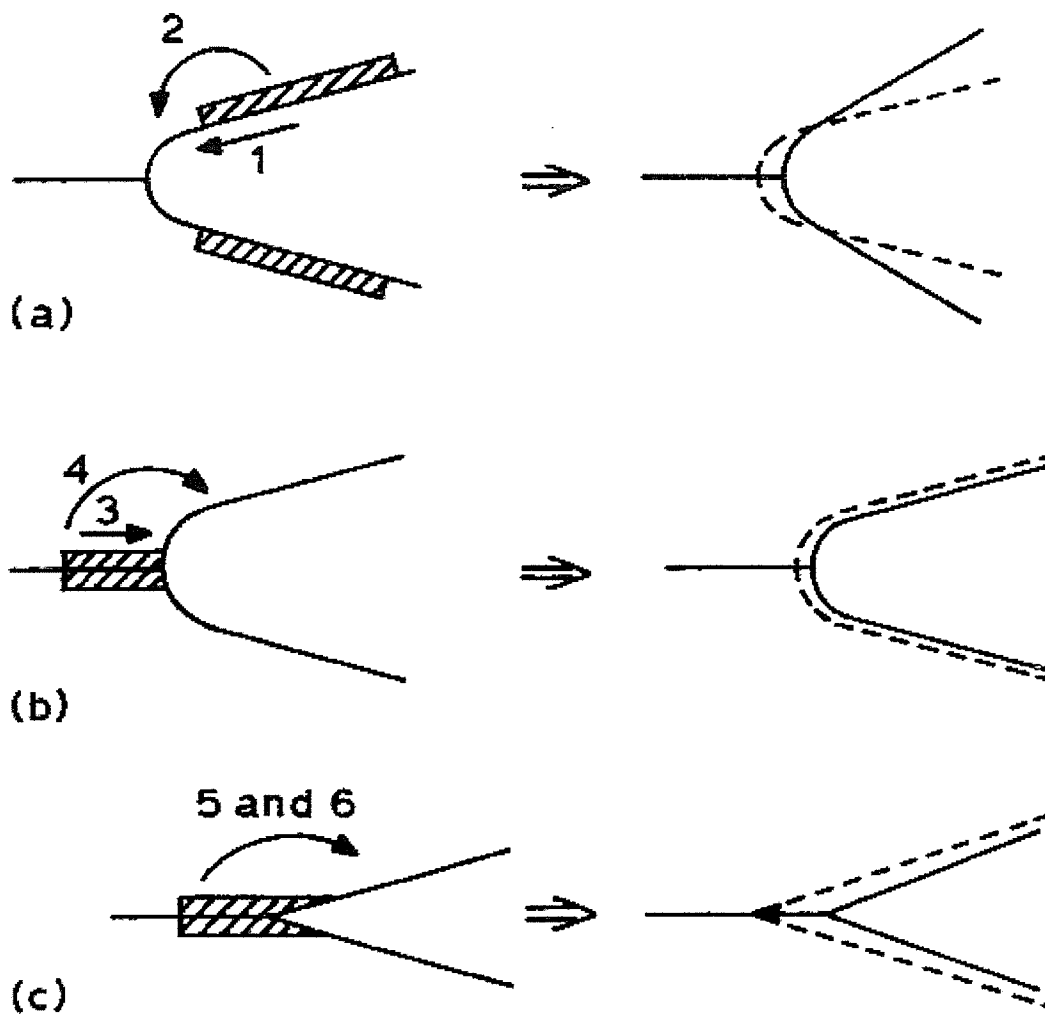


Figure 4.28: Schematic view of growing bond showing routes of six methods of mass transfer[86] a) surface transfer process (1 and 2); b) bond-line transfer process (3 and 4); c) bulk deformation process (5 and 6)

These processes have different driving forces, which are as follow: surface source transfer processes i.e., process 1 and 2 in Figure 4.28 which are driven by differences in surface curvature across the surface of an interfacial void that is subsequently arrested when a void of uniform curvature develops. In addition, the bond-interface transfer processes i.e., 3 and 4 are driven by the gradient of chemical potential along the bond line, that vary with the applied pressure and neck curvature; while the gross induced deformation i.e., 5 and 6 are driven primarily by applied pressure [86]. However, since no pressure was applied during the sintering process in this study, the most relevant process of mass transfer is suggested to be either one or all of the 1-4 mechanisms. Specifically, surface transfer processes (e.g., surface diffusion) seem to apply during the air sintering while bond-interface process (such as grain boundary and volume diffusion) were more prevalent during the vacuum sintering of the ternary compacts.

Grain boundary diffusion is a major process by which material can interact with the neighboring pores/surface leading to significant shrinkage and relatively large porosity reduction in a green compact, as seen in Figures 4.24 and 4.25. This is usually achieved by material removal from the neck surface at the initial stage of sintering or material transported from the solid to a pore at the later stage of sintering (figure 4.28b) [82]. Grain growth may reduce the system energy by decreasing the total grain boundary energy. According to Exner [82] densification is not pronounced in lattice, vapor or surface diffusion, but there can be significant grain growth and/or coarsening (Figure 4.14b and Figure 4.25b-f). Therefore, it is surface diffusion that may lead to material grain rearrangement and/or changes in shape of pores without much densification as was

seen in Figure 4.21. This is an indication that for air sintering the mechanism is related to a surface phenomenon.

In contrast, the preliminary observations of vacuum sintering indicate that grain boundary diffusion tends to be significant since rearrangement, pore changes (reduction in size), grain coarsening (Figure 4.25) in addition to both densification (Figures 4.24) and grain growth (Figure 4.26) occurred. Therefore, for the vacuum-sintered compacts, the mass transfer process 3 and 4 shown in Figure 4.28 apply.

### 4.9.3 Estimation of the mechanical properties of the air and vacuum sintered samples

#### 4.9.3.1 Hardness profile for the air sintered compacts

Figure 4.29a shows the location where indentations for measurement were made and the hardness profile of the sintered compacts is shown in Table 4.4 (for air sintered compacts) and Table 4.5 (for vacuum sintered compacts).

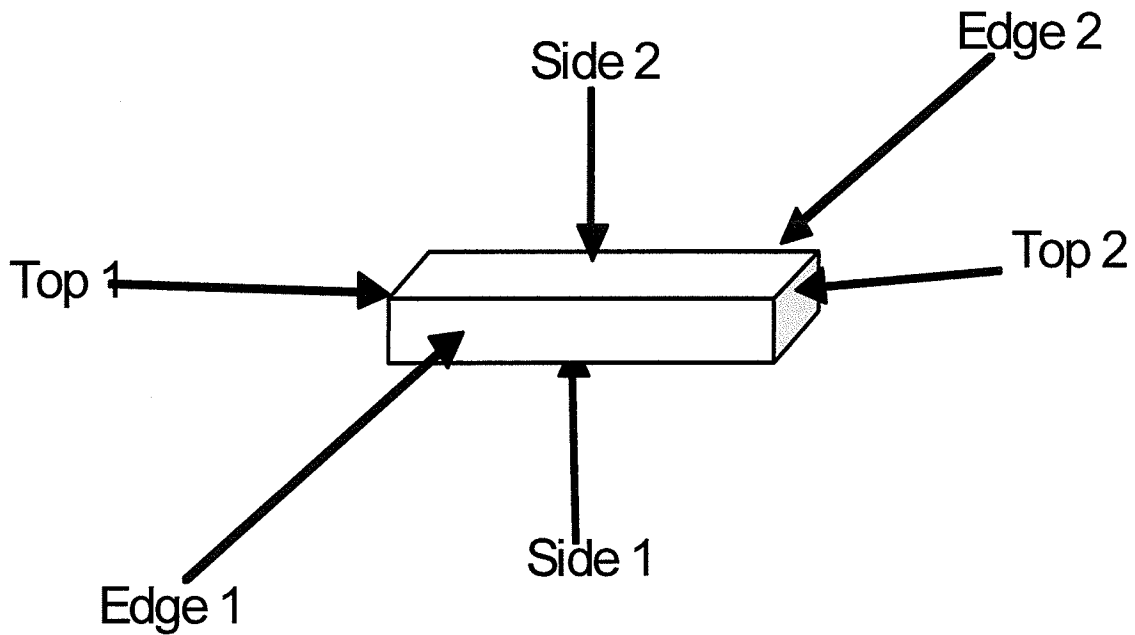


Figure 4.29a: Illustration of the sides from where hardness of the sintered samples was determined.

Table 4.4: Hardness profile for the 1270<sup>0</sup>C air sintered ternary Ni-Cr-Fe alloy

<b>Time</b>	<b>Mean</b>	<b>Standard deviation</b>
0.5h	44.01	6.15
1h	45.5	5.17
2h	45.45	5.73
5h	45.79	5.28

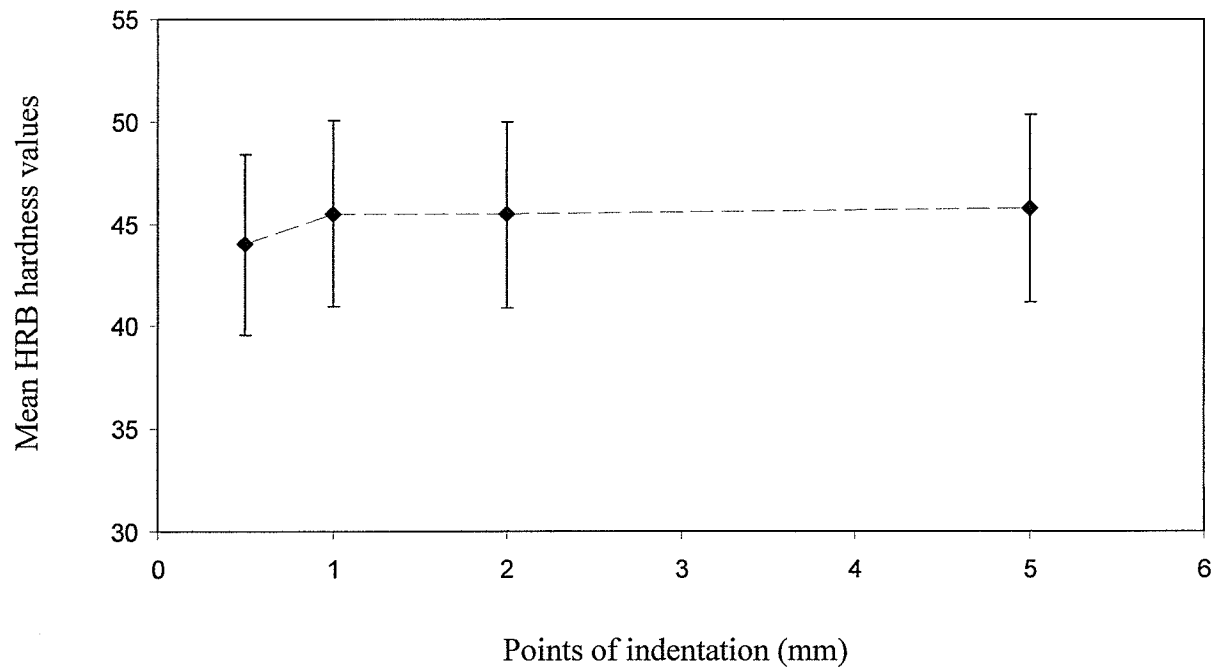


Figure 4.29b: Brinell hardness variation of various samples sintered at 1270C for 0.5, 1, 2, and 5h

Table 4.5 HRB hardness profile of the 1h vacuum sintered ternary Ni-Cr-Fe alloy

Temperature (°C)	Mean Hardness(Brinell)	Standard deviation
1260	41.63	3.34
1300	49.6	3.6
1320	51.05	5.08
1340	51.08	2.91

#### 4.9.4 Relationship between fractional porosity and tensile strength

The strength of the ternary Ni-Cr-Fe alloy is important to its application in service. Interestingly, there have been efforts to relate the porosity of P/M process produced compact to the tensile strength. Salak *et al* [87] estimated the relative ultimate tensile strength of powder compact to the ultimate tensile strength of fully dense material to be:

$$\sigma_{rel} = \frac{\sigma}{\sigma_o} = \exp(-4.3\eta) \dots\dots\dots 4.2$$

where  $\sigma_{rel}$  is the relative ultimate tensile strength of the sintered powder compact,  $\sigma$  is the ultimate tensile strength of the powder compact,  $\sigma_o$  is the ultimate tensile strength of the fully dense material and  $\eta$  is the fractional porosity. In a similar work, Fleck and Smith [88] also used a model based on layered randomly organized array of cubes. Using the probability of finding a pore at a location in the layer the relative ultimate tensile strength was estimated to be:

$$\sigma_{rel} = \frac{\sigma}{\sigma_o} = \left(1 - \eta^{\frac{2}{3}}\right)^2 \dots\dots\dots 4.3$$

where  $\sigma_{rel}$  is the relative ultimate tensile strength of the sintered powder compact,  $\sigma$  in the ultimate tensile strength of the powder compact,  $\sigma_o$  is the ultimate tensile strength of the fully dense material and  $\eta$  is the fractional porosity.

Exner and Pohl [89] modeled the equation and determined that:

$$\sigma_{rel} = \frac{\sigma}{\sigma_o} = \exp(-K\eta) \dots\dots\dots 4.4$$

The notations in equations 4.4 are similar to equations 4.2 and 4.3 where K is the shape of the pore. According to Exner and Pohl [89] K is close to 1 for spherical and cylindrical pore morphologies; however, some authors have obtained K values to be close to 10. In another publication [90] it was determined that the equations are only accurate for low pore fraction (0.23) for stainless steels compacts while the values were found to be inconsistent with higher-porosity samples. Hence, extreme care has to be taken when estimating the tensile strength of a P/M product after fabrication, because the equations may greatly overestimate the relative strength values.

Therefore using equation 4.4 and assuming that the shape of the pore is spherical (i.e., K=1) and using  $23/100 \pm 5$  as the fractional porosity (calculated from the image analysis of the optimized vacuum sintering conditions  $1300^{\circ}\text{C}/2\text{hr}$ ), the relative strength of the ternary Ni-Cr-Fe compact was estimated to be about 80% of the theoretical strength of an ideal composition and an ideal process.

#### **4.9.5 Post sintering operation: cold rolling**

Since the Ni-Cr-Fe alloy, a derivative of IN600, is used in various nuclear and high temperature applications, often after being mechanically worked, the effect of cold rolling on some preliminary properties of the sintered alloy sample is of interest. Specifically, the effects of cold rolling on the theoretical density and hardness were examined. This is shown in Figure 4.33, which is a 3-D deformation diagram of a cold rolled specimen sintered for 2h at 1300<sup>0</sup>C in vacuum. From this figure, it may be observed that near theoretical density (98.12%) was obtained by cold rolling to 40% of the original thickness, while the hardness of the cold rolled specimen was approximately 253Vickers (10kgf). An un-cold rolled ternary alloy value compares well with processed wrought IN600 [85].

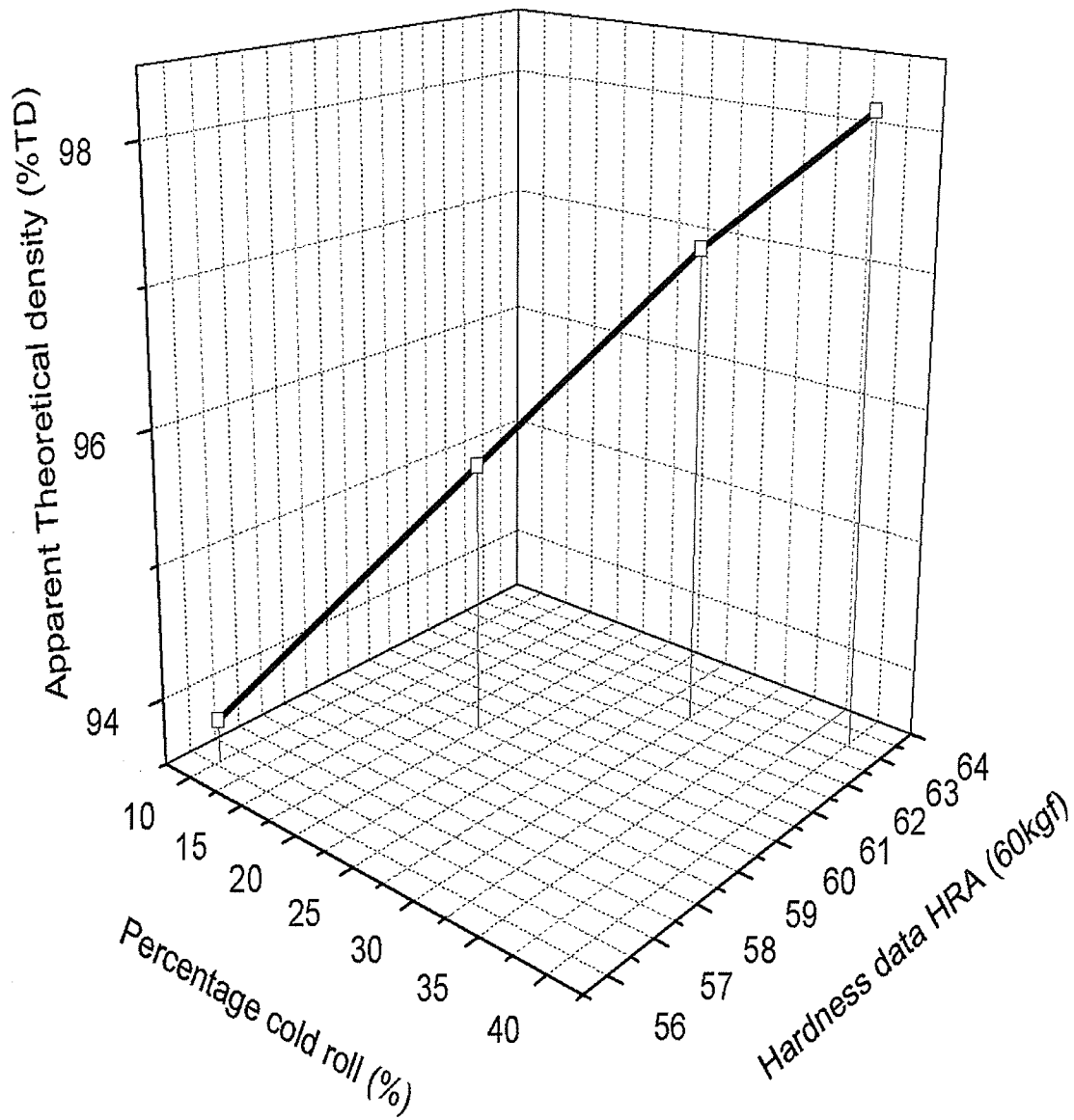


Figure 4.30: 3-D deformation diagram for the cold rolled sintered compact

## 4.10 Effect of Al on the ternary powder

### 4.10.1 Thermodynamic predictions

Before analyses were carried out on the compacts, JMatPro thermodynamic software was first used to predict the phase(s) formed based on the addition of Al to the ternary Ni-Cr-Fe alloy compact as listed in Table 4.6. Briefly, the phase identification was based on a determination of the minimum free energy based on CALPHAD analysis [11, 12] and simplified into equation:

$$\Delta G = \Delta G^0 + \Delta G_{mix}^{ideal} + \Delta G_{mix}^{xs} \dots\dots\dots 4.5$$

where,  $\Delta G$  = Gibbs free energy,  $\Delta G^0$  is the Gibbs free energy due to contributions from pure components,  $\Delta G_{mix}^{ideal}$  is the ideal mixing term, and  $\Delta G_{mix}^{xs}$  is the excess free energy of mixing ( $\text{J}\cdot\text{mol}^{-1}$ ). As stated earlier, most thermodynamic calculations are usually based on equilibrium conditions without much regard to kinetic considerations. Hence, not all phases may be present in the experimental samples. The phase(s) with the minimum free energy is/are selected by the software and displayed as stable phase. The thermodynamic calculations are shown for the effect of a variation in Al addition on the ternary Ni-Cr-Fe alloy.

Table 4.6: Table showing the varying Al w/o and the ternary Ni-Cr-Fe alloy

Elements	Ternary Ni-Cr-Fe alloy (w/o)	Ternary Ni-Cr-Fe plus 1w/o Al	Ternary Ni-Cr-Fe plus 3w/o Al	Ternary Ni-Cr-Fe plus 6w/o Al	Ternary Ni-Cr-Fe plus 12w/o Al
Ni	Balance	78.16	76.58	74.22	67.58
Cr	12.00	11.88	11.88	11.28	11.64
Fe	9.00	8.91	8.91	8.46	8.23
C	trace	trace	trace	trace	trace
Al	0	1.00	3.00	6.00	12.00
Calculated Density(g/cm <sup>3</sup> )	8.56	8.46	8.21	7.87	7.24

#### 4.10.2 Ni-Cr-Fe ternary alloy

First a thermodynamic prediction was done for the as-sintered ternary. Figure 4.31a shows the JMatPro prediction for the formation of phases in the ternary Ni-Cr-Fe alloy from 400°C to 1400°C. It shows that the only phase to form in the temperature range specified for the alloy will be austenitic gamma ( $\gamma$ ) phase, with a face centered cubic structure. It is also seen that under equilibrium transformation conditions the volume fraction of gamma phase would be 100% at about 400°C and remain stable to the melting point of the alloy at about 1430°C. A test was carried out to examine the melting temperature of the compact by heating the sample in the DSC (Figure 4.31b). The melting temperature of the ternary alloy was found to be 1437°C $\pm$ 5. In another test carried out in a furnace, melting occurred at 1428°C. These temperatures were very close to the predicted values. An optical micrograph of the ternary alloy sintered for 2h at 1300°C is shown in Figure 4.32a while the SEM image of the as-sintered ternary Ni-Cr-Fe, using backscattered electrons (BSE) is shown in Figure 4.32b. It is seen that the matrix consists of a single phase with some residual porosity.

Also, the sintered compact was examined by X-ray diffraction and the diffractogram is shown in Figure 4.33. Unlike the XRD pattern of the “as-received” powders that showed the presence of individual alloying elements e.g., Ni (Figure 4.6), the XRD analysis of the as-sintered ternary Ni-Cr-Fe shows a composition that is free of individual elements. It is also seen that all the peaks can be indexed on the basis of a FCC  $\gamma$  phase. The lattice parameter of the  $\gamma$  phase, as determined by applying the Bradley-Jay correction factor, was calculated to be  $0.35427 \pm 0.003$  nm, which is close to the value quoted for Inconel 600 in the literature [84].

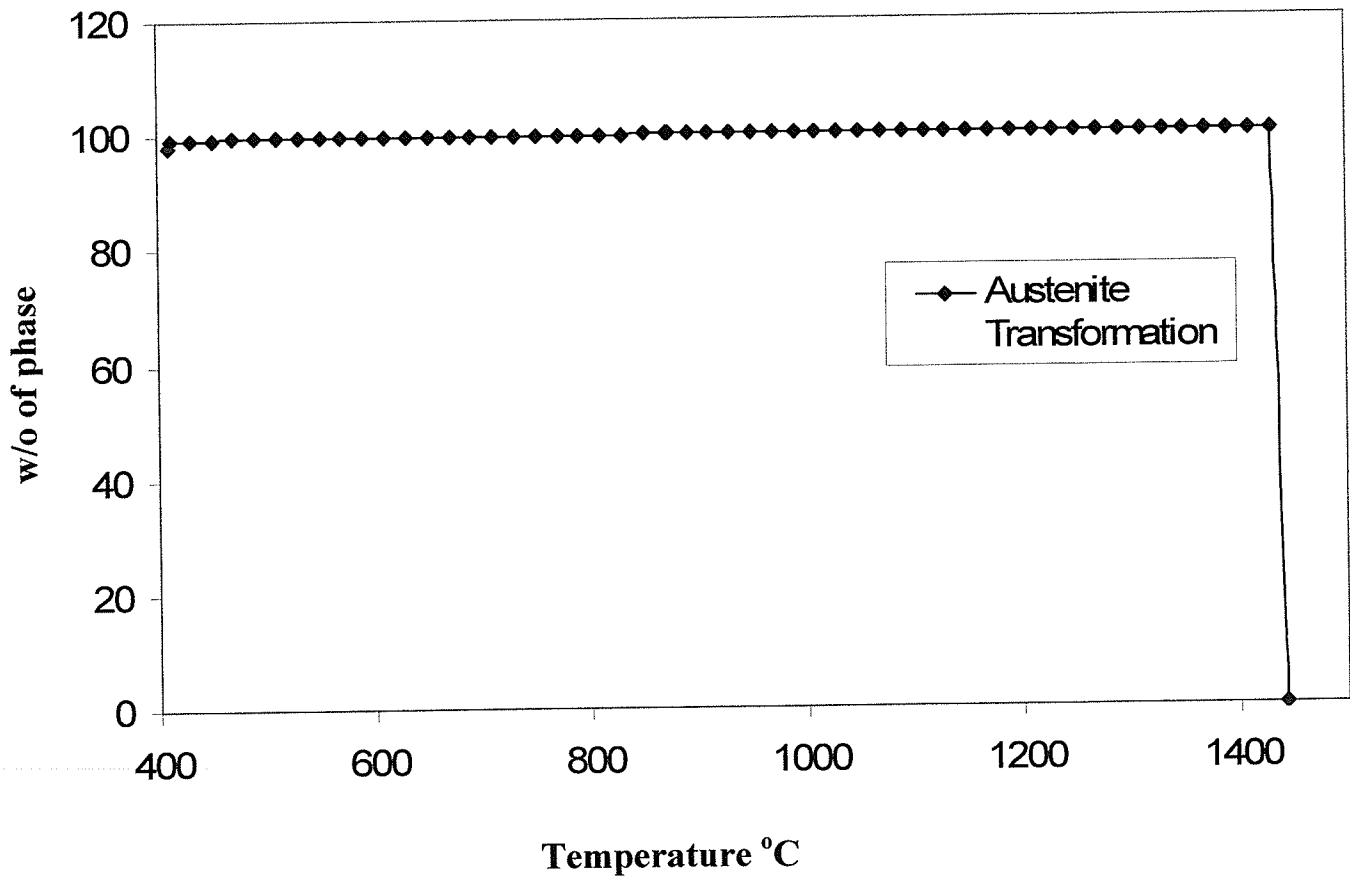


Figure 4.31a: The JMatPro thermodynamic calculation for the base ternary Ni-Cr-Fe alloy showing presence of austenite

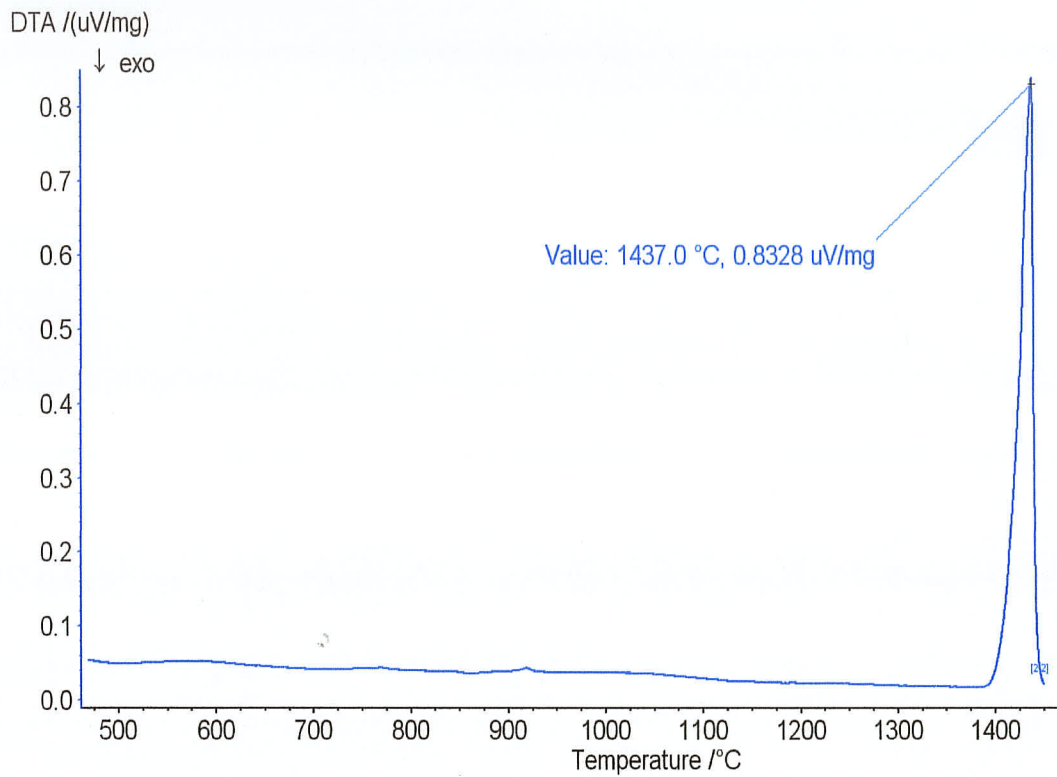


Figure 4.31b: DSC trace of the ternary Ni-Cr-Fe alloy as it was heated to the melting temperature

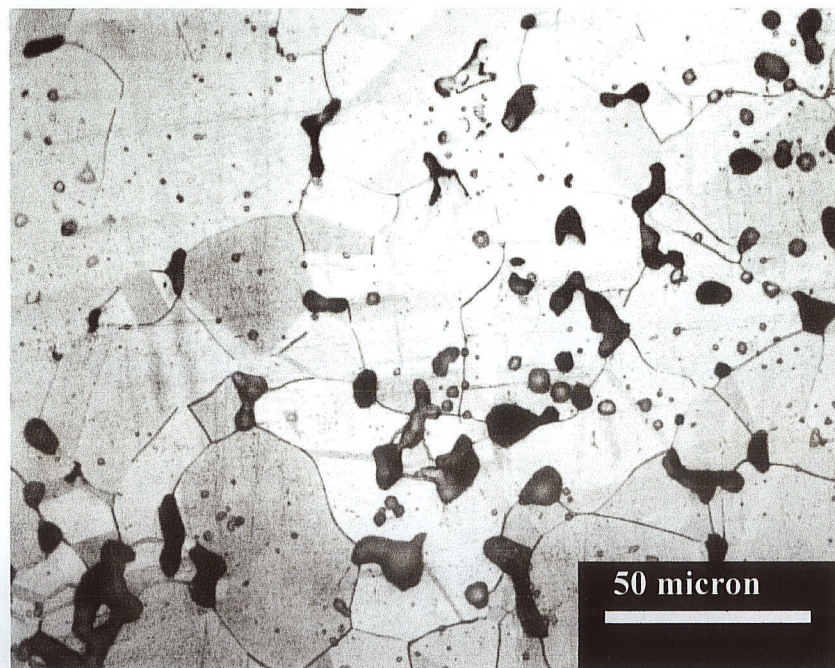


Figure 4.32a: Optical Micrograph of the ternary Ni-Cr-Fe alloy after heating to 1300°C /2h and furnace cooling showing the presence of fine grains and porosity.

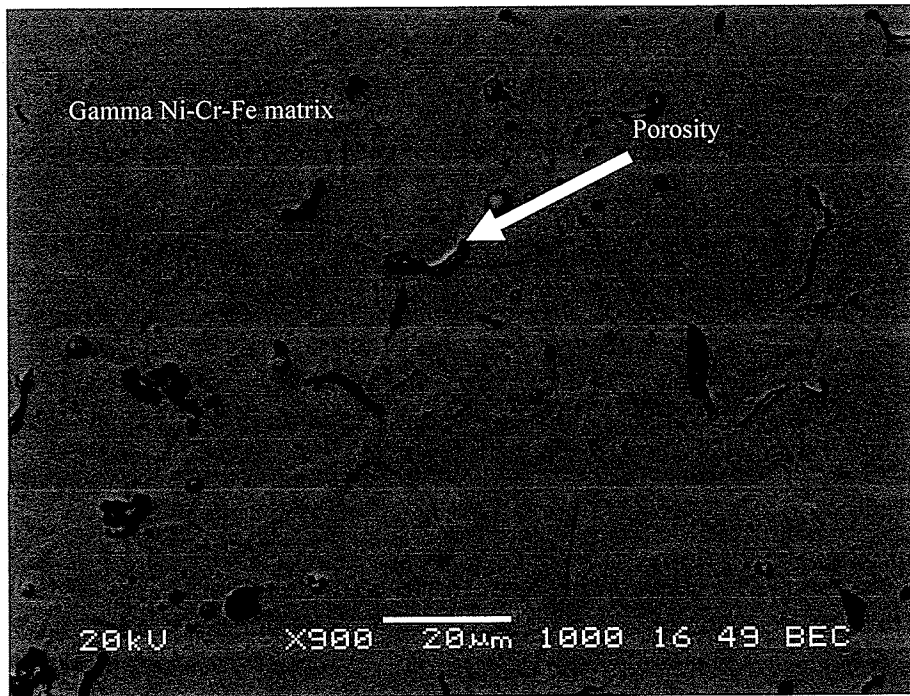


Figure 4.32b: SEM-BSE image of the ternary Ni-Cr-Fe alloy.

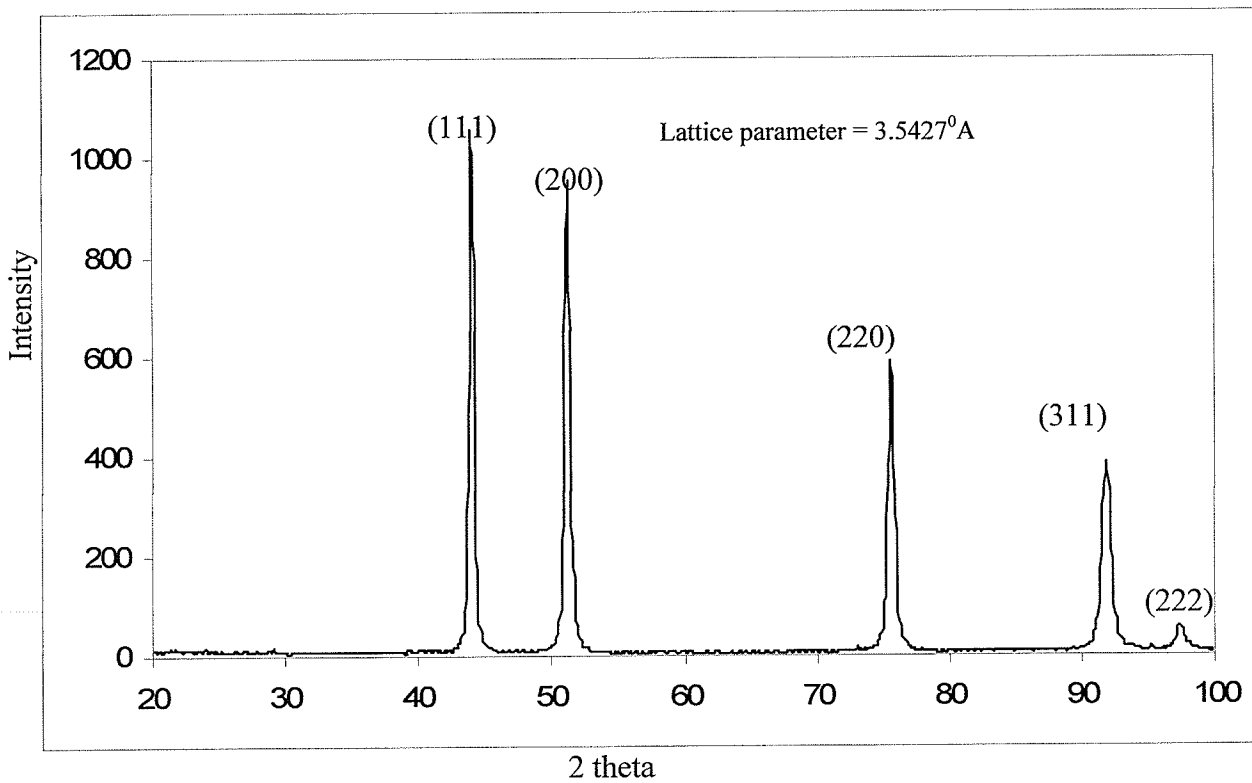


Figure 4.33: XRD pattern of the ternary powder after sintering

#### 4.10.3 Effect of Al on the density of ternary Ni-Cr-Fe alloy

Figure 4.34 shows the effect of Al on density of the optimized pre-alloyed composition. From Figure 4.34, it can be seen that an increase in Al addition, caused a decrease in the density of the compacts. This can be related to the smaller density of Al as compared to other alloying elements (Ni, Cr and Fe). Huppmann [45] has classified sintering into different classes which are solid, liquid and activated sintering. The presence of a specific amount of liquid phase in some compacts may enhance the sintering process (i.e., activating the sintering process) [91] because sintering occurs by diffusion. Al can act as an activator for sintering [1, 47, 91], but the amount of Al necessary for activating sintering is usually small, in the range of 1-3w/o. In this study, there is likelihood that the amounts of Al present in the compact may have exceeded the quantity required for sintering activation. When this occurs, a rigid skeletal structure of sintered compact is formed in which the prior location of the activator is vacant due to diffusion into the base powder or evaporation after sintering creating pores in the compact. This can also lead to the decrease in the density. An example of this phenomenon is seen (Figure 4.34) when Al additions of 1, 3, 6 and 12 w/o were investigated.

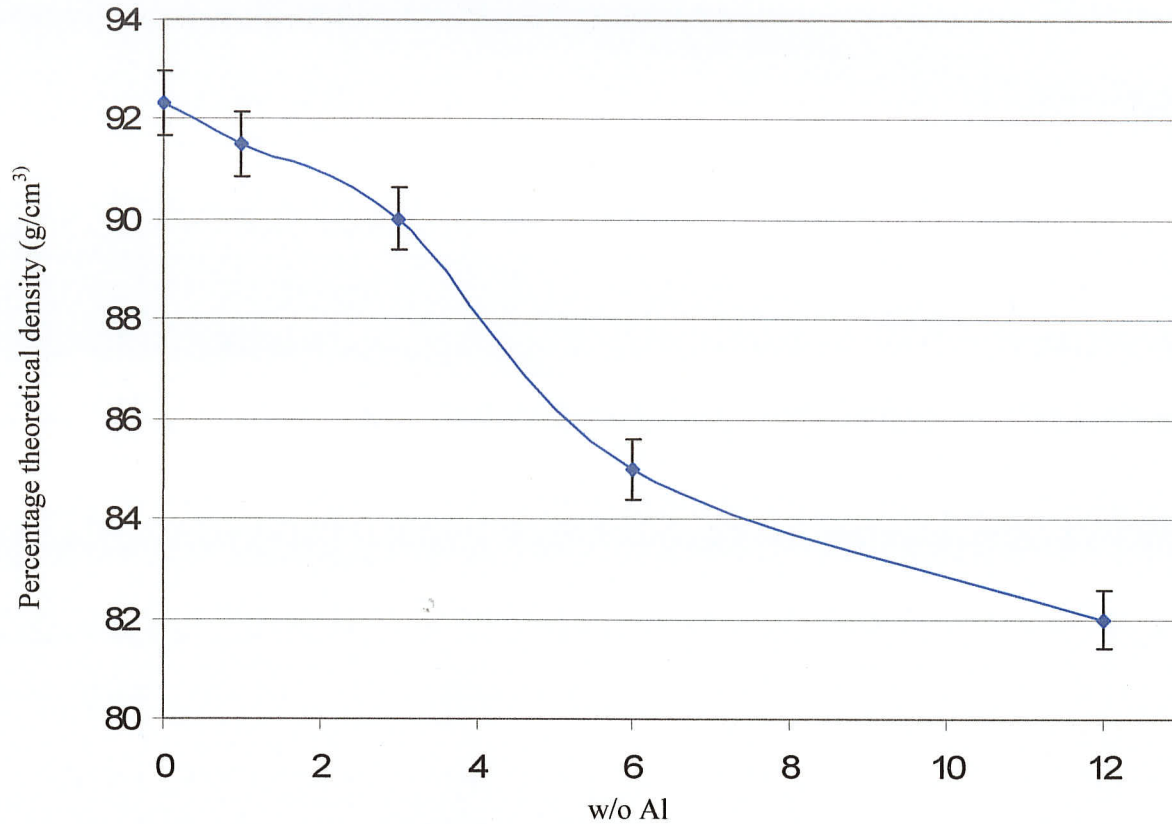


Figure 4.34: Effect of Al on the sintered density of the Ni-Cr-Fe ternary alloy

#### 4.11 1w/o Al modified ternary Ni-Cr-Fe alloy

Figures 4.35a-b show the step calculation (Figure 4.35a) and the CCT curve (Figure 4.35b) for the 1w/o Al modified Ni-Cr-Fe alloy. Although some phases such as  $Ni_2M$  and gamma prime were also predicted to form by JMatPro (Figure 4.35a), however, these phases were not expected to form in the present alloy due to reaction kinetics. This prompted the need for using a more appropriate method such as a CCT curve. Therefore, although step calculations were done for all the Al concentrations, it is the CCT curves that were used to predict the phases that were expected to form. The cooling curve which

represents cooling rate of the 1w/o Al modified ternary Ni-Cr-Fe alloy from the sintering temperature of 1300°C is also shown in Figure 4.35b. Based on 0.5% transformation, the phases that are expected to form are  $M_{23}C_6$  and  $M_7C_3$ . The region above the transformation curve is the gamma phase region. From the figure it is seen that the cooling curve did not cut across either of the  $M_{23}C_6$  or  $M_7C_3$  transformation curves, which indicates that in the as sintered condition the 1 w/o Al modified Ni-Cr-Fe alloy will not have any other phase present in its microstructure except the austenitic gamma phase. For the carbides predicted in Fig 4.35b to be formed, an appropriate heat treatment of the compact would be necessary after sintering.

The XRD pattern of the 1w/o Al modified ternary Ni-Cr-Fe alloy is shown in Figure 4.35c. All the peaks could be indexed on the basis of  $\gamma$  phase, and its lattice parameter was calculated to be 0.35499 nm. This is 0.2% larger when compared to the lattice parameter of “as-sintered” ternary Ni-Cr-Fe (0.3527nm). This indicates that the addition of 1w/o Al increased the inter-atomic distance due to the higher atomic diameter of Al as compared to the ternary Ni-Cr-Fe alloy (Atomic radius: Al:0.143nm, Ni:0.125nm, Cr:0.128nm, Fe:0.124nm) as it occupies the lattice points of the ternary alloy.

### Ni-1.0Al-11.88Cr-8.91Fe-0.04752C wt(%)

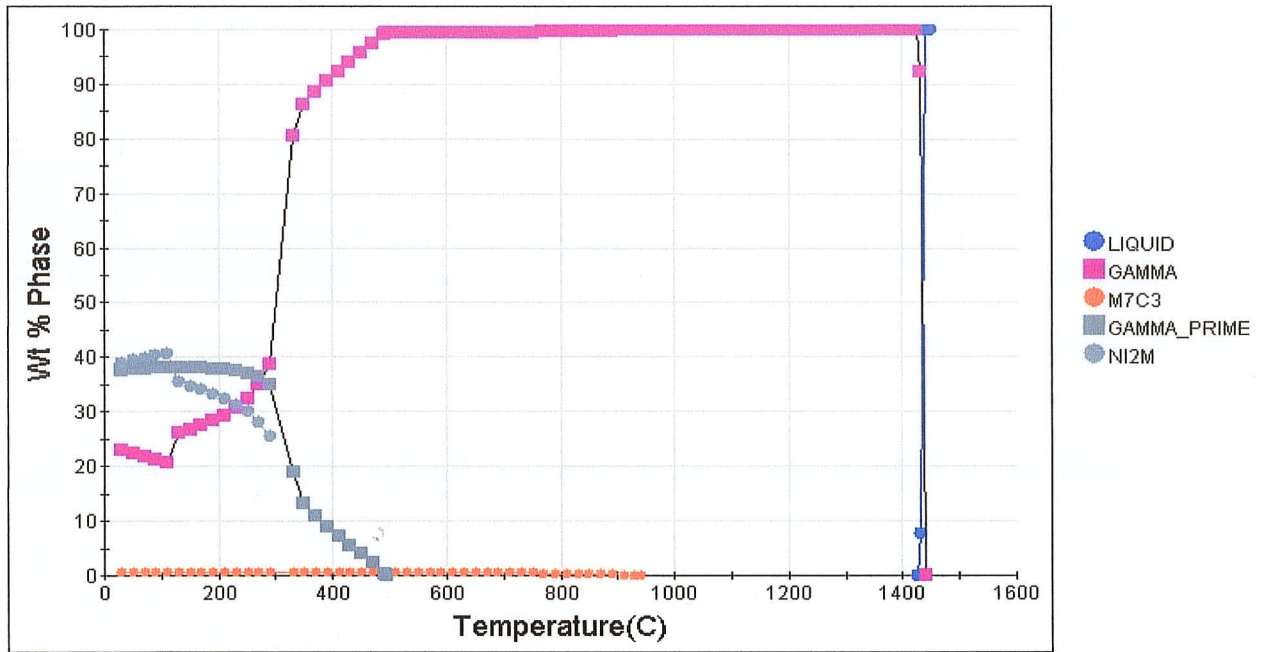


Figure 4.35a: JMatPro prediction for the step calculations of the 1w/o Al modified Ni-Cr-Fe ternary alloy

### CCT Nickel Based Superalloy

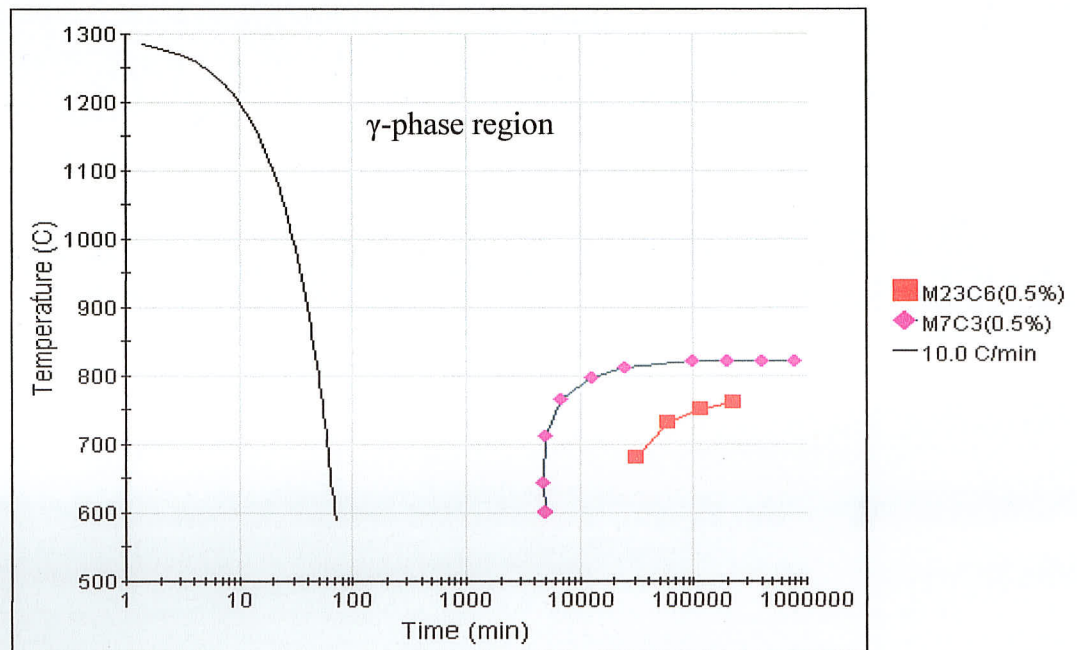


Figure 4.35b: JMat Pro prediction of the CCT curve of the 1w/o Al modified Ni-Cr-Fe ternary alloy

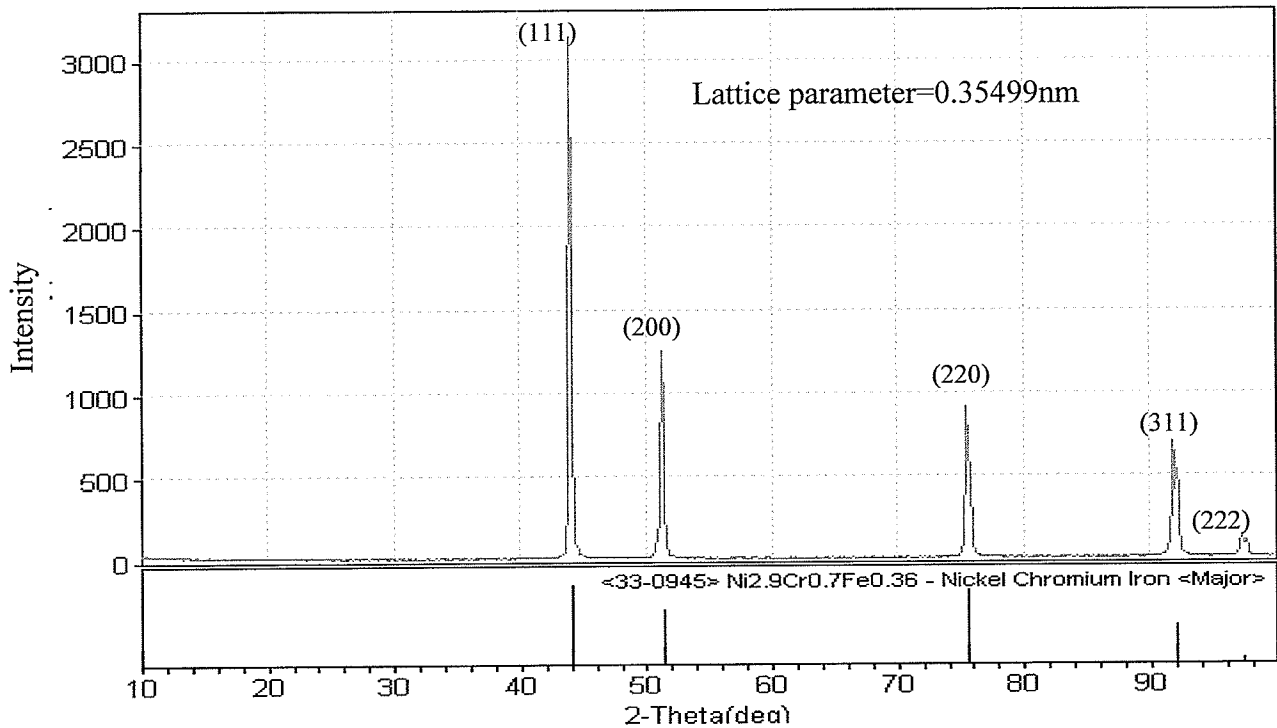


Figure 4.35c: XRD pattern of the 1w/o Al modified ternary powder after sintering

The microstructure of 1w/o Al modified Ni-Cr-Fe ternary alloy was also examined by SEM. The SEM image and results of the EDS analysis of the alloys are shown in Figure 4.35d and Table 4.7 respectively. It is observed that, as predicted by JMatPro in Figure 4.35b and as shown by the XRD analysis, there was absence of resolvable gamma prime precipitates in the microstructure. During sintering and cooling of compacts, the atoms would diffuse into each other's lattice. Al diffusion into Ni-Cr-Fe lattice is usually by a substitution mechanism which involves Al atoms taking up positions in the Ni-Cr-Fe crystal structure. This phenomenon was observed in the XRD analysis as the lattice parameter increased. In addition, since the Al content is lower

(1w/o) than that required for the formation of gamma prime precipitate, the amount of Al diffusing into the Ni-Cr-Fe ternary alloy necessary to reach the critical amount for formation of gamma prime precipitate (i.e.,  $A_3B$ ) would not be reached. Therefore, there would be no gamma prime precipitation, as was observed in the 1w/o Al modified Ni-Cr-Fe ternary alloy (Figure 4.35d) and its XRD pattern Figure 4.35c.

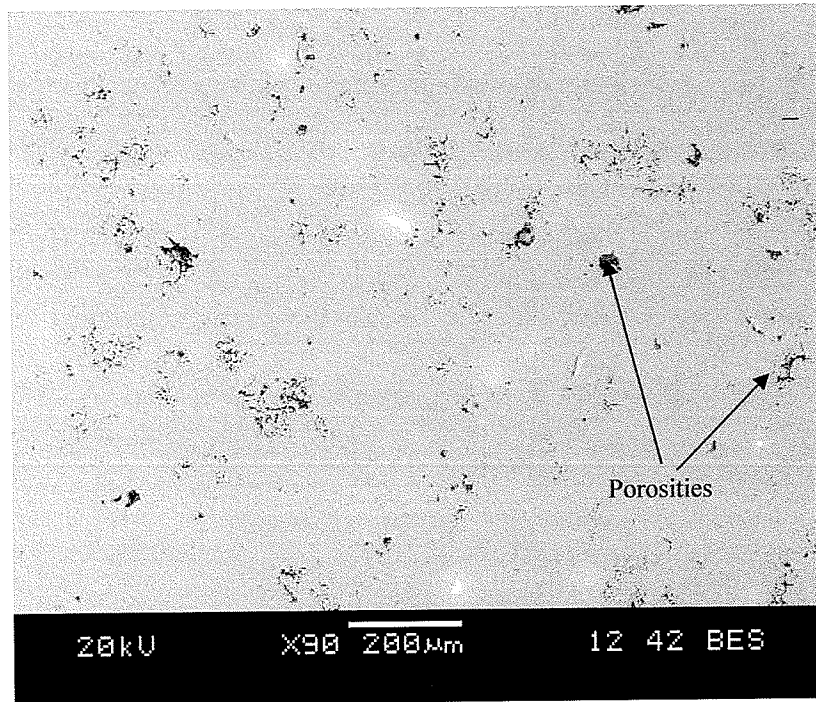


Figure 4.35d: Backscattered electron image showing the area of EDS analysis (Table 4.7) of the 1 w/o Al modified Ni-Cr-Fe alloy

Table 4.7: EDS chemical analysis of the SEM-BES image of Figure 4.35d

Element	w/o
Al	0.85
Cr	12.16
Fe	8.64
Ni	78.43

#### 4.12 3w/o Al modified ternary Ni-Cr-Fe alloy

Figures 4.36a-b show the thermodynamic predictions for the 3w/o Al modified Ni-Cr-Fe alloy. It is seen that in comparison to the predictions shown in Figures 4.35a and 4.35b, gamma prime phase was also predicted to be present in addition to  $M_{23}C_6$  and  $M_7C_3$ . However, considering the cooling profile used in this study, it is seen that at a selected transformation (assumed to be 0.5%), the cooling curve did not cut any of the three possible transformation curves (gamma prime,  $M_{23}C_6$  and  $M_7C_3$ ) indicating that they will not be present.

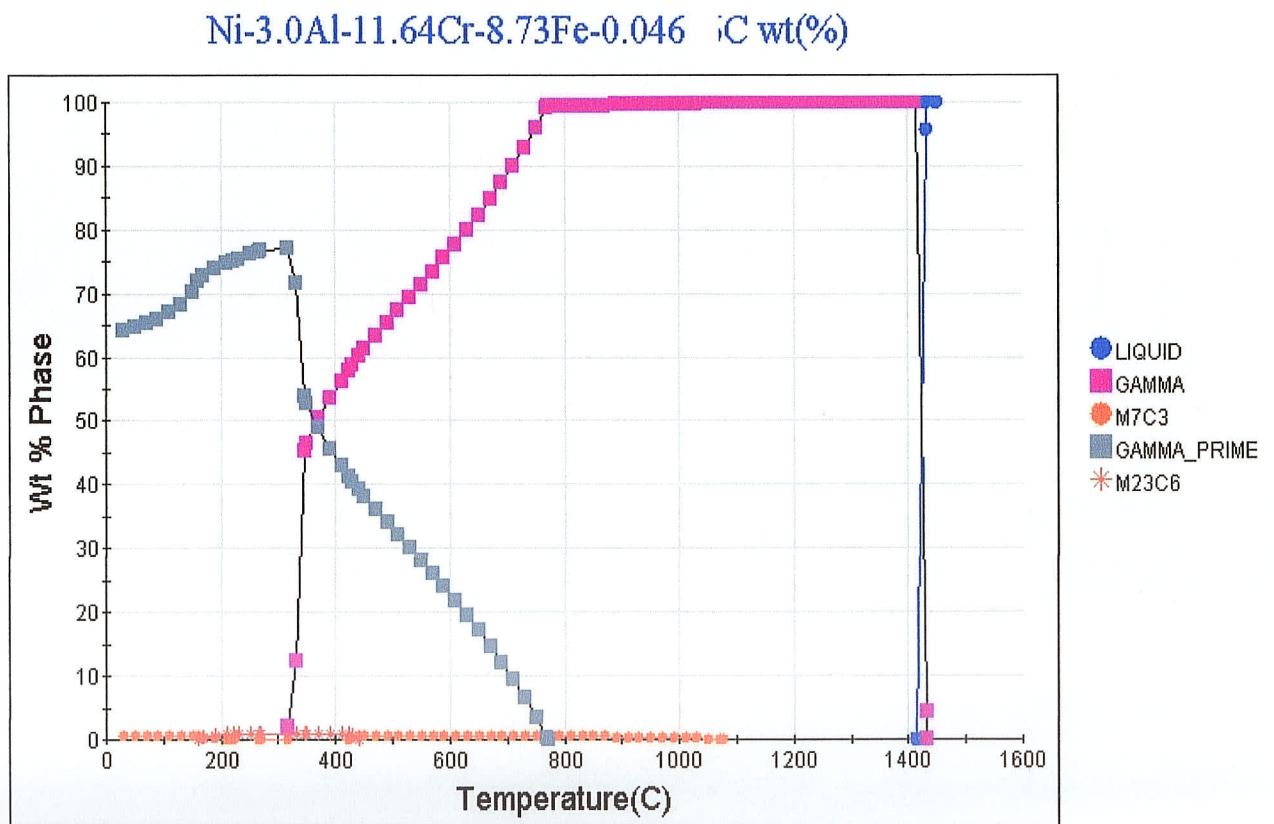


Figure 4.36a: JMatPro prediction of the phases expected to form in the 3w/o Al modified Ni-Cr-Fe ternary alloy

## CCT Nickel Based Superalloy

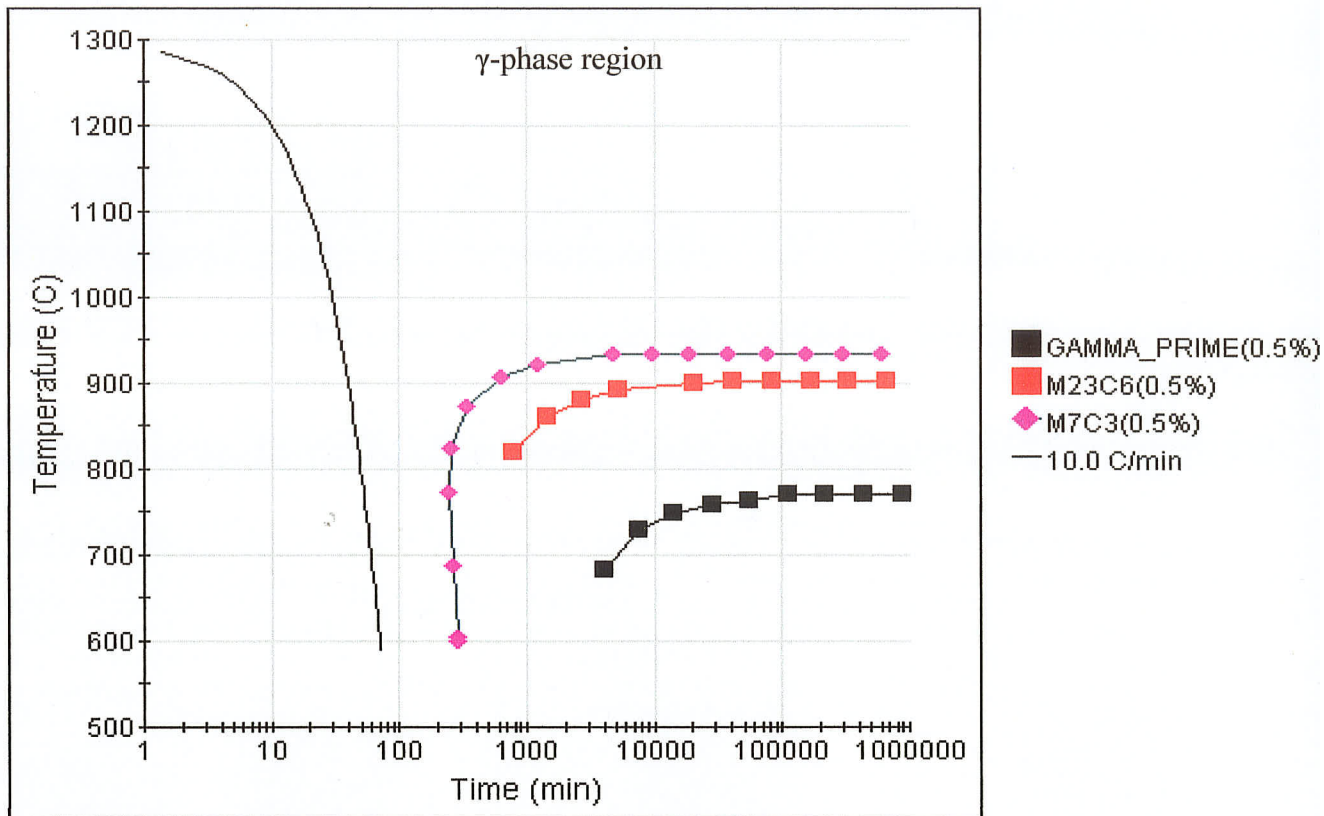


Figure 4.36b: JMatPro prediction of the CCT curve of the 3w/o Al modified Ni-Cr-Fe ternary alloy

Furthermore, as predicted by the thermodynamic software JMatPro, the XRD analysis (Figure 4.36c) did not reveal the presence of any other phases, while the lattice parameter of the alloy after being modified by 3w/o Al increased from 0.35499 nm (1w/o Al modified ternary) to 0.35551nm. In addition, gamma prime was not observed by the XRD analysis, although it was predicted to form by JMatPro. This was subsequently confirmed by the SEM/EDS analysis (Figure 4.36d) and Table 4.8. The absence of other phases can be due to the insufficient amount of Al present.

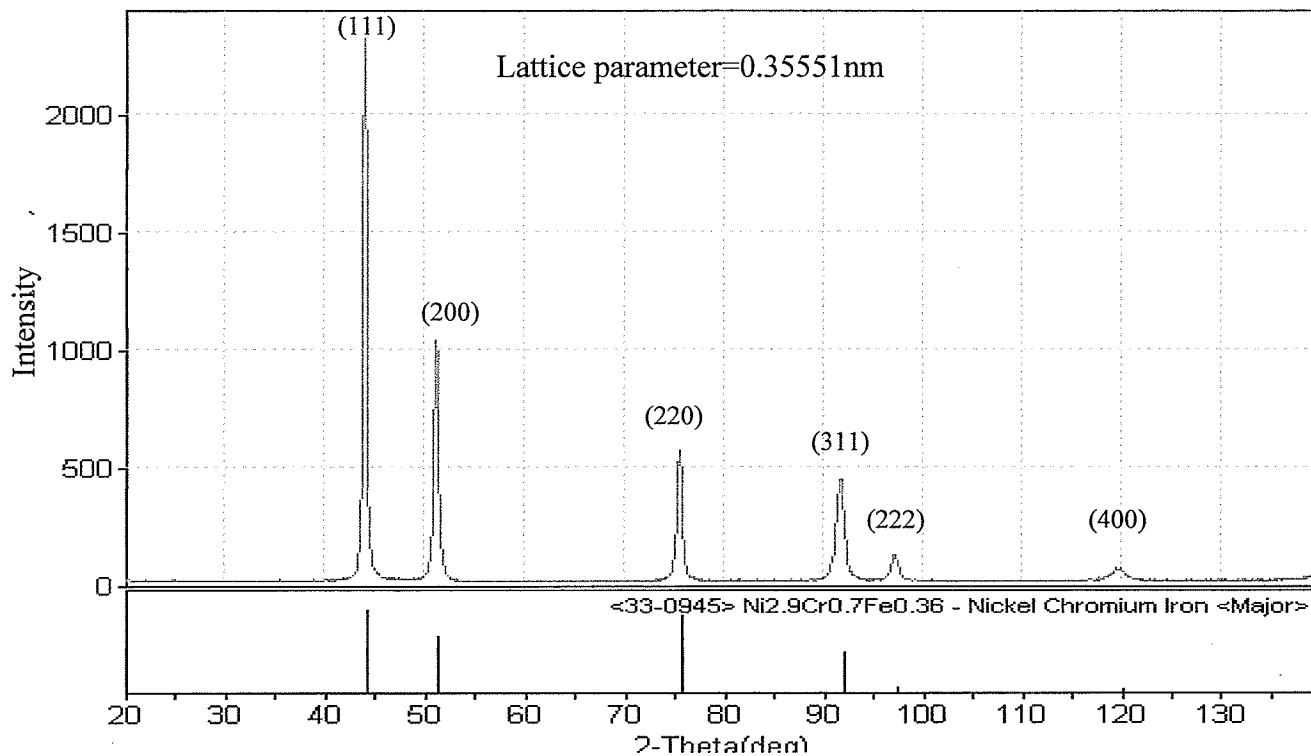


Figure 4.36c: XRD pattern of the 3w/o Al modified ternary alloy compact after sintering

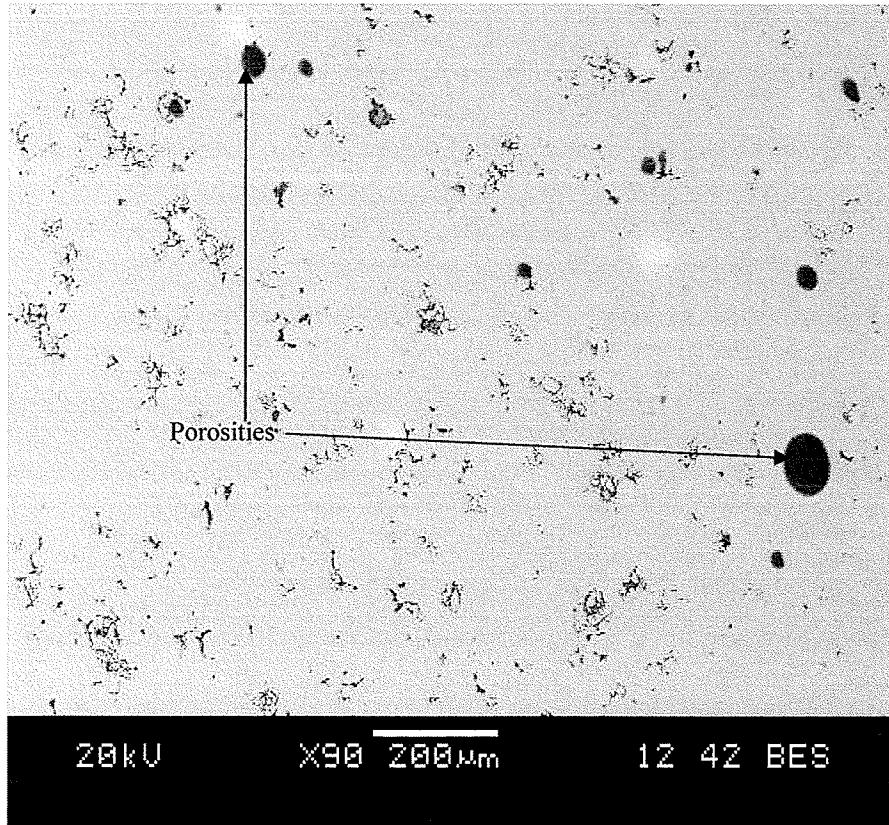


Figure 4.36d: Backscattered electron image and EDS area analysis of the 3w/o Al modified Ni-Cr-Fe alloy

Table 4.8: EDS analysis of the SEM-BES image of Figure 4.36d

Element	w/o
Al	2.51
Cr	12.58
Fe	7.95
Ni	76.95

#### 4.13 6w/o Al modified ternary Ni-Cr-Fe alloy

Figures 4.37a-c show the thermodynamic predictions for the 6w/o Al modified Ni-Cr-Fe ternary alloy. The results of the step calculation are shown in Figure 4.37a while the CCT transformation curves are shown in Figures 4.37b-c. For a detectability limit of 0.5% transformation (Figure 4.37b), the presence of gamma prime,  $M_{23}C_6$  and  $M_7C_3$  was predicted. In addition, the cooling profile that replicates the actual cooling from the sintering temperature indicates that the cooling curve cuts across 0.5% transformation curve of gamma prime,  $M_{23}C_6$  and  $M_7C_3$  phases. A series of CCT transformation curves was simulated starting from 1, 3, 5, 10, 15, 20, 25 through to, and including 30% phase detectability limit (only 20, 25 and 30% transformations are shown in Fig 4.37c). The cooling curve was also constructed. From these simulations, it is shown in Figure 4.37c that the cooling curve cuts across the 25% CCT transformation showing that based on prediction, about 25% w/o gamma prime would be present in the 6w/o Al modified Ni-Cr-Fe ternary alloy. However, when the transformation detectability limit was assumed to be more than 0.5%  $M_7C_3$  carbide was predicted not to form.

Ni-6.0Al-11.28Cr-8.46Fe-0.04512C wt(%)

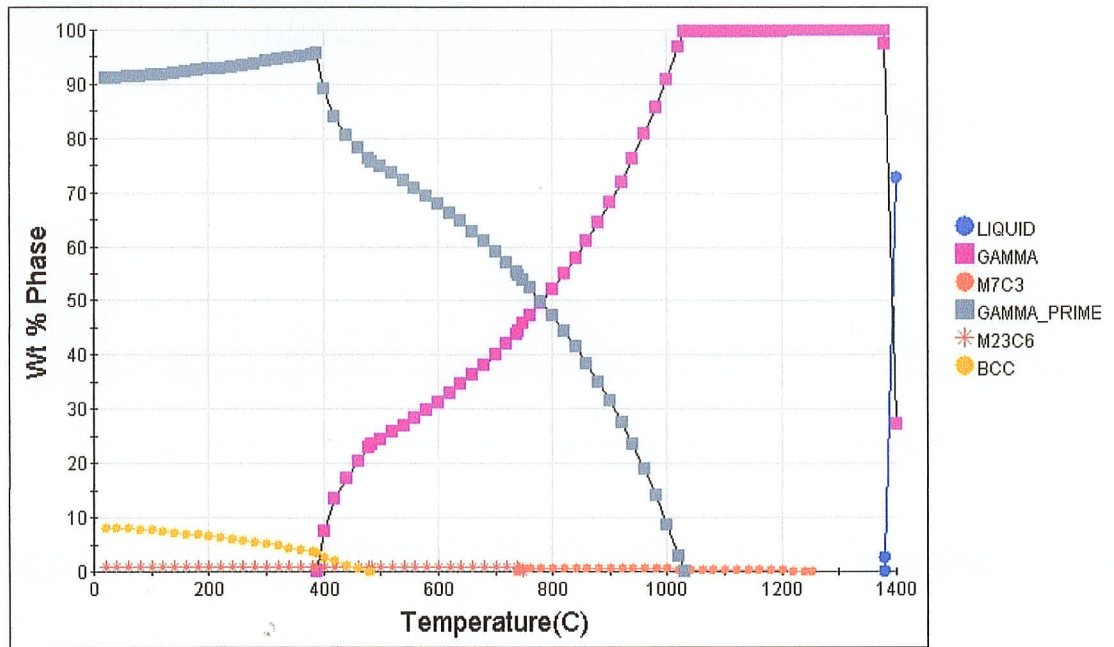


Figure 4.37a: JMatPro predictions for the 6w/o Al modified Ni-Cr-Fe ternary alloy

CCT Nickel Based Superalloy

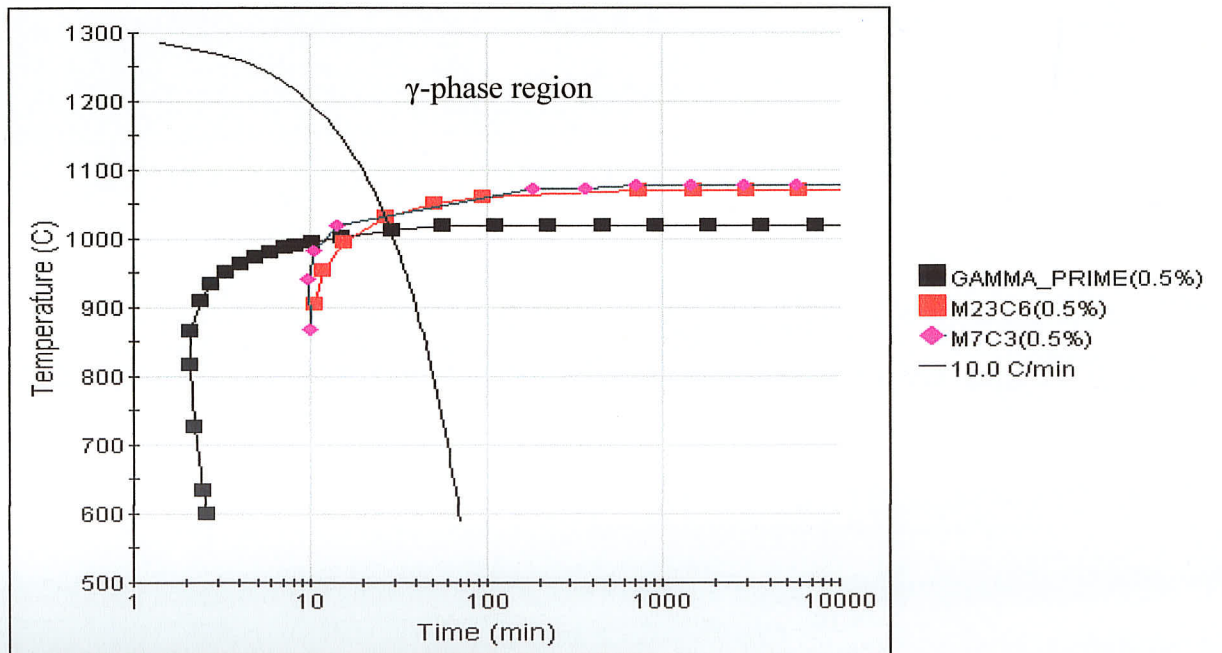


Figure 4.37b: JMatPro prediction of the CCT curve for the 6 w/o Al modified Ni-Cr-Fe ternary alloy at 0.5% transformation

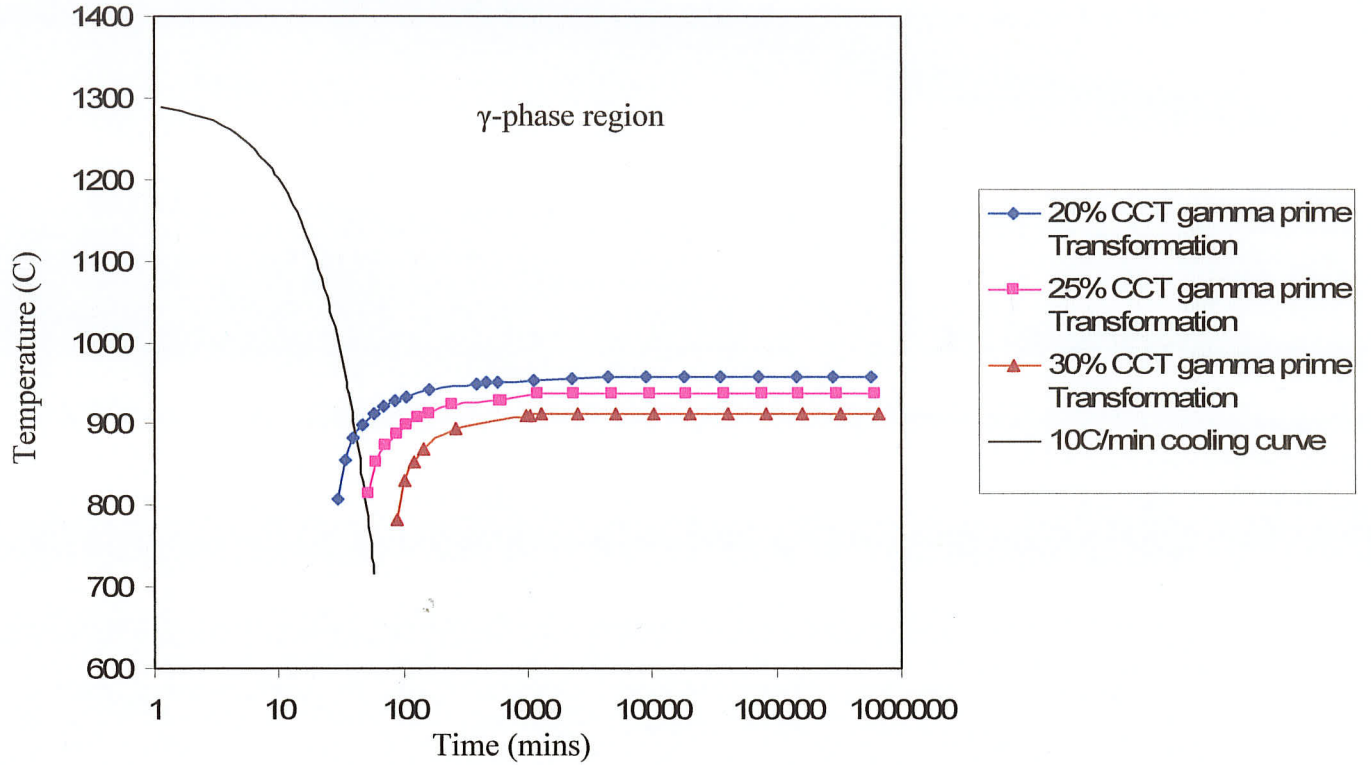


Figure 4.37c: JMatPro prediction of the CCT curve for the 6 w/o Al modified Ni-Cr-Fe ternary alloy

To verify the results of the simulation, compacts were fabricated with 6 w/o Al and sintered at 1300°C/2h and cooled at 10°C/min in vacuum (i.e., optimum conditions). EDS analysis suggested the presence of gamma prime in the compact. The SEM microstructural analysis (Figures 4.37d and 4.37e) revealed two main types of gamma prime precipitates. The first type was fine well-distributed gamma prime phase (A), whereas the other was the gamma prime phase that formed along the grain boundaries, being larger and identified as (B). The EDS chemical composition is given in Table 4.9.

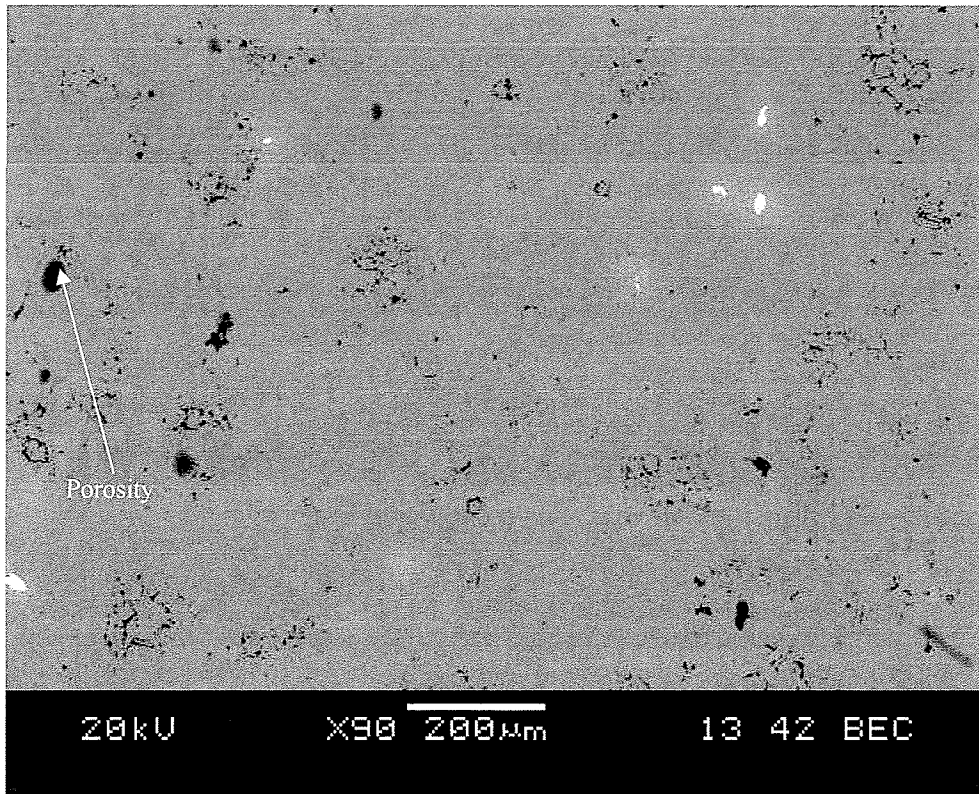


Figure 4.37d: Backscattered electron image of the 6 w/o Al modified Ni-Cr-Fe alloy

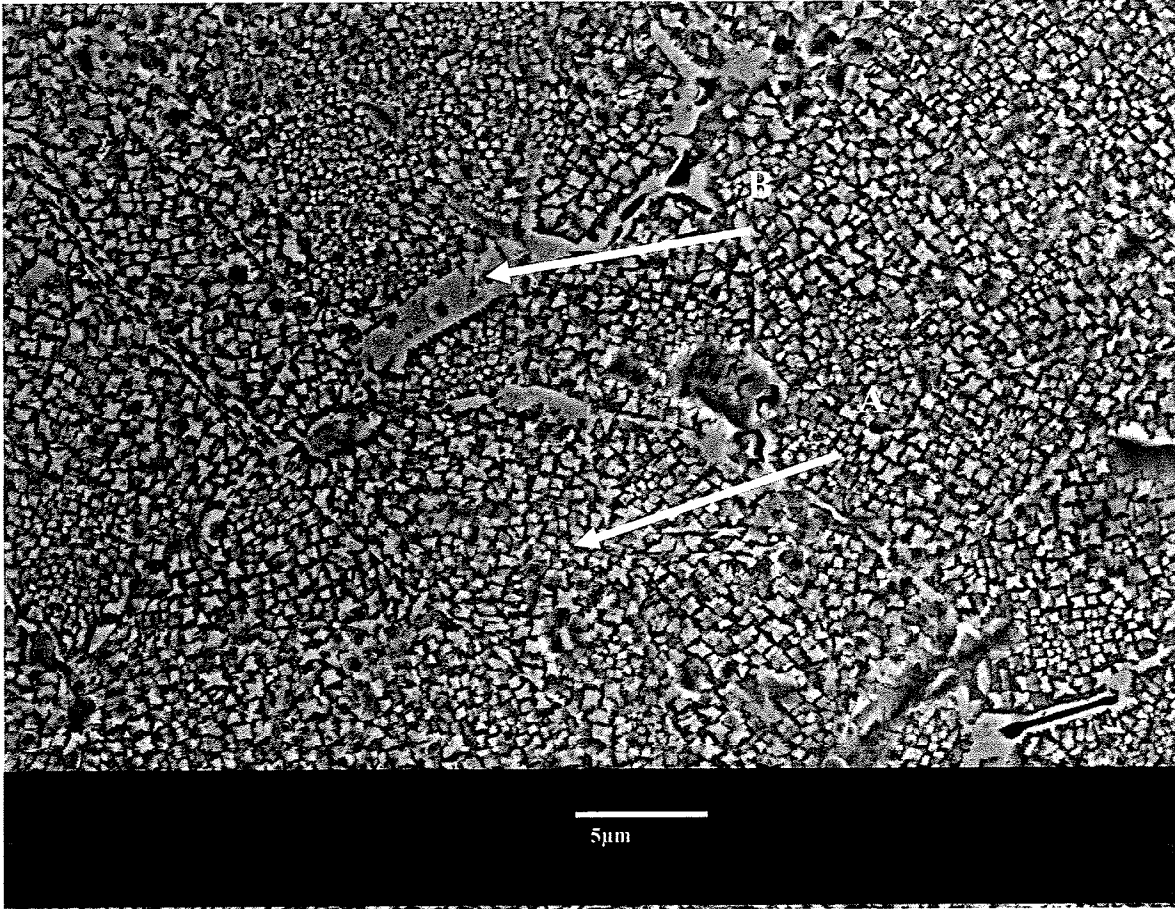


Figure 4.37e: SEI-SEM image of the as sintered 6w/o Al modified Ni-Cr-Fe ternary alloy, showing fine (A) and coarse (B) gamma prime precipitates.

Table 4.9: EDS chemical analysis of the area shown in Figure 4.37e

	Point A	Point B
Element	w/o	w/o
Al	5.9	12.8
Cr	10.6	8.7
Fe	6.0	5.2
Ni	77.5	73.3

X-ray diffraction (XRD) analysis was carried out on the as-sintered compact to identify all the phases present, to estimate their lattice parameters and to also determine

any lattice mismatch present between the gamma prime and gamma phase. Figure 4.37f shows an XRD spectrum of an as-sintered compact.

The presence of superlattice reflections, i.e., (100), (110), (210) and (211) of gamma prime phase in Figure 4.37f confirms the presence of  $\gamma'$  in the alloy as predicted by JMatPro. The lattice parameter of the  $\gamma$  phase was calculated from each of the diffraction peaks and then extrapolated to  $\theta=90$  using Bradley-Jay correction factor function (i.e.,  $\cos^2 \theta$ ). The extrapolated value of  $\gamma$  was observed to be  $0.3557 \pm 0.0005nm$ . Similarly, the diffraction peaks of  $\gamma'$  phase were used to calculate its lattice constant which was found to be  $0.3589 \pm 0.0005nm$ .

Using equation 4.6 [92] the lattice parameter mismatch,  $\delta$ , may be written as:

$$\delta = \frac{a_{\gamma'} - a_{\gamma}}{a_{\gamma}} \dots\dots\dots 4.6$$

where  $a_{\gamma'}$  is the lattice parameter of the gamma prime phase and  $a_{\gamma}$  is the lattice parameter of the gamma phase, the lattice parameter mismatch,  $\delta$ , which can be used as an indication of strength (resistance to dislocation movement), was estimated to be 0.19%. The coherency strains introduced into the crystal structure due to the formation of gamma prime, in addition its volume fraction, would enhance the strength of the sintered compact.

Vickers hardness values of the 6w/o Al modified Ni-Cr-Fe alloy were  $183 \pm 5$  as measured and 192 as predicted from JMatPro. Although the predicted value was slightly higher than the experimental values, but it is within experimental error.

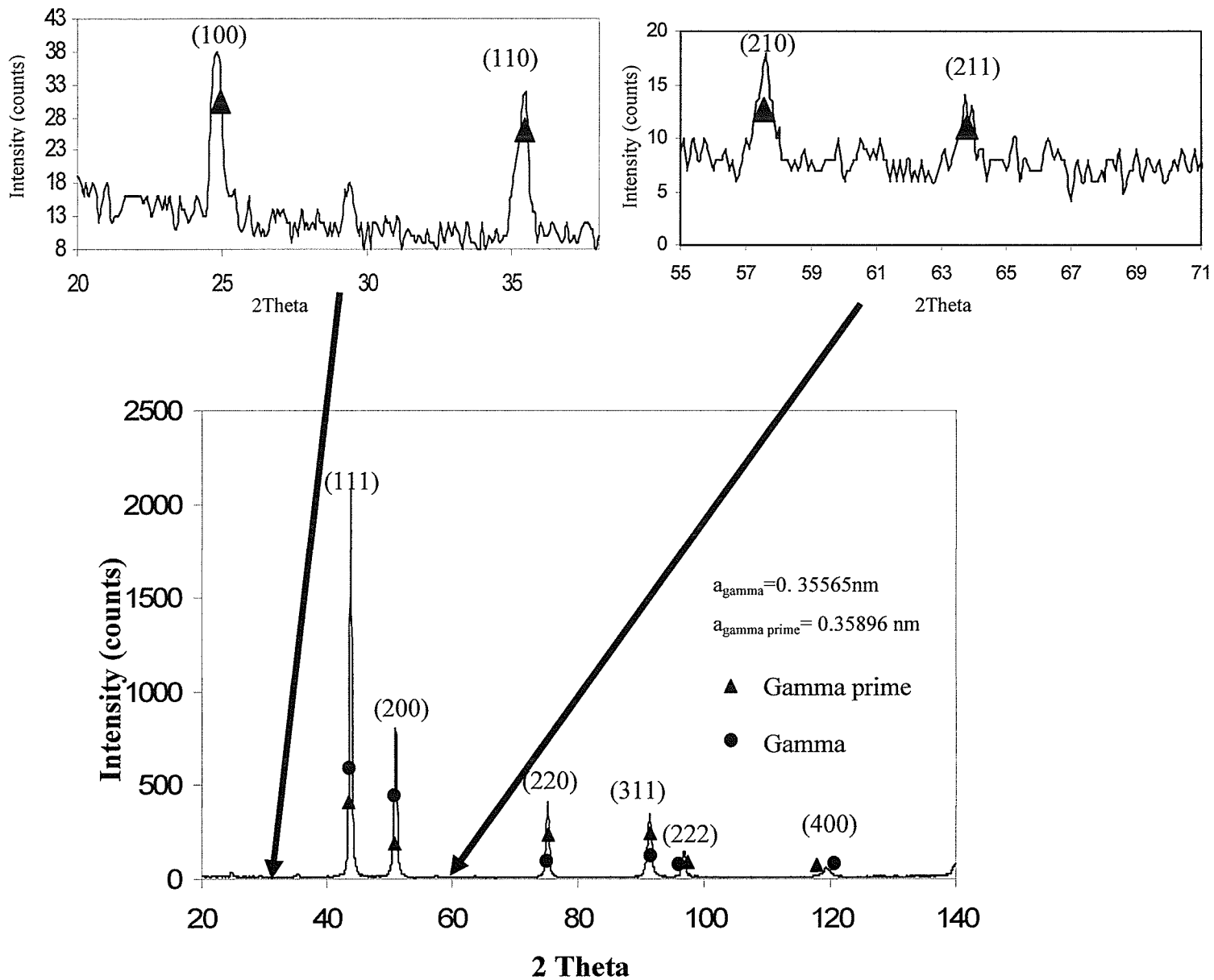


Figure 4.37f: X-ray diffractogram of the 6w/o Al modified ternary Ni-Cr-Fe alloy after sintering for 2h at 1300°C

#### 4.13.1 Analysis of the Continuous Cooling Transformation (CCT) Curves of 6w/o Al Modified Ternary alloy

The CCT curves for the 6w/o Al modified ternary predicted by the JMatPro software are shown in Figure 4.37c. JMatPro uses the following Johnson Mehl Avrami Kolmogorov equation [93] for constructing temperature-time transformation (TTT) curves.

$$f(t) = 1 - e^{(-\pi/3)NG^3t^4} \dots\dots\dots 4.7$$

where,  $f(t)$  is the fraction of a phase transformed in time  $t$ ,  $N$  is the nucleation rate and  $G$  is the growth rate. Using the Scheil's additive rule, CCT curves were then derived from the TTT curves.

Specifically, during the construction of the CCT curves of the 6w/o Al modified ternary, it was assumed that  $\gamma'$ (Ni<sub>3</sub>Al) transformation started at 0.5w/o and the completion of  $\gamma'$  occurred when all the Al in the alloy, namely 6w/o was used up to form  $\gamma'$ . If the entire Al was to be used up, then the maximum amount of  $\gamma'$  to form would be 58v/o (56w/o) and therefore, the completion of  $\gamma'$  transformation occurred at 56w/o. The cooling curve representing the cooling rate used in this study is also shown in Figure 4.37c. From the CCT curve, it is predicted that at the cooling rate used in the sintering of the compact, 25w/o (26.2v/o) of  $\gamma'$  would be produced. This means that 25w/o of the compact would transform to  $\gamma'$  and transformation will terminate at 800°C.

It is also seen in Figure 4.37e that the shape of the precipitates at the prior Al / Ni-Cr-Fe particle boundary regions of the sintered compact were blocky (A in Figure 4.37e), while within the particles  $\gamma'$  precipitates were fine and relatively homogenously

distributed (B in Figure 4.37e). The average size of the blocky precipitates was calculated to be approximately  $0.8\mu\text{m}$  (Figure 4.37e). To determine the cause of the formation of blocky  $\gamma'$  at the boundaries and fine  $\gamma'$  within the grain, a previously sintered sample was heated to  $1200^\circ\text{C}$ , held for 4h and quenched in water. This was done so as to dissolve all the precipitated phases and to also determine the Al concentration in the sintered product. Figure 4.37g shows an EDS-XRD line scan across the interface between the prior Al particle location, where Al is observed to be segregated.

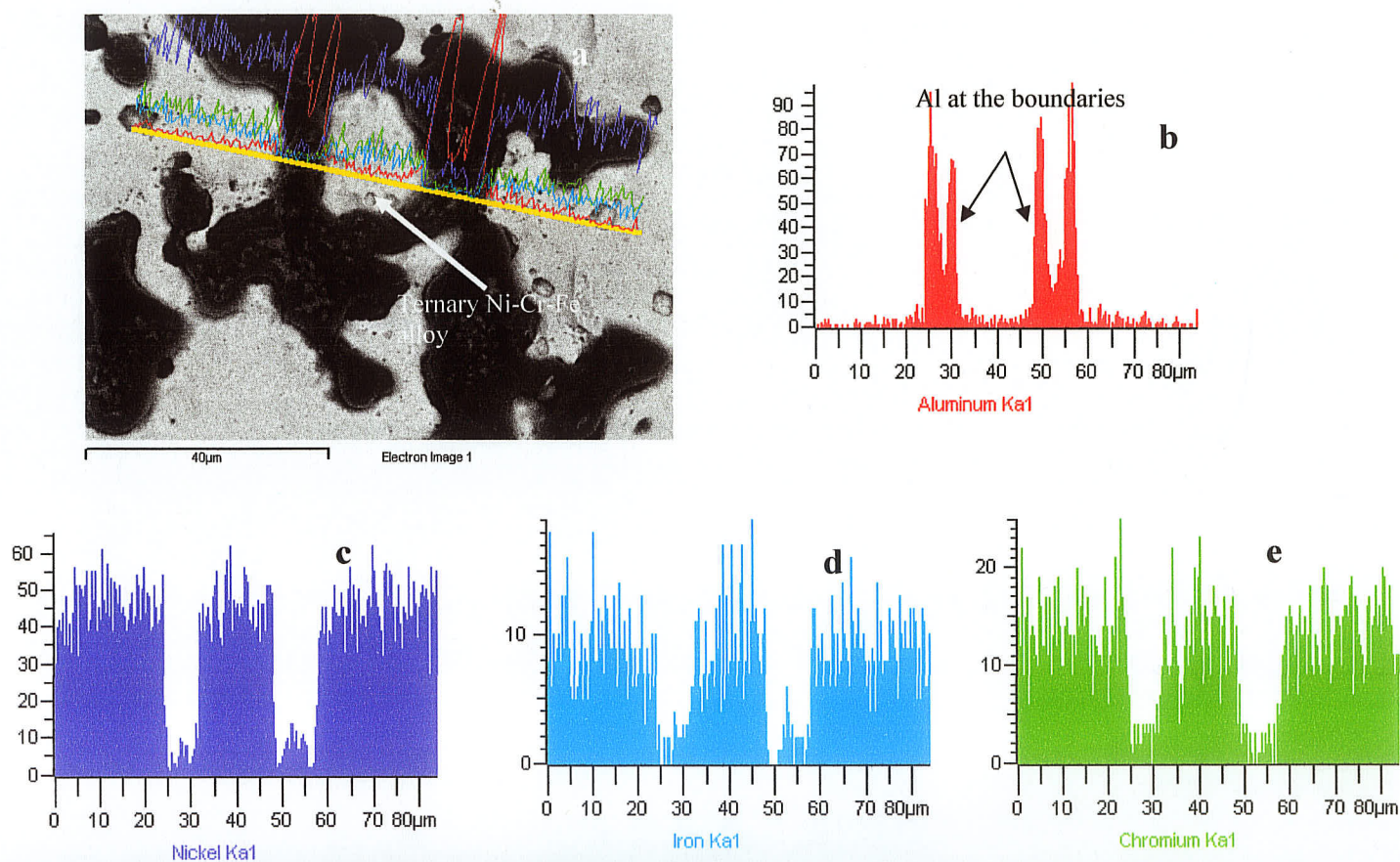


Figure 4.37g: SEM EDS line scan of the interface between Al and ternary Ni-Cr-Fe alloy after sintering, reheating to  $1200^\circ\text{C}$  for 4h and quenching. a) SEM-SEI image; b) Al elemental scan, c) Ni elemental scan; d) Fe elemental scan and e) Cr elemental scan

It can be seen from Figure 4.37c that the weight fraction of  $\gamma$  phase was predicted by JMatPro to be 25w/o (26.2v/o). However, the image analysis of the microstructure of the as-sintered compact showed that the amount of gamma prime formed was in the range of  $62 \pm 5$ v/o. To verify the relationship between cooling rate and  $\gamma'$  transformed a different green compact was heated to the sintering temperature and cooled at a much lower heating rate ( $2.5^\circ\text{C}/\text{min}$ ). The corresponding transformation curves are shown in Figure 4.37h.

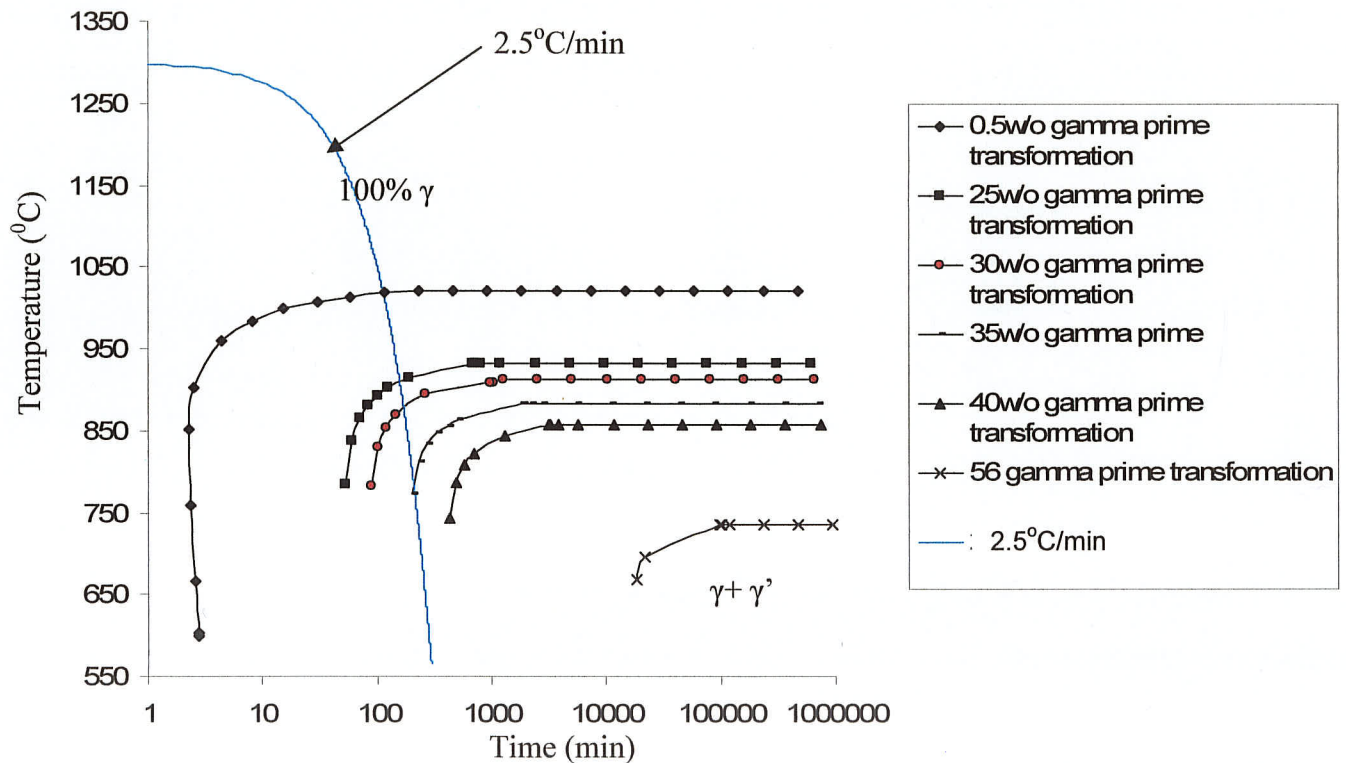


Figure 4.37h: JMatPro CCT curves for the 6w/o Al modified ternary Ni-Cr-Fe alloy showing the gamma prime transformation curves based on the  $2.5^\circ\text{C}/\text{min}$  cooling rate

Here in Figure 4.37h it can be seen that during the  $2.5^{\circ}\text{C}/\text{min}$  cooling, the cooling curve cuts across the 35w/o fraction of the gamma prime transformation curve whereas the corresponding value for the  $10^{\circ}\text{C}/\text{min}$  was 25w/o.

SEM image analysis was carried out to examine the microstructure of the  $2.5^{\circ}\text{C}/\text{min}$  cooled sample and an SEI-SEM is shown in Figure 4.37i. The image analysis showed that despite the slower cooling rate, the volume fraction of  $\gamma'$  present in the compact was 60v/o similar to that observed in a specimen that was cooled at  $10^{\circ}\text{C}/\text{min}$  but the size of the precipitates was slightly larger at  $1.0\text{-}1.2\mu\text{m}$ .

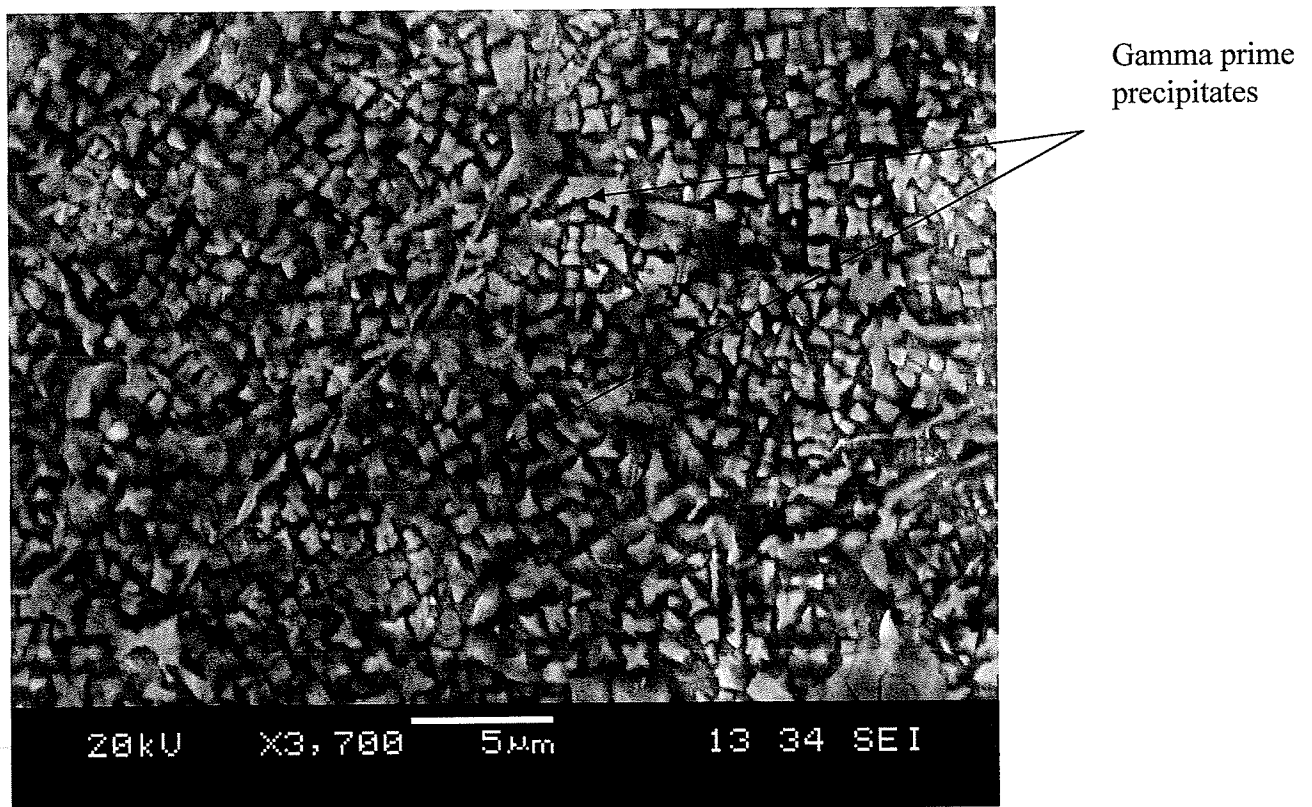


Figure 4.37i: SEM image of the 6w/o Al modified ternary Ni-Cr-Fe alloy after cooling from the sintering temperature at  $2.5^{\circ}\text{C}/\text{min}$

The DSC trace of the specimen on cooling at 2.5°C/min from the sintering temperature (1300 °C) to room temperature is shown in Figure 4.37j. A transformation is seen to occur at 1041±5°C, which is comparable with the JMatPro prediction for the start of  $\gamma'$  transformation of 1090-1029 °C (Figure 4.37a).

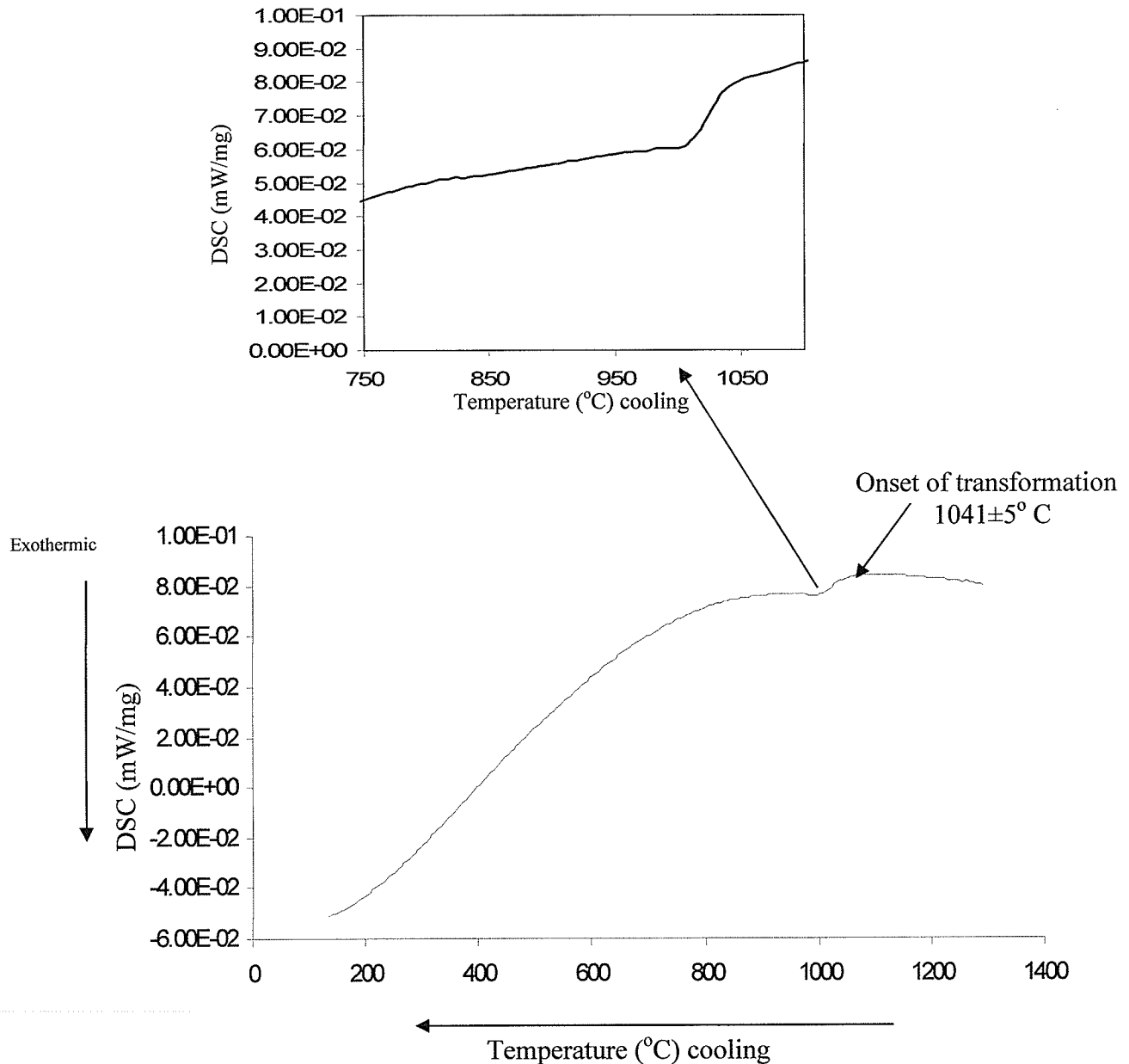


Figure 4.37j: DSC trace of the quaternary (6w/o Al modified ternary Ni-Cr-Fe alloy) as it was cooled from the sintering temperature to room temperature. The onset of  $\gamma'$  transformation is noted.

#### **4.13.2 Discussion of the phase transformation on cooling of 6w/o Al modified ternary alloy**

The phase diagram is an important tool for metallurgists as it allows prediction of the amount of phases that are or can be present in an alloy at equilibrium. The tool used in the present study uses a CALPHAD approach to predict both the phase(s) present and other thermodynamic properties.

A CCT curve was used to predict the phases that would be present and their compositions in a powder compact of 6w/o Al modified ternary (quaternary) alloy. The maximum amount of gamma prime that could form in the compact was estimated to be 56w/o (60v/o) using an atomic number ratio approach. Using the 10°C/mins cooling condition, the cooling curve was seen to intersect the 25w/o (26.2v/o) of gamma prime transformation curve (Figure 4.37c). However, image analysis (Figure 4.37e) revealed that the volume fraction of gamma prime in the compact to be about 60v/o. To verify if the prediction was valid for the v/o observed, another compact was heated and cooled at 2.5°C /min (Figure 4.37i). The image analysis revealed that the v/o of the gamma prime was again similar (60v/o) to the 10°C/min sample i.e., the actual volume fraction observed in the specimen was higher than the predicted value.

The formation of larger quantity of  $\gamma'$  may be related to the processing conditions experienced by the compacts. In particular, the high compacting pressure (500MPa) used to compact the powders prior to sintering may cause the green compact to be deformed resulting in more lattice defects; these can cause significant increase in diffusion rate. In addition, the presence of numerous boundaries [94], low wetting angle of Al on Ni-Cr-Fe ternary particles and the fact that liquid that forms during heating would allow effective

spreading/interaction around the boundaries of ternary particles. This may have increased the concentration of Al in the alloy at the boundaries which could increase the precipitation rate of  $\gamma'$  and its volume fraction in the compact.

Porosity was also observed in the sintered product. The porosity was caused by the melting of the Al and subsequent wetting of the ternary thereby increasing the surface to volume ratio of the Al leaving pores in the compact (Figure 4.37d).

The preferential enrichment of Al at the boundaries is noted in Figure 4.37g. The SEM analysis revealed that the shape of gamma prime was irregular and they were relatively larger at the grain boundaries while those within the grains were finer (Figure 4.37e). This gamma prime morphology may be related to the transformation kinetics of the gamma prime precipitates. As the compact is cooled from the sintering temperature, a temperature would be reached where  $\gamma$  starts to transform to  $\gamma'$ . This temperature according to JMatPro should be in the range of 1090-1029°C. This was subsequently evaluated by DSC, Figure 4.37j, and the transformation temperature was seen to be  $1041 \pm 5^\circ\text{C}$ .

The precipitation reaction would have started at the interparticle grain boundaries where the concentration of Al was higher (Figure 4.37g(b)). As the nuclei form at the grain boundaries, they would continue to grow into precipitates. However, since the composition of Al at the grain boundary was higher than within the grains, the degree of undercooling needed for  $\gamma'$  to form in the grains would be lower, while the particles that form at the boundaries would continue to grow and increase in size as cooling continues until a temperature is reached at which no further diffusion can occur.

Subsequently, since the temperature for transformation of  $\gamma$  to  $\gamma'$  at the grain boundaries is reached before the transformation of  $\gamma$  to  $\gamma'$  within the grains, there would be a shorter time available for growth of the precipitates within the grains after they have formed. Therefore, the  $\gamma'$  precipitates formed at the particle boundaries were observed to be larger than those within the interior of the particles.

#### 4.14 12w/o Al modified ternary Ni-Cr-Fe alloy

Figures 4.38a-b show the thermodynamic predictions for the 12w/o Al modified Ni-Cr-Fe ternary alloy. Figure 4.38c is the SEM backscattered image, while Figure 4.38d is the XRD pattern of the 12w/o Al modified Ni-Cr-Fe alloy. In Figure 4.38c, it is seen that the formation of phases in 12w/o Al modified Ni-Cr-Fe was not uniform. Around each Ni-Cr-Fe ternary alloy phase, gamma prime is non-uniformly distributed. Also, Figure 4.38d suggests the presence of intermetallics such as NiAl, Ni<sub>3</sub>Al and Ni-Cr-Fe as predicted by the thermodynamic software.

One of the goals of this research was to optimize the amount of gamma prime precipitates in the compact and to also select a compact with homogeneous distribution of second phase without segregation or presence of undesirable microstructure.

The 0.5% transformation detectability curves predicted gamma prime and sigma phase to be present. While gamma prime phase is an ordered phase coherent with the gamma matrix and is the desired phase, sigma phase on the other hand is a plate-like phase. Its presence in Superalloys results in lowered rupture strength and ductility. A typical composition of sigma phase is (Cr, Mo)<sub>x</sub>(Ni, Co)<sub>y</sub>, where x and y can vary from 1 to 7 [20]. Sigma ( $\sigma$ ) phase forms at the grain boundaries where the concentration of elements critical to its formation such as Cr is abundant. The cell structure of either  $\sigma$ ,  $\mu$  and Laves phases are characterized by close-packed layers of atoms with layers separated by relatively large inter-atomic distances. They possess a topologically close-packed structure, hence they are termed TCP phases. Conversely A<sub>3</sub>B-type  $\gamma'$  compounds close packed in all directions are characterized as geometrically close-packed phase (GCP).

Furthermore,  $\sigma$  is structurally related closely to  $M_{23}C_6$  carbide that forms in many nickel-base alloys. The removal of carbon atoms from an  $M_{23}C_6$  lattice results into a shift in atom-to-atom dimension yielding the  $\sigma$  structure. That is, decarburization of  $\sigma$  prone  $M_{23}C_6$  leads to  $\sigma$  formation, while carburization results into elimination of  $\sigma$  phase.  $\mu$  phase has a close structural resemblance to  $M_6C$ . Excessive concentration of Mo and Cr leads to the formation of  $\mu$  rather than  $\sigma$ . Hence, alloys that are susceptible to the formation of  $M_{23}C_6$  can also form  $\sigma$  in them if conditions are favorable, while alloys that form  $M_6C$  tend to form  $\mu$  phase.  $\sigma$  precipitation occurs on carbide particles, whereas,  $\gamma'$  does not contribute to  $\sigma$  formation.

Hence, in this study, the prediction of the presence of sigma phase by JMatPro coupled with the possibility of forming TCP phase(Figure 4.38b) did not encourage the use of 12w/o Al modified ternary Ni-Cr-Fe composition. Also, the precipitate ( $Ni_3Al$ ) that formed in the 12w/o Al modified sample was not homogenously distributed. Therefore, subsequent calculations and further studies were not carried out on the 12 w/o Al modified Ni-Cr-Fe ternary alloy.

Ni-12.0Al-11.64Cr-8.73Fe-0.04656C wt(%)

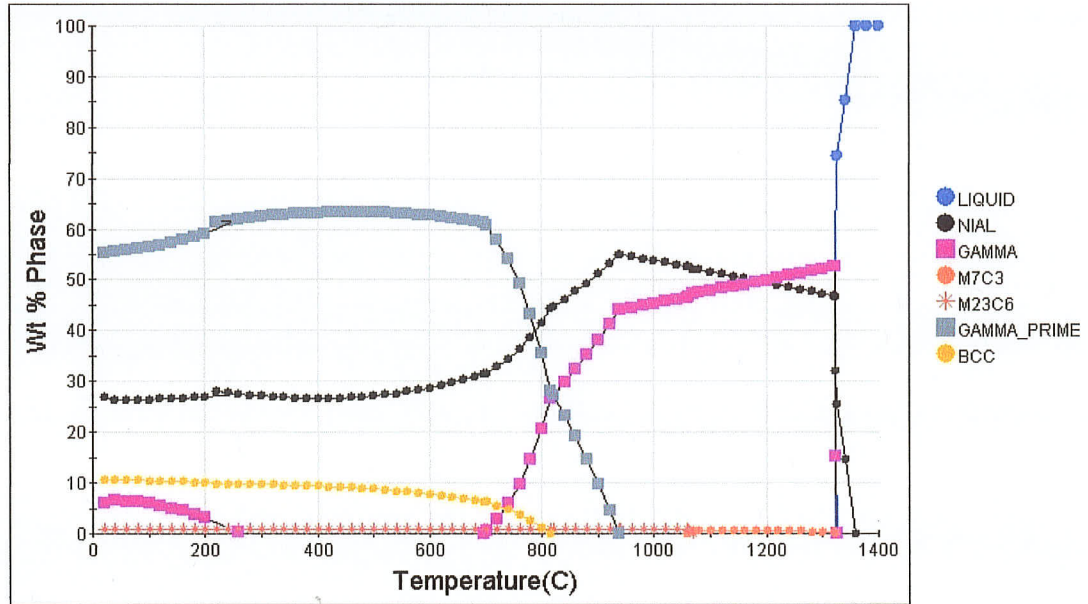


Figure 4.38a: JMatPro prediction of phase likely to form in 12 w/o Al modified Ni-Cr-Fe ternary alloy

CCT Nickel Based Superalloy

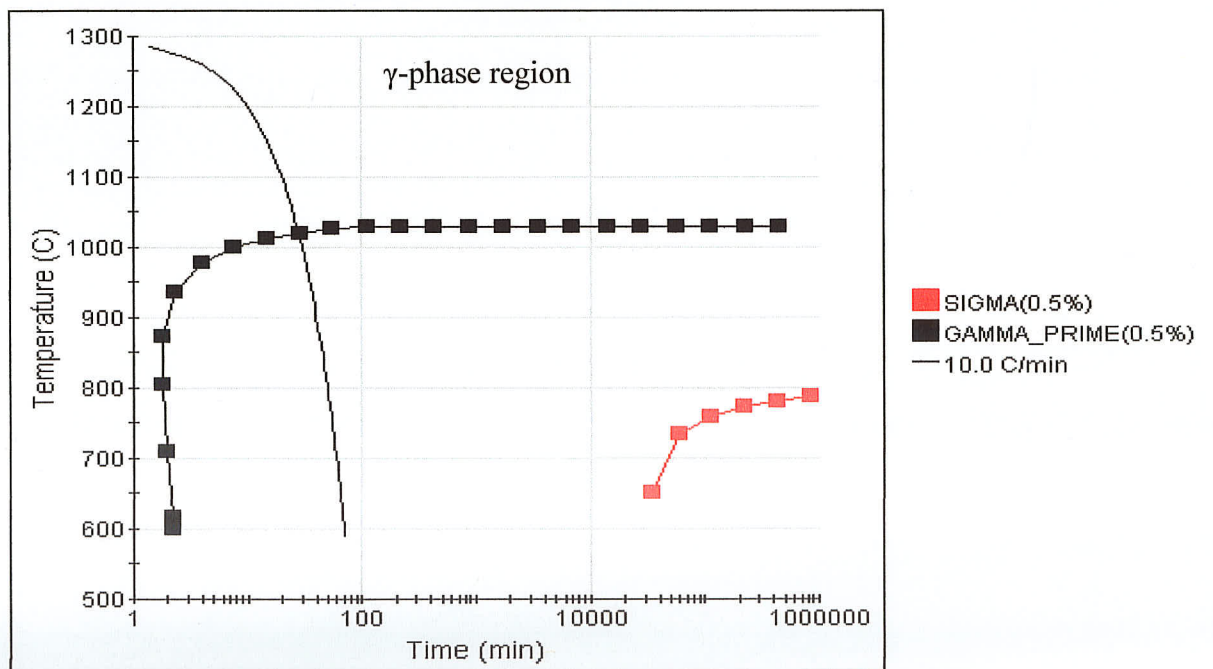


Figure 4.38b: JMatPro prediction of the 0.5% phase detectability limit curve for the 12 w/o Al modified Ni-Cr-Fe ternary alloy

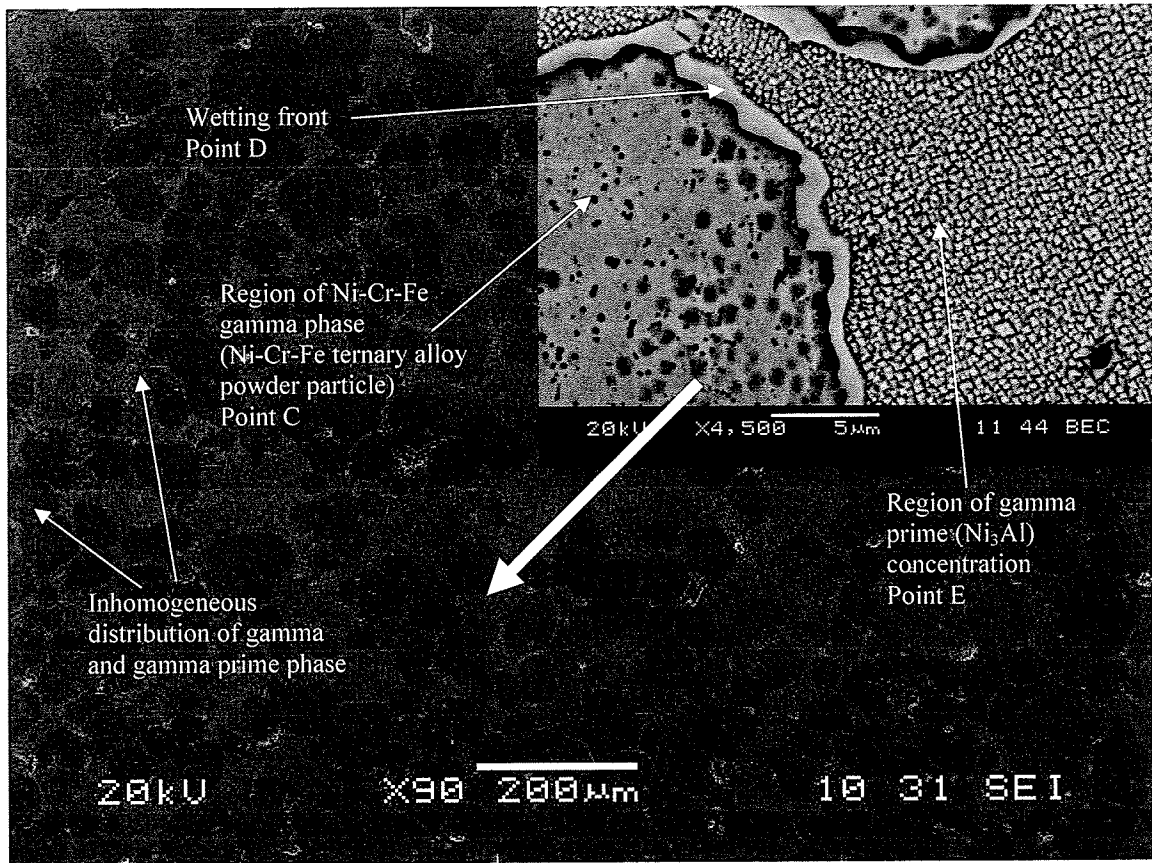


Figure 4.38c: Backscattered electron image of the 12 w/o Al modified Ni-Cr-Fe alloy sinter for 2h at 1300°C.

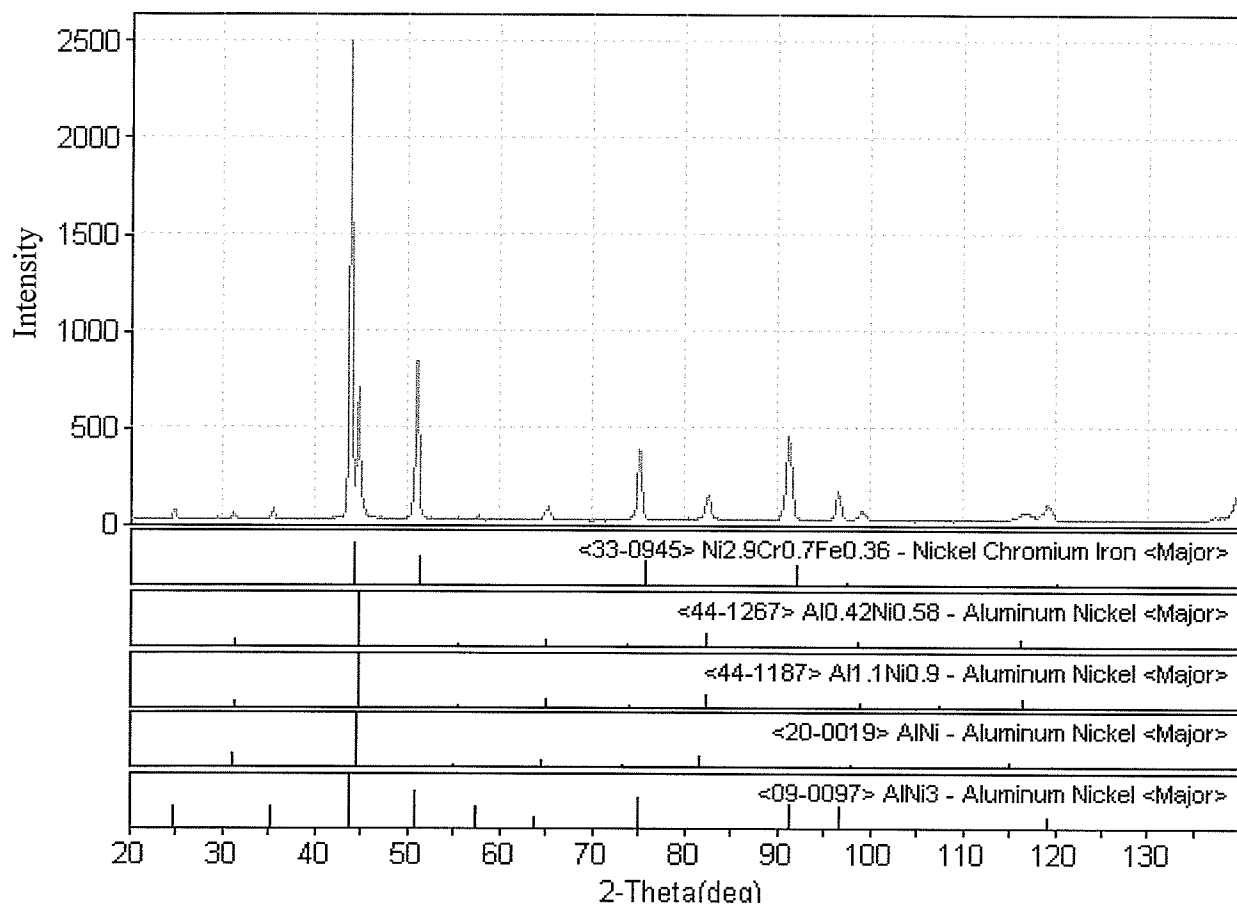


Figure 4.38d: XRD pattern and analysis of the 12w/o Al modified ternary powder after sintering

#### 4.15.1 Differential scanning calorimetry (DSC)/scanning electron microscopy SEM

Alloys produced by powder metallurgy (P/M) are capable of producing near net shape components with a fine grain microstructure. In a P/M process, either individual metal or pre-alloyed powders are mixed and compacted to produce a near net-shape component. This green compact is then heated to the sintering temperature to produce a near net-shape finished component. During powder mixing, reaction may or may not occur. In some cases reaction(s) that occur are spontaneous giving out significant amount of heat, while other reactions need to be thermally activated. A differential scanning calorimeter can be used for measuring heat flow and other thermo-physical properties of such reactions.

In this study, because of the relatively homogenous microstructural distribution of gamma prime phase and gamma phase in the 6w/o Al modified ternary relative to other compositions (1, 3, and 12w/o Al modified ternary), the 6w/oAl modified composition was considered to be the optimum blend. During heating of a Ni-Cr-Fe plus 6w/oAl compact to the sintering temperature, Al and the ternary powders would interact with each other forming different types of intermetallics that could be based on the binary Ni-Al, Fe-Cr, Al-Fe, Al-Cr, Ni-Cr, or Fe-Ni, ternary and quaternary systems based on Ni, Cr, Fe and Al depending on the thermodynamic and kinetic conditions for their formation being favorable.

To understand the sintering mechanism when Ni-Cr-Fe and Al powders are reacted, it is essential to understand the type and sequence of reactions that take place, especially as Al melts well before the sintering temperature of 1300<sup>0</sup>C is reached.

Therefore, the type/nature of reactions and phases that form at various temperatures during sintering were investigated by DSC and characterized by SEM with EDS capability, and XRD. The experimental techniques were described in chapter 3 of this thesis.

The DSC and SEM-EDS techniques were used to determine the temperature and sequence of formation of various intermetallics on heating the 6 w/o Al-modified Ni-Cr-Fe ternary alloy to 1300°C i.e., the sintering temperature. In a DSC spectrum, a deviation from linearity is an indication of a possible reaction and the magnitude of deviation depends on the extent of the reaction [14, 95]. As seen in Figure 4.39, at a heating rate of 10°C/min a major exothermic peak was evident with the onset of the reaction at about  $570 \pm 5^\circ\text{C}$  (Point X1 stage 1) and exothermic peak at  $626 \pm 5^\circ\text{C}$  (Point X2 stage 2). On continued heating, the DSC spectrum indicated the occurrence of an endothermic reaction in the range 790-860°C (stage 3, Figure 4.39) and another small exothermic reaction at about 900°C. Further heating (Stage 4) showed no evidence of any other reaction taking place.

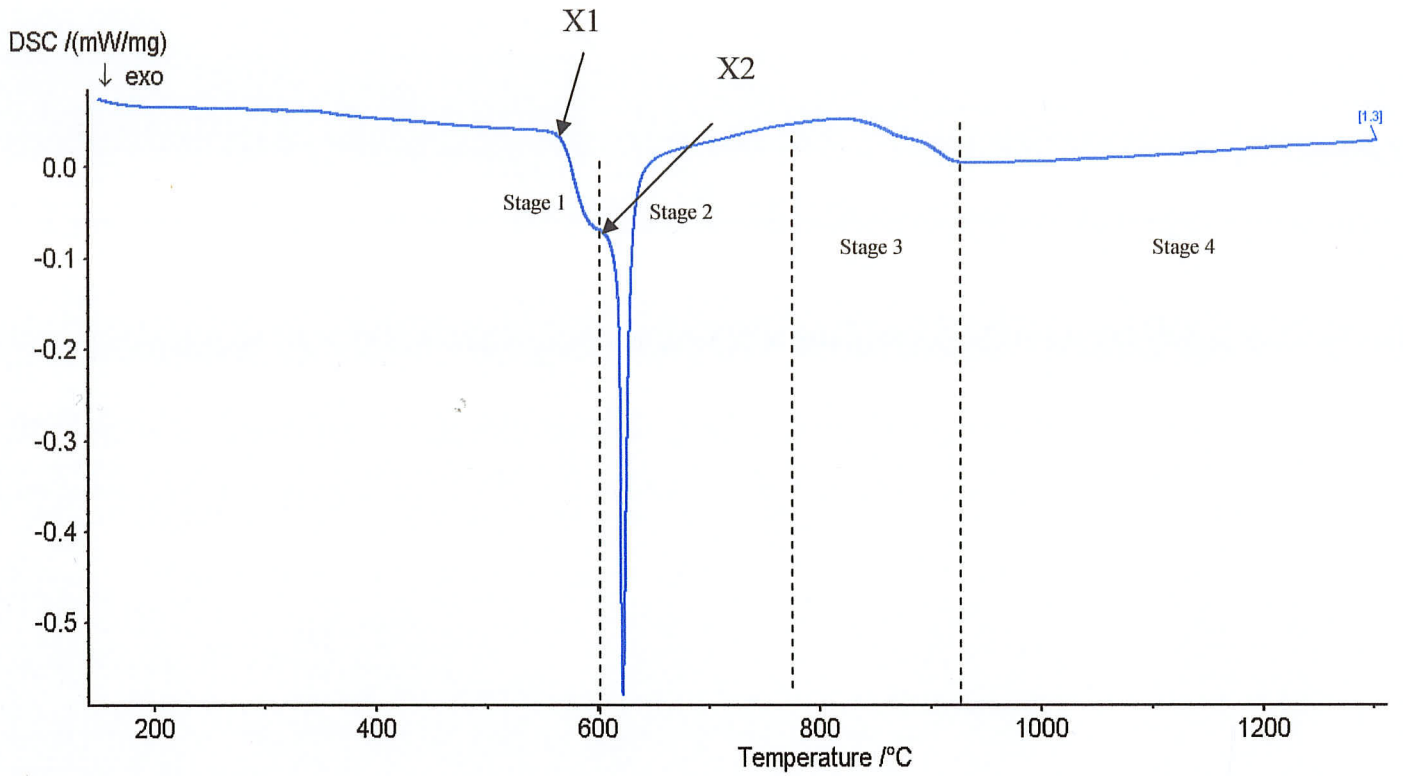


Figure 4.39: DSC trace of the 6w/o Al modified ternary Ni-Cr-Fe alloy at 10°C/min up to the melting temperature { X1 is onset of exothermic reaction for stage 1 and X2 is the onset of exothermic reaction peak for stage 2 }

Figure 4.40 is a DSC spectrum of the 6 w/o Al modified Ni-Cr-Fe compact heated at a slower heating rate of 2.5°C/min. This was done to attempt to detect any peak that might not have been observed during the 10°C/min heating. As seen, two exothermic peaks were observed in the temperature range of 500-640°C, the first at  $566 \pm 5^\circ\text{C}$  (Point a) and the second at  $634 \pm 5^\circ\text{C}$  (Point b), where Y1 and Y2 represent the onset of the main exothermic reactions, respectively. These observations suggest that the stage 1 in Figure 4.38 represents two exotherms that could only be resolved by decreasing the heating rate to 2.5°C. The spectrum in Figure 4.40 also shows the occurrence of other reactions at  $791 \pm 5^\circ\text{C}$  (Point c) endothermic,  $830 \pm 5^\circ\text{C}$  (Point d) exothermic,  $880.0 \pm 5^\circ\text{C}$  (Point e) exothermic, and  $1120.1 \pm 5^\circ\text{C}$  (Point f) exothermic. Several exo/endothermic reactions are seen to occur whose temperatures of occurrence are better delineated in the differential DSC curve shown in Figure 4.41. Subsequently, to characterize microstructural changes that may be occurring at these temperatures of interest, six green samples were heated to Points (a) through to (f) of Figure 4.40 and quenched in argon.

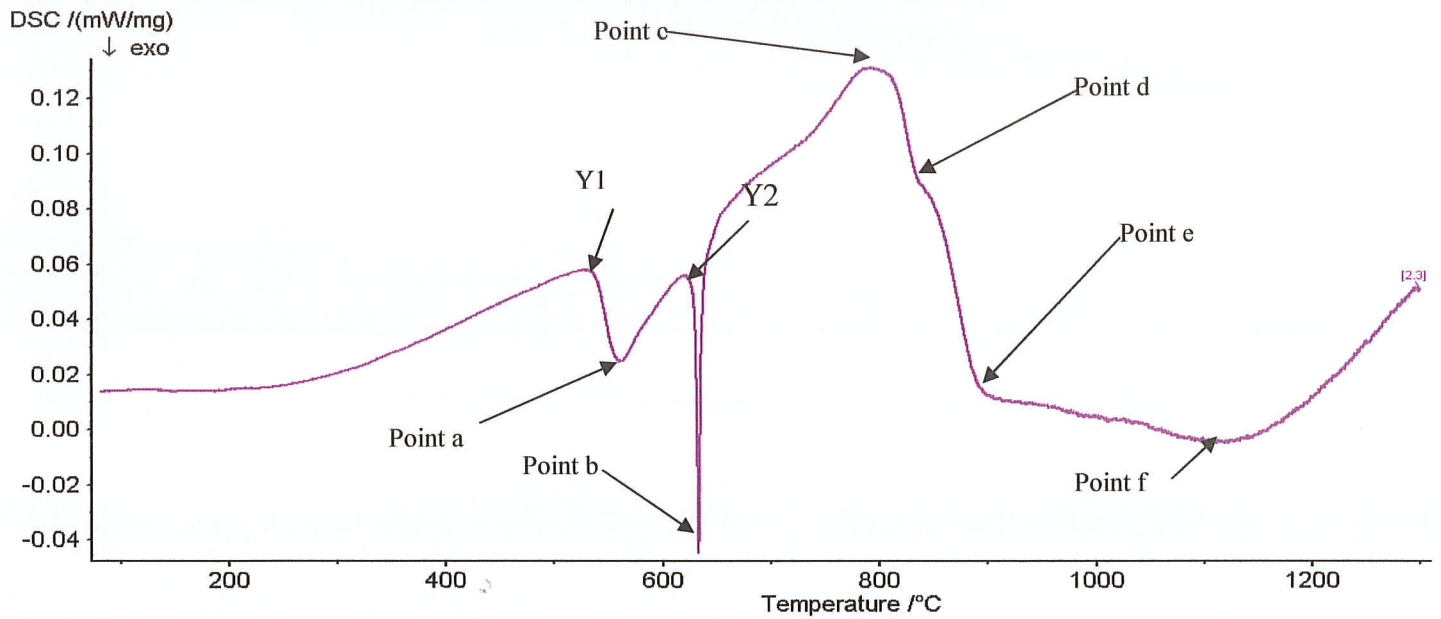


Figure 4.40 DSC trace of the 6w/o Al modified ternary Ni-Cr-Fe alloy at 2.5°C/min up to the sintering temperature (1300°C) {Y1 is onset of first exothermic reaction peak and Y2 is the onset of the second exothermic reaction peak}

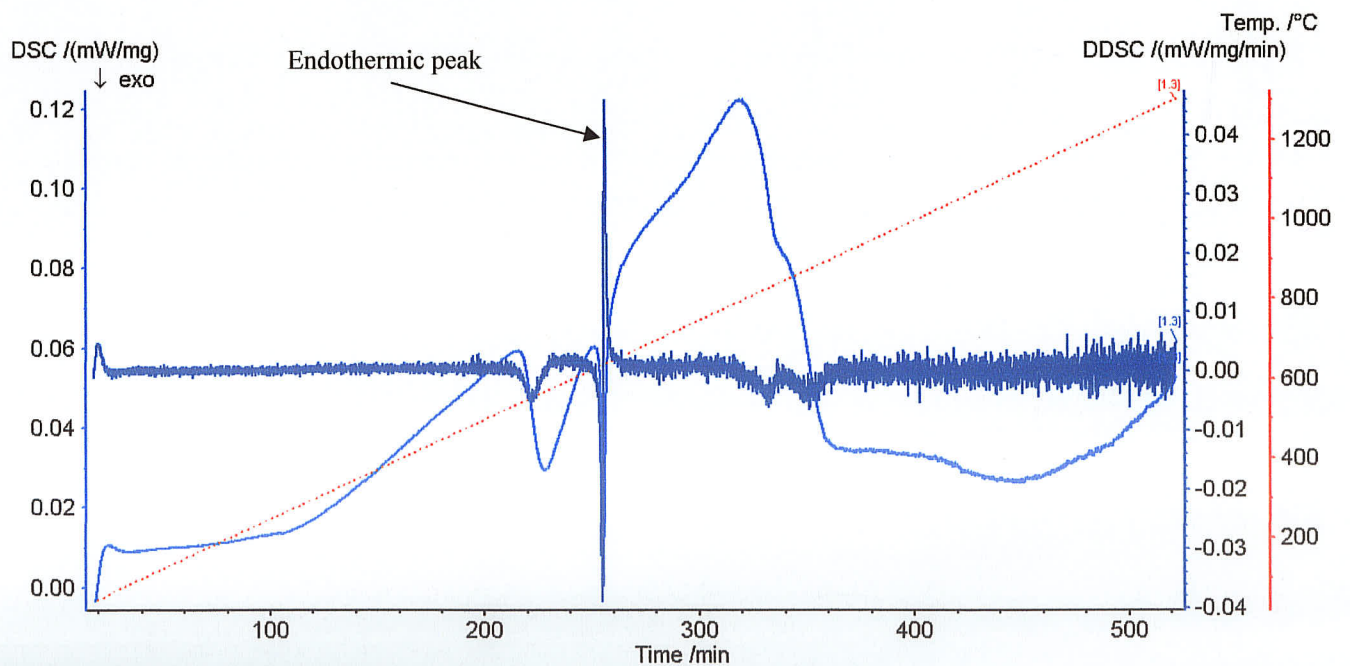


Figure 4.41: The differential DSC trace of the 6w/o Al modified ternary Ni-Cr-Fe alloy at 2.5°C/min up to the sintering temperature (1300°C)

#### 4.15.1.1 SEM/EDS analysis of the DSC sample argon-quenched from 560°C

The SEM image of the 560°C sample (i.e., sample argon-quenched from point a in Figure 4.40) along with X-ray line scans to analyze Al, Ni, Cr and Fe are given in Figure 4.42. The inset in Figure 4.42a represents the line scan trajectory and the numbers refer to the location where the EDS point analysis was done. The results are shown in Table 4.10. Al migration into the ternary particles is indicated by the presence of grey level contrast based on atomic number, in Figure 4.42a. This is confirmed by the X-ray line scans in Figures 4.42b-e that indicate the presence of various intermetallics (Figure 4.42b, c, d and e). Typical EDS analyses of the intermetallics, marked as Points 1, 2, and 4 in Figure 4.42a, are given in Table 4.10. It is seen that among the constituents of the ternary powder, the interaction of Ni with Al was most pronounced. For example,  $\text{Al}_{0.48}\text{Ni}_{0.52}$  (AlNi) and  $\text{Al}_{0.7}\text{Ni}_{0.3}$  ( $\text{Al}_3\text{Ni}$ ) intermetallics were observed and the location of  $\text{Al}_{0.7}\text{Ni}_{0.3}$  was closer to the initial Al particle than that of the  $\text{Al}_{0.48}\text{Ni}_{0.52}$  intermetallic as the concentration of Al decreased into the ternary particle. The presence of other unreacted starting constituents such as Ni-Cr-Fe, Ni-Cr, Fe, Ni-Fe and Al was also observed by EDS analysis.

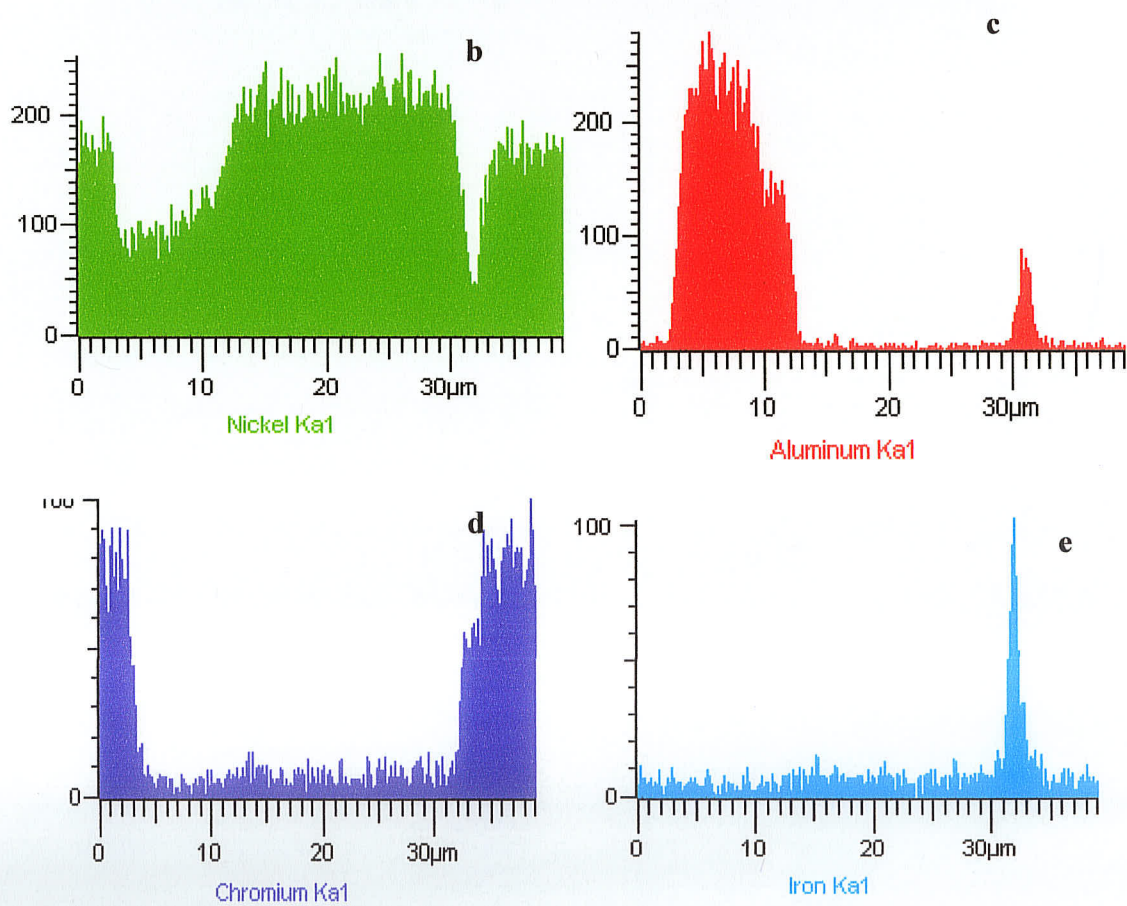
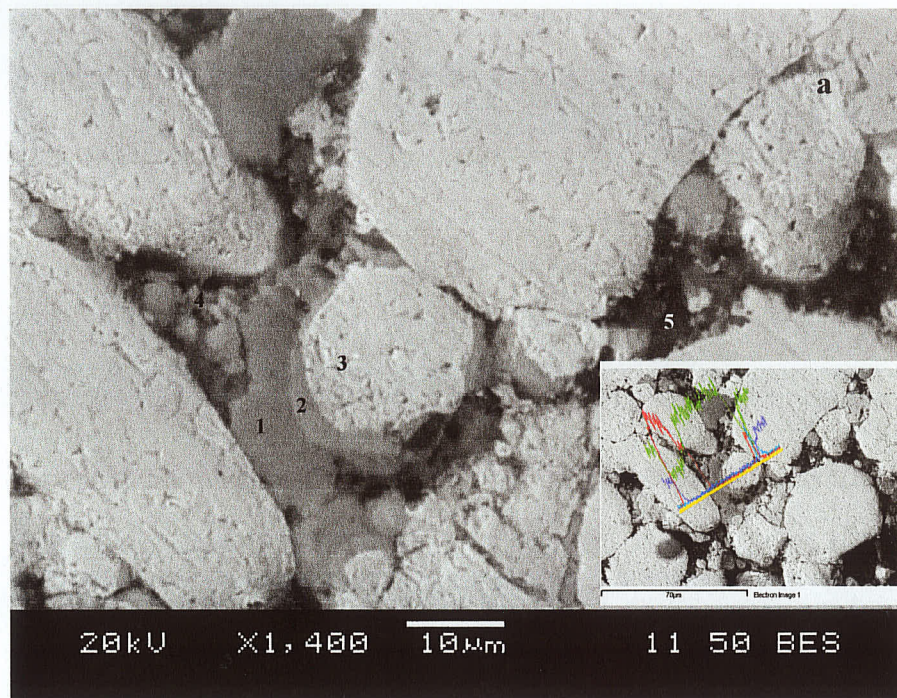


Figure 4.42: SEM BSE Image showing the points of EDS analyses (a) and EDS line scans for b)Ni, c)Al, d)Cr and e)Fe of the sample heated to 560°C and argon-quenched

Table 4.10: EDS analysis of the quaternary compact after quenching from 560°C

Element	Atomic%	Atomic%	Atomic%	Atomic%	Atomic%	Fe, Ni, Ni-Cr-Fe, and Al were also present
	Point 1	Point 2	Point 3	Point 4	Point 5	
Al	68.8	47.6	0.0	63.8	100.0	
Cr	0.3	0.4	20.8	0.3	0.0	
Fe	0.3	0.3	0.0	12.8	0.0	
Ni	30.6	51.7	79.2	23.1	0.0	

#### 4.15.1.2 SEM/BSE analysis of the DSC sample argon-quenched from 640°C

Figure 4.43 shows the SEM-BSE image and line scans of the sample argon-quenched from 640°C (i.e., point b in Figure 4.40). The inset in Figure 4.43a shows the line scan trajectory. The SEM-BSE images showed an atomic number contrast of the reaction products as seen in Figure 4.43a. The EDS line scans suggested that their composition was different than that of the phases observed at 560°C (Figure 4.42), and that the prior Al location no longer contained pure Al, and more enrichment of Al into the ternary particle was noticed. The EDS analysis, Table 4.11 shows that various types of  $Al_xNi_y$  type intermetallics formed. In addition to this, EDS analysis revealed the presence of  $Al_xFe_y$  type intermetallics. It was also observed that various intermetallics formed closer to where an Al particle had contacted the ternary alloy powder particle rather than inside the ternary particle. This suggested that once an intermetallic formed, at the surface of the ternary particles, additional Al did not diffuse through the ternary to continue the reaction. The composition of the intermetallics was observed to be close to  $Al_3Ni_2$  (Points 4 and 7),  $AlNi$  (Point 1), and  $Al_3Fe$  (Point 3) intermetallics. The presence of Fe, Ni-Cr-Fe, Ni and Ni-Cr was also confirmed.

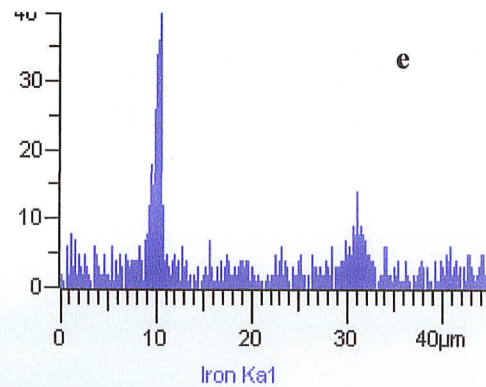
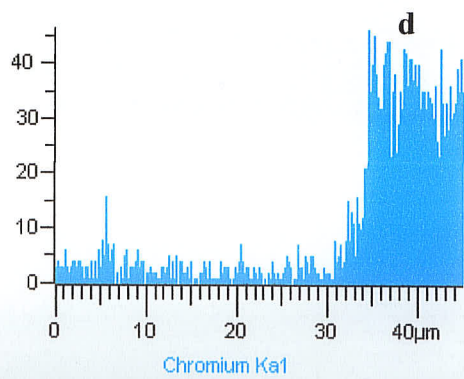
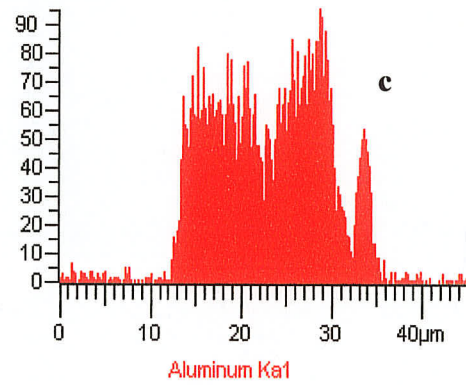
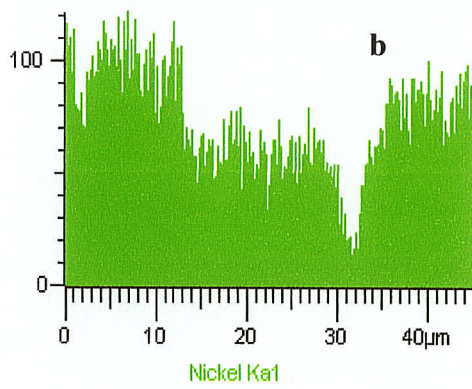
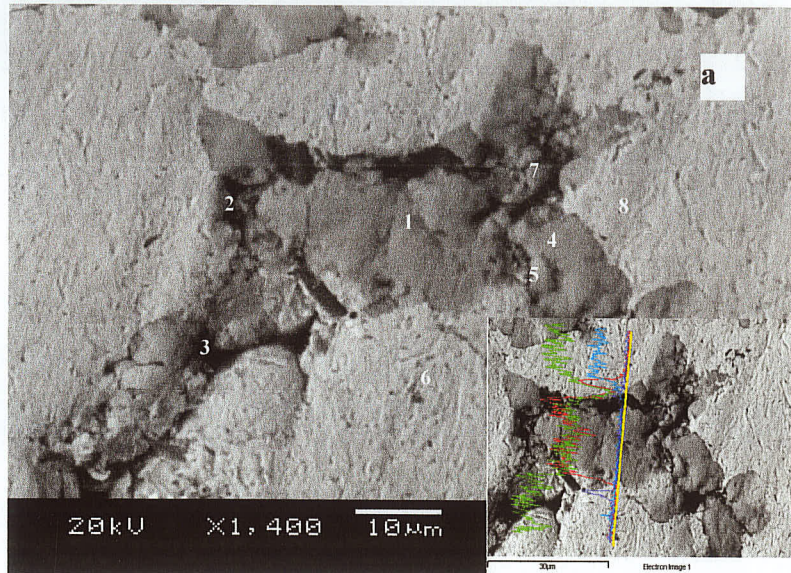


Figure 4.43: SEM BSE Image showing the points of EDS analyses (a) and EDS line scans for b)Ni, c)Al, d)Cr and e)Fe of the sample heated to 640°C and quenched

Table 4.11: EDS analysis of the quaternary compact after heating to 640°C and quenched

Element	Atomic% Point 1	Atomic% Point 2	Atomic% Point 3	Atomic% Point 4	Atomic% Point 5	Atomic% Point 6	Atomic% Point 7	Atomic% Point 8	Fe, Ni- Cr-Fe, Ni were also present
Al	51.8	23.1	74.1	56.8	56.1	1.1	61.8	0.4	
Cr	0.2	0.0	0.0	0.0	0.0	0.3	1.1	18.6	
Fe	0.3	59.9	19.9	1.0	0.8	0.4	0.9	0.0	
Ni	47.7	17.1	6.0	42.2	43.1	98.2	36.2	81.0	

#### 4.15.1.3 SEM/EDS analysis of the DSC sample argon-quenched from 790°C

Figure 4.44 shows the SEM-BSE image and the corresponding points of EDS analysis and EDS line scans of the sample heated to 790°C, where an endothermic reaction was observed (point c in Figure 4.40). The insert in Figure 4.44a represents the line scan trajectory. The darker atomic contrast in Figure 4.44a at a number of locations suggests that enrichment of ternary particles by Al has increased. This is also corroborated by X-ray line scan (Figures 4.44b-e) and the EDS analysis. For example, the EDS analyses at points 2, 3, and 4, given in Table 4.12, indicate compositions that correspond to Fe-Al based intermetallics seen in the 640°C sample. In addition, there was evidence of presence of AlNi phase (Point 5) along with a phase whose composition was closer to Ni<sub>3</sub>Al<sub>2</sub> intermetallic (Point 6).

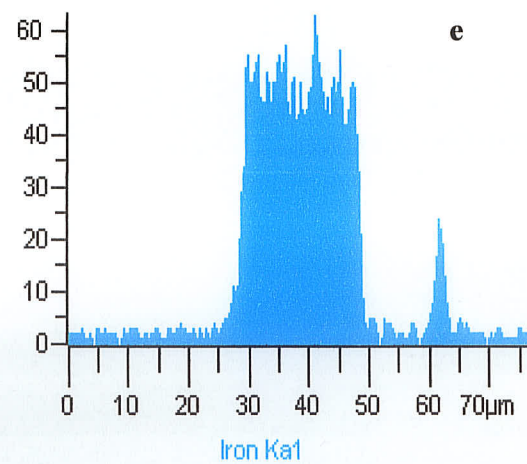
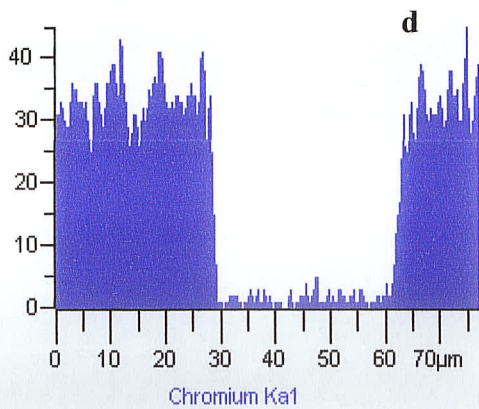
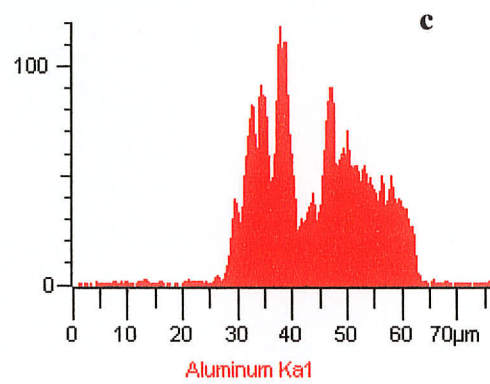
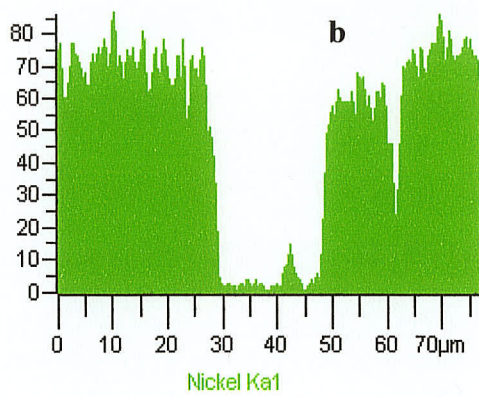
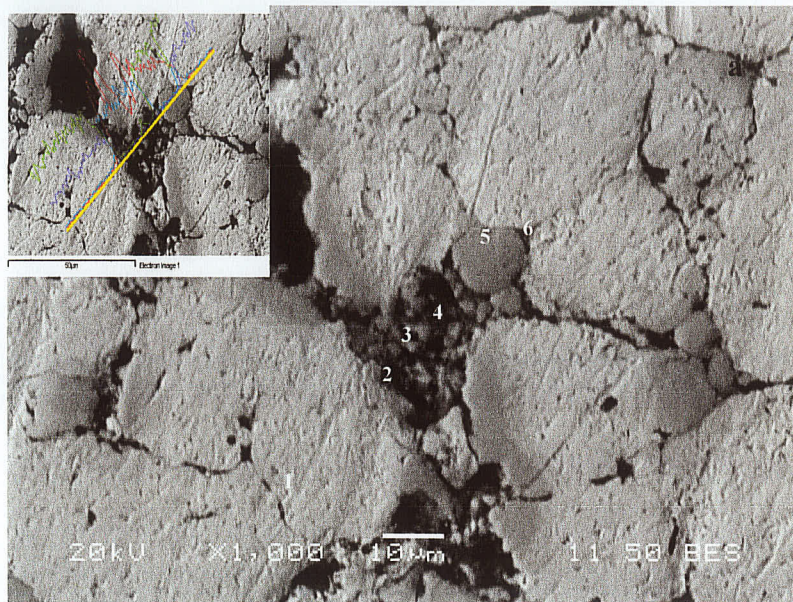


Figure 4.44. SEM BSE Image showing the points of EDS analyses (a) and EDS line scans for b) Ni, c) Al, d) Cr and e) Fe of the sample heated to 790°C and quenched

Table 4.12: EDS analysis of the quaternary compact after heating to 790 °C and quenched

Element	Atomic% Point 1	Atomic% Point 2	Atomic% Point 3	Atomic% Point 4	Atomic% Point 5	Atomic% Point 6	NiCrFe, Fe, and Ni were also noted
Al	0.6	33.0	65.8	52.5	48.9	42.1	
Cr	20.7	3.1	0.3	0.3	0.2	0.4	
Fe	0.2	57.9	32.2	44.0	0.9	0.6	
Ni	78.5	6.0	1.7	3.2	50.0	56.9	

#### 4.15.1.4 SEM/EDS analysis of the DSC sample argon-quenched from 830°C

Figure 4.45 shows the SEM-BSE micrograph and line scans of the sample heated to 830 °C and argon-quenched. The results of the EDS analysis of the sample at various locations are given in Table 4.13. They suggest that at this temperature reaction between Al and Ni resulted in the formation of intermetallics with increasing Ni content as compared to those that formed at lower temperatures. For example, the Al<sub>3</sub>Ni<sub>5</sub> intermetallic formed at Point 1 and Ni<sub>3</sub>Al formed at Point 4.

Table 4.13: EDS analysis of the quaternary compact after heating to 830°C and quenched

Element	Atomic% Point 1	Atomic% Point 2	Atomic% Point 3	Atomic% Point 4	Atomic% Point 5	Atomic% Point 6	Atomic% Point 7
Al	37.4	30.7	42.0	19.0	54.0	29.3	0.4
Cr	4.1	30.9	0.5	0.5	0.4	0.4	19.8
Fe	0.8	2.1	0.4	0.5	4.4	66.5	0.3
Ni	57.7	36.3	57.1	80.0	41.2	3.8	79.5

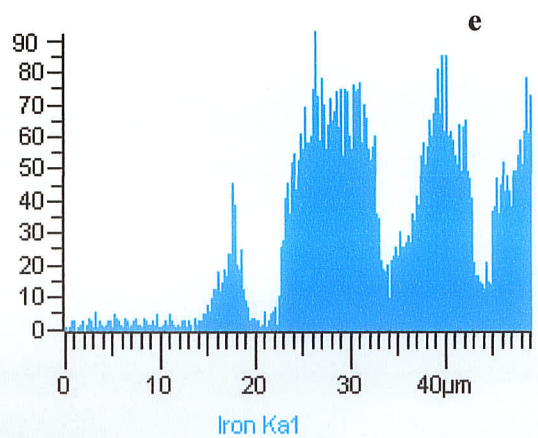
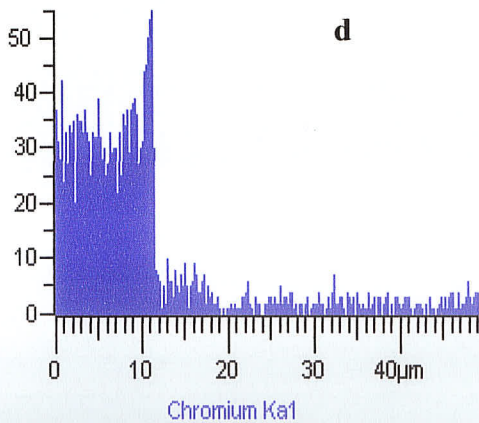
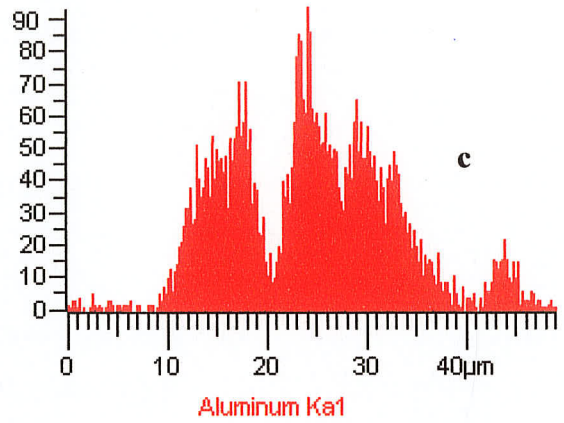
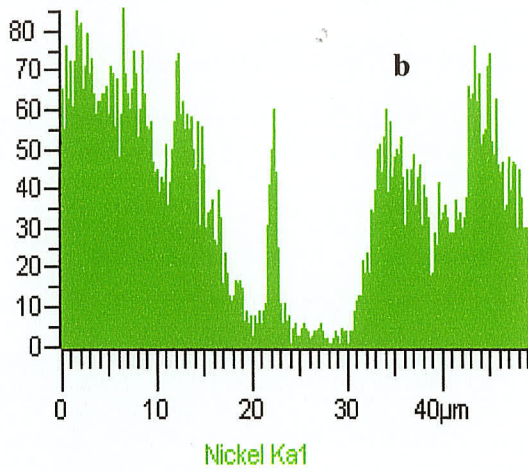


Figure 4.45: SEM BSE Image showing the points of EDS analyses (a) and EDS line scans for b) Ni, c) Al, d) Cr and e) Fe of the sample heated to 830°C and argon-quenched

#### 4.15.1.5 SEM/EDS analysis of the DSC sample argon-quenched from 880°C

In Figure 4.46, the SEM BSE image of the sample heated to 880°C and argon-quenched (i.e., point e in Figure 4.40) is shown. The EDS analysis, Table 4.14, showed that the ratio of Ni and Al concentration in different reacted region varied from 1:1 and 3:1, suggesting NiAl and Ni<sub>3</sub>Al intermetallics were both present in the sample.

Table 4.14: EDS analysis of the compact after heating to 880 °C and quenched

Element	Atomic% Point 1	Atomic% Point 2	Atomic% Point 3	Atomic% Point 4	Ni-Cr-Fe, Ni-Cr, Fe, and Ni were also present
Al K	1.5	30.1	47.8	46.5	
Cr K	0.4	0.5	0.3	0.4	
Fe K	0.6	1.1	0.5	0.9	
Ni K	97.5	68.3	51.4	52.3	

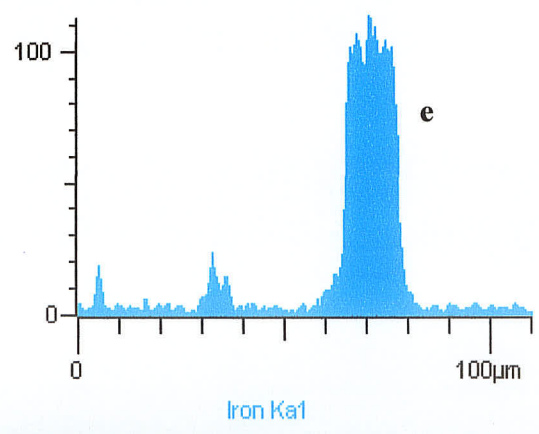
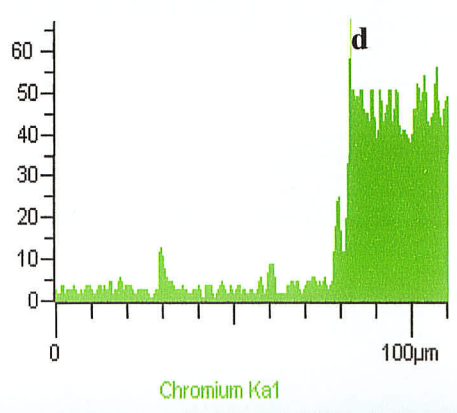
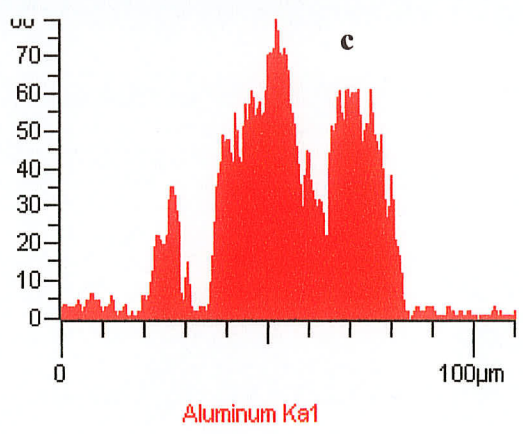
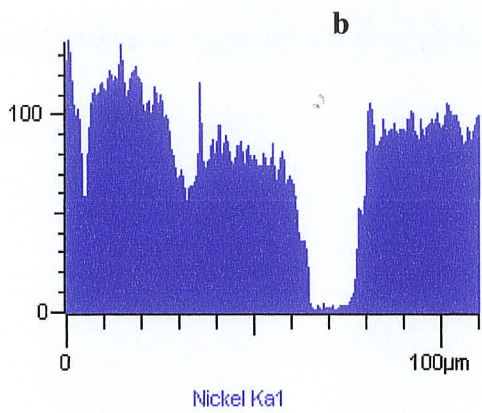
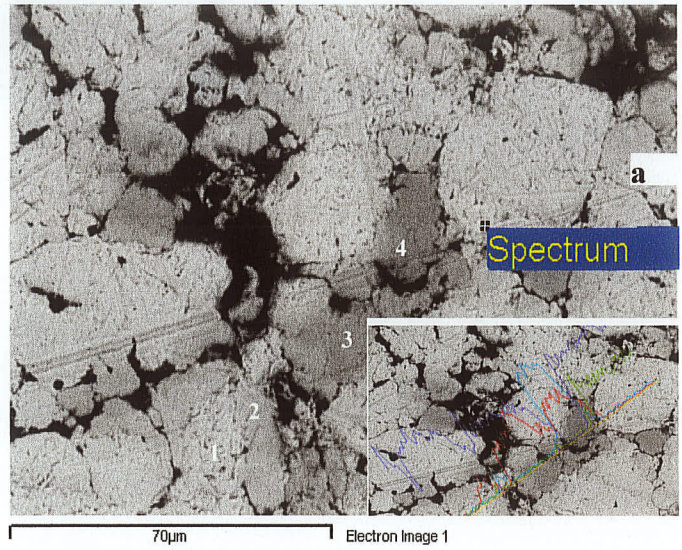


Figure 4.46 SEM BSE Image showing the points of EDS analyses (a) and EDS line scans for b) Ni, c) Al, d) Cr and e) Fe of the sample heated to 880°C and quenched

#### 4.15.1.6 SEM/EDS analysis of the DSC sample argon-quenched from 1120°C

Figure 4.47 shows the SEM BSE image, the points of EDS analysis and trajectory of line scan of a sample argon-quenched from 1120°C (point f in Figure 4.40). The EDS analysis of this sample, Table 4.15, suggests that in general, a non-stoichiometry concentration of Ni, Cr, Fe and Al occur in the grains. However, in some regions, the concentration of (Ni-Cr-Fe) and Al corresponded to that of (Ni-Cr-Fe)<sub>3</sub>Al phase (Figure 4.47 and 4.48) .

Table 4.15: EDS analysis of the compact after heating to 1120°C and quenched

Element	Atomic% Point 1	Atomic% Point 2	Atomic% Point 3	Atomic% Point 4	Atomic% Point 5	Atomic% Point 6
Al	1.7	13.0	13.3	9.2	16.6	2.1
Cr	78.8	11.1	8.1	14.8	2.7	61.7
Fe	1.5	8.5	24.9	3.6	4.5	2.4
Ni	18.0	67.4	53.7	72.4	76.2	33.8

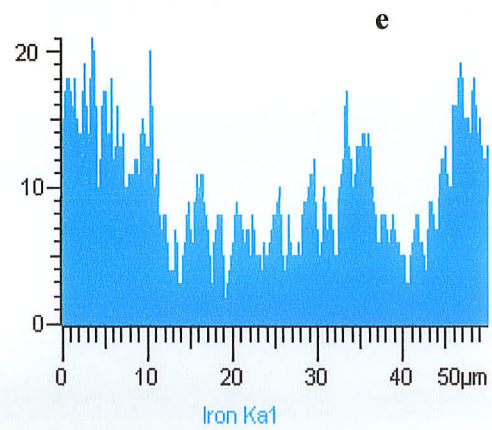
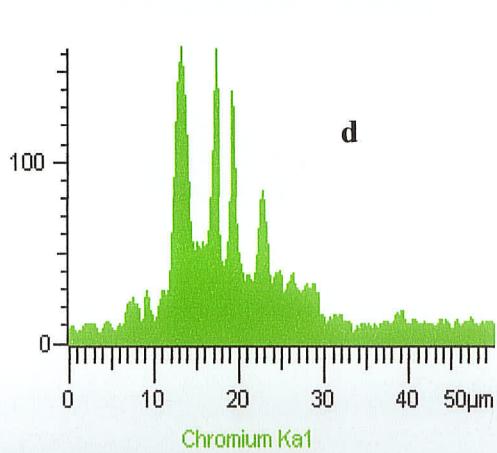
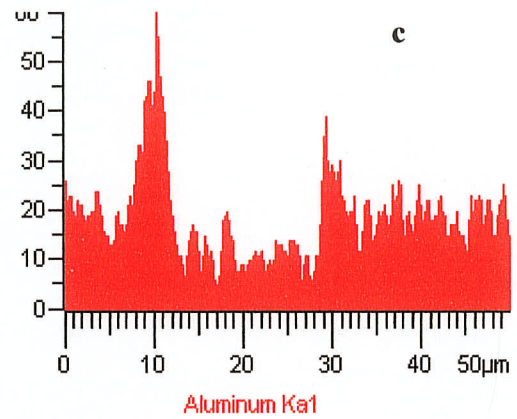
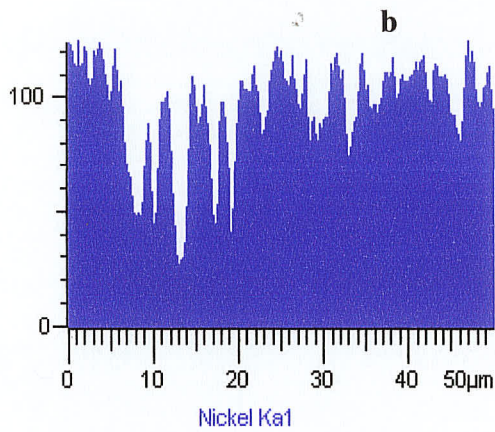
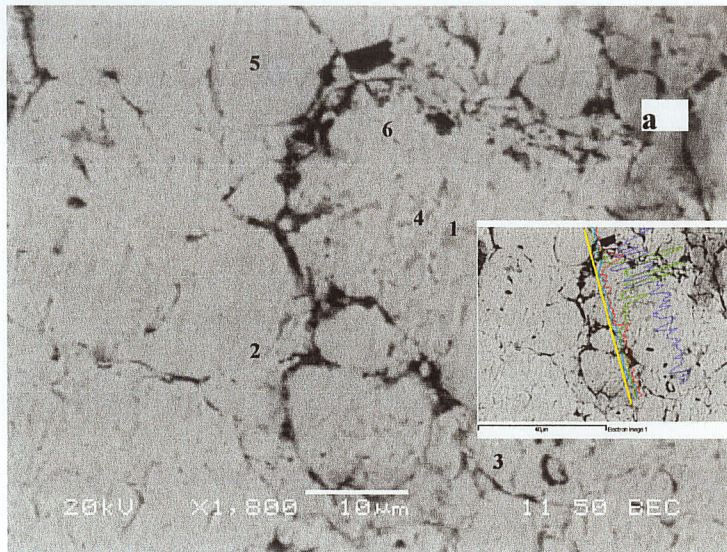


Figure 4.47 SEM BSE Image showing the points of EDS analyses (a) and EDS line scans for b) Ni, c) Al, d) Cr and e) Fe of the sample heated to 1120°C and quenched

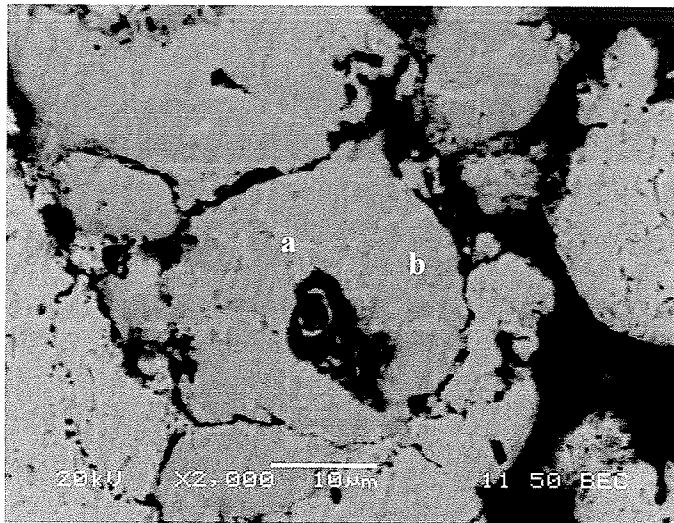


Figure 4.48 SEM BSE micrograph showing the points of EDS analyses of Table 4.13 that correspond to the Ni<sub>3</sub>Al intermetallic composition

Table 4.16: Selected EDS analysis of the compact after heating to 1120°C and quenched

Element	Atomic% Point a	Atomic% Point b
Al	26.5	27.3
Cr	3.3	3.5
Fe	1.1	1.4
Ni	69.2	67.8

Furthermore, to better understand the nature of the phase transformations, samples were heated to 560°C and 640°C in the DSC cell and held for times ranging from 0, 10 and 30mins. These samples revealed that the same phases as those that were observed in the specimens argon-quenched from 560°C and 640°C respectively were present and did not change on prolonged heating at these temperatures. A summary of suggested phases as identified by the EDS analyses of specimens heated to all the different temperatures of

interest is shown in Table 4.17. As can be seen, the occurrence of  $Al_xNi_y$  type of intermetallics varied from  $Al_3Ni$  to  $Ni_3Al$  depending upon the sintering reaction temperatures, as would be expected from the Al-Ni and Al-Fe binary phase diagrams Figure 4.49.

Table 4.17: Summary of the results of EDS analysis of various phases present in the compact at various temperatures during heating to 1120°C

Stage	Suggested phases from EDS analyses	Reaction type (Exothermic or Endothermic)
As received powders	NiCrFe, Al, Ni-Cr, Fe, Ni	-
560°C Quenched	$Al_3Ni$ , AlNi, while other phases such as Ni-Cr, Al, Fe, Ni, and NiCrFe (from as-received powder) were present	Exothermic
640°C Quenched	AlNi, $Al_3Fe$ , $Al_3Ni_2$ , while other phases such as Ni, Ni-Cr, Fe, and NiCrFe (from "as-received" powder) were present	Exothermic
790°C Quenched	$Fe_3Al$ , FeAl, NiAl, while other phases such as Ni, Ni-Cr, Cr, Fe NiCrFe, (from "as-received" powder) were present	Endothermic
830°C Quenched	$Ni_3Al$ , $Fe_3Al$ , NiAl, $Ni_5Al_3$ , Ni-Cr, Fe, Ni, Cr, NiCrFe (from "as-received" powder)	Exothermic
880°C Quenched	$Ni_3Al$ , NiAl, $Ni_5Al_3$ , AlFe, $Fe_3Al$ , while other phases such as Ni-Cr, Fe, Ni, Cr and NiCrFe were also present	Exothermic
1120°C Quench	$Ni_3Al$ and Ni-Cr-Fe-Al (suggested phases: AlFe, NiAl)	Exothermic

# Al-Ni

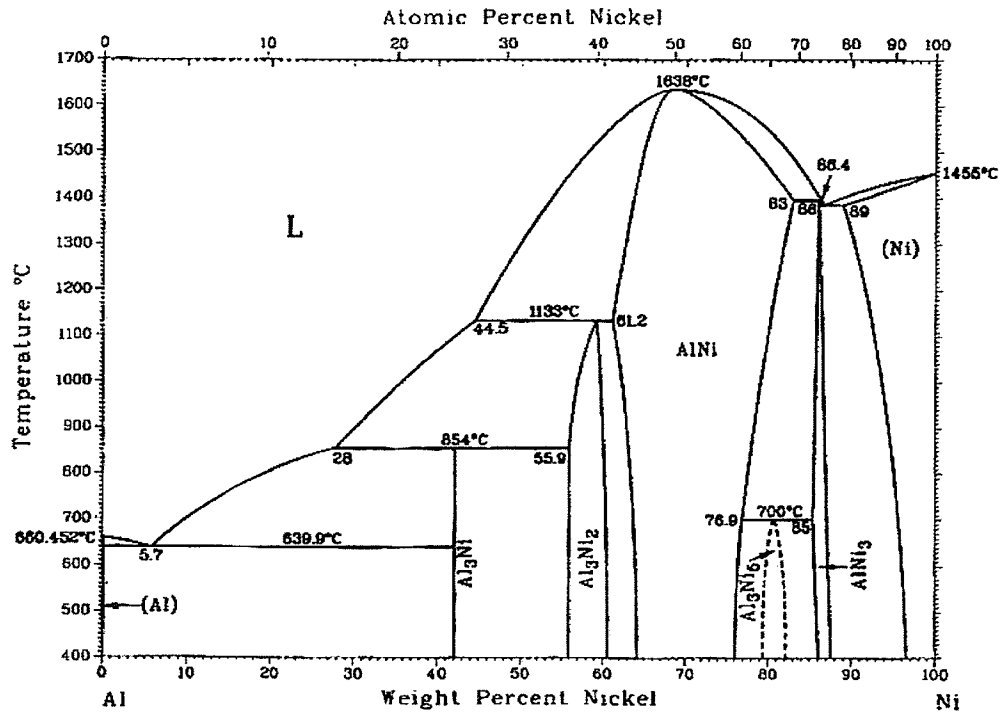


Figure 4.49 a): the Al-Ni binary phase diagram [77]

# Al-Fe

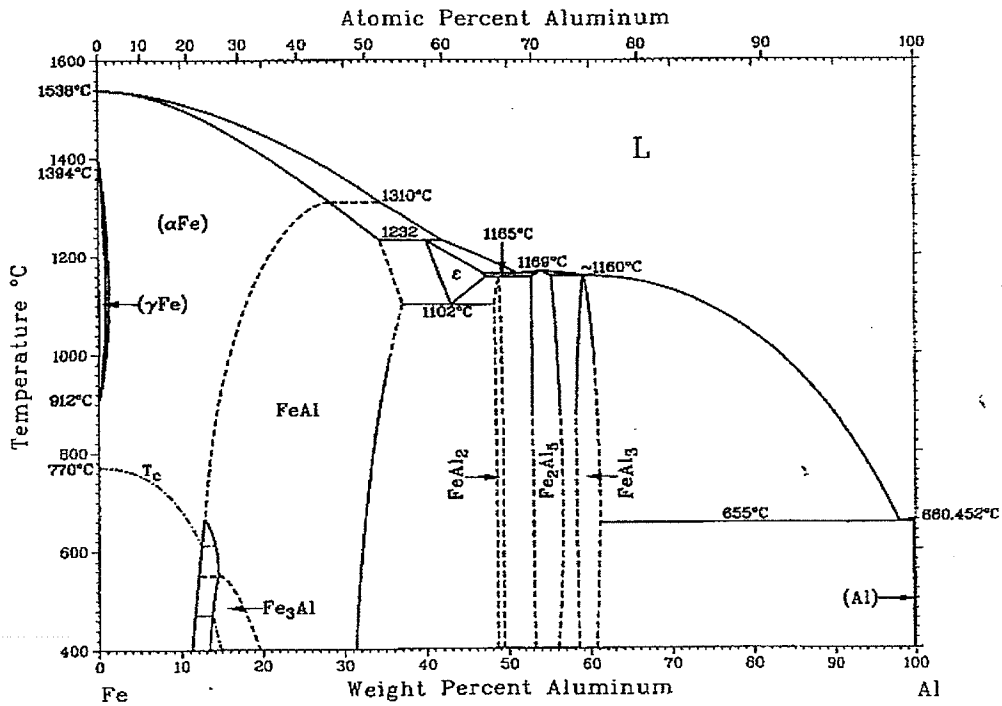


Figure 4.49 b): the Al-Fe binary phase diagram [77]

#### 4.15.2 XRD analysis of phase changes on heating the Ni-Cr-Fe + Al quaternary

The products of the phase transformations that occurred in green compacts heated in a DSC cell to temperature corresponding to various peaks observed in Figure 4.40, were also investigated by XRD. Figures 4.50a-f show the X-ray diffractograms of the various samples and Table 4.18 summarizes various phases that were observed in these specimens.

In the compact heated to 560°C, diffraction peaks of AlNi were observed along with those due to the presence of unreacted Ni, and Ni-Cr-Fe solid solution particles. A few diffraction peaks of Al and Fe were also observed.

At 640°C, a strong exothermic reaction occurred and strong diffraction peaks of AlNi along with peaks of FeAl, and Al<sub>3</sub>Ni<sub>2</sub> were observed. At 790°C the reaction was endothermic and is reflected in the reduced intensity of the diffraction peaks of the intermetallics due to partial dissolution. At 830°C, where a weak exothermic peak occurred, a new intermetallic, Ni<sub>3</sub>Al<sub>5</sub>, was observed along with diffraction peaks of AlNi and AlFe. At 880°C, where the DSC peak of a weakly exothermic reaction was observed the intermetallic AlNi<sub>3</sub> was also detected and the peaks due to Ni<sub>5</sub>Al<sub>3</sub> weakened suggesting its dissolution or transformation to Ni<sub>3</sub>Al. At 1120°C, where an exothermic peak was observed, diffraction peaks of Ni<sub>3</sub>Al, NiAl, AlFe were observed in the diffraction pattern. These XRD results basically corroborate the SEM-EDS observations.

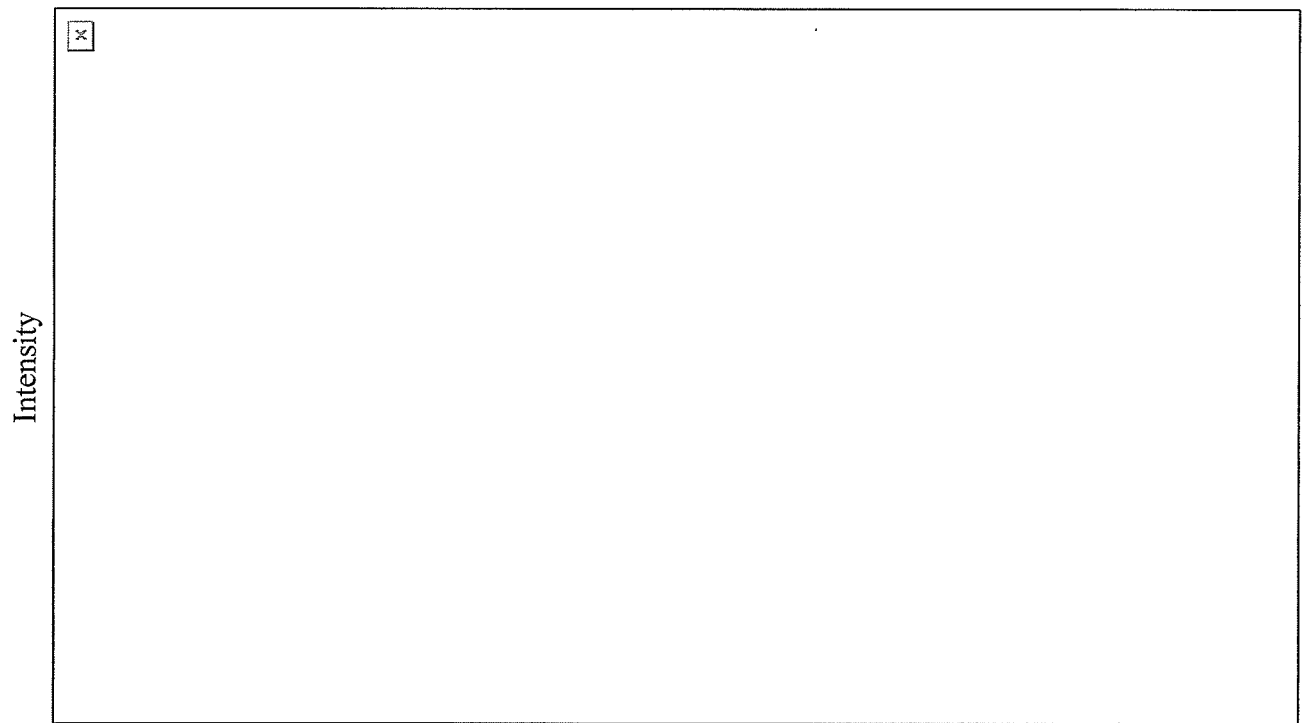


Figure 4.50a: X-ray diffractogram of the sample argon-quenched from 560°C

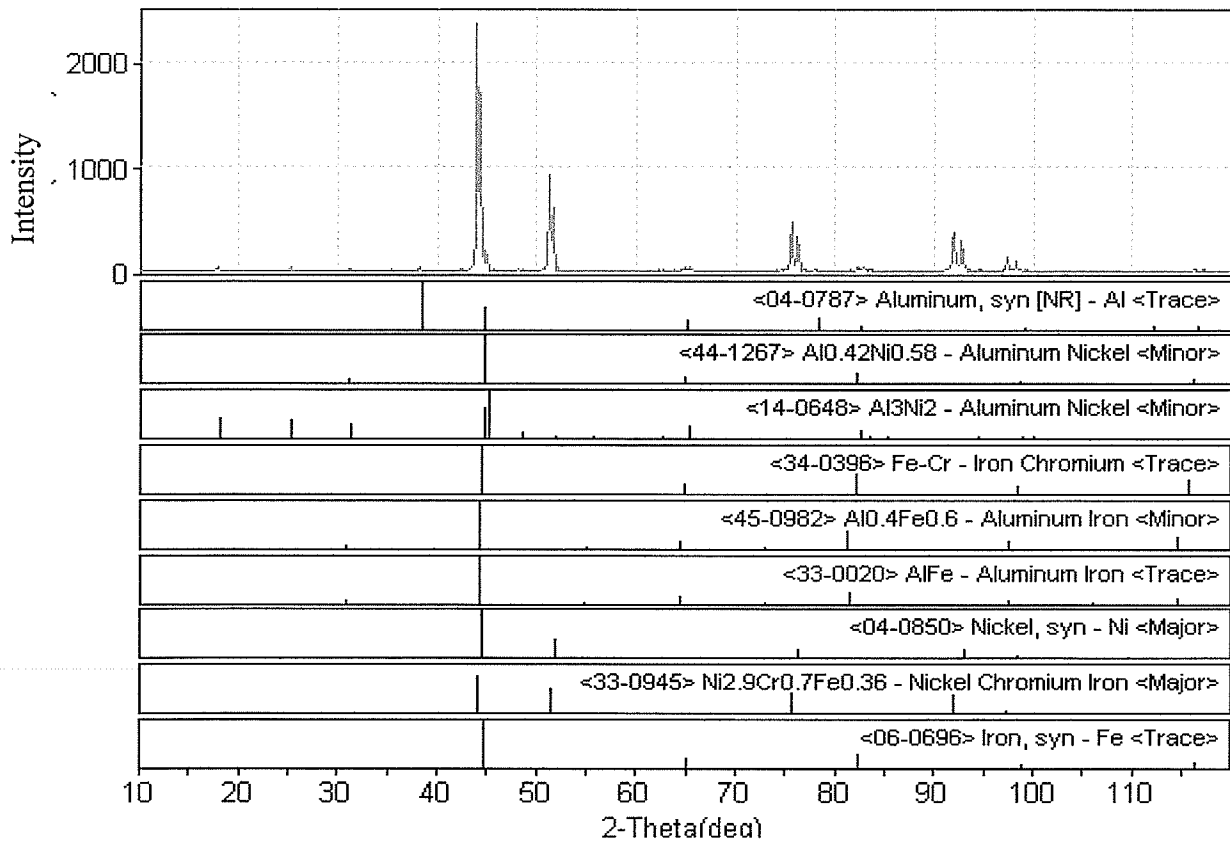


Figure 4.50b: X-ray diffractogram of the sample argon-quenched from 640°C

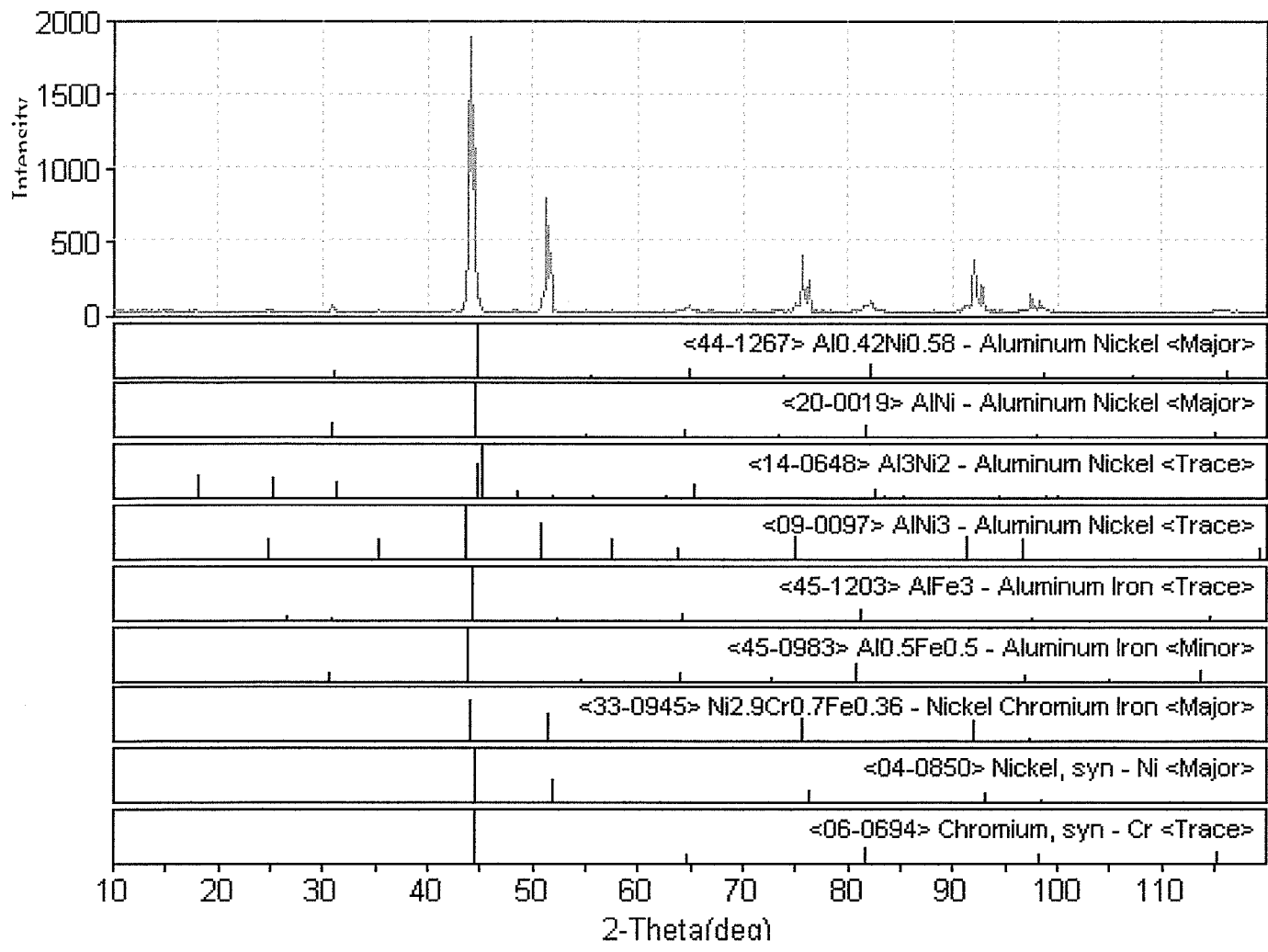


Figure 4.50c: X-ray diffractogram of the sample argon-quenched from 790°C

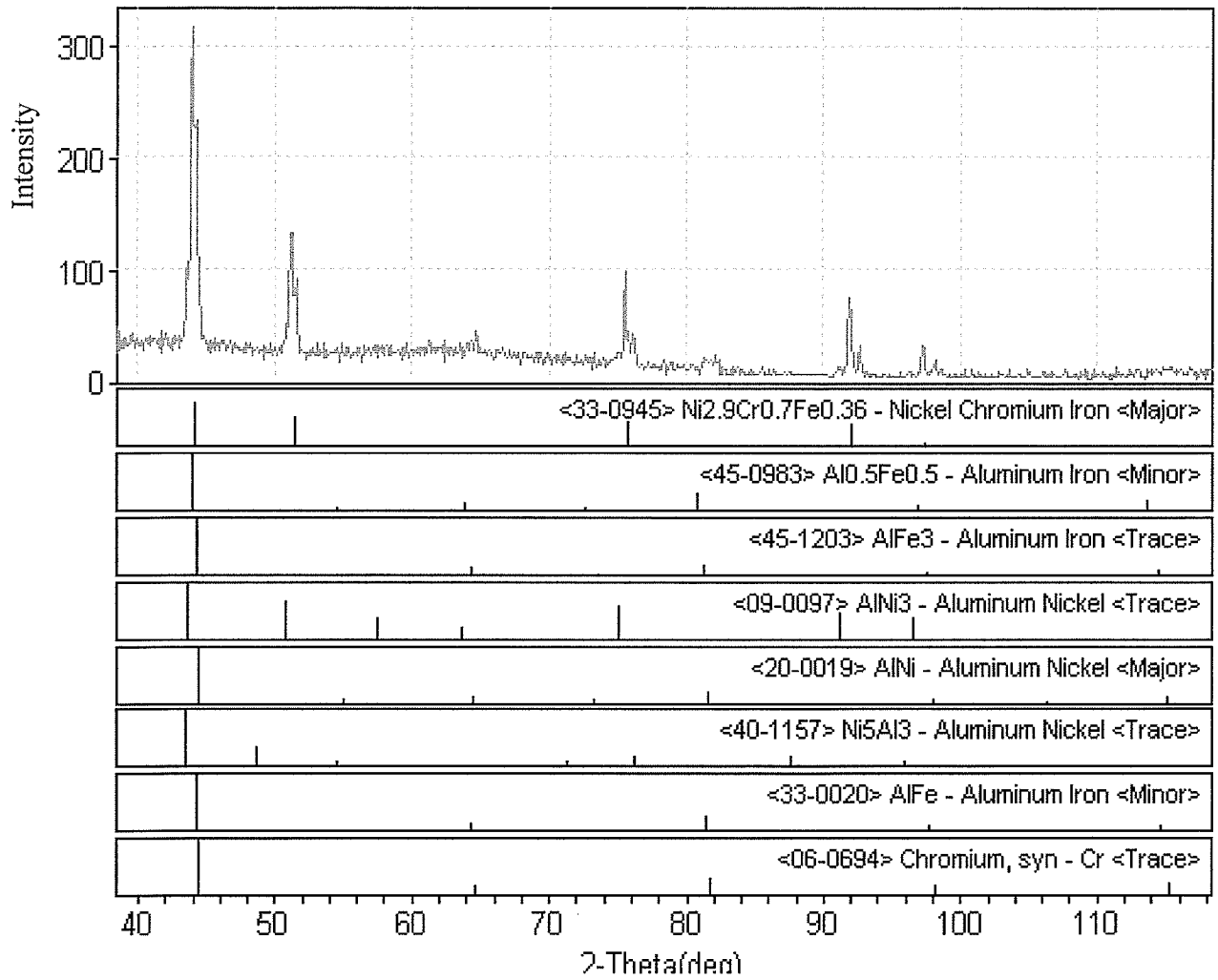


Figure 4.50d: X-ray diffractogram of the sample argon-quenched from 830°C

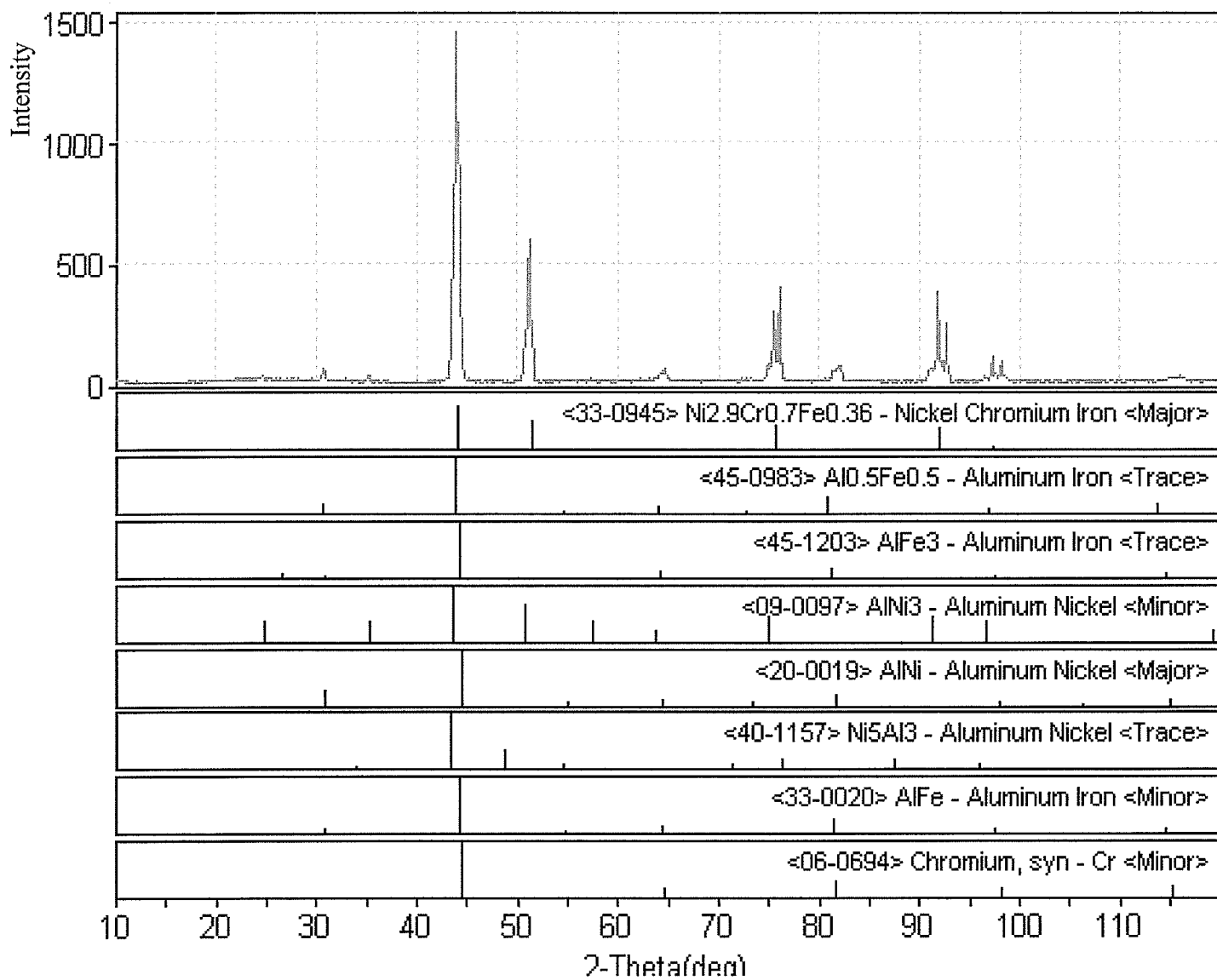


Figure 4.50e: X-ray diffractogram of the sample argon-quenched from 880°C

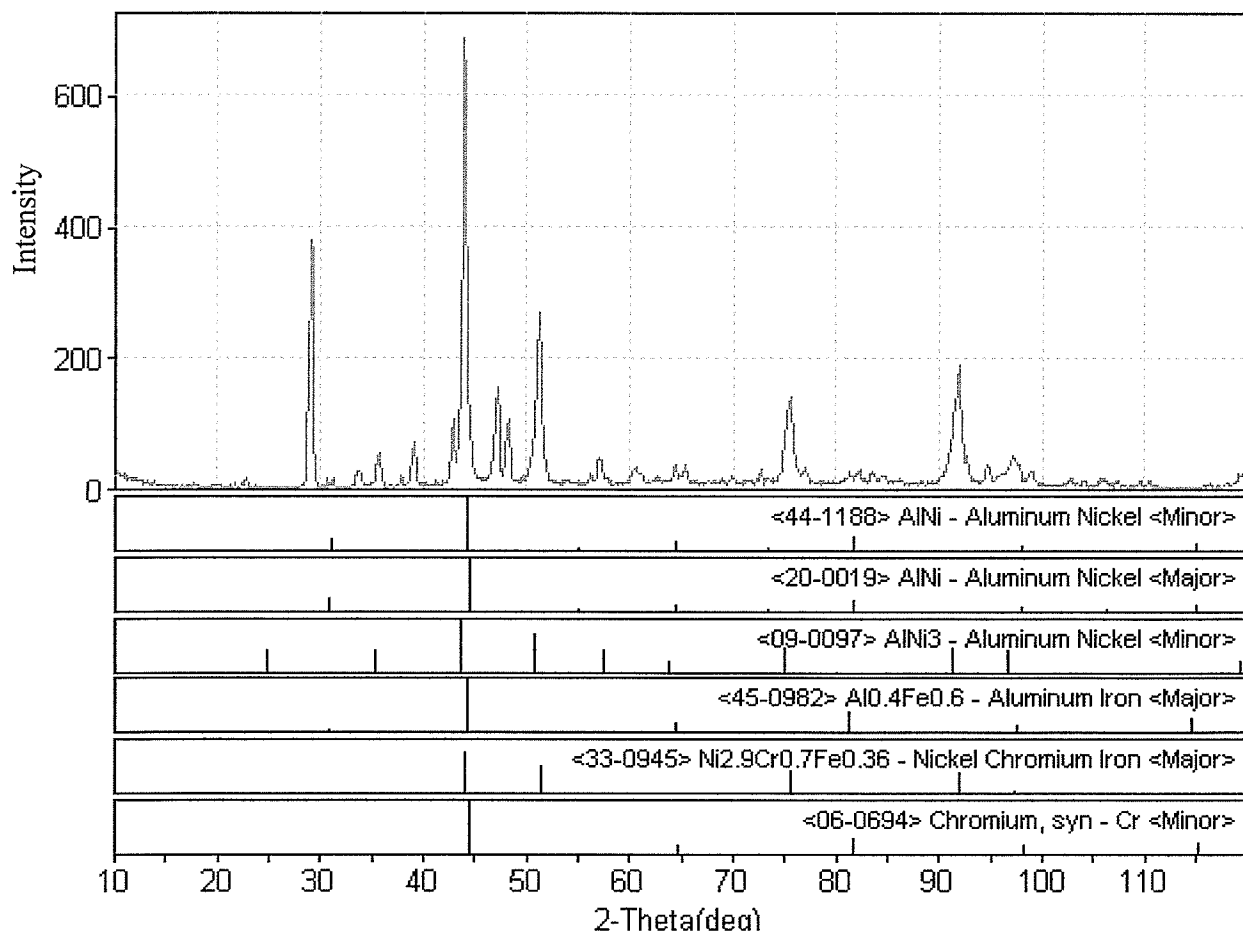


Figure 4.50f: X-ray diffractogram of the sample argon-quenched from 1120°C

Table 4.18: XRD analysis of various points of interest

Temperatures of interest	560 °C	640 °C	790 °C	830 °C	880 °C	1120 °C
Phases present / suggested	Al	Al	-	-	-	-
	Ni-Cr-Fe	Ni-Cr-Fe	Ni-Cr-Fe	Ni-Cr-Fe	Ni-Cr-Fe	Ni-Cr-Fe
	Ni	Ni	Ni	Ni	Ni	-
	Fe	Fe	-	-	-	-
	-	-	AlFe <sub>3</sub>	AlFe <sub>3</sub>	AlFe <sub>3</sub>	
	AlNi	AlNi	AlNi	AlNi	AlNi	AlNi
	-	AlFe	AlFe	AlFe	AlFe	AlFe
	-	-	-	Ni <sub>5</sub> Al <sub>3</sub>	Ni <sub>5</sub> Al <sub>3</sub>	-
	-	Al <sub>3</sub> Ni <sub>2</sub>	Al <sub>3</sub> Ni <sub>2</sub>	-	-	-
	-	-	AlNi <sub>3</sub>	AlNi <sub>3</sub>	AlNi <sub>3</sub>	AlNi <sub>3</sub>
	-	-	Cr	Cr	Cr	-

N.B. At 1120°C, preliminary observation of peaks matching carbide (PDF # 45-975) was also noticed. The carbon may have originated from the residual carbon after the delubrication procedure.

#### 4.15.3 Mechanisms of reactions observed during heating of 6w/o Al modified ternary Ni-Cr-Fe to the sintering temperature

The X-ray mapping analysis (Figure 4.4) revealed that the starting ternary Ni-Cr-Fe powder particles also contained Fe, Ni and Ni-Cr. The cause of such in-homogeneity in the powder is attributed to the atomization process whereby sedimentation of relatively heavier elements could occur causing some powder particles to have varying composition. In the present work, the addition of a low melting point element (Al) to the starting ternary blend to promote the formation of intermetallics resulted in a more complex sequence of phase changes. Heating to the sintering temperature gave rise to phases which eventually dissolved at 1300°C, and on cooling the single phase  $\gamma$  dissociated in to  $\gamma + \gamma'$  phases due to the rapid precipitation rate of  $\gamma'$ .

As noted earlier, at 2.5°C/min heating rate there were two exothermic peaks noted in the 560-640°C range, compared to just one at 10°C/min heating rate. Also, the temperature of initiation of exothermic reaction at 10°C/min heating rate was slightly higher than that observed at 2.5°C/min rate. In a study of reaction between Ni and Al powder particles, Philphot *et al* [95] observed that with an increase in heating rate, the temperature for the initiation of a reaction increased, as was observed in this study (Figures 4.39 and 4.40).

At the temperature where the initial reaction started (560°C), none of the starting interacting components was liquid. Therefore, the reaction that occurred at this temperature was exothermic solid-solid state reaction. In the synthesis of Al-Ni intermetallics using nanoparticles, Hunt *et al* [96] showed that diffusion played a significant role in initiating a reaction between fine Al and Ni powders, while subsequent

ignition (or combustion synthesis) reaction between Al and Ni could occur in the solid state. This diffusive interaction can be affected by various factors one of which is the gasifying agent i.e., combustion medium (air) [96]. However, no gasifying agent was used in this study leaving diffusive interaction in the solid state as the only mode. EDS analysis revealed that at 560°C the composition of the intermetallics that formed was similar to AlNi and Al<sub>3</sub>Ni. Based on the location of Al<sub>3</sub>Ni and AlNi, relative to the location of original Al and ternary alloy particles, and the decrease in Al concentration into ternary beyond the region where AlNi formed, it is concluded that interaction of Al-Ni occurred at the powder interface leading to the formation of the observed intermetallics.

Although AlNi formed at powder particle contact points, its amount was small as seen in Figure 4.40 Point 'a', and thus the reaction ceased due to the reduced mobility of Al and Ni through the AlNi phase. As the temperature increased, sufficient AlNi would have formed so that Al and Ni could diffuse more rapidly through the AlNi layer, and at about 640°C the differentiated DSC curve, Figure 4.41, showed an endothermic reaction as well as exothermic reaction. The endothermic reaction indicates formation of an Al-rich Ni containing liquid phase, which would wet the particles and increase the contact area and the reaction rate. The exothermic peak at 640°C resulted in increased amounts of the AlNi intermetallics being formed as substantiated by the presence of AlNi diffraction peaks in the X-ray diffractogram (Table 4.18 and Figure 4.50b).

The presence of the very strong and sharp peak at 640°C suggests the reaction to be spontaneous in nature. By definition, reactions which occur spontaneously and continue until the reactants are completely consumed are referred to as combustion

synthesis. Combustion synthesis may be of two types, self-propagating or simultaneous [14]. In the former, the reaction is initiated when combustion temperature is reached and a reaction front propagates through the rest of the material. The simultaneous combustion synthesis, also referred to as thermal explosion [14] involves the instantaneous and total combustion of all the reactants at the same time when the ignition temperature is reached. The prevailing mode of combustion synthesis depends on the green compact composition, pressure, particle size, reactive volume, initial temperature and shape among other factors [14]. It has been suggested [14], that there are four main temperatures in combustions synthesis. These are the initial temperature before ignition occurs ( $T_0$ ), the ignition temperature ( $T_{ig}$ ) which is the temperature of the reactants at the onset of combustion, the adiabatic temperature ( $T_{ad}$ ) or the maximum temperature theoretically achievable, and the combustion temperature ( $T_c$ ) which is the temperature achieved at non-adiabatic conditions, or the temperature actually reached on combustion. Hunt *et al* [96] synthesized  $Al_xNi_y$  by combustion synthesis using nanoparticles, while Krasnowski *et al* [97] synthesized it by mechanical alloying and hot press consolidation. The characteristics of the reaction observed by them are important to determine if the reaction that occurred in this study was combustion synthesis.

Combustion synthesis can be initiated by a heat source, and finer particles have been shown to reduce the ignition delay time and activation energy [96]. Also, once combustion synthesis is initiated it is self sustaining with the reactants attaining relatively high temperatures. In this study it was noted that the thermal energy supplied played a major role in initiating the reaction that occurred at 560°C and 640°C. In an effort to establish the mechanism, similar green compact samples were heated to 560°C and held

for 0, 10mins and 30mins. This caused an insignificant change in composition of the reaction product and its thickness remained unchanged at an average of value of  $5\mu\text{m}$ , even after 30 minutes of holding at this temperature. This suggests that the reaction did not proceed to completion as unreacted Al remained, and its diffusion would continue on further heating. Although diffusion through AlNi is possible due to the higher number of vacancies and crystal structure [98] in comparison to other  $\text{Al}_x\text{Ni}_y$  type intermetallics, diffusion through other intermetallic compositions would not have been as rapid as was noted in the present work at higher temperatures, unless favorable conditions (e.g., a transformation temperature) was attained. Therefore, the reaction at  $540^\circ\text{C}$  might have been initiated by combustion synthesis as reflected by the exothermicity of the reactions. However, due the relatively small quantity of Al in the compact, in addition to a relatively low reaction temperature for significant diffusion to occur, the reaction might not have proceeded to completion, because the compact would act as a heat sink thereby suppressing the combustion synthesis reaction. At  $640^\circ\text{C}$ , however, the reaction did exhibit all the characteristics of a combustion synthesis type reaction and is suggested to be the mechanism of formation of the NiAl at this temperature.

At Point c ( $790^\circ\text{C}$ ) in Figure 4.40, further interaction between the elements continued resulting in the formation of  $\text{Al}_3\text{Ni}_2$ , AlFe, AlNi, with some ternary alloy remaining unreacted. These phases formed due to increased atomic migration, which is consistent with the conclusion in a similar system at similar temperatures [13], that diffusion is the main mechanism of atomic migration. Therefore the sequence of phases that form in Ni-Cr-Fe ternary powder particles from surface to interior would be successively lower in Al content, as was observed.

In the sample quenched from 830°C, Figure 4.45, it was observed that the Al concentration decreased on traversing from a location that was originally a pure Al particle into a Ni-Cr-Fe particle, this has been previously reported [13, 95, 99, 100]. Furthermore, the presence of Ni<sub>3</sub>Al was also observed along with the precipitates that formed at lower temperatures. Finally, at 1120°C Point f (Figure 4.40) only Ni<sub>3</sub>Al, AlFe and AlNi in the matrix of solid solution Ni-Cr-Fe-Al were observed, which is in accordance with the Al-Ni and AlFe binary diagrams.

In order to estimate the mechanical properties of the alloy after completion of transformations, micro hardness of the sample corresponding to the completion of transformations (i.e., compact cooled from 1120°C) was carried out. The average value obtained was 103HV which is comparable to the hardness value of the as-sintered ternary alloy of 98HV.

In summary, the various reactions that occurred in 6w/o Al contrary ternary Ni-Cr-Fe alloy heated to the sintering temperature indicate a variety of mechanisms which depend on a combination of diffusion-based reaction and combustion synthesis.

## 4.16 Heat treatment of the 6w/o Al modified ternary Ni-Cr-Fe alloy

### 4.16.1 Ageing of the 6w/o Al modified compact

In this study, ageing of compacts were carried at two selected temperatures. These were at 650°C and 800°C. These temperatures were selected to simulate the probable conditions under which the alloy may be used.

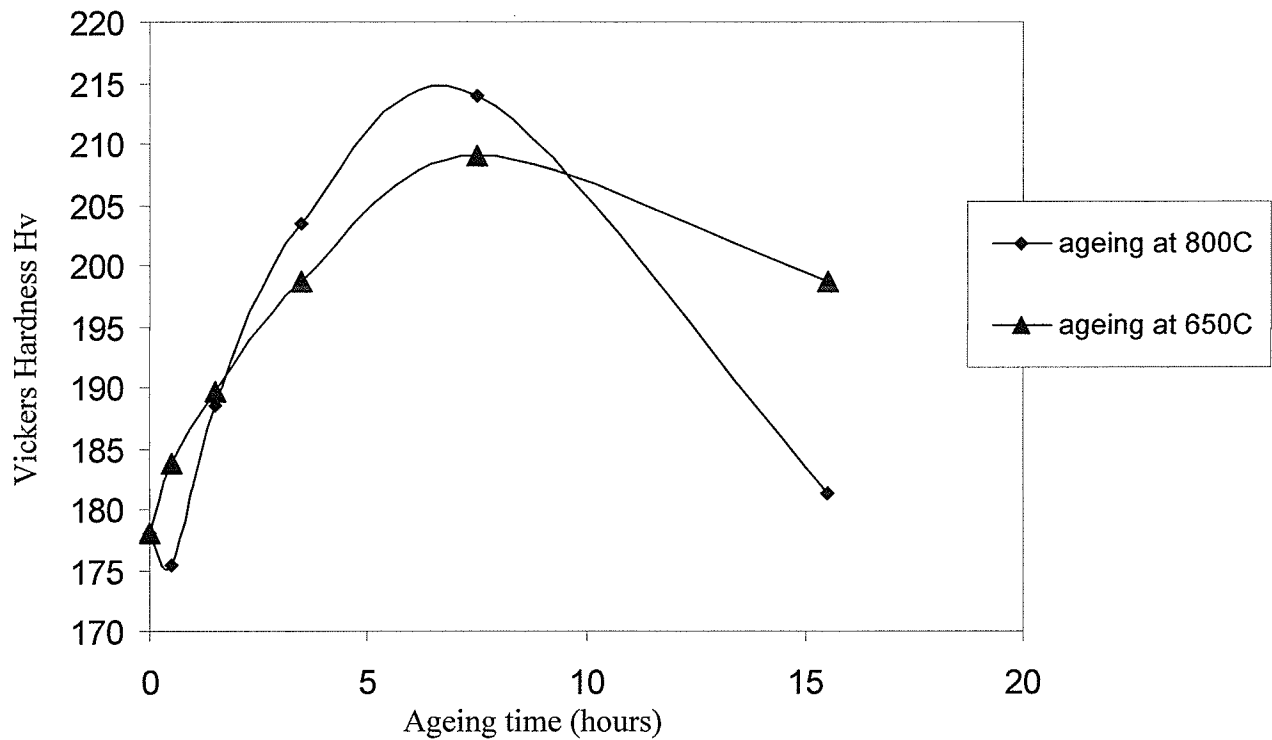


Figure 4.51: Vickers hardness of the alloy versus ageing from 0.5h to 15.5h at 650°C and 800°C

From Figure 4.51, it can be seen that at 650°C, the alloy hardness peaked after a slightly longer time than at 800°C. Specifically, the alloy hardness peaked at 7.5h 800°C.

#### 4.16.2 Dissolution of the gamma prime precipitates

Further, heat treatments were carried out at 970, 1010, and 1050°C for 1h each after solutionising at 1200°C for 4hs and the corresponding micrograph are given in Figure 4.52. This was done in order to evaluate the shape of the gamma prime precipitates and their effect on the 6w/o Al modified alloy. The as-sintered 6w/o Al modified ternary is also shown so as to compare the shape of the precipitates (Figure 4.52a).

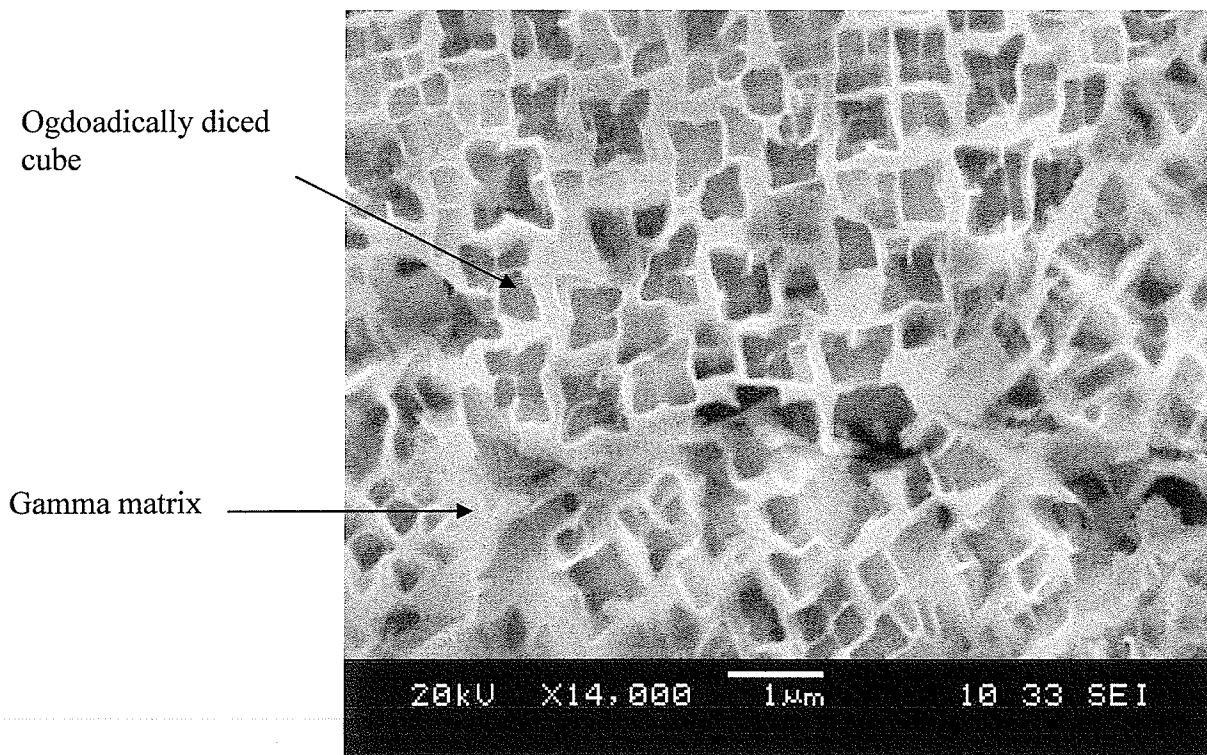


Figure 4.52a. Ni-Cr-Fe alloy with 6 w/o Al modified ternary

A changed and dissolving gamma prime

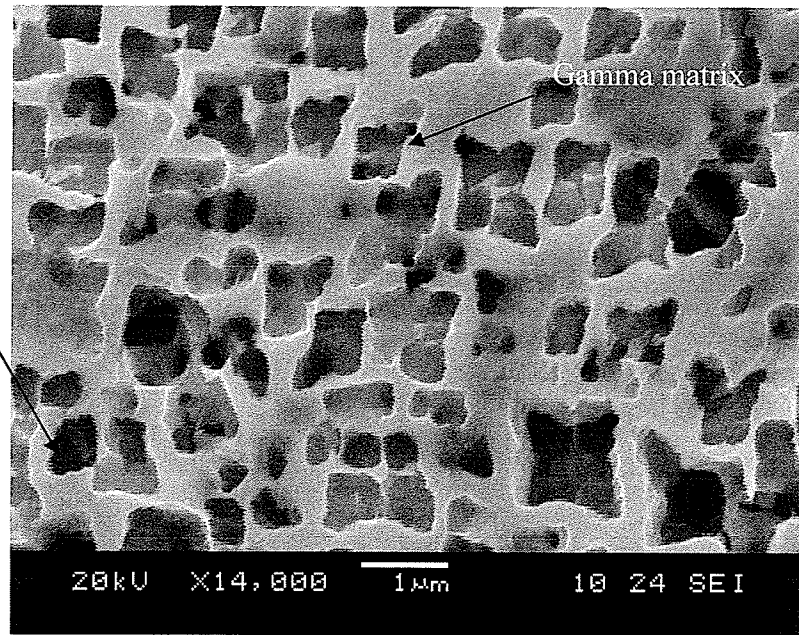


Figure 4.52b: SEM-SEI micrograph of 6w/o Al modified ternary Ni-Cr-Fe alloy after heat treatment at 970°C for 1h followed by air cool

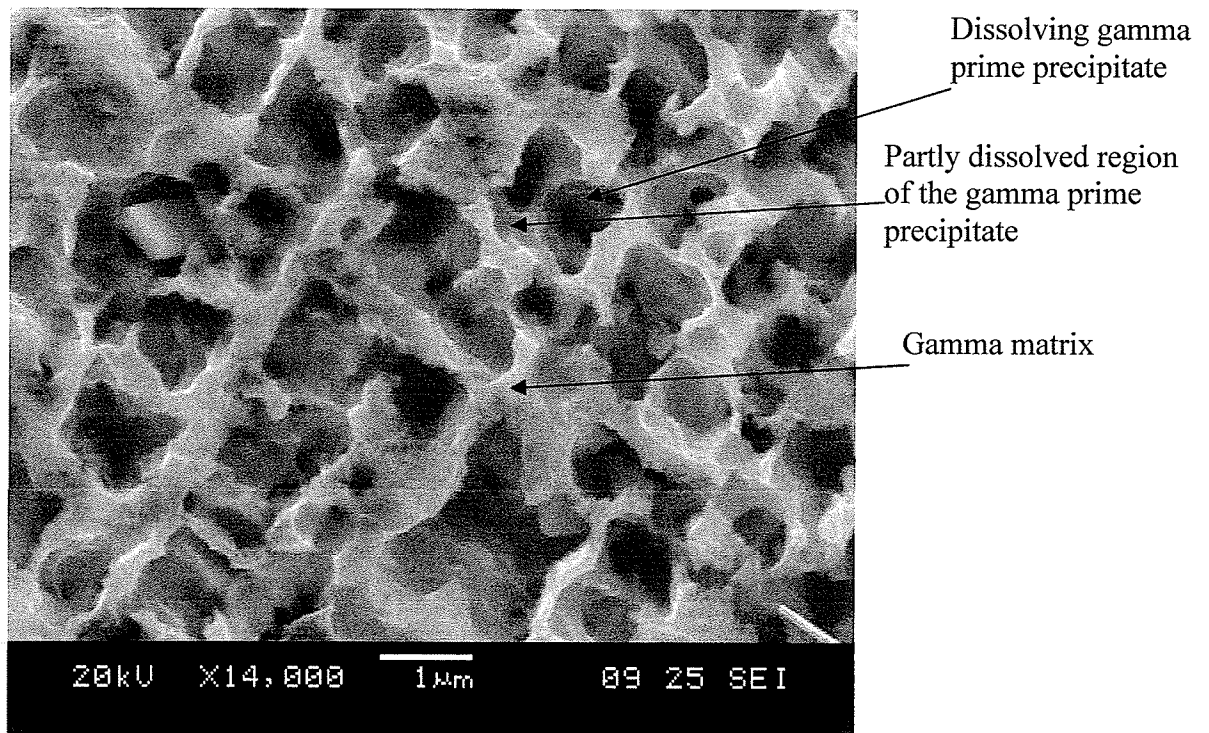


Figure 4.52c: SEM-SEI micrograph of 6w/o Al modified ternary Ni-Cr-Fe alloy after heat treatment at 1010°C for 1h followed by air cool

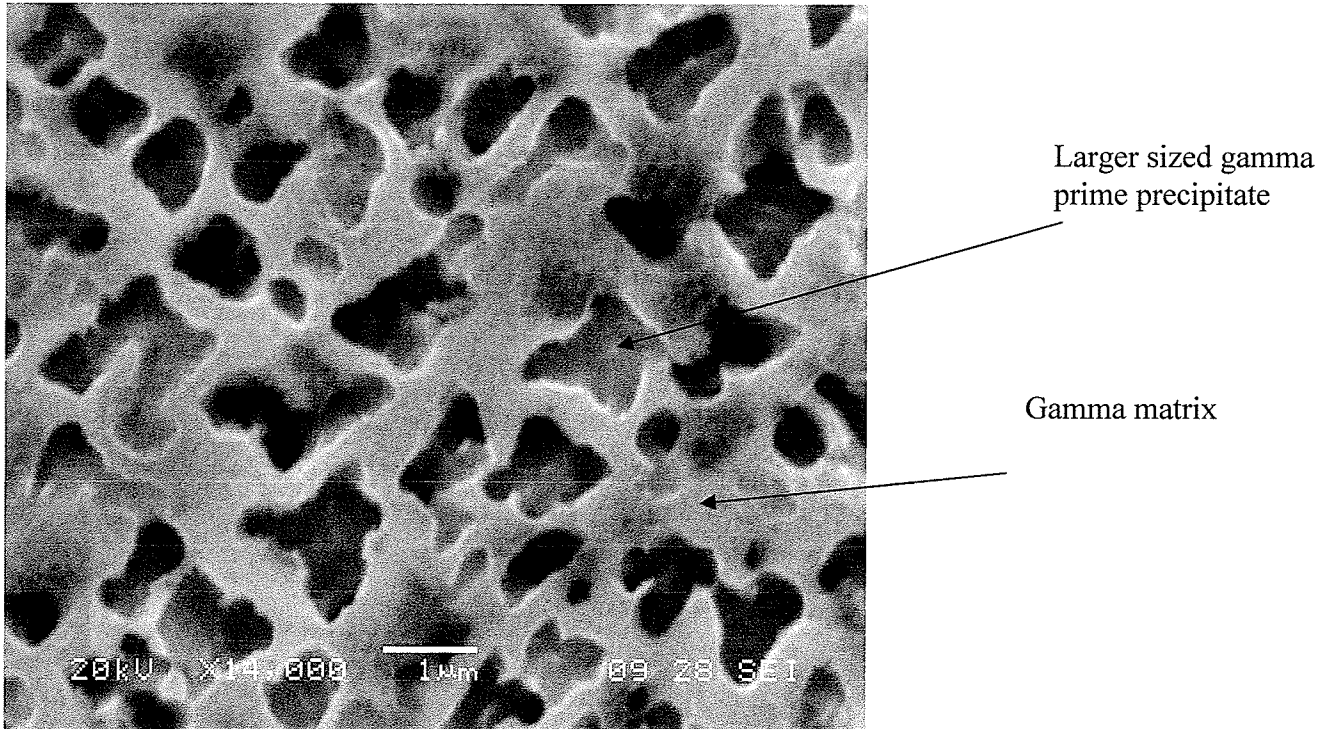


Figure 4.52d: SEM-SEI micrograph of 6w/o Al modified ternary Ni-Cr-Fe alloy after heat treatment at 1050<sup>0</sup>C for 1h followed by air cool

Basically, the Figure 4.52 reveals the dissolution of the gamma prime precipitates as temperature increases. In Figure 4.52d, it can be seen that the amount of gamma prime precipitates has reduced in number relative to Figures 4.52b-c. In addition, the shape of the gamma prime changed from octahedrally diced cubes to a more irregular shape, probably owing to the dissolution of gamma prime. This was previously observed by Grosdidier, *et al* [101].

## CHAPTER FIVE

### 5.0 SUMMARY AND CONCLUSIONS

#### 5.1 Optimisation of processing parameters for the ternary Ni-Cr-Fe alloy

1. For the Ni-Cr-Fe ternary alloy investigated, it was found that the optimum processing occurred when green compact, that contained 0.75w/o microwax was compacted at 500MPa pressure followed by sintering at 1300<sup>0</sup>C for 2h.
2. Cold-rolling the ternary Ni-Cr-Fe sample to approximately 40% of the original thickness resulted in 98.2% theoretical density and hardness of 63HRA (60kgf) or approximately 253Vickers (10kgf) which compares well with processed wrought IN600.
3. During air sintering for times less than or equal to 2h, the formation of chromium oxides at the grain boundaries was restricted, despite thermodynamic predictions, while at sintering times >5h, chromium enrichment took place predominantly at the particle boundaries due to oxidation.
4. During vacuum sintering neither oxidation nor chromium enrichment was pronounced.
5. Therefore, it may be concluded that vacuum sintering (<6 millitorr, 1300<sup>0</sup>C, 2h) is optimum to produce a P/M compact with good compressibility and reasonable mechanical properties as reflected by the hardness values. The method used in optimising the processing parameters of the ternary was relatively simple, did not require the P/M Superalloy to be in a 100% dense condition, and should be applicable to a broad spectrum of P/M Superalloy compositions.

## 5.2 Effect of Al on the ternary Ni-Cr-Fe alloy

Optimized P/M processing was successfully used to fabricate several Al modified Ni-Cr-Fe ternary alloys, and thermodynamic predictions were compared with the experimental results. Based on the results obtained, the following conclusions may be made.

1. The P/M process used in this study produced a fine grain microstructure in 1, 3 and 6w/o Al modified Ni-Cr-Fe ternary alloy but not in 12 w/o Al modified Ni-Cr-Fe alloy.
2. The thermodynamic software JMatPro, provided a reasonably accurate prediction of the phases observed in the 1, 3, 6, and 12 w/o Al modified Ni-Cr-Fe ternary alloys.
3. The volume fraction of  $\gamma'$  as predicted for the 6w/o Al modified Ni-Cr-Fe alloy did not accurately match the experimental observations. This was related to the powder particle processing conditions and lack of thermodynamic equilibrium in the compacts.

### **5.3 Thermodynamic modelling of 6w/o Al modified ternary Ni-Cr-Fe alloy**

1. The thermodynamic software JMatPro predicted correctly the main phases observed in the Superalloy, including the types and number of phases, as well as the transformation temperature for gamma prime precipitates. The latter was subsequently confirmed by a DSC study.
2. Despite various problems in P/M processing of a typical Superalloy, the thermodynamic predictions by JMatPro of the phases that form offer a reasonable approach for modeling the alloy system composition.

#### **5.4 Phase transformation on heating the 6w/o Al modified ternary Ni-Cr-Fe alloy to 1300°C sintering temperature**

Based on the DSC study of the 6w/o Al-modified Ni-Cr-Fe P/M alloy the following conclusions were made.

1. At the heating rates considered, 2.5 and 10°C/min, the exotherm peak (between 560-640°C) shifted to higher values when the heating increased from 2.5°C/min to 10°C/min, while the temperatures corresponding to other peaks remained unaffected.
2. Whereas self-propagating combustion synthesis might have initiated the reaction at 640°C its continuation was by a diffusion process due to the unavailability of enough Al to sustain the reaction.
3. Both  $Al_xNi_y$  and  $Al_xFe_y$  type intermetallics formed on heating and the sequence of their formation as the sintering temperature, 1300°C, approached was suggested to be as follows:  $\{Al_3Ni, AlNi\}$ ,  $\{Al_3Ni_2, Al_3Fe, AlNi\}$ ,  $\{AlFe, Al_3Ni_2, AlNi, \}$ ,  $\{Al_3Ni_5, AlNi, AlFe\}$  and  $\{Ni_3Al, AlFe, AlNi\}$ .
4. The crystal structure and composition of the phases that formed were in agreement with that indicated by the binary Al-Ni and Al-Fe equilibrium phase diagrams.
5. The hardness of the Al modified ternary Ni-Cr-Fe alloy at the completion of transformation compared well with that of the ternary alloy with no addition of Al.

## **Future work**

Based on the work carried out in this thesis, the suggested future work are as follow:

- Investigate the oxidation properties of the alloy
- Investigate and characterize the phases present when 1 and 3w/o Ti is added to the 6w/o Al modified alloy.
- Carry out a phase transformation study on the types, nature and mechanisms of phase formations during the sintering of the 1 and 3w/o Ti modified quaternary 6w/o Al modified alloy.

## APPENDIX A

### Effect of 1w/o and 3w/o Ti on the 6w/o Al modified ternary Ni-Cr-Fe alloy

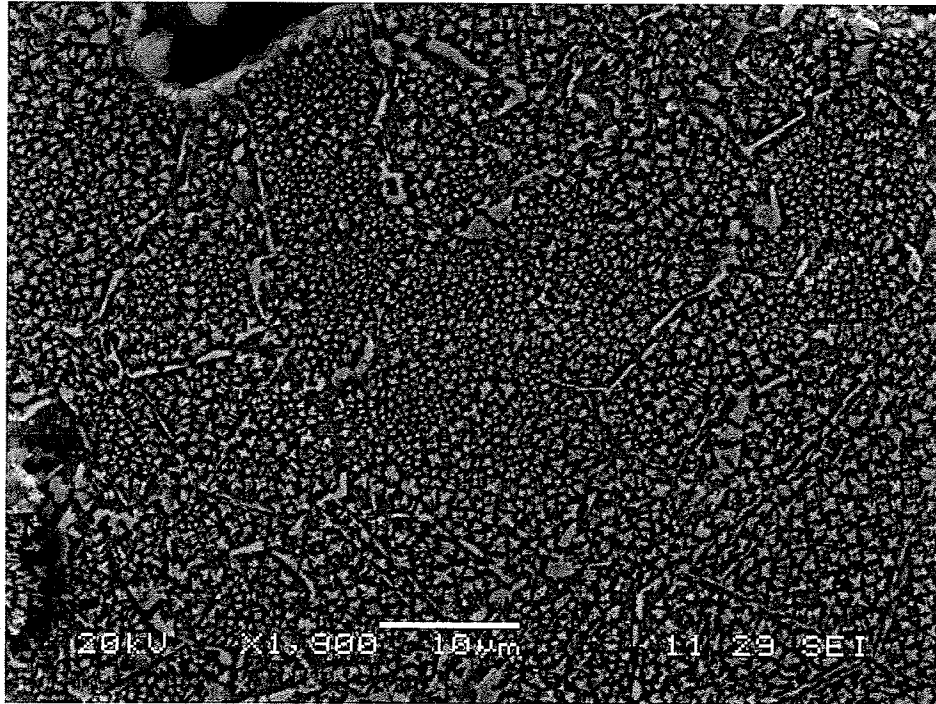


Figure A.1: The SEM secondary electron image for the 6w/oAl 1w/o Ti modified ternary Ni-Cr-Fe alloy

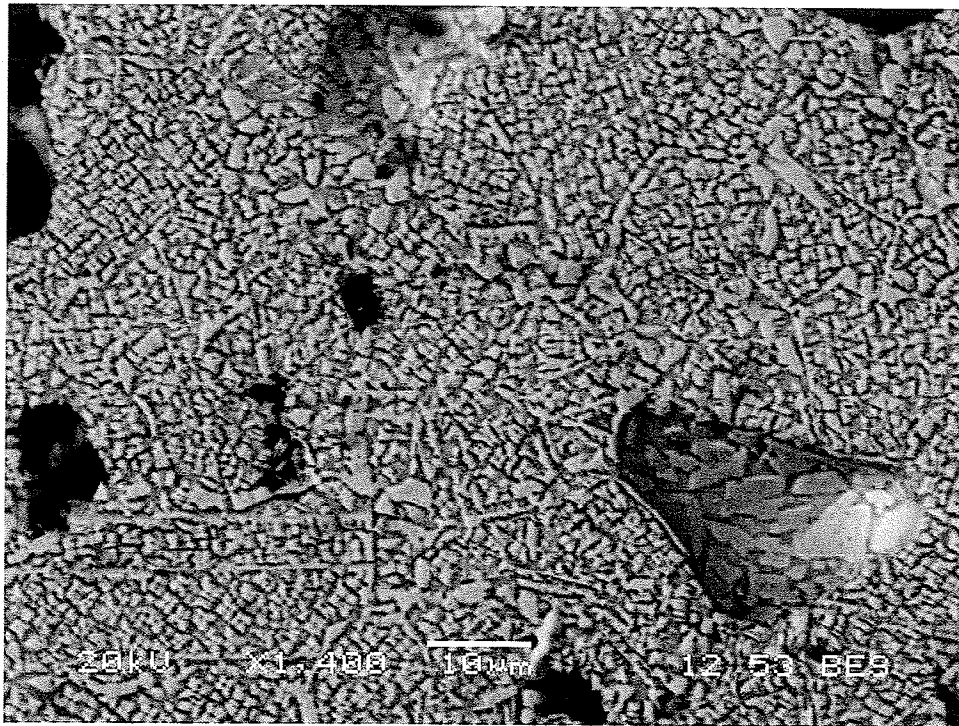


Figure A.2: The SEM secondary electron image for the 6w/oAl 3w/o Ti modified ternary Ni-Cr-Fe alloy

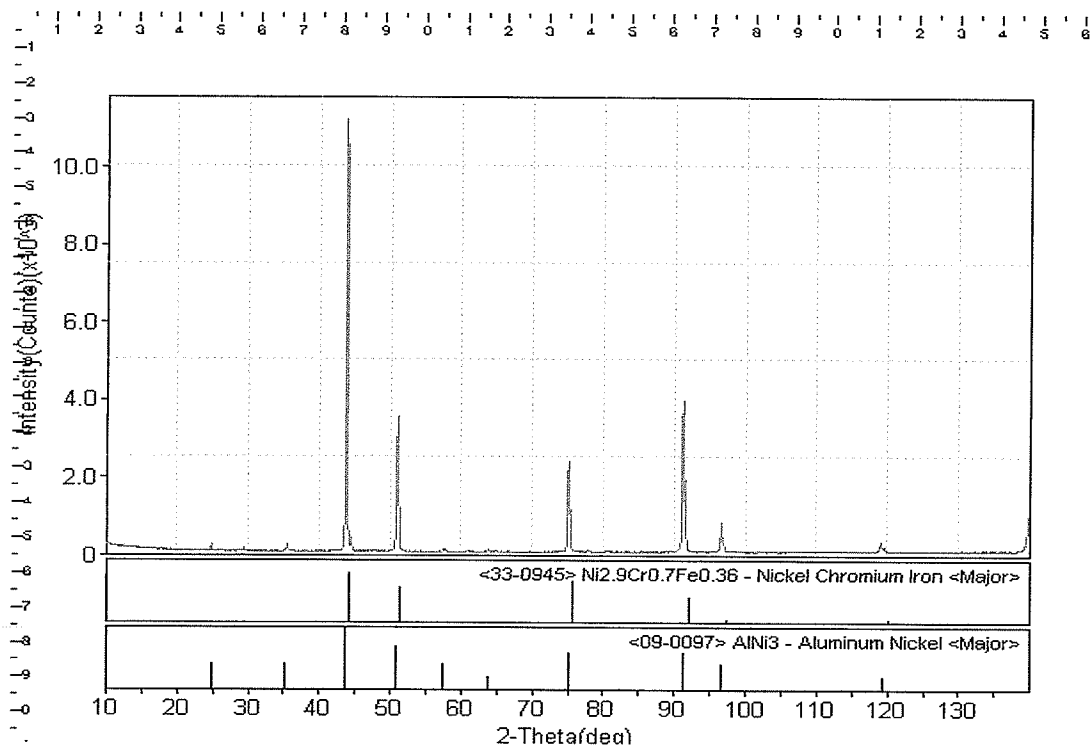


Figure A 3: The XRD analysis for the 6w/oAl 3w/o Ti modified ternary Ni-Cr-Fe alloy

## APPENDIX B

### B. 1 Catalogue of step calculations for selected compositions

In the course of writing this thesis step calculations for various compositions of interests were carried out. These are shown in the figures below.

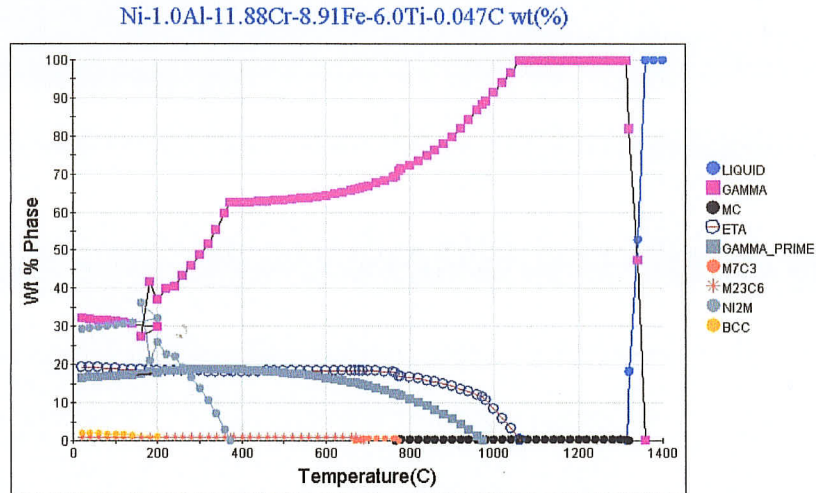


Figure B. 1: JMatPro step calculations for the 1w/o Al, 6w/o Ti on the ternary Ni-Cr-Fe alloy

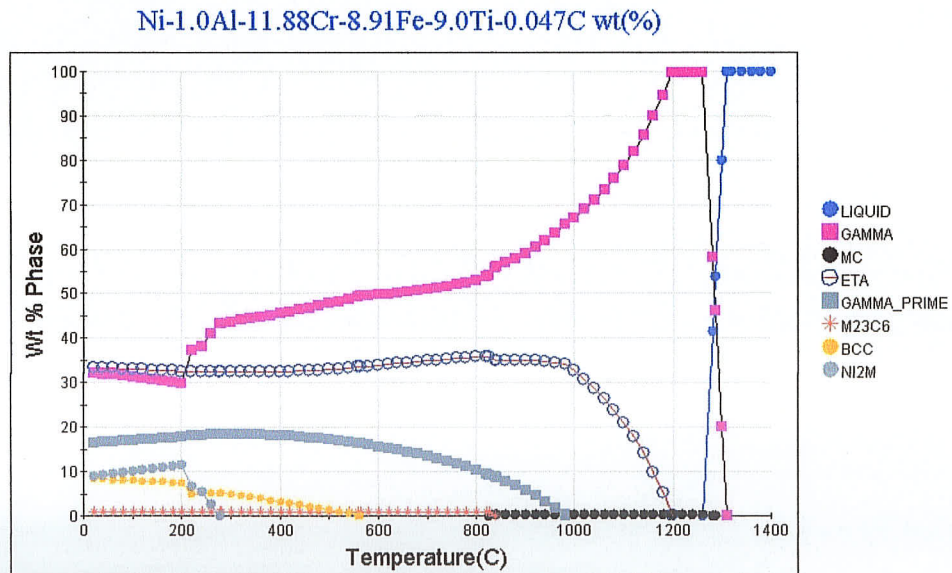


Figure B. 2: JMatPro step calculations for the 1w/o Al 9w/o Ti modified ternary Ni-Cr-Fe alloy

Ni-1.0Al-11.88Cr-8.91Fe-12.0Ti-0.047C wt(%)

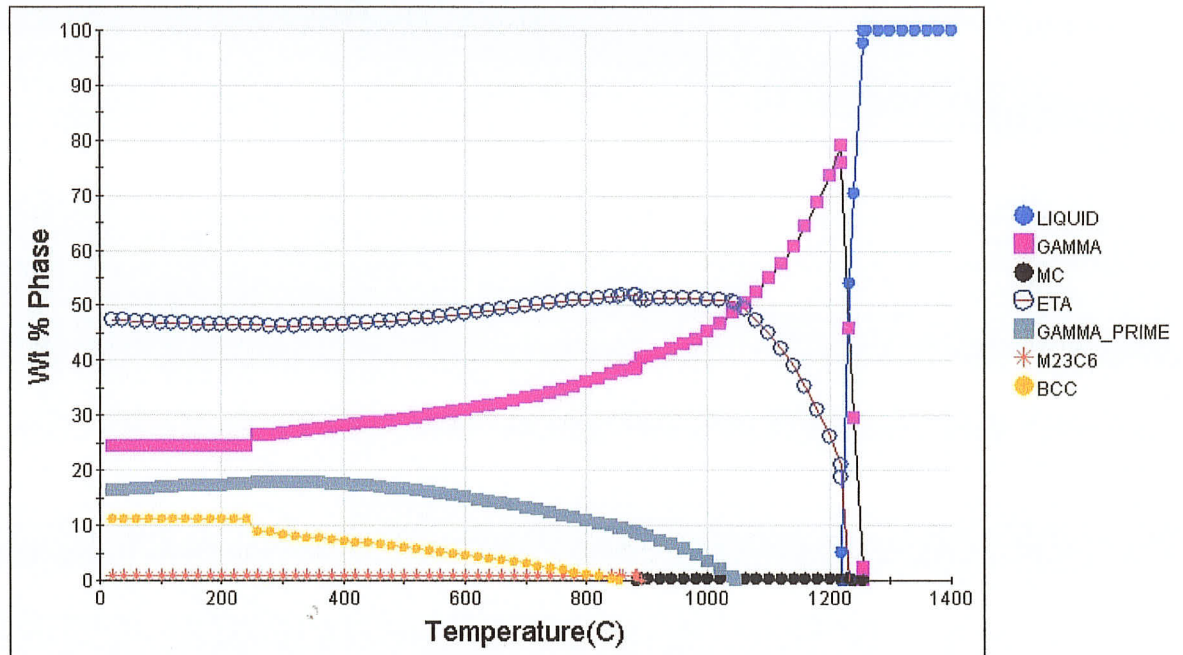


Figure B. 3: JMatPro step calculations for the 1w/o Al 12w/o Ti modified ternary Ni-Cr-Fe alloy

Ni-12.0Cr-9.0Fe-1.0Re wt(%)

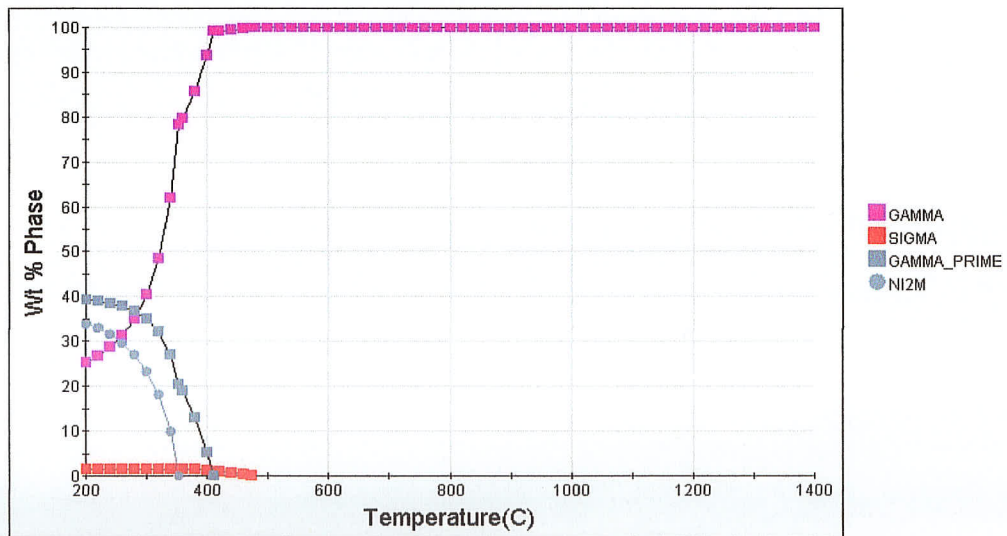


Figure B. 4: JMatPro step calculations for the 1w/o Re modified ternary Ni-Cr-Fe alloy

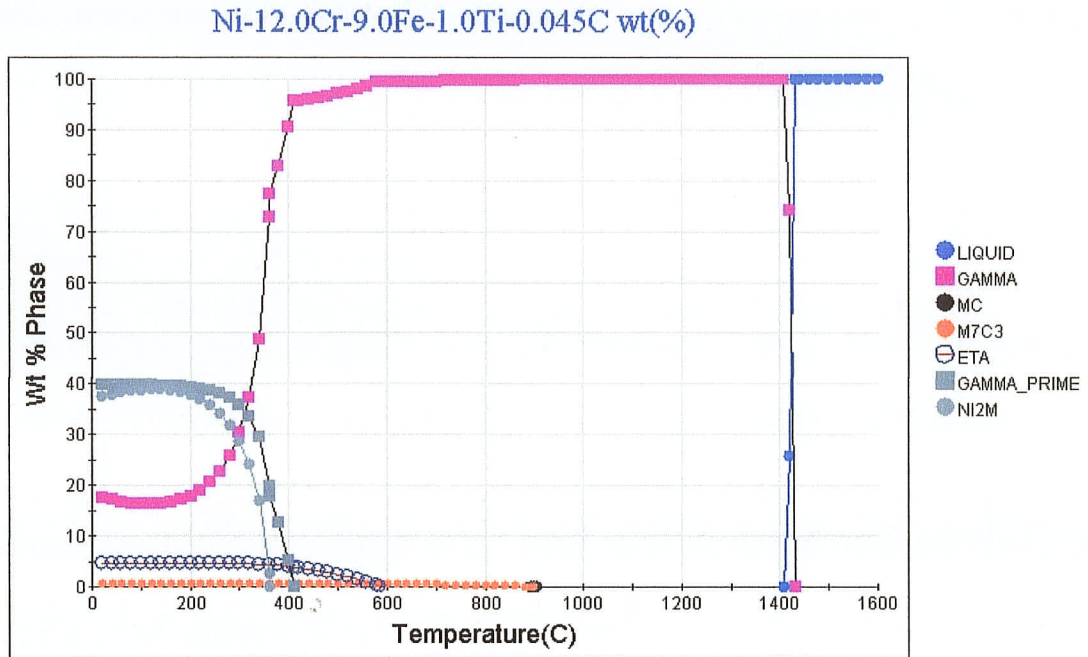


Figure B.5: JMatPro step calculations for the 1 w/o Ti modified ternary Ni-Cr-Fe alloy

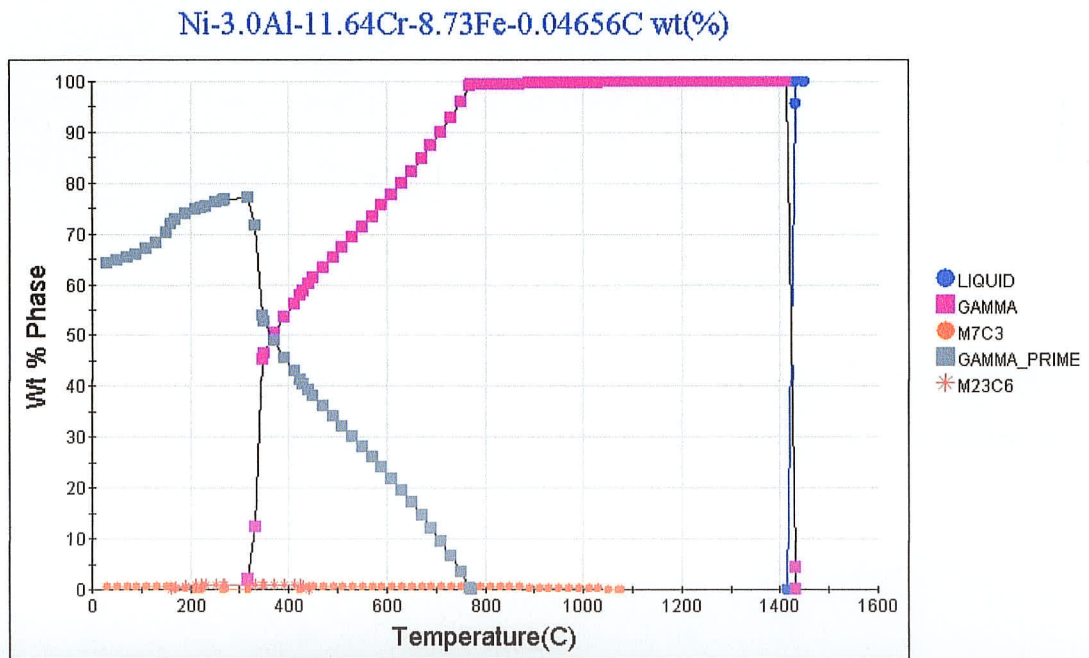


Figure B.6: JMatPro step calculations for the 3w/o Al modified ternary Ni-Cr-Fe alloy

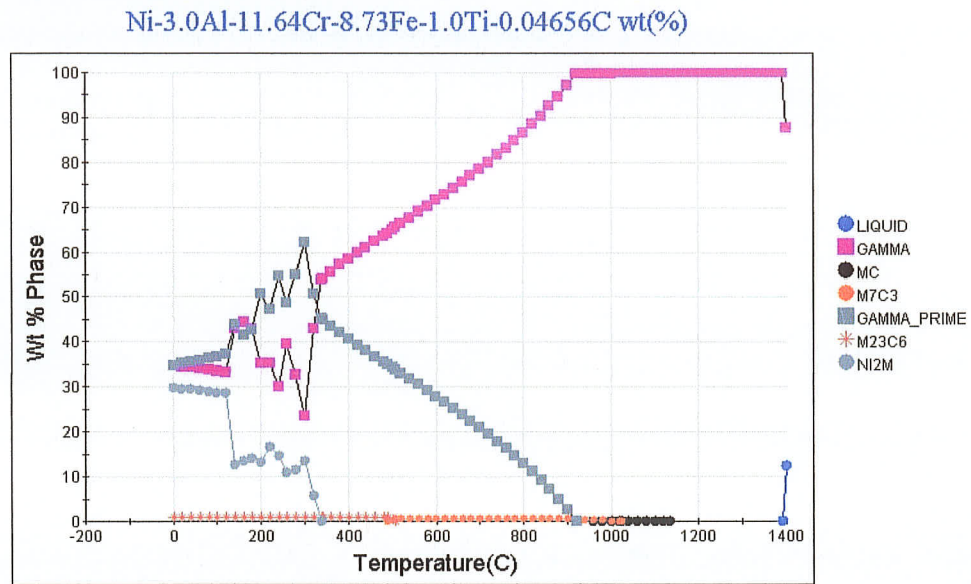


Figure B.7: JMatPro step calculations for the 3w/oAl 1w/o Ti modified ternary Ni-Cr-Fe alloy

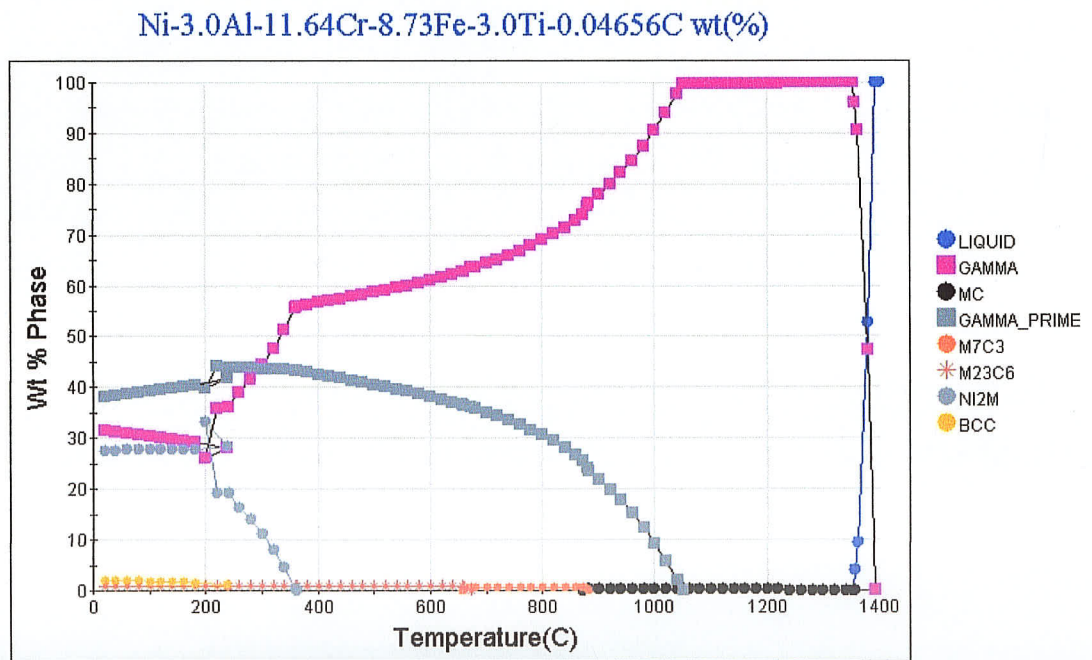


Figure B.8: JmatPro step calculations for the 3w/oAl 3w/o Ti modified ternary Ni-Cr-Fe alloy

Ni-3.0Al-11.64Cr-8.73Fe-6.0Ti-0.04656C wt(%)

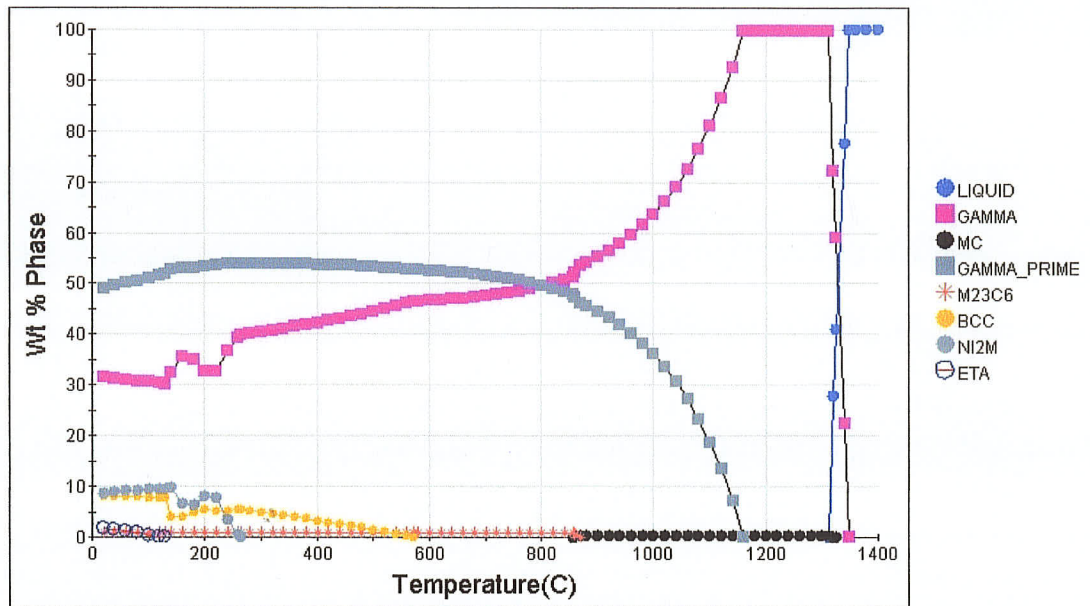


Figure B.9: JmatPro step calculations for the 3w/oAl 6w/o Ti modified ternary Ni-Cr-Fe alloy

Ni-3.0Al-11.64Cr-8.73Fe-9.0Ti-0.04656C wt(%)

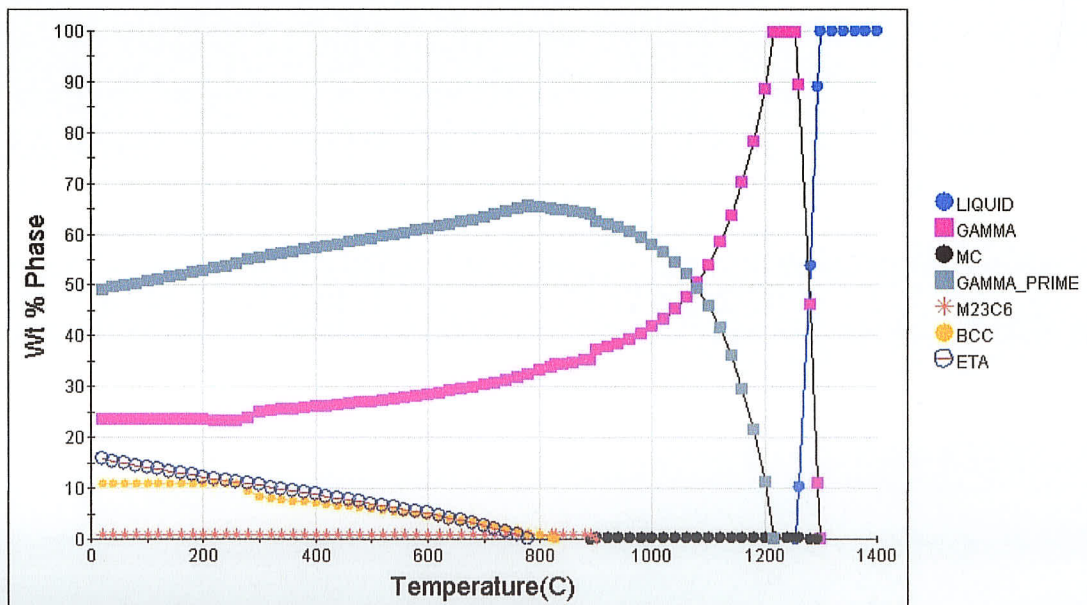


Figure B.10: JmatPro step calculations for the 3w/oAl 9w/o Ti modified ternary Ni-Cr-Fe alloy

Ni-3.0Al-11.64Cr-8.73Fe-12.0Ti-0.04656C wt(%)

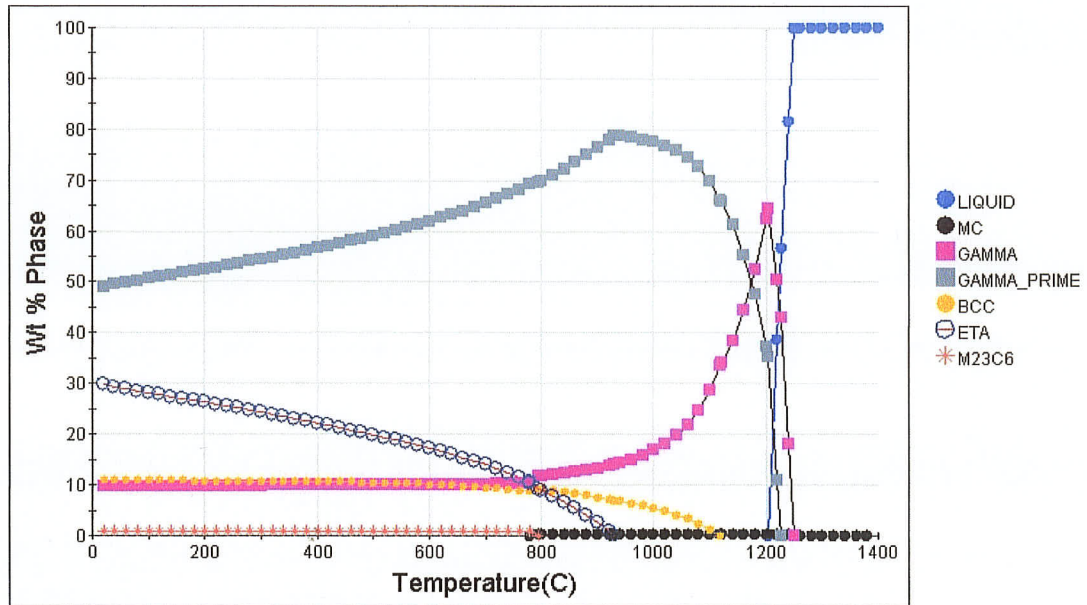


Figure B.11: JmatPro step calculations for the 3w/oAl 12w/o Ti modified ternary Ni-Cr-Fe alloy

Ni-12.0Cr-9.0Fe-3.0Ti-0.045C wt(%)

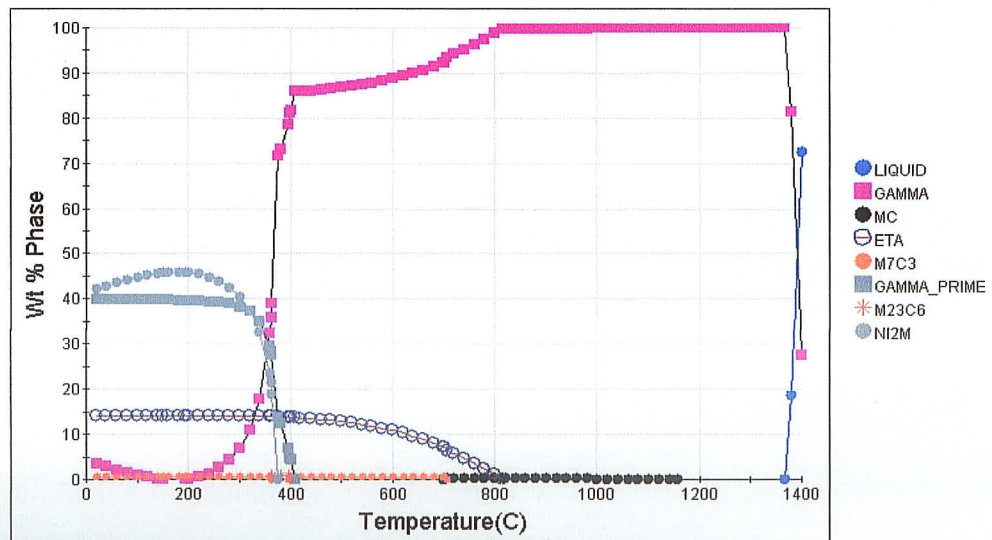


Figure B.12: JmatPro step calculations for the 3w/o Ti modified ternary Ni-Cr-Fe alloy

Ni-6.0Al-11.28Cr-8.46Fe-1.0Re wt(%)

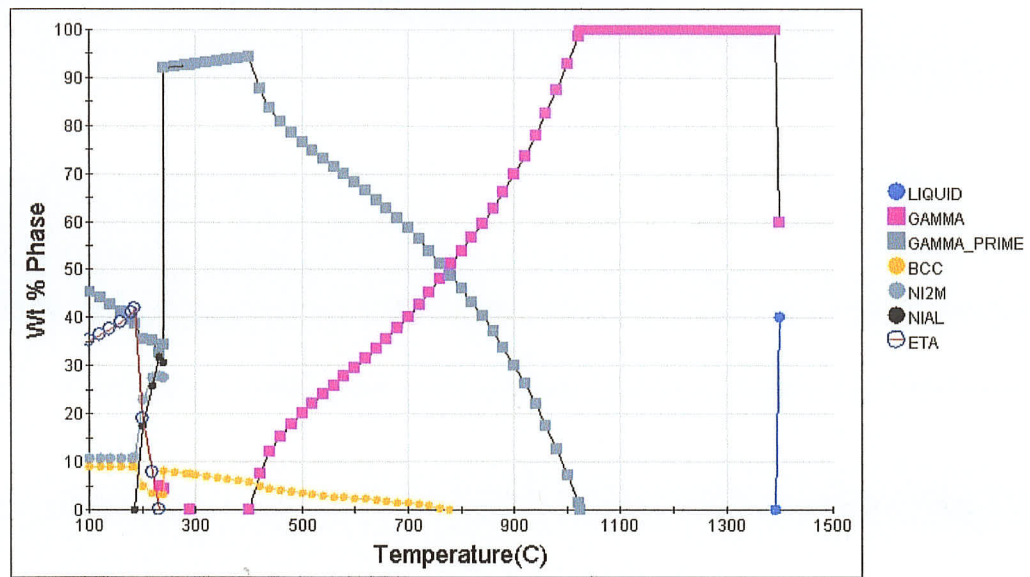


Figure B.13: JmatPro step calculations for the 6w/oAl 1w/o Re modified ternary Ni-Cr-Fe alloy

Ni-6.0Al-11.28Cr-8.46Fe-1.0Ti-0.04512C wt(%)

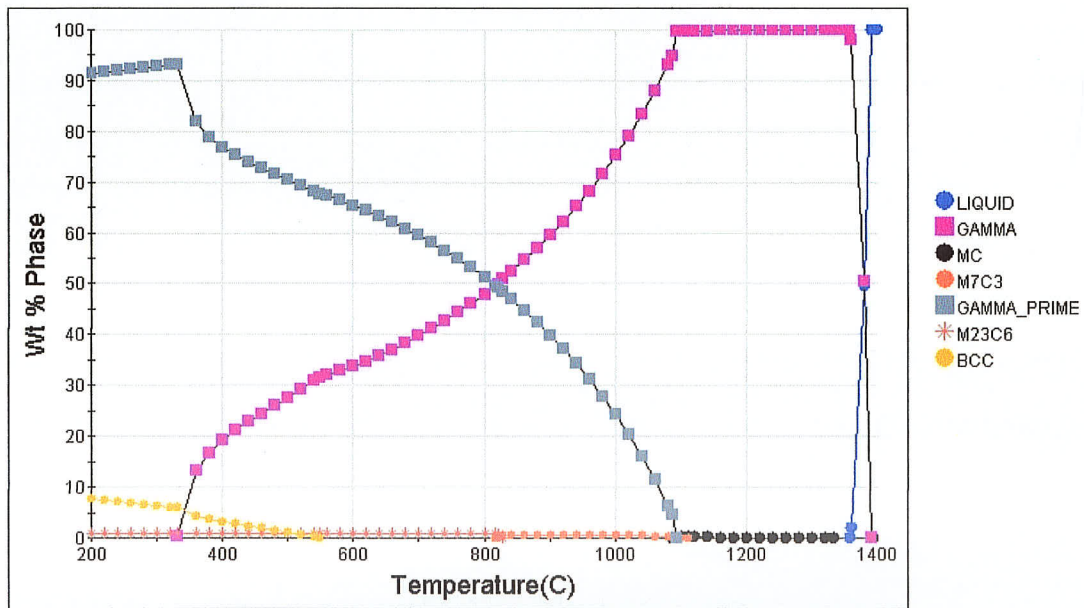


Figure B.14: JmatPro step calculations for the 6w/oAl 1w/o Ti modified ternary Ni-Cr-Fe alloy

Ni-6.0Al-11.28Cr-8.46Fe-3.0Ti-0.04512C wt(%)

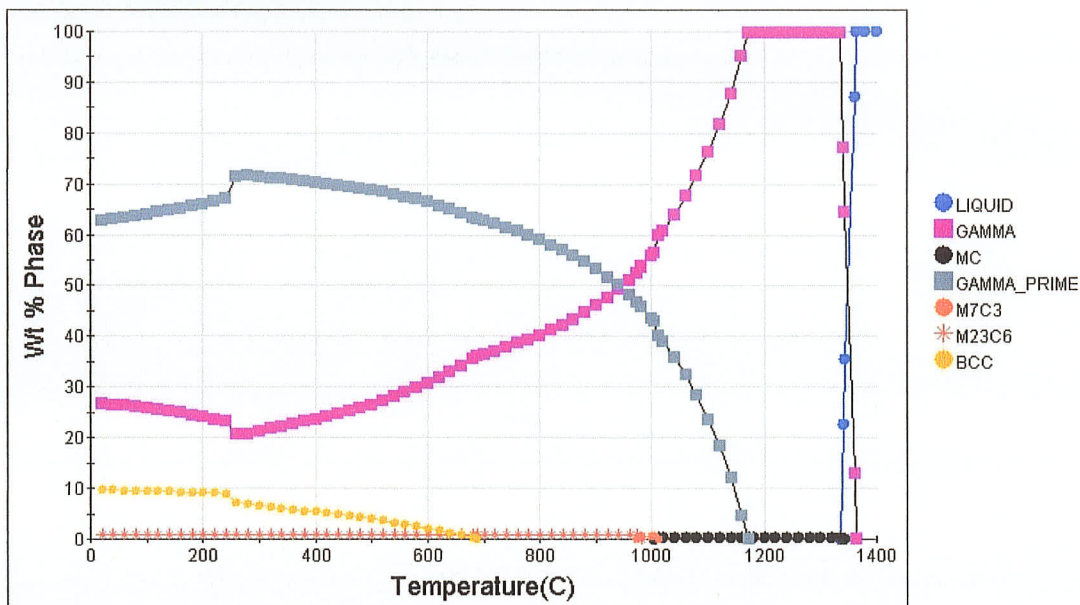


Figure B.15: JmatPro step calculations for the 6w/oAl 3w/o Ti modified ternary Ni-Cr-Fe alloy

Ni-6.0Al-11.28Cr-8.46Fe-6.0Ti-0.04512C wt(%)

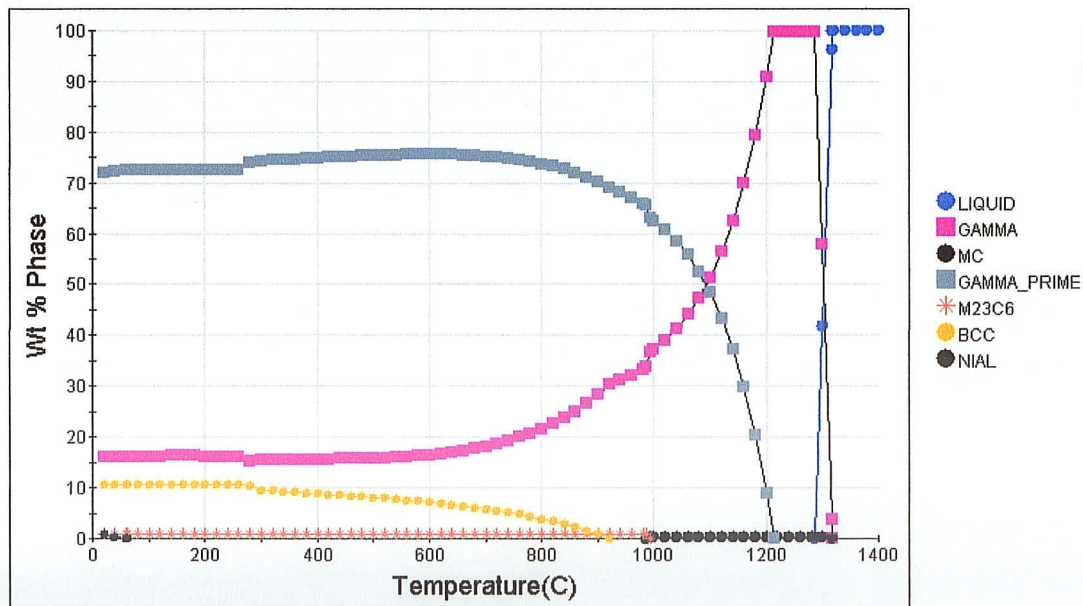


Figure B.16: JmatPro step calculations for the 6w/oAl 6w/o Ti modified ternary Ni-Cr-Fe alloy

Ni-6.0Al-11.28Cr-8.46Fe-9.0Ti-0.04512C wt(%)

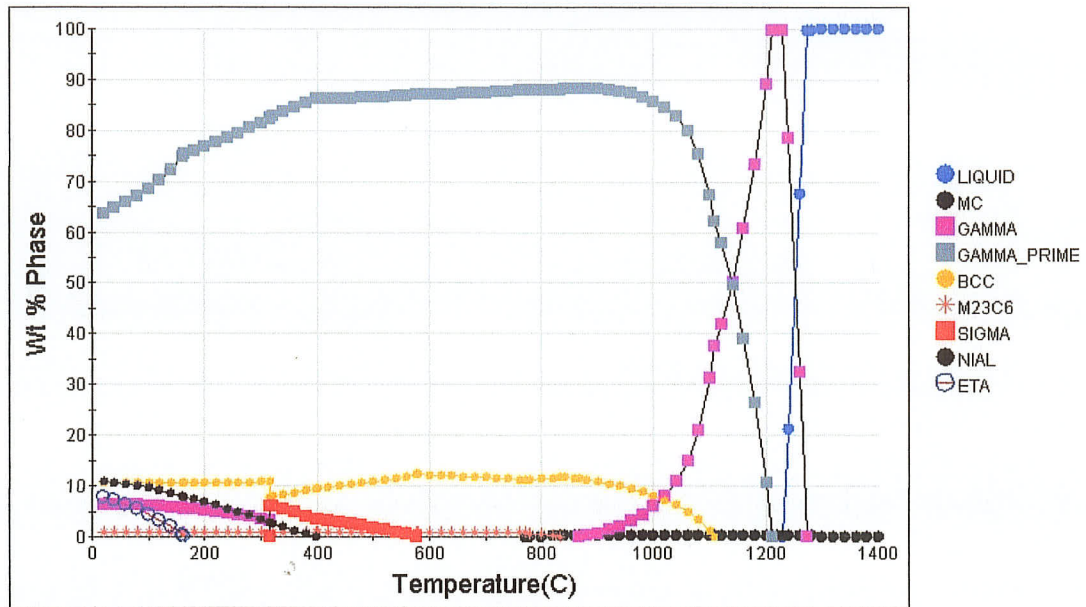


Figure B.17: JmatPro step calculations for the 6w/o Al 9w/o Ti modified ternary Ni-Cr-Fe alloy

Ni-6.0Al-11.28Cr-8.46Fe-12.0Ti-0.04512C wt(%)

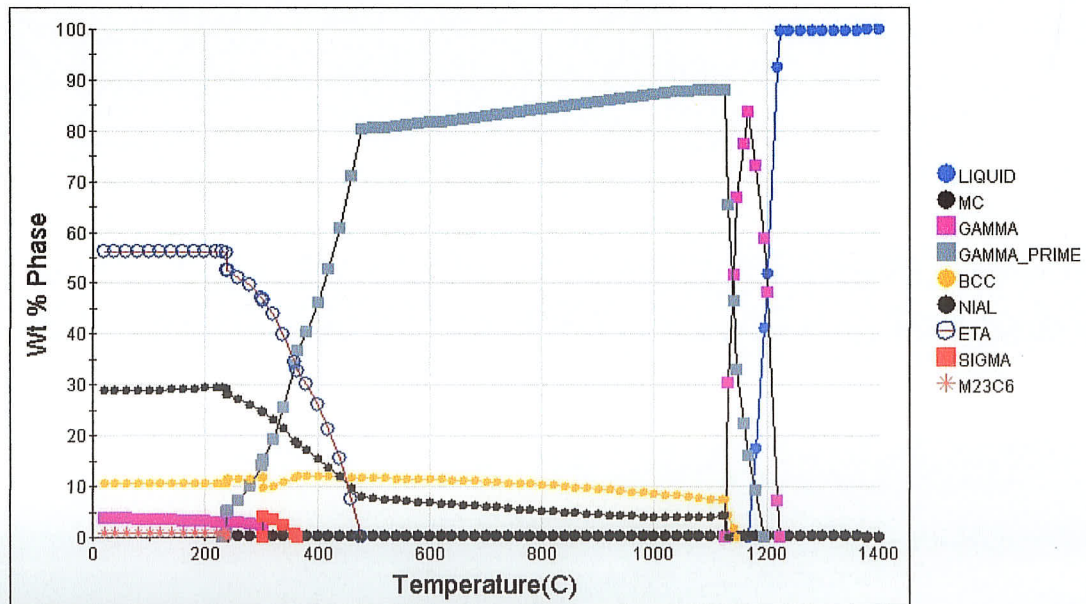


Figure B.18: JmatPro step calculations for the 6w/o Al 12w/o Ti modified ternary Ni-Cr-Fe alloy

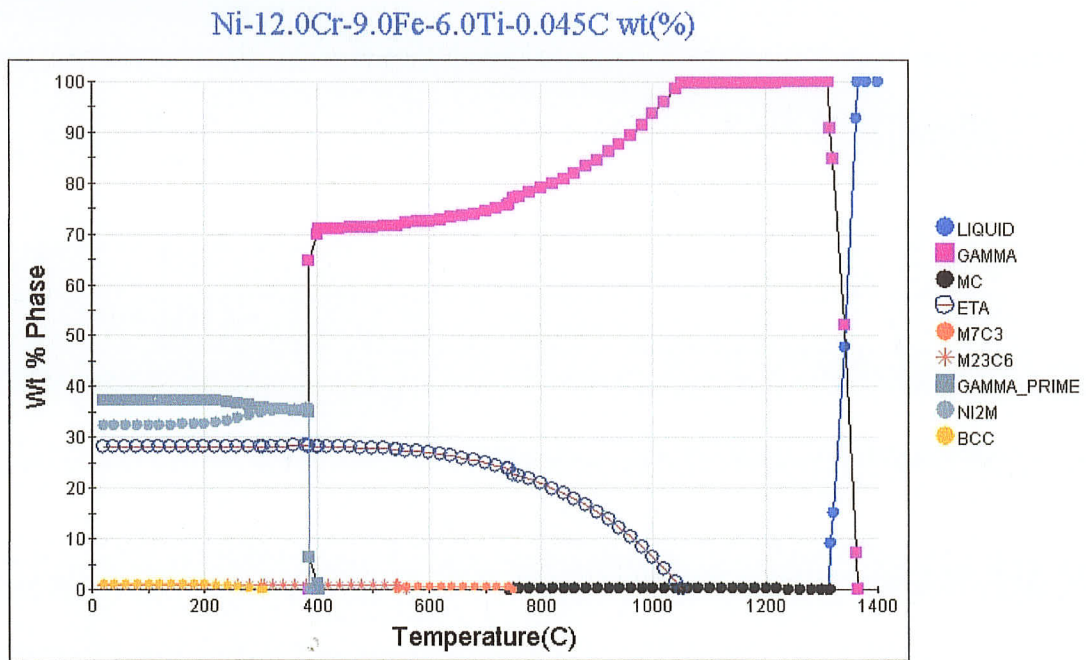


Figure B.19: JmatPro step calculations for the 6w/o Ti modified ternary Ni-Cr-Fe alloy

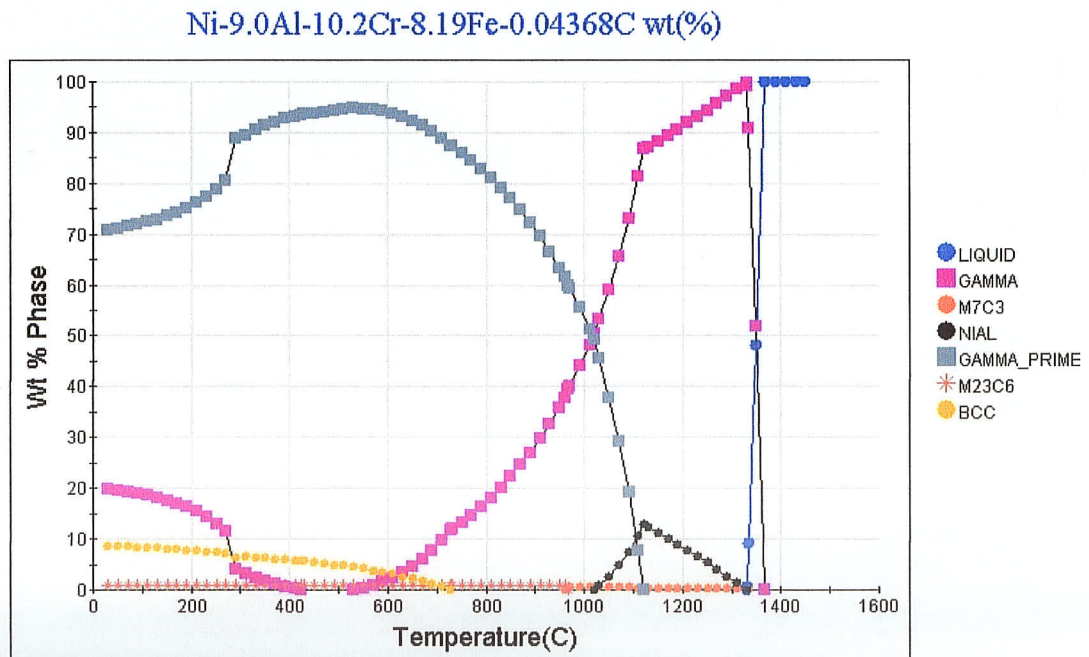


Figure B.20: JmatPro step calculations for the 9w/o Al modified ternary Ni-Cr-Fe alloy

Ni-12.0Al-11.64Cr-8.73Fe-0.04656C wt(%)

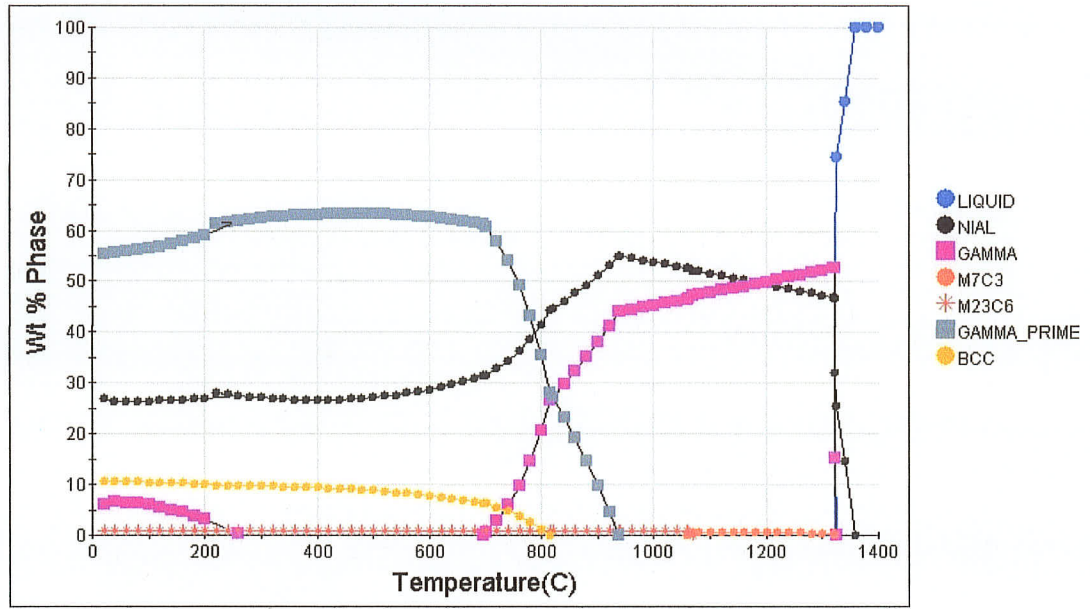


Figure B.21: JmatPro step calculations for the 12w/o Al modified ternary Ni-Cr-Fe alloy

Ni-12.0Al-11.64Cr-8.73Fe-1.0Ti-0.04656C wt(%)

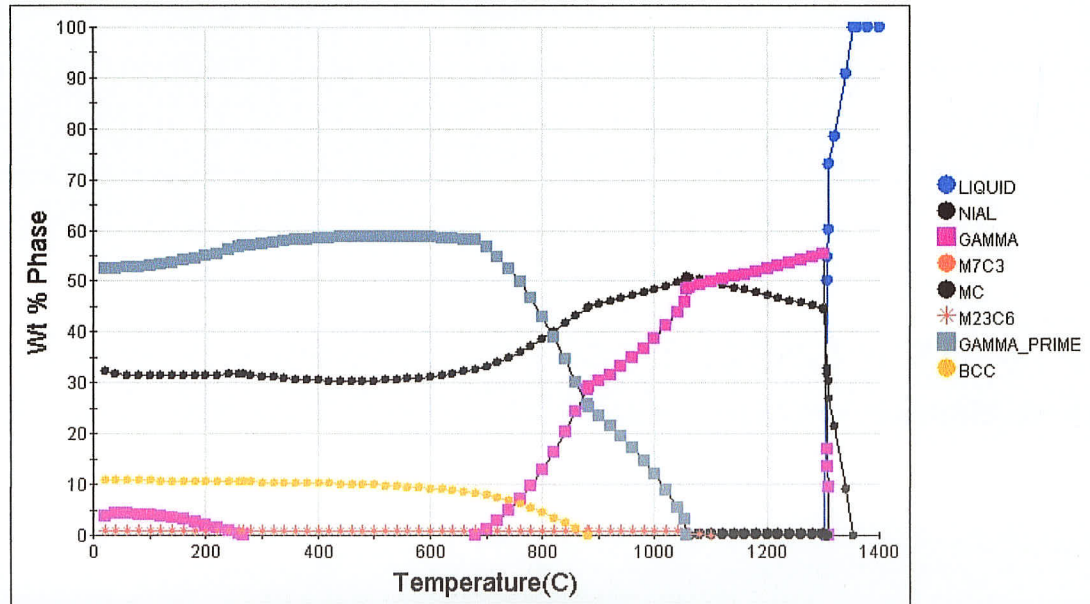


Figure B.22: JmatPro step calculations for the 12w/o Al 1w/o Ti modified ternary Ni-Cr-Fe alloy

Ni-12.0Al-11.64Cr-8.73Fe-3.0Ti-0.04656C wt(%)

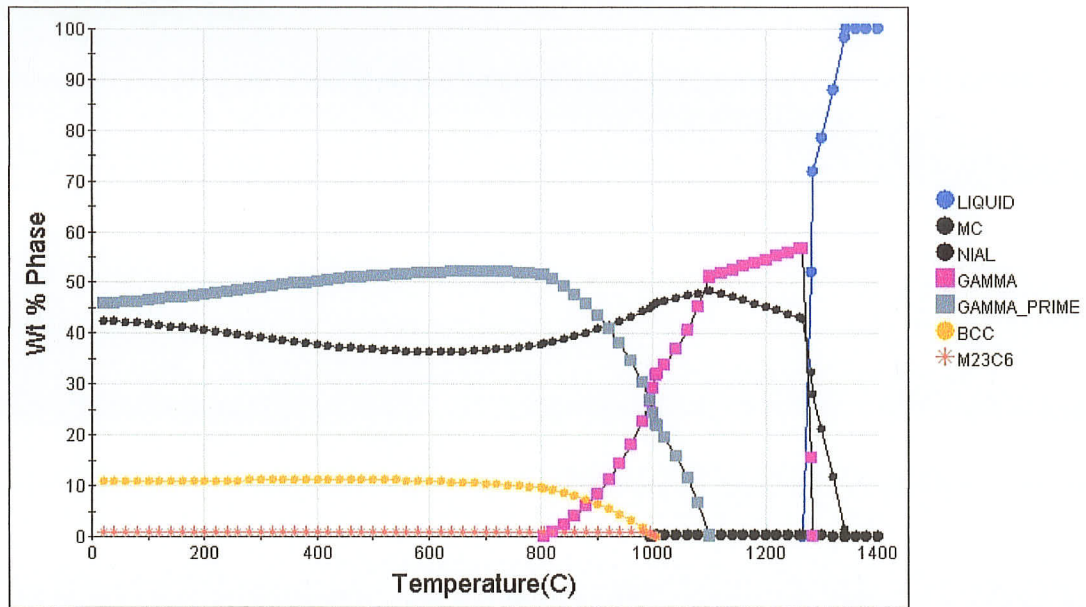


Figure B.23: JmatPro step calculations for the 12w/o Al 3w/o Ti modified ternary Ni-Cr-Fe alloy

Ni-12.0Al-11.64Cr-8.73Fe-9.0Ti-0.04656C wt(%)

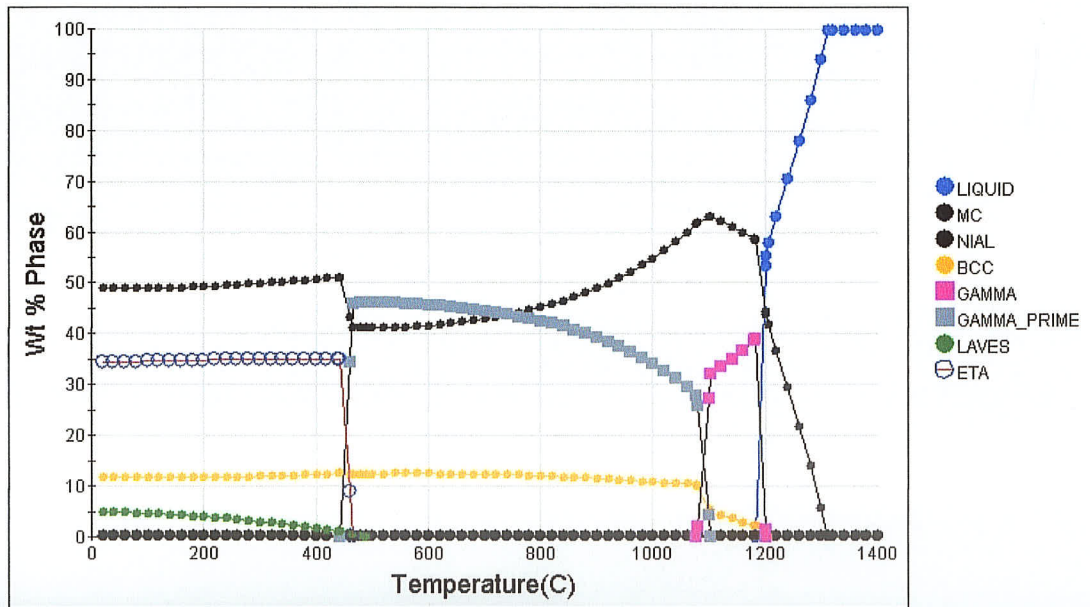


Figure B.24: JmatPro step calculations for the 12w/o Al 9w/o Ti modified ternary Ni-Cr-Fe alloy

Ni-12.0Al-11.64Cr-8.73Fe-12.0Ti-0.04656C wt(%)

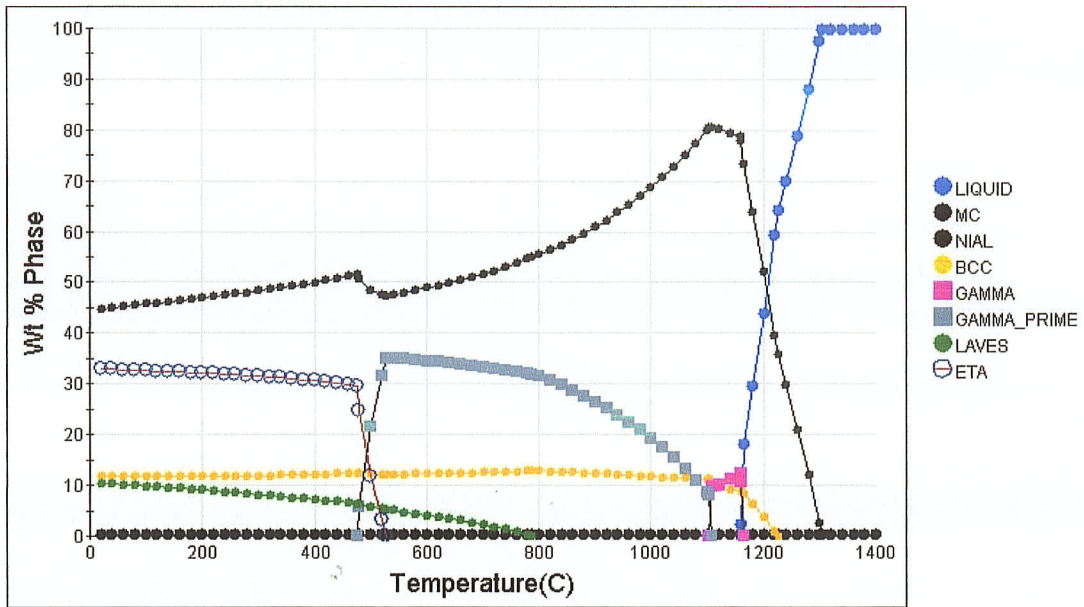


Figure B.25: JmatPro step calculations for the 12w/o Al 12w/o Ti modified ternary Ni-Cr-Fe alloy

Ni-12.0Cr-9.0Fe-12.0Ti-0.045C wt(%)

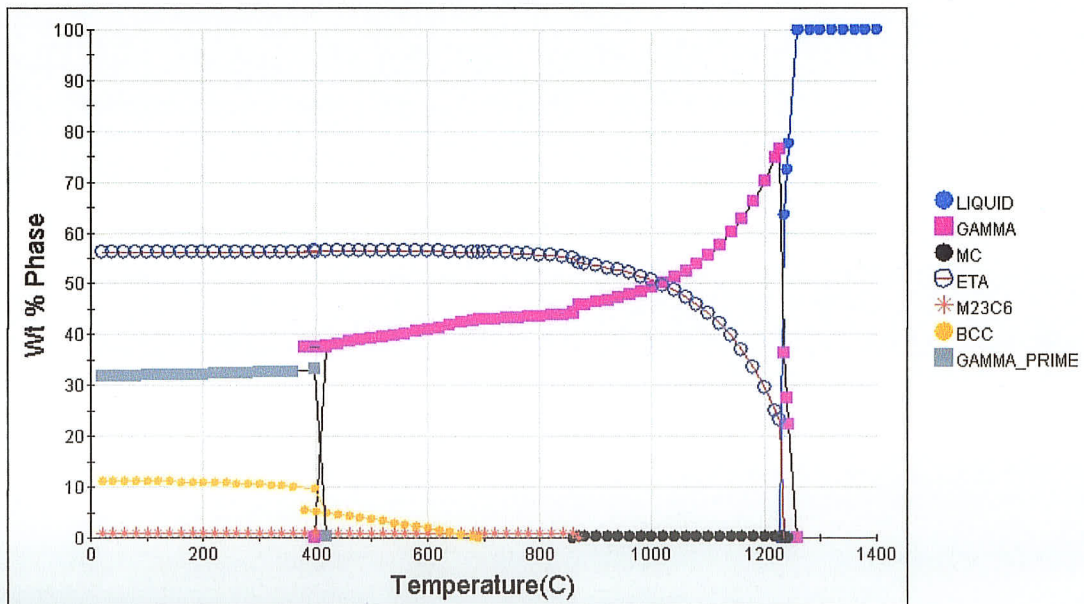


Figure B.26: JmatPro step calculations for the 12w/o Ti modified ternary Ni-Cr-Fe alloy

## REFERENCES

1. Gessinger, G.H. 1984. "*Powder Metallurgy of Superalloys*", Butterworth and Co., London, 347 pages
2. German, R. 2001. "*Powder Metallurgy Science*", Metal powder Industries Federation. New Jersey, U.S.A, 472 pages
3. Justus, S.B., and Eckenrod JJ. 1993. "P/M alloy N690 as A Solution for Intergranular Stress Corrosion Cracking". *Sixth International Symposium on Environmental Degradation of Materials in Nuclear Power Systems-Water Reactors*. The Minerals, Metals and Materials Society.
4. Maurer, G.E. and Castledine, W. 1996. "Development of HIP consolidated P/M Superalloys for conventional forging to gas turbine engine components", *Superalloy*, The Mineral, Metal and Materials Society.
5. Iacocca, R.G. 1996, "Microstructural developments in a P/M braze Superalloy, the effect of thermal cycle", *Metallurgical and Materials Transactions A: Physical Metallurgy and Materials Science*. 27A, p145-153
6. Davies, P.A., Dunstan, G.R., Hayward, A.C. and Howells, R.I.L. 2004. "Metal Injection Moulding of Heat-Treated Alloy 718 Master Alloy". *PM 2004 World congress in Vienna under the auspices of the European Powder Metallurgy Association*.
7. Mankins, W.L., and Lamb, S., eds. 1992. "Nickel and Nickel alloys", *ASM Metals Handbook*. Vol. 2. 10th ed. p 438.

8. Thamburaj, R., Kroul, A.K., Wallace, W., and deMalherbe, M.C., 1984. "Prior particle boundary precipitation in P/M Superalloys" *Modern Developments in Powder Metallurgy, Proceedings of the 1984 International Powder Metallurgy Conference*. Metal Powder Industries, 635-674
9. Kaufman, L., 1970, *Computer calculation of phase diagrams*, Academic Press, New York, USA
10. Chen SL, Zhang F, Daniel S, and Xie FY. 2003. *Journals of Materials*. 55 : p 48
11. Saunders, N., Fahrmann, M., and Small, C.J., 2000. *Superalloys*, p 803-811.
12. Saunders N, Guo Z, Li X, Miodownik AP, and Schille J. 2004. *Superalloys*. 849-858
13. Naiborodenko, Y.S., Itin, V.I., Savitskii, K.V., 1968, "Exothermic Effects During Sintering of a Mixture Of Nickel And Aluminium Powders I". *Soviet Physics Journal*, Vol 11 : 19
14. Moore, J.J., and Feng, H.J., 1995. "Combustion Synthesis of Advanced Materials: Part I: Reaction Parameters". *Progress in Materials Science*, Vol. 39 : p243-273
15. White, D.G., 2002, "History of Powder Metallurgy" In *ASM Handbook: Powder Metal Technologies and Applications*, Eds. Lee, P. W., Trudel, Y., Iacocca, R German, R.M., Ferguson, B.L. Eisen, W.B., Moyer, K., Madan, D., Sanderow, H., The Minerals, Metals and Materials Society, Vol. 7 : p 3-7.
16. International Nickel Company, 1957, *The romance of Nickel*, International Nickel Company, New York.

17. Boldt, J.R., and Queneau, P., 1967, *The winning of nickel*. p 359, Van Nostrand Publishers.
18. Marsh, A.L. 1906. British Patent, *Patent No.2129*
19. Gray, R.D., 1981. "Stellite (R), A history of the Haynes Stellite company" Cabot Corporation, 20, p1912-1972
20. Sims, C.T., Stoloff, N.S., and Hagel, W.C., 1987. *Superalloys II* p101 & p217
21. Decker, R.F., 1969, "Strengthening Mechanisms in Nickel-base Superalloys" *Presentation at the Steel Strengthening Mechanisms Symposium*. Zurich, Switzerland, p 1-23
22. Smith, W.F., 1993, *Structure and Properties of Engineering Alloys*, New York: McGraw-Hill, Inc., p 502-503
23. Stoloff, N.S., 1990, "Wrought and P/M Superalloys in Properties and Selection: Iron, Steels, and High Performance Alloys" *ASM International*. The Mineral Metal and Materials Society, Vol. 1 p 950-977
24. Holt, R.T., and Wallace, W., 1976. *International Metal Reviews*. Vol 21, p 1
25. Muzyka, D.R., 1972, *In Superalloys I*, Eds. Sims, C.T., Hagel, W.C., New York: John Wiley. 33 pp
26. Tracey, V.A., Poyner, G.T., and Watkinson, J.F., 1961. *Journal of Metals*. 13 : 363

27. Tracey, V.A., and Cutler, C.P., 1981, "High-Temperature Alloys from Powders"  
*Powder Metallurgy*. p 32-40
28. Durand-Charre, M., 1997. "*The microstructure of Superalloys*", Gordon and Breach  
Science Publisher.
29. Erickson GL. 1990. "Polycrystalline Cast Superalloys, In Properties And Selection:  
Iron, Steels, And High-Performance Alloys", *ASM Metals Handbook*., The  
Minerals, Metals and Materials Society *Vol. 1*, 981-994.
30. Harris, K., Erickson, G.L., and Schwer, R.E., 1990. "Directionally Solidified And  
Single-Crystal Superalloys, in Properties and Selection: Iron, Steels, and High  
Performance Alloys". *ASM Metals Handbook*, The Minerals, Metals and Materials  
Society, *Vol. 1*, p 995-1006,
31. Trudel, Y., 2002, "Introduction", In *ASM Handbook: Powder Metal Technologies  
and Applications*, Eds. Lee, P.W., Trudel, Y., Iacocca, R., German, R. M., Ferguson,  
B.L., Eisen, W.B., Moyer, K., Madan, D., Sanderow, H., ASM International , The  
Minerals, Metals and Materials Society, *Vol. 7*, p 33-34.
32. Lawley, A., 1992, "Atomisation", Metal Powder Industries Federation, New Jersey,  
USA.
33. Dunkley, J.J., 2002, "Atomisation" In *ASM Handbook: Powder Metal  
Technologies and Applications*, Eds. Lee, P.W., Trudel, Y., Iacocca, R., German,  
R. M., Ferguson, B.L., Eisen, W.B., Moyer, K., Madan, D., Sanderow, H., ASM  
International, The Minerals, Metals and Materials Society, *Vol. 7*, p 35-51.

34. Salak, A., 1995, *Ferrous powder metallurgy*, U.K, Cambridge International Science Publishing, U.K.
35. Goetzel, C.G., 1963, *Treatise on powder metallurgy*, Vol. 2, Akademie-Verlag, Berlin.
36. Ruscoe, M.J.H., and Tuffrey, N.E., 1994, "Fine metal powders by close coupled gas atomisation" PM2TEC Toronto conference proceedings, published as *Advances in Powder Metallurgy and Particle Materials-1995*, p 73-84.
37. Dombrowski, N., and Johns, W.R., 1963, "The Aerodynamics Instability and Disintegration of Viscous Liquid Sheets" *Chem Eng. Sci. Vol. 18*, p 203-214.
38. Wentzell, J.M., 1986, "Particle Size Prediction from Spinning Disk Atomizer", *Powder Metallurgy International, Vol.18*, p 16.
39. Lubanska, H., 1970, "Correlation of Spray Ring Data for Gas Atomisation of Liquid Metals". *J. Me., Vol. 22*, p 45-49.
40. Miller, S.A., and Miller, R.S., 1992, "Real Time Visualization of Close-Coupled Gas Atomisation" *Advances in Powder Metallurgy and Particulate Materials*, Vol. 1, p 112-125.
41. Stencel, J.M., Li, T.X., Neathery, J.K., and Lherbier, L.W., 2000, "Removal Of Ceramic defects from a Superalloy Powder using Triboelectric Processing", *Superalloys, Eds. Pollock, T.M., Kissinger, R.D., Bowman, R.R., Green, K.A.*,

McLean, M., Olson, S., and Schirra, J.J., *The Minerals, Metals and Materials Society*

42. Lenel, F.V., 1980, *Powder metallurgy: Principles and applications*, Metal Powder Industries Federation.
43. Beiss, P., Dalal, K., and Peters, R., 2002, *International Atlas of Powder Metallurgical Microstructures*, p. 3. MPIF, New Jersey, U.S.A
44. Tandon, R., and Johnson, J., 1998, "Liquid-Phase Sintering", Eds. Lee, P. W., Trudel, Y., Iacocca, R German, R.M., Ferguson, B.L. Eisen, W.B., Moyer, K., Madan, D., Sanderow, H., *ASM Handbook, Powder Metal Technologies and Applications*, The Materials Information Society, Vol. 7, pp 565-573.
45. Huppmann, W.J., 1985, "Sintering to high density" *The International Journal of Powder Metallurgy and Powder Technology*. 21 :
46. Exner HE. 1979. Principles of single phase sintering. *Rev. Powder Metall. Phys. Ceram.* ,. 1 :
47. Johnson DL, ed. 1986. "Solid State Sintering" *Encyclopedia of Material Science and Engineering*, MIT Press. Vol. 6. pp 4520-4525.
48. German RM. 1985. The contiguity of liquid phase sintered microstructures. *Metall. Trans.* ,. 16A : 1247-1252
49. Kingery WD. 1959. Densification during sintering in the presence of a liquid phase. *Journal of Applied Physics*. 30 : 301-306

50. Farooq S, Bose A, German RM. 1987. Theory of liquid phase sintering: Model experiments on the W-ni-fe heavy alloy system. *Progress in Powder Metallurgy*. 43 : 65-77
51. Park HH, Yoon DN. 1985. Effect of dihedral angle on the morphology of grains in a matrix phase. *Metall. Trans. .*, 16A : 923-928
52. Uffelmann D, Bender W, Ratke L, Feuerbacker B. 1994. Ostwald ripening in lorentz-force stabilized cu-pb dispersion at low volume fractions. part I: Experimental observations. *Acta Metall. Mater.* 43 : 173-180
53. German RM, Churn KS. 1984. Sintering atmosphere effects on the ductility of W-ni-fe heavy metals. *Metall. Trans. .*, 15A : 747-754
54. Small CJ, Saunders N. 1999. *The application of CALPHAD techniques in development of a new gas-turbine disk alloy. MRS bulletin.*
55. Saunders N, Miodownik AP. 1998. CALPHAD, A comprehensive guide.
56. Jansson B, Schalin M, Selleby M, Sundman B. 1993. Computer software in chemical and extractive metallurgy. 57
57. Saunders N, ed. 1996. *Phase Diagram Calculations for Ni-Based Superalloys*, Warrendale: TMS. 101 pp
58. Kaufman L, Nesor H. 1975. *Met. Trans.* 6A : 2115
59. Kaufman L, Nesor H. 1974. *Met. Trans.* 5 : 1623

60. Kaufman L, Nesor H. 1974. *Met. Trans.* 5 : 1617
61. Rzyman K, Moser Z. 2004. Calorimetric studies of the enthalpies of formation of  $\text{Al}_3\text{Ni}_2$ ,  $\text{AlNi}$  and  $\text{AlNi}_3$ . *Progress in Materials Science.* 49 : 581-606
62. Speyer RF. 1994. *Thermal analysis of materials*, USA: Marcel Dekker Inc
63. Smith EB. 1990. *Basic chemical thermodynamics*, Oxford, England: Oxford University Press. 4th ed.
64. Kissinger HE. 1957. Reaction kinetics in differential thermal analysis. *Analytical Chemistry.* 29 : 1702-1706
65. Porter DA, Easterling KE. 1981. Diffusion. In *Phase Transformation of Metals and Alloys*, 60-102. England: Van Nostrand Reinhold Company Ltd
66. Stringer J. 1987. *High-temperature corrosion of superalloys.* 1987, 3 : 481-493.
67. Smialek JL, Meier GH. 1987. High-temperature oxidation. *Superalloys II.* 293-323
68. Rapp RA. 1973. *High Temperature Corrosion of Aerospace Alloys.* 147-173
69. Wagner C. 1965. *Corr. Sci.* ,. 5 : 751
70. Birks N, Meier GH. 1983. Introduction to high temperature oxidation of metals.
71. Wagner C. 1959. *Z. Elektrochem.* ,. 63 : 772
72. ASTM E967-03 "Standard Test Methods for Temperature Calibration of Differential Scanning Calorimeters and Differential Thermal Analyzers, 2005. 291-294 pp

73. Pruthi DD, Anand MS, Agarwala RP. 1977. Diffusion of chromium in inconel-600. *Journal of Nuclear Materials.* 64 : 206-210
74. Iacocca RG, German RM. 1999. The experimental evaluation of die compaction lubricants using deterministic chaos theory. *Powder Technology.* 102 : 253-265
75. Suryanarayana C, Grant Norton M. 1998. , X-ray diffraction, A practical approach. In 97-105. New York, and London: Plenum Press
76. Hugh Baker, ed. 1992. *ASM Ternary Phase Diagram, Vol. 3.* The Material Information Society.
77. Raynor GV, Rivlin VG. 1988. Phase equilibria in iron ternary alloys.
78. Kortovich CS. 1969. *Rep. AFML-TR-69-101,*
79. Jiang G, Dehn GS, Lannutti JJ, Fu Y, Wagoner RH. 2001. Effect of lubrication and aspect ratio on the consolidation of metal matrix composites under cyclic pressure. *Acta Materialia.* 49 : 1471-1477
80. Armstrong S, Aesoph MD, and Gurson AL. 1995. Effects of lubricant content and relative powder density on the elastic, yield and failure behavior of a compacted metal powder. *Adv. Powder Metallurgy Particulate Mater.* 1 : 31-44
81. Bochini GF, Srl HI, and Genoa R. 1995. *Adv. Powder Metallurgy Particulate Mater.* ,. 1 : 115
82. Exner HE. 1982. Role of interfaces in sintering (*critical assessment*). *Metal Science.* 16 :

83. Thuvander M, Miller MK, and Stiller K. 1999. Grain boundary segregation during heat treatment at 600<sup>0</sup>C in a model alloy 600. *Material Science and Engineering A*. 270 : 38-43
84. Brandes EA, Brook GB, eds. 1999. *Smithell's Metal Reference Book*, Woburn, MA.: Butterworth-Heinemann. . 7th ed.
85. Arendt SA, Bailey SJ, Baldini NC, McElrone EK, Peters KA, et al, eds. 2005. *ASTM Standards B 168, Annual Book of ASTM Standard, Section 2, Non-Ferrous Metal Products*, Vol. 02.04. ASTM international. 145-155 pp
86. Derby B, Wallach ER. 1982. Theoretical model for diffusion bonding. *Metal Science*. 16 : 49-56
87. Salak A, Miskovic V, Dudrova E, Rudnayova E. 1974. *Powder Metall. Int.* 6 :
88. Fleck NA, Smith RA. 1981. *Powder Metallurgy*. 24 :
89. Exner HE, Pohl D. 1978. *Powder Metall. Int.* 10 :
90. Baron RP, Wawner FE, Wert JA. 1998. *Scripta Materialia*. 39 : 269-275
91. German RM. 1989. *Particle packing characteristics*, Princeton, New Jersey, USA: Metal Powder Industries Federation
92. Muller L, Glatzel U, Feller-Kniepmeier. 1992. Modelling thermal misfit stresses in nickel-base superalloys containing high volume fraction of  $\gamma'$  phase. *Acta Metallurgical et Materialia*. 40 : 1321

93. Harding RA, Saunders NJ. 1997. *AFS Transactions*. 49 : 451-458
94. Akinlade DA, Caley WF, Richards NL, Chaturvedi MC. 2006. Development of a nickel base superalloy. *International Journal of Powder Metallurgy*. 42 : 43-56
95. Philpot KA, Munir ZA, Holt JB. 1987. An investigation of the synthesis of nickel aluminides through gasless combustion. *Journal of Materials Science*. 22 : 159-169
96. Hunt EM, Pantoya ML, Jouet RJ. 2006. Combustion synthesis of metallic foams from nanocomposite reactants. *Intermetallics*. 14 : 620-639
97. Krasnowski M, Antolak A, Kulik T. 2007. *J. Alloy & Comp*. 434-435 : 344-347
98. Dey GK. 2003. Physical metallurgy of nickel aluminides. *Sadhana*. 28 : 247-262
99. Alman DE. 1994. Reaction synthesis of ni-36.8at % al. *Journal of Materials Science Letters*. 13 : 483-486
100. Gasparyan AG, Shteinberg AS. 1988. *Combust. Explos. Shock Waves*. 24 : 324-330
101. Grosdidier T, Hazotte A, Simon A. High temperature  $\gamma/\gamma+\gamma'$  transformation in single crystal Ni-based Superalloys; part I: Investigation of the precipitation and dissolution processes, . *Submitted to Acta Materialia*.

## ARTICLES FROM THIS THESIS

1. **Akinlade, D.A.**, Caley, W.F., Richards, N.L., and Chaturvedi, M.C., (2006)  
Development of a powder metallurgy (PM) nickel base Superalloy. International Journal of Powder Metallurgy, 42, 43-56, Metal Powder industries.
2. **Akinlade, D.A.**, Caley, W.F., Richards, N.L., and Chaturvedi, M.C., (2007)  
Microstructural investigation of phase transformations and properties during thermal processing of a 6w/oAl modified Ni-Cr-Fe ternary alloy. Materials Science and Engineering A. *Accepted, article in press* (38pages).
3. **Akinlade, D.A.**, Caley, W.F., Richards, N.L., and Chaturvedi, M.C., (2007)  
Microstructural response of an Al-modified Ni-Cr-Fe ternary alloy during thermal processing. Materials Science and Engineering A. *Accepted, article in press* (8pages)
4. **Akinlade, D.A.**, Caley, W.F., Richards, N.L., and Chaturvedi, M.C, (2007),  
“Thermodynamic Modelling of a 6w/o Al P/M Processed Ni Based Superalloy”,  
in Comp. Met. & Exp. Matls. Characterization, WIT Transactions on Engineering Sciences, 57, 85-94, Italy.
5. **Akinlade, D.A.**, Caley, W.F., Richards, N.L., and Chaturvedi, M.C., (2007)  
Effect of Aluminum Concentration on the Formation of various Phases in Powder Metallurgically Processed Ni-Cr-Fe Superalloy, in PM-07, 4<sup>th</sup> International Conference and Exhibition on Emerging Solutions through Powder Metallurgy in Automotive and Engineering Industry, Noida, India, Feb. 9-11,(12 pages).

6. **Akinlade, D.A.**, Caley, W.F., Richards, N.L., and Chaturvedi, M.C, Arrhenius constants for powder metallurgy processed Ni-Cr-Fe and 6w/o Al modified Ni-Cr-Fe alloys, being reviewed for journal publication.
7. **Akinlade, D.A.**, Caley, W.F., Richards, N.L., and Chaturvedi, M.C., (2008) A study into the effects of heating and cooling rates on an Al modified ternary Ni-Cr-Fe alloy. Abstract submitted to the Conference of Metallurgist (COM).
8. **Akinlade, D.A.**, Caley, W.F., Richards, N.L., and Chaturvedi, M.C., (2006) Thermodynamic modeling of an Aluminum modified P/M nickel-based Superalloy, Oral presentation, 18th annual materials science conference, at McGill University, Montreal, Canada.
9. **Akinlade, D.A.**, Caley, W.F., Richards, N.L., and Chaturvedi, M.C., (2005) Development of Nickel Based Superalloy by Powder Metallurgy Process (Air Sintering), Oral presentation, 17th annual materials science conference, at University of B.C, Vancouver, Canada.

## **Others**

- 1 **Akinlade, D.A.**, and Birur, A., Comparison of Plasma Arc Welding and Gas Tungsten welding process. Phase I, SAL-NRC Project #106-9, Feb 2008, Industrial Technical publication, *Under final review*, Standard Aero Ltd, Winnipeg, Canada.
- 2 Birur, A., Cuddy, J. and **Akinlade, D.A.**, Comparison of Laser and Conventional welding process for Joining of Ti-6Al-4V alloy, abstract submitted to the conference of Metallurgist, Winnipeg, August 2008.

- 3 **Akinlade, D.A.** and Tsakirooulos, P. (2004) A preliminary study into the interactions between chromium molybdenum steel and some molten aluminum alloys, Poster presentation, 16th Annual Materials science conference, Carleton University, Ottawa, Canada.